METEORIC ABLATION IN PLANETARY ATMOSPHERES

by

Juan Diego Carrillo Sánchez

Submitted in accordance with the requirements for the degree of Doctor of Philosophy

University of Leeds

School of Chemistry

January 2017

DECLARATION OF AUTHORSHIP

The candidate confirms that the work contained in the thesis is his own, except where work which has formed part of jointly-authored publications has been included. The contribution of the candidate and the other author to this work has been explicitly indicated below. The candidate confirms that appropriate credit has been given within the thesis where reference has been made to the work of others.

The work contained in *Chapter 2* forms the basis of a jointly-authored paper [*Carrillo-Sánchez et al.*, 2015] published in *Geophysical Research Letters*. The candidate performed all the analyses and prepared the manuscript with the guidance from the co-authors. The author derived the Meteor Input Function – which defines the injection rate of each meteoric element as a function of time a location – using three quite different models of cosmic dust mass/velocity distribution and the meteoric Chemical ABlation MODel (CABMOD) developed by T. Vondrak.

Carrillo-Sánchez, J. D., J. M. C. Plane, W. Feng, D. Nesvorny, and D. Janches (2015), On the size and velocity distribution of cosmic dust particles entering the atmosphere, *Geophysical Research Letters*, *42*(15), 6518-6525, doi:10.1002/2015gl065149.

The results shown in *Chapter 3* pertaining to the development of a novel instrument – the Meteoric Ablation Simulator (MASI) – to measure differential ablation of meteoric metals form part of two jointly-authored manuscripts [*Bones et al.*, 2016; *Gómez-Martín et al.*, 2016]. The first paper has been published in *Review of Scientific Instruments*, whereas the second manuscript is under review for publication in *Astrophysical Journal*. Work by the candidate – to analyze the ablation rates provided by CABMOD for similar sizes and compositions used in MASI, and develop a new and improved version of CABMOD – served to refine and validate CABMOD using the laboratory experimental set-up.

Bones, D. L., J. C. G. Martin, C. J. Empson, J. D. C. Sanchez, A. D. James, T. P. Conroy, and J. M. C. Plane (2016), A novel instrument to measure differential ablation of meteorite samples and proxies: The Meteoric Ablation Simulator (MASI), *Rev. Sci. Instrum.*, *87*(9), 12, doi:10.1063/1.4962751.

Gomez-Martín, J. C., D. Bones, J. D. Carrillo-Sánchez, and J. M. C. Plane (2016), Novel experimental simulations of the atmospheric injection of meteoric metals, *Astrophysical Journal*, *Submitted*.

The results in *Chapter 4* form part of a jointly-authored manuscript [*Carrillo-Sánchez et al.*, 2016] which has been accepted for publication in *Geophysical Research Letters*. All the analyses and the preparation of the manuscript were performed by the candidate with the guidance from the co-authors. The candidate fitted the contribution of different cosmic dust sources which comprises the Zodiacal Cloud – Jupiter-Family comets, asteroids, and Long-Period comets – to the cosmic spherule accretion rate and the Na and Fe fluxes in the mesosphere.

Carrillo-Sánchez, J. D., D. Nesvorný, P. Porkorný, D. Janches, and J. M. C. Plane (2016), Sources of Cosmic Dust in the Earth's Atmosphere, *Geophysical Research Letters*, *Submitted*.

The work contained in *Chapter 5* pertaining to the MAVEN IUVS observations of the comet Siding Spring on Mars form part of a jointly-authored manuscript [*Schneider et al.*, 2015], which has been published in *Geophysical Research Letters*. The candidate modelled the injection rates for Mg using CABMOD and the size/velocity cosmic dust distribution provided by D. Nesvorný using the IRAS observations. The candidate provided the vertical profiles of the injected metals using the 1-D atmospheric model developed by J. M. C. Plane, which contains detailed chemistry of magnesium and iron based on laboratory studies.

Schneider, N. M., et al. (2015), MAVEN IUVS observations of the aftermath of the Comet Siding Spring meteor shower on Mars, *Geophysical Research Letters*, *42*(12), 4755-4761, doi:10.1002/2015gl063863.

Part of the work contained in *Chapter* 5 pertaining to the study of the meteoric ablation in the upper atmosphere of Venus forms part of a jointly-authored manuscript [*Frankland et al.*, 2016b], which has been accepted for publication in *Icarus*. Work by the candidate – development of a version of CABMOD for the Venus atmosphere, and estimate of the contribution of each cosmic dust source to the global mass influx – served to demonstrate that an important fraction of the incoming mass does not ablate, providing a significant surface for the heterogeneous oxidation of CO and CO_2, and the corresponding removal of O_2, below 40 km. The candidate performed and provided analysis for Section 4.1 of the paper 'Modelling the cosmic dust abundance'.

Frankland, V. L., A. D. James, J. D. Carrillo-Sánchez, D. Nesvorný, and J. M. C. Plane (2016a), CO Oxidation and O2 Removal on Meteoric Material in Venus' Atmosphere, *Icarus*, *In progress*.

The third part of *Chapter 5* pertaining to the impact of cosmic dust in the upper atmosphere of Titan form part of a jointly-authored manuscript [*Frankland et al.,* 2016a], which has been published in *Icarus*. Work by the candidate – development of a version of CABMOD for the Titan atmosphere and analysis of cosmic dust particles entering Titan's atmosphere – demonstrated that ablation is not significant, providing a significant surface on cosmic dust particles for heterogeneous chemistry. The candidate performed and provided analysis for Section 4.1 of the paper 'Modelling the cosmic dust abundance'.

Frankland, V. L., A. D. James, J. D. C. Sanchez, T. P. Mangan, K. Willacy, A. R. Poppe, and J. M. C. Plane (2016b), Uptake of acetylene on cosmic dust and production of benzene in Titan's atmosphere, *Icarus*, *278*, 88-99, doi:10.1016/j.icarus.2016.06.007.

ACKNOWLEDGMENTS

Firstly, I would like to thank my supervisor – Prof. John M. C. Plane – who has mentored and guided me throughout these four years, and has provided valuable advice. Without his guidance, this work and the production of this thesis would not have been possible. I would like to extend my thanks to David Nesvorný, Diego Janches, Chester S. Gardner, and Petr Pokorný, all of whom have provided data and valuable suggestions.

A big thank you to all the members of my reseach group. Thanks for your support and invaluable friendship over these years. Without doubt, all of you have made possible for me not to feel like a foreigner or a stranger. I will not ever forget your courtesy and friendship. I would also like to give an special thanks to Wuhu Feng in whom I have found not only a collaborator but a great friend, Juan Carlos Gómez Martín who has become a reference for me because of his brilliance and talent, and David Bones in whom I have discovered a great person.

Finally, I would like to give my sincerest thank you to my parents, my sister, our great family’s friend Vicente Gradillas, and Thuzar Oo. A few words are not enough to give back all your support. I am eternally indebted to you.

ABSTRACT

The magnitude of the rate at which cosmic dust enters the Earth's atmosphere has been highly uncertain, with a daily mass influx ranging between 5 t d^{-1} and 270 t d^{-1}. In fact, this issue has an important implication because if the upper limit of the estimates is correct, then vertical transport in the middle atmosphere must be faster than is generally assumed. On the other hand, if the lower limit is correct, then our understanding of the cosmic dust evolution in the solar system, and the transport mechanisms from the middle atmosphere to the Earth's surface will need to be revised.

The aim of the work described in this thesis is to estimate a Meteor Input Function (MIF) that allows to understand different atmospheric phenomena in the Mesosphere-lower Thermosphere (MLT). For this purpose, the Zodiacal Cloud Model (ZCM) which is contrained by mid-Infrared observations of the zodiacal dust is evaluated. The ZCM is a detailed dynamical model that attempts to explain the origin of cosmic dust and accounts for the directionality, and mass and velocity distribution of Interplanetary Dust Particles (IDPs) in the inner solar system.

The thesis is divided into four parts. First, the ZCM – constrained by measurements of the Infrared Astronomical Satellite (IRAS) – is evaluated using the Chemical ABlation MODel developed at the University of Leeds. These results are compared with those obtained from two quite different distributions: the Long Duration Exposure Facility (LDEF) and the incoming flux measured by meteor head echo detections with High-Power and Large-Aperture (HPLA) radars. Second, a newly-developed laboratory Meteor Ablation Simulator (MASI) is used to test the thermodynamic model within CABMOD as well as the use of the Hertz-Knudsen relation to describe the kinetics of evaporation; the Na, Fe, and Ca ablation rate profiles modelled by CABMOD are then refined. Third, the absolute contribution of each cosmic dust population –Jupiter-Family Comets (JFCs), Asteroids (ASTs), and Long-Period Comets (LPCs)– to the global input is estimated accounting for the most recent version of the ZCM constrained by Planck satellite observations, the cosmic flux accretion rate at the bottom of an ice chamber at the the Amudsen-Scott base at South Pole, and recent measurements of the vertical fluxes of Na and Fe atoms above 87.5 km in the atmosphere. Finally, the impact of cosmic dust on the atmospheres of Venus, Mars and Titan is examined.

TABLE OF CONTENTS

LIST OF FIGURES

LIST OF TABLES

LIST OF ACRONYMS

AMOR	Advanced Meteor Orbit Radar
ASTs	Asteroids
AURIC	Atmospheric Ultraviolet Radiance Integrated Code
CABMOD	Chemical ABlation MODel
CAI	Calcium-Aluminum Inclusions
CAMO	Canadian Automated Meteor Observatory
CI	Carbonaceous Ivuna
CME	Chemistry of Micrometeoroids Experiments
CMOR	Canadian Meteor Orbit Radar
COBE	COsmic Background Explorer
DAR	Differential Ablation Ratio
DIRBE	Diffuse Infrared Background Experiment
EKB	Edgeworth-Kuiper Belt
EPDM	Ethylene Propylene Dienemonomer Mat
ESABASE	European Space Agency Meteoroid/Debris DataBASE
FIRAS	Far-Infrared Absolute Spectrophotometer
FRECOPA	FREnch COoperative PAyload
FWHM	Full Width at Half Maximum
GMCs	Giant Molecular Clouds
HASI	Cassini-Huygens Atmospheric Structure Investigation
HPLA	High-Power and Large-Aperture
HRMP	Harvard Radio Meteor Project
HTCs	Halley-Type Comets
IDE	Interplanetary Dust Experiment
IDPs	Interplanetary Dust Particles
IRAS	Infrared Astronomical Satellite
IRIS	Infrarred Radiometer Interferometer Spectrometer
IUVS	Imaging UltraViolet Spectrograph
JFCs	Jupiter-Family Comets
KBOs	Kuiper Belt Objects
LDEF	Long Duration Exposure Facility
LEO	Low Earth Orbit

LIF	Laser-Induced Fluorescence
LINEAR	Lincoln Laboratory Near-Earth Asteroid Research project
LONEOS	Lowell Observatory Near-Earth Object Search
LPCs	Long-Period Type Comets
MAGMA	Gas-melt chemical equilibrium code
MAP	MicroAbrasion Package
MASI	Meteor Ablation SImulator
MASTER	Meteoroid And Space debris Terrestrial-Environment Reference
MAVEN	Mars Atmosphere and Volatile EvolutioN
MD-SIG	Meteoroid and Debris Special Investigation Group
MIF	Meteoric Input Function
MLT	Mesosphere and Lower Thermosphere
MMs	Micrometeorites
MSPs	Meteoric Smoke Particles
NCP	North Celestial Pole
NEAs	Near-Earth Asteroids
NEAT	Near-Earth Asteroid Tracking
NGIMS	Neutral Gas and Ion Mass Spectrometer
OC	Ordinary Chondrite
OCCs	Oort-Cloud Comets
ONMS	Orbiter Neutral Mass Spectrometer
RCS	Radar Cross-Section
RSS	Radio-Science Subsystem
RTI	Range-Time-Intensity
SDC	Student Dust Counter
SDIE	Space Debris Impact Experiment
SMR	Specular Meteor Radar
SOR	Starfire Optical Range
SPWW	South Pole Water Well
TIM	Total Input Mass
UHCRE	Ultra-Heavy Cosmic Ray Experiment
UMMs	Unmelted Micrometeorites
UVS	Ultraviolet Spectrometer

WACCM	Whole Atmosphere Community Climate Model
WHAM	Wisconsin H-Alpha Mapper
ZA	Zenith Angle
ZCM	Zodiacal Cloud Model

LIST OF ABBREVIATIONS

a	semi-major axis of the comet's orbit
a_i	thermodynamic activity for i-th component
a_J	semi-major axis of Jupiter's orbit
β	ratio of the force of radiation pressure to the force of gravity
C	specific heat capacity of the meteoroid
δ_S	distance from the Sun of a particle in the Zodiacal Cloud
ε	emissivity of the meteoroid
$f(T)$	phase transition factor
f_0	pre-exponential factor (power law)
γ_i	apparent evaporation coefficient
γ_i^*	Raoultian activity coefficient of the oxide relative to the pure liquid oxide
Γ	dimensionless free-molecular drag coefficient
g	gravitational acceleration
H_{10}	cometary absolute magnitude
H_N	magnitude of the comet nucleus would have at 1 AU
i	inclination of the comet's orbit respect the galactic plane
Λ	free molecular heat transfer coefficient
L	latent heat of vaporization/sublimation
k_B	Boltzmann's constant
k_{zz}	Eddy diffusion coefficient
μ_i	molecular weight
$M_\oplus$	Mass of the Earth
M_t	atomic number of the target
ψ_{AST}	global mass accretion rates of Na, Fe or spherules from AST population
ψ_{JFC}	global mass accretion rates of Na, Fe or spherules from HTC population
ψ_{LPC}	global mass accretion rates of Na, Fe or spherules from LPC population
ψ_{Total}	total global mass accretion rate of Na atoms, Fe atoms or cosmic spherules
p_i	gas-liquid equilibrium vapour pressure
ρ_a	mass density of the atmosphere
ρ_i	number density of the i-th atmospheric compound
ρ_m	mass density of the meteoroid

τ_{col}	collisional lifetime of a particle
τ_{PR}	Poynting-Robertson drag timescale
Q_{pr}	radiation pressure coefficient
q	perihelion distance
P	orbital period
R	meteor radius
S	Area of the meteoroid
σ	Stefan-Boltzmann constant
θ	impact angle of the meteoroid respect the zenith
T_a	effective temperature of the atmosphere in the region of the meteoroid
T_c	melting temperature (center of the sigmoid)
T_J	Tisserand parameter
v	velocity of the meteoroid
v_{1AU}	velocity of meteoroids at 1 AU
v_J	average velocity for a circular orbit of Jupiter
v_{rel}	relative velocity between comet and Jupiter
$\bar{v}_{Titan}$	Mean velocity of meteoroids entering into Titan's upper atmosphere
v_∞	escape velocity from the surface of the planet
x_i	element atomic fractions in the meteoroid
Y_i	sputtering cross-section for the *i*-th atmospheric component
η_e	gravitational enhancement

CHAPTER 1: INTRODUCTION

1.1. OVERVIEW

The magnitude of the rate at which cosmic dust enters into the Earth's atmosphere has been discussed widely. Table 1.1 shows recent estimates of the daily mass input of Interplanetary Dust Particles (IDPs) that vary between 5 t d^{-1} and 270 t d^{-1} [*Plane*, 2012]. Zodiacal cloud observations and space-based dust collectors (blue shading in Table 1.1) indicate an input of 41-270 t d^{-1}, which is mostly in agreement with the accumulation rates of cosmic elements in polar ice cores and deep-sea elements (green shading). In contrast, measurements in the middle atmosphere (yellow shading) performed by radar, lidar, high-flying aircraft, and satellite remote sensing, indicate that the input is only 5-50 t d^{-1}.

As outlined in *Plane* [2012], this has an important implication because if the upper range of the estimates is correct, then vertical transport in the middle atmosphere must be faster than it is generally thought to be, and meteoritic material is removed more rapidly; if the lower range is correct, then our understanding of the dust evolution in the solar system, and transport mechanisms from the middle atmosphere to the Earth's surface will need to be revised.

The main purpose of the work described in this thesis is: 1. To analyze the impact of the most recent model describing the dynamics of the Zodiacal Dust Cloud constrained by infrared observations of the zodiacal light [*Nesvorný et al.*, 2010; *Nesvorný et al.*, 2011]; 2. To test and refine the Chemical ABlation MODel (CABMOD) [*Vondrak et al.*, 2008] using the newly-developed laboratory Meteor Ablation SImulator (MASI) [*Bones et al.*, 2016; *Gomez-Martín et al.*, 2016]; 3. To estimate the contribution of the different dust sources of the Zodiacal Cloud to the global influx at the Earth [*Carrillo-Sánchez et al.*, 2016]; and 4. To extend the analysis of the meteoric layers to other solar system bodies such as Venus, Mars and Titan using CABMOD.

This chapter provides an introduction to the subject. In Section 1.2, an overview of the different sources of cosmic dust in the Zodiacal Cloud is provided. The processes involved in the meteor ablation, as well as the structure of CABMOD, are introduced and discussed in Section 1.3. A brief overview of the meteoric layers in Venus, Mars and

Titan is presented in Section 1.4. The specific aims and objectives of this thesis are outlined in Section 1.5, and finally the thesis layout is presented in Section 1.6.

Table 1.1. *Estimates of the global cosmic dust input rate to the Earth's atmosphere (blue = extra-terrestrial estimate; green = middle atmosphere estimate; yellow = ice core/deep-sea estimate). Adapted from Plane [2012]*.

Technique	**IDPs input $t\ d^{-1}$**	**Reference**	**Potential problem of technique**
Zodiacal Dust Cloud modelling	270	*Nesvorný et al.* [2010]	Needs to be constrained by terrestrial meteor radars
Zodiacal Dust Cloud modelling	41	*Nesvorný et al.* [2011]	Needs to be constrained by terrestrial meteor radars
Long Duration Exposure Facility	110 ± 55	*Love and Brownlee* [1993]	Sensitive to cosmic dust velocity distribution
High performance radars	5 ± 2	*Mathews et al.* [2001]	Possible velocity bias/selective mass range
Conventional meteor radars	44	*Hughes* [1978]	Extrapolation, selective mass/velocity distribution
Na layer modelling	20 ± 10	*Plane* [2004]	Sensitive to vertical eddy diffusion transport
Fe layer modelling	6	*Gardner et al.* [2011]	Depends on vertical transport
Fe/Mg in stratospheric sulphate layer	22-104	*Cziczo and Froyd* [2011]	Data has limited geographic extent
Optical extinction measurements	10-40	*Hervig et al.* [2009]	Particle refractive indices uncertain
Fe in Antarctic ice core	15 ± 5	*Lanci et al.* [2012]	Very little wet deposition by snow
Fe in Greenland ice core	175 ± 68	*Lanci and Kent* [2006]	Uncertain atmospheric transport/deposition
Ir and Pt in Greenland ice core	214 ± 82	*Gabrielli et al.* [2004a]	Uncertain atmospheric transport/deposition
Os in deep-sea sediments	101 ± 36	*Peucker-Ehrenbrink* [1996]	Focusing by ocean currents
Ir in deep-sea sediments	240	*Wasson and Kyte* [1987]	Focusing by ocean currents

1.2. SOURCES OF COSMIC DUST

The meteoroid influx can be divided into a shower and a sporadic component. A meteor shower occurs when the Earth passes through the annulus of debris produced by a decaying comet [*Jacchia*, 1963]. The meteoroid dust is blown away from the cometary nucleus by gas pressure in all directions. The maximum gas efflux occurs near perihelion, so this is the place where the majority of the dust is introduced into the meteor stream. The meteor stream decays into the solar system dust cloud by the effect of radiation forces and gravitational perturbations from close encounters with planets, whereas collisions between the stream particles and particles that already exist in the dust cloud may have a less significant contribution. Accordingly, all these effects together contribute to form the sporadic background.

Figure 1.1 shows that particle mass can vary by 30 orders of magnitude, although the largest contribution of mass entering the atmosphere on a daily basis has been thought to come from particles with a mass of ~10 µg [*Flynn*, 2002]. However, the input flux of meteoroids is uncertain because a single technique cannot observe particles over the mass range from about 10^{-12} to 1 g. Interestingly, there is a population of huge impactors with masses larger than 10^{10} g which would make a significant contribution, although only on a geological scale.

Optical camera networks can observe visible meteors larger than about 1 mg. Meteor radars can detect particles with masses between about 10^{-9} g and 10^{-3} g, covering the most important mass range. The population of IDPs smaller than 10^{-9} g can only be measured by impact detectors on satellites. An important estimate of the IDP input was provided by the Long Duration Exposure Facility (LDEF), an orbital detector placed on a spacecraft for several years [*Love and Brownlee*, 1993; *Love et al.*, 1995; *McDonnell et al.*, 1993].

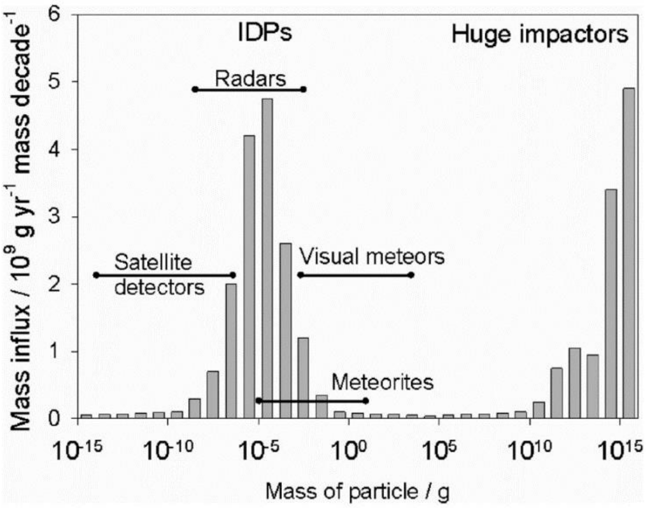

Figure 1.1. *Mass influx per decade of mass plotted against mass. Reproduced from Flynn [2002].*

The main sources of cosmic dust are collisions between asteroids, and the sublimation of comets as they approach the Sun on their orbits through the solar system [*Ceplecha et al.*, 1998; *Plane*, 2012; *Williams*, 2002]. If all the dust in the solar system between the Sun and Jupiter were compressed together it would form a sphere of 25 km of diameter [*Nesvorný et al.*, 2010].

1.2.1. Jupiter-Family Comets.

Jupiter-Family comets (JFCs) have orbital periods $P \leq 20$ yrs, and low inclination orbits [*Lowry et al.*, 2008]. Their orbital behavior is chaotic due to strong gravitational interactions with Jupiter. Their aphelia are generally around 5-6 AU from the Sun, although some can eventually evolve to orbits within the orbit of Jupiter, such as Comet 2P/Encke. In fact, Encke-type comets are simply old JFCs. Most active JFCs were only recently captured in not a one-step process but rather a cascade. Close encounters with Jupiter can both speed up and slow down the comet.

JFCs are defined by their dynamical Tisserand [*Tisserand*, 1896] parameter T_J, with respect to Jupiter. T_J is conserved in the circular restricted three-body problem, and can provide a measure of the relative velocity of approach to Jupiter. The Tisserand parameter is defined as:

$$T_J = \frac{a_J}{a} + 2cos(i)\sqrt{(1 - e^2)\frac{a}{a_J}} \qquad [1.1]$$

where a_J refers to the semi-major axis of Jupiter ($a_J \sim 5.20336$ AU), and a, e, and i are the semi-major axis, the eccentricity, and the inclination of the comet (or meteoroid), respectively [*Jenniskens*, 2006]. Moreover, the relative velocity between the comet and Jupiter is approximately $v_{rel} = v_J\sqrt{3 - T_J}$, with $v_J = 13.06$ km s^{-1} being the average value for a circular orbit of Jupiter. In this sense, the Tisserand parameter is a convenient way of discriminating JFCs from asteroids (ASTs) or Halley-Type Comets (HTCs), since $2 < T_J < 3$ for JFCs. HTCs have $T_J < 2$, while ASTs $T_J > 3$. *Duncan and Levison* [1997] reported that T_J does not vary significantly for JFCs, according to numerical simulations: 8% of comets moved in or out of this dynamical class throughout their computer simulations.

Several authors have tried to explain the origin of JFCs (Figure 1.2). *Kazimirchak-Polonskaya* [1967] and *Vaghi* [1973] postulated the capture by Jupiter of elliptical comets with intermediate period, concluding that the whole capturing process takes place through successive steps where the outer planets act as a powerful transformer of the original elliptical orbits. *Fernández* [1980] proposed that the origin of the JFCs is in the inner region of the Kuiper Belt beyond Neptune. In principle, the Oort cloud cannot produce short period comets with low inclinations and the observed orbital distribution, while a disk-like source solves the JFCs origin problem. In essence, Kuiper Belt objects (KBOs) with perihelia close to Neptune can be perturbed into Neptune-crossing orbits or out of stable resonances by gravitational interactions with giant planets, collisions, or by non-gravitational forces due to surface outgassing. Once this happens, the KBOs can be handed down through the giant planets region toward the terrestrial planets in the inner solar system [*Horner et al.*, 2004; *Lowry et al.*, 2008].

There has been a long debate about the existence of very small comets with diameters $\lesssim$1 km. While small comets can exist in huge numbers in the outer planetary region, the trans-neptunian belt or the Oort cloud, it seems probable that solar radiation prevents small comets from staying for too long in the inner of the solar system without being destroyed. *Fernández and Morbidelli* [2006] estimated a population between 400 and 1300 faint JFCs with $q < 1.3$ AU and $10 < H_{10} < 15$ (diameter ~0.2-1.0 km)[1].

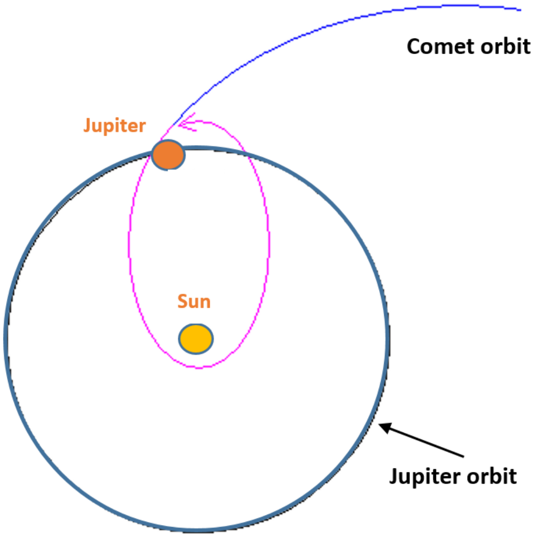

Figure 1.2. *Capture process of a comet into a shorter orbit. If it passes by Jupiter and is slowed down by Jupiter's gravity, it falls in toward the Sun. It will travel back out about to where its original orbit was disturbed, that is, somewhere near Jupiter's orbit. Normally, the comets are rarely captured following this simple process because there are multiple encounters involved. Adapted from https://www.uwgb.edu/dutchs/PLANETS/Comets.htm.*

Due to the low inclination prograde nature of their orbits, JFCs approach the Earth with slow velocities, arriving from the Helion and anti-Helion directions (see Chapter 2 and Chapter 4 for more details). Consequently, their meteoroids tend to have speeds

---

[1] When a comet passes close by the Sun, it emits a considerable amount of gas and dust and, consequently, the nucleus decreases in both mass and size [*Hughes*, 1989]. *Hughes* [1988a] found that the relationship between the mass of a cometary nucleus, M(g), and its absolute magnitude is given by:

$$\log \mathrm{M(g)} = 21.166 + \log \rho - 0.6\, H_{10}$$

where ρ is the mean density of the nucleus in g cm^{-3} and H_{10} is the cometary absolute magnitude that an active comet would have at 1 AU from the Sun and 1 AU from the Earth, assuming that cometary brightness varies with heliocentric δ_S, as δ_S^{-4} [*Bottke et al.*, 2002b]. It can be seen that if the mass of a comet decreases, the absolute magnitude should increase. However, *Hughes and Daniels* [1983] found that the change in H_{10} is very small and slow, being around 5.5×10^{-4} per apparition in the particular case of P/Halley.

between 11 and 35 km s^{-1}, typically 14 km s^{-1} (Chapter 2), and their meteor showers are best seen just after midnight, while HTCs and long-period Oort-Cloud comets (OCCs) showers are best seen just before dawn [*Jenniskens*, 2006]. Comets can survive in JFC orbits for about 4.5×10^5 years, but long before that time they will have lost most of the ices that drive the creation of meteoroid streams, once their perihelion distance is below q ~ 2.7 AU where water ice sublimates. *Hughes* [2003] estimated that 10%, 20%, and 30% of JFCs decay away after 1000, 2000, and 3000 yrs, respectively. After that, most of them will be dormant [*Jenniskens*, 2006].

There are several peculiarities that distinguish between OCCs and JFCs. OCCs emit dust of small grain sizes between 0.1 and 10 µm, which scatter light efficiently with albedos of ~0.1-0.4 and a high rate of mass loss, ~10,000 kg s^{-1}. In contrast, JFCs expel dust grains with sizes >10 µm and albedos of only 0.05-0.07, and at a much lower mass loss rate of ~100-1000 kg s^{-1} [*LevasseurRegourd et al.*, 1996]. Moreover, while OCCs may still have their original crust exposed, many JFCs are a mere kernel of the original comet and fragments are broken off. It is likely that most of the physical properties of the JFCs may be related more to their dynamical history in the inner solar system, instead of the processes that occurred during their formation in the Kuiper Belt.

There are between 20 and 100 JFCs of $D \geq 1$ km that have perihelia $q < 1.3$ AU at any time, although only some of these will come close to Earth's orbit. In particular, of all known JFCs only 13 have crossed Earth's orbit in the recent past and 7 of those are known parents of meteor showers. In fact, faint/small JFCs are still being discovered by survey programs such as the Lincoln Laboratory Near-Earth Asteroid Research project (LINEAR), the Lowell Observatory Near-Earth Object Search (LONEOS), Near-Earth Asteroid Tracking (NEAT), Catalina and Siding Spring, which are adding potential small comets with $H_N > 18.5$ to the list[2] [*Fernández and Morbidelli*, 2006]. Table 1.2 lists the total and nuclear magnitudes for several JCFs [*Fernández and Morbidelli*, 2006; *Jenniskens*, 2006].

---

[2] H_N is defined as the magnitude of the comet nucleus would have at 1 AU [*Fernández J. A.*, 2005]. The nucleus radius can be derived from the absolute nuclear magnitude, although it requires knowledge of the nucleus's geometric albedo, p_v, [*Fernández et al.*,2006]:

$$H_N = 14.11 - 5\ log\ R_N - 2.5\ log\ p_v$$

where the values of p_v derived for a selected set of well-observed comets are always quite low, with an average of p_v~0.04 [*Lamy et al.*, 2004].

Table 1.2. *A list of Jupiter-Family Comets. The orbital period P, the perihelion distance q, and the inclination of the cometary orbit with respect to the galactic plane i are given, as well as the absolute magnitude near perihelion of the comet (H_{10}), the absolute magnitude of the nucleus (H_N), and the most probable meteor shower associated to that comet. Adapted from Jenniskens [2006] and Fernández and Morbidelli [2006].*

Comet	P (yr)	q (AU)	i (º)	H_{10}	H_N	Meteor shower
2P/1786B1 (Encke)	3.30	0.33	11.76	9.2	16.0	Taurids?
3D/1772E1 (Biela)	6.62	0.86	12.55	7.1	—	Andromedids
5D/1846D2 (Brorsen)	5.46	0.59	29.38	8.3	—	
6P/1851M1 (d'Arrest)	6.54	1.04	19.51	7.8	16.5	Sept Bootids
7P/1819L1 (Pons–Winnecke)	6.37	0.97	22.28	9.0	16.3	June Bootids?
11P/1869W1 (Tempel–Swift–LINEAR)	6.37	1.58	13.46	11.2	—	
15P/1886S1 (Finlay)	6.51	0.94	6.80	9.5	17.2	Future showers
21P/1900Y1 (Giacobini–Zinner)	6.62	1.00	31.81	9.2	17.6	Draconids
26P/1808C1 (Grigg–Skjellerup)	5.31	0.99	22.36	11.4	17.2	π-Puppids
45P/1948X1 (Honda–Mrkos–Pajdušáková)	5.25	0.60	4.26	10.8	20.0	Future showers
67P/1969R1 (Churyumov–Gerasimenko)	6.44	1.24	7.04	8.3	16.0	
73P/1930J1 (Schwassmann–Wachmann 3)	5.36	0.94	11.38	10.6	17.7	τ-Herculids
103P/1986E2 (Hartley 2)	6.46	0.96	13.60	8.6	17.2	Future showers
D/1819W1 (Blanpain)	5.18	0.92	9.23	8.3	—	Phoenicids
D/1978R1 (Haneda–Campos)	5.97	1.10	5.95	11.4	—	Oct. Capricornids
P/2000G1 (LINEAR)	5.32	1.00	10.42	16.0	—	
P/2001MD7 (LINEAR)	7.83	1.25	12.9	9.0	—	
P/2001WF2 (LONEOS)	5.02	0.98	16.91	13.7	19.6	
P/2002T1 (LINEAR)	6.99	1.32	21.33	14.9	—	
P/2003KV2 (LINEAR)	4.85	1.06	25.54	13.0	—	
P/2003O3 (LINEAR)	5.47	1.25	8.36	13.8	—	
P/2004CB (LINEAR)	5.02	0.97	19.48	14.1	—	Future showers
162P/2004TU12 (Siding Spring)	5.34	1.24	27.79	12.2	—	
P/2004X1 (LINEAR)	4.84	0.78	5.14	14.3	—	

1.2.2. The Asteroid Belt.

The asteroid belt is the remnant of the original planetesimal population in the inner solar system, where ices did not remain frozen on dust grains and matter was compacted into rock. Nowadays, the asteroids have orbits with all possible values of eccentricities and inclinations compatible with long-term dynamical stability, whereas the initial planetesimal orbits should have been quasi-circular and almost coplanar. The total mass contained in the asteroid population corresponds to a small fraction of that existing primordially [*Morbidelli et al.*, 2015] and, altogether, it would make an object only about a twentieth the size of the Moon. In fact, *Kuchynka and Folkner* [2013] concluded that the total mass contained in the asteroid belt is $\sim 4.5\times10^{-4}$ $M_{\oplus}$. This value is very low compared to the original total mass that the primordial disk should have, which is on the order of ~1 $M_{\oplus}$ [*Weidenschilling*, 1977]. *Bottke et al.* [2005] concluded that: 1. The 3-orders-of-magitude mass depletion could not come solely from collisional erosion, and 2. The mass depletion occurred very early.

The formation and evolution of the asteroid belt can be reconstructed by observational constraints of large asteroids, larger than ~50-100 km in diameter, since they were not generated in large numbers of collisional breakup events of larger parent bodies [*Bottke et al.*, 2005; *Morbidelli et al.*, 2015]. A second feature of the asteroid belt population is the orbital excitation, namely, many asteroids have large eccentricities and inclinations [*Petit et al.*, 2002]. The median inclination of D > 100 km asteroids is 11° and the average proper eccentricity is 0.145 [*Morbidelli et al.*, 2015]. In the particular case of the largest asteroids, the values of eccentricities and inclinations are dispersed with the former ranging between 0 and 0.30, and 0° and 33°, respectively. Although planetesimals are expected to have formed on circular and coplanar orbits, there were dynamical excitation mechanisms within the primordial asteroid belt to excite eccentricities and inclinations to randomly dispersed values.

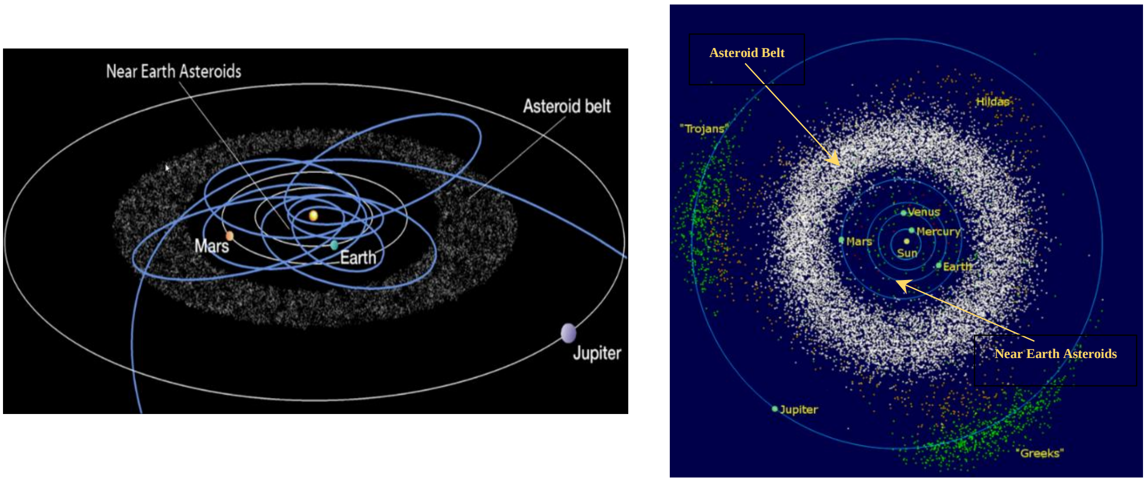

Figure 1.3. *Left: position of the main Asteroid belt and the Near-Earth Asteroids (http://geology.isu.edu/Alamo/impact/astronomy.php). Right: Position of all known asteroids (North polar view) (http://www.universetoday.com/32856/asteroid-belt/).*

The distribution of asteroids in the main asteroid belt is not uniform. In particular, there are regions which contain very few asteroids known as Kirkwood gaps. Kirkwood gaps can be used to break up the asteroid belt into the inner, middle, and outer belt. The inner part of the belt extends from 2.06 to 2.50 AU, the middle part extends from 2.50 to 2.82 AU, and the outer part extends from 2.82 to 3.27 AU [*Burbine*, 2017]. Trojan asteroids lie outside the main belt with an average semi-major axis of about 5.2 AU, located in the Lagrangian points where the gravitational pull of the Sun and the planet are balanced. *Near-Earth asteroids* (NEAs) with q < 1.2 AU return normally to Earth and contribute ~80% of the bodies impacting on Earth with diameter D > 1 km [*Jenniskens*, 2006]. Those NEAs that do not cross the Earth's orbit are called *Amor-type*, after 1221 Amor, whereas those which cross the Earth's orbit but have an aphelion outside of Mars' orbit are called *Apollo-type*, after 1862 Apollo. Finally, those that cross Earth's orbit and have their aphelion inside Mars' orbit are called *Aten-type*, after 2062 Aten (see Figure 1.4). The *Atiras* or *Apohele* asteroids (i.e. 163693 Atira, provisionally designed as 2003 CP_{20}) have orbits strictly inside Earth's orbit. *Hsieh and Haghighipour* [2016] analyzed the potential contamination of the main asteroid belt by JFCs and found that the fraction of real JFCs occasionally reaching the main belt could be on the order of ~0.1-1%. Figure 1.5 summarizes our current knowledge of the population of NEAs.

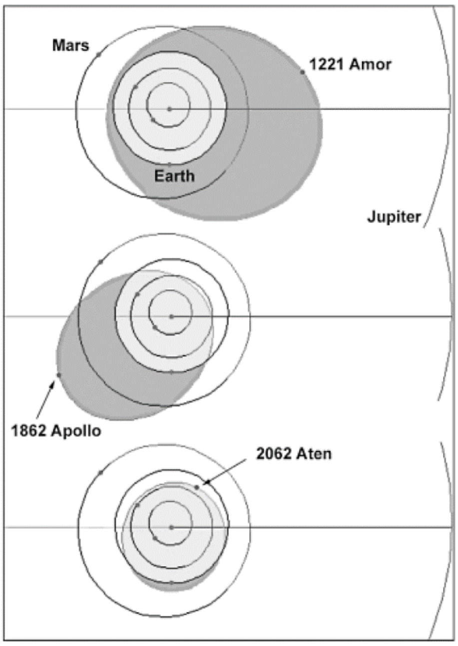

Figure 1.4. *Near-Earth asteroid orbit archetypes. Reproduced from Jenniskens [2006].*

Rocky asteroids can cause meteoroid streams as a result of frequent small impacts with asteroid boulders or during a rare catastrophic in which both asteroids break into fragments which disperse more like a dust trail. Many meteorites from the asteroid belt begin the process of evolving into an Earth-crossing orbit by being ejected at high velocity from the parent body by a major impact [*Greenberg and Nolan*, 1989]. Although the meteoroids and fragments disperse much like a dust trail, they differ from cometary streams in being rare and transient in nature, and composed of rocky material [*Jenniskens*, 2006].

Asteroids are grouped into many taxonomic classes according to the colour (spectral shape) of their reflected light, and from the albedo or percentage of reflected light. In essence, some have a broad absorption band at 1 µm from mafic silicates. These are more reflective and are called S-complex asteroids (for stony). The C-complex (for carbonaceous) corresponds to those asteroids with a flat spectrum and normally with an absorption band at 0.7 µm [*Chapman et al.*, 1975] due to the presence of oxidized iron in phyllosilicates resulting from aqueous alteration [*Jenniskens*, 2006]. Apart from these taxonomic classes, many outliers exist and the complexes themselves have been sub-divided into different taxonomic types. Figure 1.6 shows that asteroids with different chemical and mineralogical properties are not ranked in an orderly manner with mean heliocentric distance, but are partially mixed [*Morbidelli et al.*, 2015].

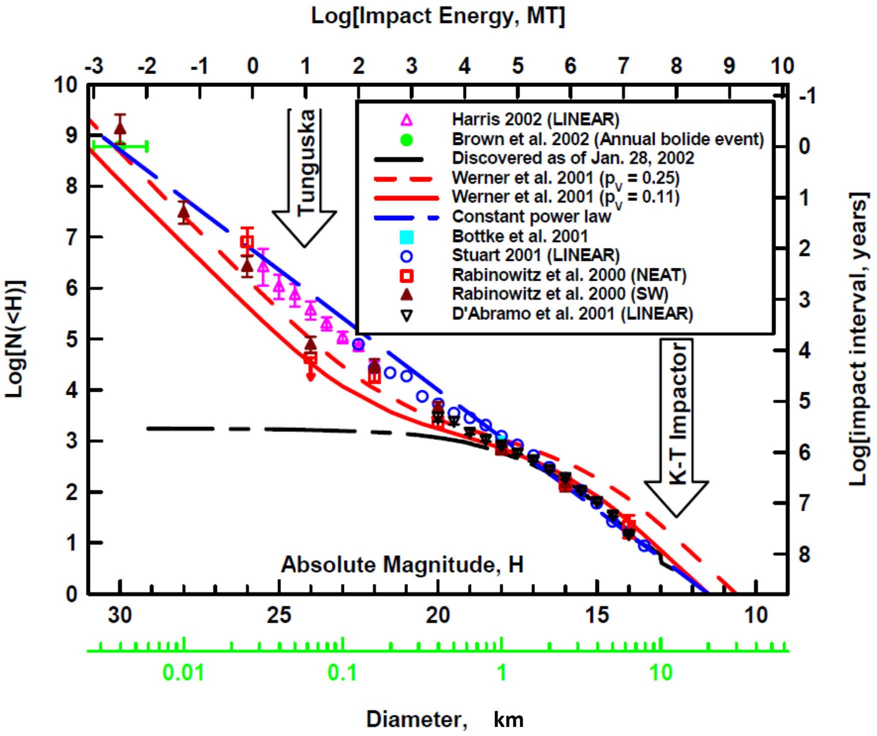

Figure 1.5. *The population of Near-Earth asteroids. This distribution considers all asteroids with perihelion q < 1.3 AU. Reproduced from Stokes et al. [2003].*

The letters D, P, C, X, and K are used for the dark primitive asteroids, least affected by heating process, and include the Hilda family (D-type). These asteroids are found dispersed in the asteroid belt at distances > 2.3 AU. In fact, the central belt (2.5-3.2 AU) is dominated by C-complex asteroids. It is remarkable to note that more than 75% of known main belt asteroids and NEAs are type C [*Stuart and Binzel*, 2004], and they are probably related to carbonaceous CI- and CM-types chondrites [*Burbine et al.*, 2002; *Jenniskens*, 2006]. Most of the C-type asteroids have suffered aqueous alteration which leads to mineralogical changes due to the melting of ice and the incorporation of liquid water into the mineral structure of stony compounds.

The types S, A, E, R, V, J, and M represent asteroids with an igneous composition which may have been subjected to heating. In the main belt, these asteroids tend to be clustered in groups dispersed throughout the belt. In essence, *Gradie and Tedesco* [1982] reported that the inner belt (< 2.3 AU) is dominated by S-complex asteroids (17%), many of which are probably related to ordinary chondrites. The remainder are M-type (metallic), E-type (enstatite), and V-type (achondrites) [*McCord et al.*, 1970].

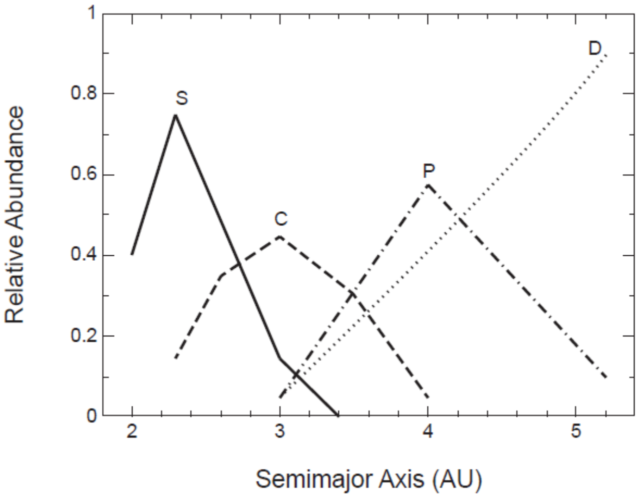

Figure 1.6. *The relative distribution of large asteroids (D > 50 km) of different taxonomic types as originally observed Gradie and Tedesco [1982]. Reproduced from Morbidelli et al. [2015].*

1.2.3. Halley-Type Comets.

HTCs represent a subset of short-period comets, a group traditionally defined by their short orbital periods $P < 200$ yrs. As discussed in Section 1.2.1., JFCs have orbital periods $P < 20$ yrs and low inclination orbits that are strongly perturbed by Jupiter. However, HTCs have intermediate orbital periods, $20 < P < 200$ yrs, high eccentricities, perihelion distances $q < 1.5$ AU, and a wide range of inclinations $0^{\circ} < i < 180^{\circ}$ [*Bailey and Emelyanenko*, 1996]. The Tisserand parameter with respect to Jupiter is $T_J < 2$. Table 1.3 lists the main parameters of 24 HTCs [*Wang and Brasser*, 2014].

The question of the number of HTCs plays a crucial role in theories of the origin of short-period comets. For instance, the production of HTCs depends on possible sources and reservoirs such as the Kuiper belt [*Duncan et al.*, 1987; *Quinn et al.*, 1990], or the inner core of the Oort cloud [*Bailey and Stagg*, 1990; *Stagg and Bailey*, 1989]. However, the origin of the HTCs has long been controversial. *Levison et al.* [2001] integrated numerically the orbits of 27700 test particles initially entering the planetary system from the Oort cloud in order to study the origin of the HTCs. They included in their model the gravitational influence of the Sun, giant planets, and Galactic tides. Consequently, in order to match the observations, an isotropically distributed Oort cloud does not reproduce the observed orbital distribution of the HTCs, that is, the initial inclination distribution of the progenitors of the HTCs must be similar to the observed HTC inclination distribution. *Levison et al.* [2001] concluded that original bodies had inclinations ranging from 10º to 50º. In fact, passing stars and giant molecular clouds (GMCs) exert a gravitational influence, shifting cometary perihelia from the outer solar system to the observable region and *vice versa* [*Nurmi et al.*, 2002].

Table 1.3. *A list of 24 Halley-Type Comets. The semi-major axis a, the eccentricity e, and the inclination of the comet orbit respect the galactic plane i is given, as well as the perihelion q, and the Tisserand parameter T_J. Adapted from Wang and Brasser [2014].*

Comet	*a* (AU)	*e*	*i* (º)	*q* (AU)	T_J	year
1P/Halley	17.8	0.97	162.3	0.6	-0.6	1758
8P/Tuttle	5.7	0.82	55.0	1.0	+1.6	1790
12P/Pons-Brooks	17.1	0.95	74.2	0.8	+0.6	1812
13P/Olbers	16.9	0.93	44.6	1.2	+1.2	1815
23P/Brorsen-Metcalf	17.1	0.97	19.3	0.5	+1.1	1847
35P/Herschel-Rigollet	28.8	0.97	64.2	0.7	+0.6	1788
161P/Hartley-IRAS	7.7	0.84	95.7	1.3	+0.5	1984
177P/Barnard	24.3	0.95	31.2	1.1	+1.3	1889
C/1984A1 (Bradfield1)	28.5	0.95	51.8	1.4	+1.1	1984
C/1991L3 (Levy)	13.8	0.93	19.2	1.0	+1.5	1991
C/2001OG108 (LONEOS)	13.3	0.93	80.2	1.0	+0.6	2001
P/2001Q6 (NEAT)	8.0	0.82	56.9	1.4	+1.4	2001
C/2003R1 (LINEAR)	19.7	0.89	149.2	2.1	-1.2	2003
C/2003W1 (LINEAR)	25.1	0.93	78.1	1.7	+0.5	2003
C/2005Q2 (Chistensen)	23.7	0.86	148.9	3.3	-1.6	2005
P/2005T4 (SWAN)	9.3	0.93	160.0	0.6	-0.4	2005
P/2006R1 (Siding Spring)	7.8	0.84	31.9	1.2	+1.8	2005
C/2008R3 (LINEAR)	18.4	0.90	43.2	1.9	+1.5	2008
P/2010JC81 (WISE)	8.1	0.78	38.7	1.8	+1.9	2010
C/2010L5 (WISE)	8.2	0.90	147.1	0.8	-0.3	2010
C/2011J3 (LINEAR)	19.6	0.93	114.7	1.5	-0.3	2011
C/2012T6 (Kowalski)	16.3	0.93	17.6	1.1	+1.5	2011
C/2012Y3 (McNaught)	16.1	0.89	92.8	1.7	+0.2	2012
P/2013AL76 (Catalina)	6.5	0.68	144.9	2.0	-0.5	2013

However, *Levison et al.* [2006] pointed out that the previous models [*Levison et al.*, 2001] were incorrect because they did not include the long-term dynamical evolution of the Oort cloud. In particular, *Levison et al.* [2006] conclude that HTCs have their origin in the outer edge of the Scattered Disk[3]. In essence, *Levison and Duncan* [1997] report

---

[3] The Scattered Disk is the name given to a distant circumstellar disk in the solar system that is populated by small and icy objects, a subset of trans-Neptunian objects, that have inclinations as high as 40º and perihelia greater than 30 AU. It begins at the outer edge of the Kuiper belt at 30-35 AU and can extend beyond 100 AU. The Scattered Disk would represent a transit population from the Kuiper belt to other regions of the solar system or beyond [*Levison and Duncan*, 1997].

that this reservoir has a flattened inclination distribution and the effect of the galactic tide at the outer edge is able to produce retrograde HTCs. *Levison et al.* [2006] indicate that a significant number of objects leave the Scattered Disk by evolving to semi-major axes greater than 1000 AU. Approximately 0.01% of the objects reach 10^4 AU and then evolve onto orbits similar to the observed HTCs due to gravitational interactions with the giant planets.

Wang and Brasser [2014] used numerical simulations to determine whether the distribution of HTCs can be reproduced using the Oort cloud as their source distribution and when considering cometary fading. They found that the Oort cloud with cometary fading is the most likely source of the HTCs. In conclusion, the HTCs may represent the only observable link to the inner Oort cloud [*Duncan et al.*, 1987; *Levison et al.*, 2001; *Quinn et al.*, 1990]. *Fernández and Gallardo* [1994] concluded that about 300 comets present in the solar system are in a steady state at any given time. Moreover, HTCs are slightly more prograde than retrograde due to the progressive capturing processes by the planets.

HTCs are responsible for some of the most significant meteor showers because they are in relatively stable orbits that can accumulate dust from many returns. The meteoroid streams of HTCs differ dynamically from those of OCCs mainly because the comet and dust can avoid close encounters with the planet by getting trapped in a mean-motion resonance with Jupiter [*Chambers*, 1997]. Those trappings are never permanent, due to the fact that a third body can change the orbital period of the comet or meteoroid. For example, a meteoroid in resonance with Jupiter can suffer a perturbation by Saturn, changing the orbital period to bring it closer to the planet Jupiter in the next return. This is the case of the HTCs, although such encounters with Jupiter tend to be brief and inefficient [*Jenniskens*, 2006]. Thus, the next encounters with Saturn can perturb the comet into another resonance. For comets with $q < 2$ AU the average physical lifetime as a HTC is about 300-500 revolutions. Sooner or later, HTCs are either ejected from the solar system, or will impact the Sun.

The missions Giotto and Vega 1 and 2 captured about 5000 individual particles with diameters between 0.2 µm and 2 µm, and a total mass of no more than a few ng [*Kissel et al.*, 1986; *Krasnopolsky et al.*, 1987; *Krueger and Kissel*, 1987; *Simpson et al.*, 1987]. From these data, it was found that the cometary dust particles were rich in carbon, hydrogen, oxygen, and nitrogen (CHNO). *Jessberger and Kissel* [1991] concluded that elemental carbon was present at 20 weight %. However, whereas small grains consist only of CHNO, others consist of rock-forming elements. These stony bodies contain metals and silicates with ~10% iron sulfides. Rock-only particles were found mostly in the outer reaches of the coma, while CHNO particles were found in the inner coma [*Fomenkova et al.*, 1994; *Jenniskens*, 2006].

1.2.4. Oort-Cloud Comets.

OCCs have their origin in the Oort cloud, in more violent accumulation processes than those that take place in the Kuiper belt. In particular, OCCs possess an orbital period $P > 200$ years, and their orbital evolution is not tightly controlled by the major planets. OCCs originated from the giant-planet formation region of the solar system, most from the Uranus-Neptune region. Thus, billions of cometesimals moved at high relative speed in close proximity to each other. The final stages of accretion were rather violent and there might be a wide variety of nucleus properties among OCCs, from highly unstable rubble piles to relatively consolidated conglomerates. About 1% of the long-period OCCs evolve into shorter orbits, whereas the remainder are ejected from the solar system [*Jenniskens*, 2006].

The observed population of OCCs has nearly isotropic inclinations. By definition, OCCs must have a semi-major axis $a > 35$ AU, but one-third of the observed OCCs have $a > 20{,}000$ AU [*Weissman*, 1996]. *Weissman* [1979] simulated the evolution of 10^5 hypothetical OCCs and found that 65% of them are dynamically ejected from the solar system on hyperbolic orbits, 27% are randomly disrupted (10% of them in the first passage), and the remainder are lost by a variety of processes such as loss of all volatiles and collision with the Sun and planets.

OCCs can have a high content of volatile ices, impact craters and other features from the origin of the solar system, making them a potential source of unusual meteoroids [*Jenniskens*, 2006]. Unlike JFCs or HTCs, the crust has not disrupted into meteoroids. However, OCCs will have been exposed to galactic cosmic rays and heated by supernovae [*Weissman*, 1996].

The total number of comets in the dynamically active outer Oort cloud is on the order of 10^{12}, with a total estimated mass of $\sim 38\ M_\oplus$ [*Bottke et al.*, 2002; *Weissman*, 1996]. The main perturbers of the Oort cloud are Giant Molecular Clouds (GMCs) and the galactic gravitational field itself, in particular the tidal field of the galactic disk [*Weissman*, 1996]. Normally, GMC encounters are rare, occurring in an interval of ~3×10^8 yrs [*Hut and Tremaine*, 1985]. The galactic field sets the limits on the outer dimensions of the Oort cloud. Moreover, random stars can occasionally pass directly through the Oort cloud, ejecting a significant number of comets and perturbing the orbits of others. It is known that the main perturber of the Oort cloud is the galactic disk [*Delsemme*, 1987].

Actually, it is suspected that most OCCs fall apart completely in one of their first returns, rather than fading over time. In fact, 95% of all OCCs are bright for approximately five apparitions on average and then fall apart, while only 5% survive for much longer periods of time. If they survive their first return, they typically spend the next 45 million years as OCCs [*Levison et al.*, 2002].

1.3. MODELLING SPUTTERING AND THERMAL ABLATION

According to the conventional meteor ablation theory, the atmospheric passage of meteors leads to ionization and light production as a consequence of collisions with ablated meteor atoms [*Ceplecha et al.*, 1998]. In principle, the ablation of meteoroid material is assumed to occur in an intensive manner after the meteor reaches the melting point [*Rogers et al.*, 2005]. Consequently, one does not expect luminosity or significant ionization above the height of intensive vaporization, which in the case of the Earth occurs in the height range from 80 to 125 km. During the descent of the meteoroid other processes, such as in-flight fragmentation [*Ceplecha et al.*, 1998; *Fisher et al.*, 2000; *Hawkes and Jones*, 1975; *Rogers et al.*, 2005], can play an important role. *Rubio et al.* [2001] re-analyzed precise photographic meteor trails and argued that fragmentation might not be as important as previously assumed. However, more recently, studies based on optical observations of faint meteors, from 10^{-4} g to 0.1 g, collected by the Canadian Automated Meteor Observatory (CAMO) between 2010 April and 2014 May concluded that 90% of observed meteors exhibit fragmentation [*Subasinghe et al.*, 2016].

1.3.1. Sputtering process.

Öpik [1958] proposed that sputtering, in which individual atoms are released from materials by high speed atomic collision processes, may play a role in meteor ablation. Sputtering occurs when the body approaches the Earth's atmosphere at heights of 300 km to 100 km [*Ceplecha et al.*, 1998], and the surface temperature of the meteoroid rises quite rapidly, whereas the inside of most meteoroids (except small grains) remains practically unheated. The sputtering is a very quick phenomenon lasting only seconds or tens of seconds. *Coulson* [2002] and *Coulson and Wickramasinghe* [2003] have studied sputtering and its importance as a deceleration mechanism to deliver small meteoroids to the Earth with limited in-flight heating. *Rogers et al.* [2005] found that while in many cases, particularly at low velocities and for relatively large meteoroid masses, sputtering contributes only a small fraction of mass loss during atmospheric flight, in some cases sputtering is very important and may explain the light production observed at high altitudes in some Leonid meteors.

Sputtering is considered to be a primary destruction mechanism for IDPs [*Draine*, 1989; *Rogers et al.*, 2005]. It is not an important part of conventional meteoroid ablation theory, although as discussed above it has been suggested to be of some importance under certain conditions [*Coulson*, 2002; *Coulson and Wickramasinghe*, 2003; *Öpik*, 1958; *Rogers et al.*, 2005]. Physical sputtering is an atomic cascade process whereby bombarding particles (projectiles) collide with the surface atoms of the target. The target atoms, as well as the projectiles, undergo collisions with other target atoms, giving rise to a chain reaction of collisions. The energy needed to overcome the potential barrier is called the surface binding energy. If the velocity of the atoms normal to the surface corresponds to an energy equal to or greater than the surface binding energy, they will be ejected. Sputtering does not occur for all projectile/target combinations. Thus, there is a minimum projectile kinetic energy to induce sputtering for a given projectile and target.

Vondrak et al. [2008] estimated the mass loss rate assuming a spherical target:

$$\frac{dm^S}{dt} = -2\pi R^2 v M_t \sum_i \rho_i Y_i \qquad [1.2]$$

where the superscript *S* refers to sputtering, and the index *i* represents the atmospheric components (normally O_2, N_2, He, Ar, N, O, and H); ρ_i is the number density of the *i*-th atmospheric compound, and Y_i is the sputtering cross-section for the *i*-th atmospheric component. M_t is the atomic number of the target, and *R* is the particle radius. *Vondrak et al.* [2008] assumed an equal sputtering cross-section for all elements of which the target meteoroid was composed, and estimated the elemental loss rate by sputtering using the bulk element atomic fractions x_i in the meteororid:

$$\left.\frac{dm_i}{dt}\right|_S = x_i \frac{dm^S}{dt} \qquad [1.3]$$

The sputtering yields Y_i are calculated in the Chemical Ablation MODel (CABMOD) developed at the University of Leeds using a semi-empirical treatment derived from studies of ion sputtering [*Vondrak et al.*, 2008]. The sputtering mechanism described above corresponds to a physical process (atomic and molecular collisions). However, there are also many other types of sputtering mechanisms, even though they do not represent a significant mass loss mechanism compared to physical sputtering. These include chemical sputtering, thermal sputtering, electronic sputtering, transmission sputtering, and sputtering by cosmic rays, and have been analyzed for several astrophysical applications [*Barlow*, 1978; *Draine*, 1989].

1.3.2. Thermal ablation.

Meteoroids are treated as homogeneous spheres by several authors, according to the classical theory of the interaction of meteoroids with the atmosphere [*Bronshten*, 1983; *Hunten et al.*, 1980; *Kalashnikova et al.*, 2000; *McKinley*, 1961; *Öpik*, 1958]. Radial heat transfer is assumed to be fast enough, thus the particle is isothermal along the whole path through the atmosphere. This issue has important implications, so if the particle were not isothermal the composition and chemical states of elements would differ between the skin and inner region of the particle. *Vondrak et al.* [2008] concluded that a 5 µg particle is isothermal up to a very high temperature (~3000 K), while a 5 mg mass stays isothermal up to ~2000 K assuming the bulk density is 2 g cm^{-3}. However, because meteoroids lose mass extensively above ~2800 K they become much smaller at the highest temperatures. In consequence, the isothermicity condition can be fulfilled completely for the whole mass distribution up to 5 mg [*Vondrak et al.*, 2008].

According to the classical theory, the loss of momentum of a particle of density ρ_m, due to interaction with the atmosphere, is given by the drag equation which specifies the deceleration of the meteoroid [*McKinley*, 1961]:

$$\frac{dv}{dt} = -\Gamma v^2 \frac{3\rho_a}{4\rho_m R} + \rho_m g \qquad [1.4]$$

where v is the velocity of the particle, g is the gravitational acceleration, and ρ_a and ρ_m are the mass density of the atmosphere and the meteoroid, respectively. The dimensionless free-molecular drag coefficient Γ indicates the efficiency of momentum transfer between the meteoroid and the impinging air molecules, and its value depends essentially on the flow regime. In fact, the range of flow regimes over meteoroids changes from free-molecule in upper atmosphere to continuum with thin shock wave at low altitudes [*Khanukaeva*, 2003]. In free molecule regime the drag coefficient is determined by nature of the particle-surface interactions, rather than the geometry of the particle, and Γ tends to 2 [*Bird*, 1976]. In the case of a stable hypersonic continuum stream, Γ lies between 0.5 and 1 [*Hughes*, 1978], and it will depend only on the body geometry. The gravitational term $\rho_m g$ is negligible in the range of meteoroid velocities [*Rogers et al.*, 2005; *Vondrak et al.*, 2008].

The thermal energy received by the meteoroid from the impinging air molecules is balanced by radiative loss, temperature increase, melting, phase transitions, and vaporization of the meteoric constituents [*Vondrak et al.*, 2008]. Since energy is conserved [*Adolfsson et al.*, 1996]:

$$\frac{1}{2}\pi R^2 v^3 \rho_a \Lambda = 4\pi R^2 \varepsilon\sigma(T^4 - T_a^4) + \frac{4}{3}\pi R^3 \rho_m C \frac{dT}{dt} + L\frac{dm}{dt} \quad [1.5]$$

where the dimensionless parameter Λ is the free molecular heat transfer coefficient and represents the fraction of the incident kinetic energy which is transferred to the meteoroid, usually assumed to have a value near unity [*Rogers et al.*, 2005]. The emissivity of the meteoroid is ε, while σ is the Stefan-Boltzmann constant. T is the temperature of the meteoroid surface and T_a is the effective temperature of the atmosphere in the region of the meteoroid. C and L represent the specific heat capacity and the latent heat of vaporization (or sublimation if the particle has not melted). The left-hand side of equation [1.5] represents the frictional heating term. The right-hand side of the equation estimates the loss of thermal energy by the particle, where the first term is the radiation loss, the second term is the heat consumed to increase the temperature of the particle, and the third term corresponds to the heat consumed in the transfer of particle mass into the gas phase.

The change of particle height z with time is a function of its impact angle θ, defined as the angle to the zenith:

$$\frac{dz}{dt} = -v\cos(\theta) \quad [1.6]$$

The mass loss rate is calculated using Langmuir evaporation [*Love and Brownlee*, 1991; *Markova et al.*, 1986; *McNeil et al.*, 1998; *Vondrak et al.*, 2008], which assumes that the rate of evaporation into a vacuum is equal to the rate of evaporation needed to balance the rate of uptake of a species *i* in a closed system. The rate of mass release of species *i* with molecular weight μ_i, from a particle of area *S* and a temperature *T*, is given by the Hertz-Knudsen expression:

$$\left.\frac{dm_i}{dt}\right|_A = f(T)\gamma_i p_i S\sqrt{\frac{\mu_i}{2\pi k_B T}} \quad [1.7]$$

where the subscript *A* refers to thermal ablation; k_B is the Boltzmann's constant, p_i is gas-liquid equilibrium vapour pressure, and γ_i is the apparent evaporation coefficient which is equal to the probability that the molecule is retained on the surface, or within the particle, after collision. *Safarian and Engh* [2013] concluded that γ_i is unity for pure metals but may be lower than 1 in silicate melts [*Alexander et al.*, 2002], because diffusion from the bulk into the surface film may become rate-limiting. Due to a lack of experimental data, the apparent evaporation coefficient for each metal is assumed to be the same for all the compounds of the bulk, such that $\gamma_i = \gamma$ [*Vondrak et al.*, 2008]. The range of temperature where the solid and the liquid are in equilibrium is treated by applying a phase transition factor *f(T)*, which is represented by a sigmoidal temperature dependence weighting that varies between 0 and 1:

$$f(T) = \frac{1}{1+exp\left(\frac{-(T-T_C)}{\tau}\right)} \quad [1.8]$$

where τ is a constant that characterizes the width of the sigmoid profile and T_c the temperature such that $f(T_c) = 0.5$. The values T_c = 1800 K and τ = 14 K are prescribed by a the olivine Fa_{50} solid-liquid equilibrium temperature range, meaning essentially that *f*(*T < 1700 K*) = 0 and *f*(*T > 1800 K*) = 1 (this point will be discussed in detail below) [*Vondrak et al.*, 2008].

The total mass loss rate due to ablation is then the sum over all gas phase components:

$$\frac{dm^A}{dt} = \sum_i \left.\frac{dm_i}{dt}\right|_A \quad [1.9]$$

The total mass loss rate is then the sum of the sputtering and thermal ablation rates:

$$\frac{dm}{dt} = \frac{dm^A}{dt} + \frac{dm^S}{dt} \quad [1.10]$$

When the particle reaches the melting point, ~1800 K for olivine rich particles [*Vondrak et al.*, 2008], the ablation of the meteoroid starts. Deceleration can compete with ablation in consuming kinetic energy only for larger bodies and when they move lower down in the atmosphere. For example, if the meteoroid slows to 3 km s^{-1} after ablation somewhere high above the surface, and there still remains a significant mass, this mass continues to move without emitting light (dark flight) because there are not enough hot gases round the body to emit visible light [*Ceplecha et al.*, 1998].

Figure 1.7 shows schematically the sputtering and ablation process of IDPs in the upper atmosphere. If the entering body does not reach the melting point, it will produce an Unmelted micrometeorite (UMM). As discussed in detail in the following sections, the meteoroid loses the most volatile metals – Na and K – when reaching the melting point, before other elements start to evaporate. As the temperature increases, the main constituent metals – Fe, Si, and Mg – ablate. Finally, the more refractory metals – Ca, Al, and Ti – are released after reaching ~2400 K. When ablation ceases, and if the meteoroid has not completely evaporated, there is not enough kinetic energy to either evaporate, or to provide continued heating. Consequently, the body experiences rapid cooling (exponential with time [*Ceplecha et al.*, 1998]) and the crust solidifies. The impact velocities on the Earth's surface are between several tens of m s^{-1} for smaller meteorites and several hundreds of m s^{-1} for larger meteorites. Micrometeorites (MMs) can be partially or totally melted and consist of a foamy glass with variable amounts of unmelted phases – scoriaceous MMs or cosmic spherules, respectively.

1.3.3. The Chemical Ablation Model.

CABMOD, developed at the University of Leeds [*Vondrak et al.*, 2008], is used to estimate the elemental ablation rates of a meteoroid given its initial mass, entry velocity, and zenith angle. CABMOD contains the multicomponent gas-melt chemical equilibrium (MAGMA) module [*Fegley and Cameron*, 1987; *Schaefer and Fegley*, 2004; 2005] which estimates the vapour pressures of the different species evaporating from the meteoroid. MAGMA exhibits a good agreement with experimental data for a wide range of temperatures and silicate melt compositions, and takes account of the equilibria of eight metal oxides: SiO_2, MgO, FeO, Al_2O_3, TiO_2, CaO, Na_2O and K_2O. The chemical equilibria in the melt are modelled using the thermodynamic activities, a_i,which are given by:

$$a_i = \gamma_i^* x_i \qquad [1.11]$$

where x_i is the mole fraction of oxide in the melt and γ_i^* is the Raoultian activity coefficient of the oxide relative to the pure liquid oxide. CABMOD determines the mass loss rate of each component from the melt using the vapour pressure of each gas-phase estimated by MAGMA and invoking the Hertz-Knudsen expression (eq. [1.7]).

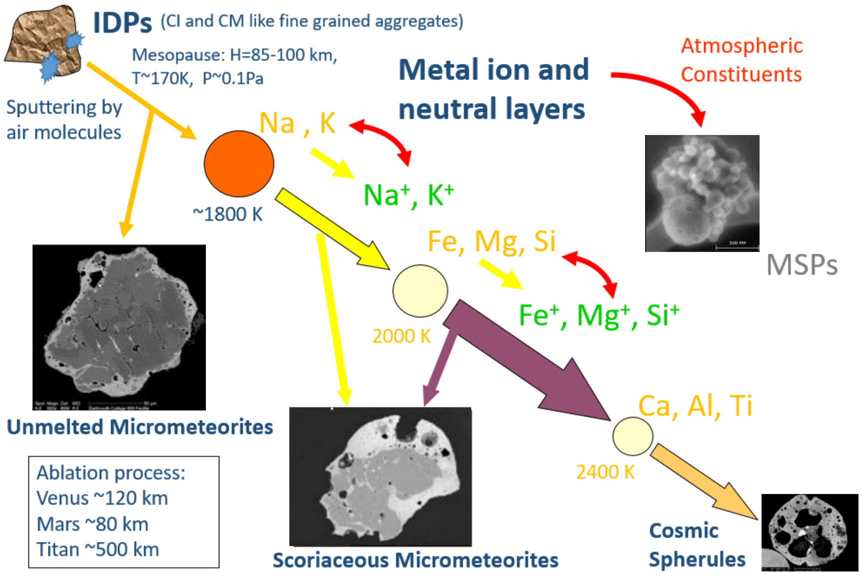

Figure 1.7*. Sputtering, ablation, and ionization process of an interplanetary dust particle entering the upper atmosphere. Unmelted Micrometeorite, scoracious micrometeorites, and cosmic spherules reproduced from Taylor et al. [2007]. Meteoric smoke particles reproduced from Della Corte et al. [2013].*

CABMOD starts the integration at an altitude of 500 km and a meteoroid temperature of 200 K (see Figure 1.8) [*Vondrak et al.*, 2008]. The integration process is stopped if the meteoroid mass decreases below 10^{-16} g or the meteoroid temperature falls below 400 K towards the end of its flight. *Vondrak et al.* [2008] estimated the ablation rates of meteoroids for the atmospheric conditions of March at 40ºN. The number densities of atmospheric constituents were calculated using the MSIS-E-90 model (http://omniweb.gsfc.nasa.gov/vitmo/msis_vitmo.html).

The MAGMA code estimates non-zero vapour pressures for metal species at temperatures below the melting temperature of the meteoroid. However, given that it is not possible to establish a thermodynamic equilibrium before the particle melts, MAGMA is not invoked before reaching the melting temperature (see Figure 1.8) [*Vondrak et al.*, 2008]. As discussed in Section 1.3.2, the apparent evaporation coefficient γ can vary between zero and unity in eq. [1.7]. CABMOD sets the uptake coefficient to zero until the temperature reaches the melting point of the particle, and the onset of particle evaporation is simulated by applying a sigmoid temperature dependence introducing the phase transition factor *f*(*T*) in eq. [1.7]. A smooth transition phase prevents possible instabilities in the numerical integration and can describe better the change phase than an instantaneous transition (see Chapter 3).

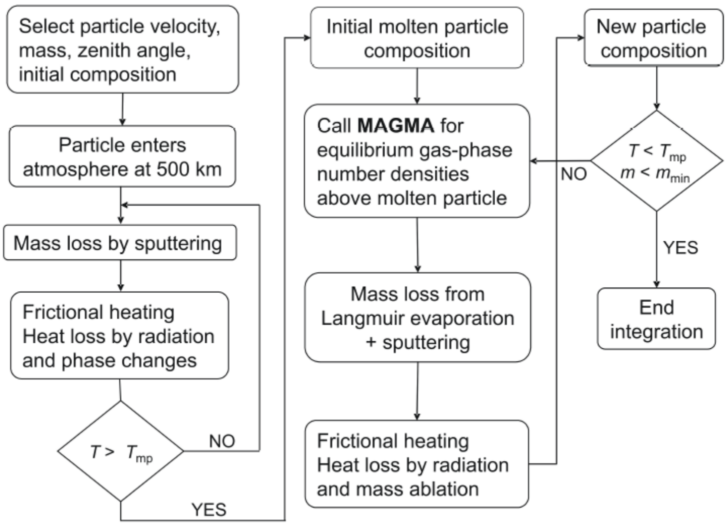

Figure 1.8. *Flowchart depicting the architecture of the chemical ablation model. Reproduced from Vondrak et al. [2008].*

Vondrak et al. [2008] assumed that meteoroids are mineralogically CI chondrites with an olivine composition [*Lodders and Fegley*, 1988; *Mason*, 1979; *Sears and Dodd*, 1988]. The elemental atomic ratio Fe:Mg is ~0.84 for a CI composition, such that the olivine starts to melt at 1730 K. *Vondrak et al.* [2008] adopted a meteoroid melting temperature of 1800 K, with γ_i varying between 0 (T < 1700 K) and 1 (T > 1900 K).

Figure 1.9 shows the phase diagram for olivine (left panel) and the ablation rate profiles for a meteoroid with an entry velocity of 18 km s^{-1} and a mass of 10 µg (right panel). Na and K are released almost completely at ~98 km before other elements start to evaporate. The ablation of the main compounds – Fe, Si, and Mg – occurs 10-15 km lower in the atmosphere and is also nearly complete. In contrast, Table 1.4 shows that less than 1% of Ca is released from the particle; that is, the Na/Ca ratio in the gas phase is 167 larger than in the meteoroid.

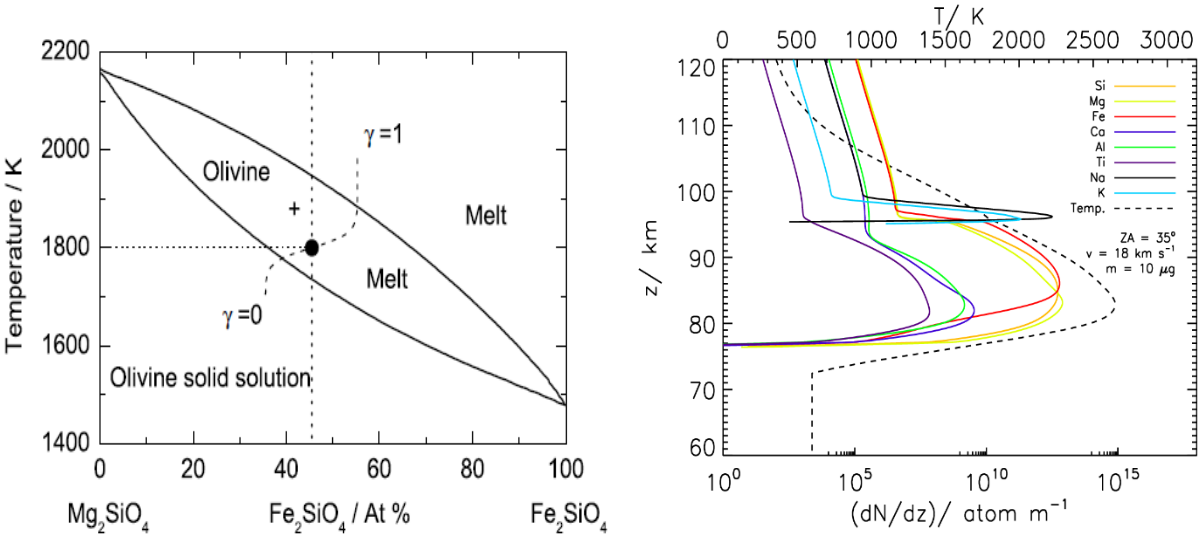

***Figure 1.9**. Left panel: Phase diagram of olivine and the assumed melting temperature of the chondritic particle; the dashed line represents the temperature dependence of the apparent evaporation coefficient γ through the phase transition factor f(T). Right Panel: Elemental deposition profiles of individual elements from a 10 μg meteoroid entering at 18 km s^{-1}, where the temperature is represented with a dashed line referenced in the top abscissa. Left panel is reproduced from Vondrak et al. [2008].*

***Table 1.4.** Ablation fraction and the ablation profile parameters from a 10 μg meteoroid entering at 18 km s^{-1}.*

Element	%Ablated fraction	Centroid/ km
Si	93.9	85.0
Mg	93.2	83.6
Fe	100	86.8
Ca	0.6	82.3
Al	0.2	83.4
Ti	4.1	83.2
Na	100	96.2
K	100	96.0
O	90.9	85.2

1.4. METEORIC LAYERS ON VENUS, MARS AND TITAN

The electron densities in planetary atmospheres can be measured using the occultation of radio waves transmitted through the atmosphere from a spacecraft, and detected at Earth. These measurements show that there is a major peak in the daytime ionosphere produced by solar radiation and photoionization. Below this main peak, one or more secondary peaks have been found. Examples of such layers have been located on Venus by Pioneer Venus [*Kliore et al.*, 1979], and Mars by Mariner IV [*Fjeldbo et al.*, 1966] and Mars Express [*Patzold et al.*, 2005] among others. The Voyager I fly-by provided infrared observations of Titan's ionosphere [*Hanel et al.*, 1981; *Maguire et al.*, 1981; *Samuelson et al.*, 1983], although following missions were not able to provide any information about meteoroid effects in its atmosphere. More recently, the Cassini-Huygens Atmospheric Structure Investigation (HASI) has collected a large amount of data that may be used to provide a new empirical model of Titan’s atmosphere that extends from the surface to the exobase [*Waite et al.*, 2013].

Table 1.5 summarizes some of the most important physical properties of these Solar System bodies. Venus and Earth are quite similar in terms of radius, mass and gravity. Nevertheless, the Venusian atmosphere is denser and the atmospheric pressure on the surface is 93 times larger than on Earth. The most important difference is that the sidereal day is ~225 times longer at Venus, so there is a large asymmetry between the midnight and noon atmospheres [*Fox and Kasprzak*, 2007; *Hedin et al.*, 1983; *Keating et al.*, 1985]. Note that Titan has the largest scale height, so that the deposition profiles during the ablation process will be rather wider than for the other bodies.

Table 1.5. *Main physical properties of Venus, Earth, Mars, and Titan. Adapted from Yung and DeMore [1999].*

	Venus	**Earth**	**Mars**	**Titan**
Mass (Earth = 1)[a]	0.815	1	0.1075	0.0225
Radius [km]	6051.5	6378.1	3389.5	2575
Gravity in equator [m s^{-2}]	8.87	9.81	3.71	1.37
Distance [AU][b]	0.71-0.73	0.98-1.02	1.38-1.67	9.54
Surface pressure [atm]	93.0	1.0	$6\cdot10^{-3}$	1.7
Scale Height [km]	15.9	8.5	11.5	40
Length of the year [Earth days][c]	224.7	365.26	687	15.970
Obliquity	-177.4º	23º27’	23º59’	0.35º
$\boldsymbol{v_\infty}$ **[km s^{-1}]**[d]	10.3	11.2	5.0	2.6

[a]1 Earth mass = 5.98×10^{24} kg, [b]1 astronomical unit (AU) = 1.496×10^{11} m, [c]Sidereal, [d]Escape velocity.

1.4.1. Meteoric layers on Venus.

Figure 1.10 shows the electron density profile measured by Pioneer Venus in the nightside ionosphere where there is a main dominant peak at 142 ± 4.1 km [*Kliore et al.*, 1979]. A double-peak structure was found during two closely spaced orbits, 55 and 57, apparently a rare phenomenon which may be related to meteoroid ablation or another ionization source, such as precipitation of electrons or protons onto the nightside.

McAuliffe and Christou [2006] studied numerically the mass-loss, deceleration and luminescence of meteoroids in the Venusian atmosphere with an entry velocity between 10 and 80 km s^{-1} and an input angle of 45°. They concluded that meteors should reach their points of maximum ablation at greater altitudes than those identical objects ablating on Earth, and their lifetime should be shorter than terrestrial meteors.

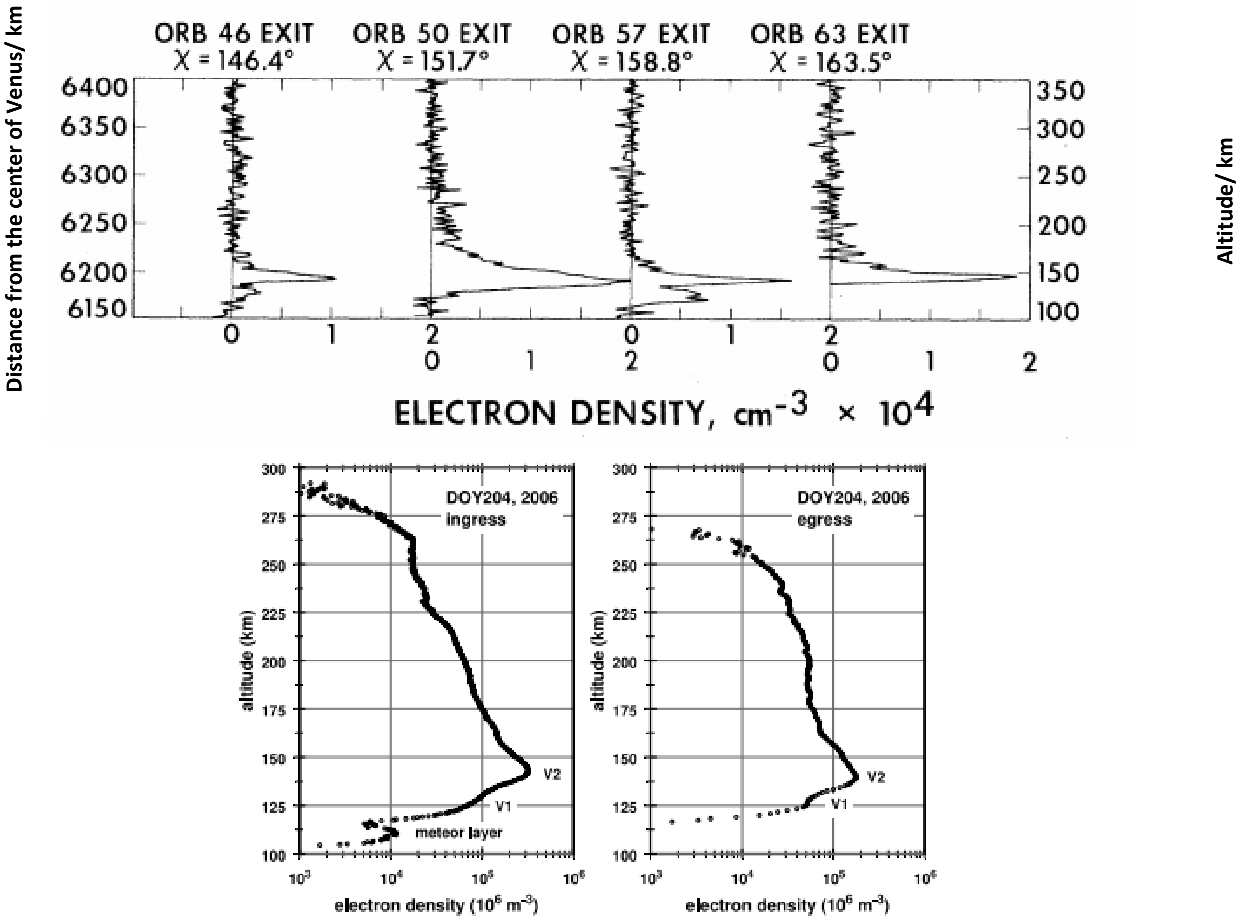

***Figure 1.10**. Top panel: electron density profiles measured by Pioneer Venus in the nightside ionosphere of Venus at solar zenith angles greater than 110º, reproduced from Kliore et al. [1979]. Bottom panel: electron density profiles provided by the Mars Express mission from occultation (left) ingress and occultation egress (right). Reproduced from Patzold et al. [2005].*

1.4.2. Meteoric layers on Mars.

The atmosphere of Mars has been sounded in more detail than the rest of the extraterrestrial solar system bodies. Studies have demonstrated that while the Martian atmosphere is thinner than the Earth's atmosphere at ground level, the ablation peak for various metallic elements occurs in a very similar range of heights on both planets [*Flynn and McKay*, 1990]; thus, the ablation peak appears between 80 and 120 km, depending on the input properties of the meteoroid. The Mars Express mission confirmed the existence of a sporadic metal layer between 65 and 110 km in altitude [*Patzold et al.*, 2005]. Mars Express could not find such layers in ionospheric observations made during the night. Theoretical models have shown that meteoroid ablation could produce enough long-lived metallic ions to explain the altitude and magnitude of the observed layers [*Molina-Cuberos et al.*, 2003; *Whalley and Plane*, 2010].

At these altitudes, the concentration of O_2 ranges from 10^{10} to 10^{12} cm^{-3} [*Keating et al.*, 1998]. This oxygen level is insufficient to ensure combustion reactions of the organic compounds that may be present in the meteoroid. *Baldwin and Sheaffer* [1971] demonstrated that stony and iron meteorites in Mars' atmosphere suffer a smaller mass loss during the ablation process compared to when they decelerate in the Earth's atmosphere. *Pandya and Haider* [2012] analyzed 1500 electron density profiles, obtained by the radio occultation technique using Mars Global Surveyor, to study the physical characteristics of low-lying plasma layers on Mars during the months of January to June of 2005. From this analysis, it was found that 65 profiles were distributed between altitudes of 70 km to 105 km, probably due to the presence of metallic ions deposited by meteoric ablation.

1.4.3. Meteoric layers on Titan.

Titan is the only moon in the solar system with a surface pressure greater than 1 bar. The main atmospheric constituent is nitrogen, followed by methane which was the first compound identified in Titan's atmosphere. CH_4 has a nearly constant mole fraction in the stratosphere of ~0.015, increasing in the troposphere with decreasing altitude [*Waite et al.*, 2013].

The main ionospheric peak has been located at 1180 ± 150 km by the Voyager I fly-by [*Bird et al.*, 1997]. However, Voyager could not provide any evidence of another peak below the main peak, and hence it could not provide any information regarding meteoric impacts in Titan's atmosphere. Some theoretical models have studied the effects of meteoric ablation on the composition of the neutral [*English et al.*, 1996] and ionized [Molina-Cuberos, 2001] atmosphere. Molina-Cuberos et al. [2001] used a simple model in order to model the electron number density vertical profile and concluded that an ionospheric layer produced by ablation could be present at 700 km with an electron density peak similar in magnitude to the one produced by solar radiation at 1000 km.

Figure 1.11 shows the electron density profiles ranging from the ground to 2000 km. the upper ionosphere layer, above 800 km, is due to electrons trapped in the magnetosphere of Saturn and solar radiation. The lower ionosphere layer, below 400 km, is due to galactic cosmic rays [*Molina-Cuberos et al.*, 1999a; *Molina-Cuberos et al.*, 1999b]. the middle ionosphere is formed by meteoric ionization. *Molina-Cuberos et al.* [2001] calculated this layer for a mean entry velocity of 18 km s^{-1} in two different assumptions: 1. without considering transport (labelled as Model II in Figure 1.11), and 2. with transport and charge exchange (Model III). If transport is included, the electron density disagrees with Voyager I observations being by a factor of 3 higher than the upper limit measure by radio occultation [*Bird et al.*, 1997].

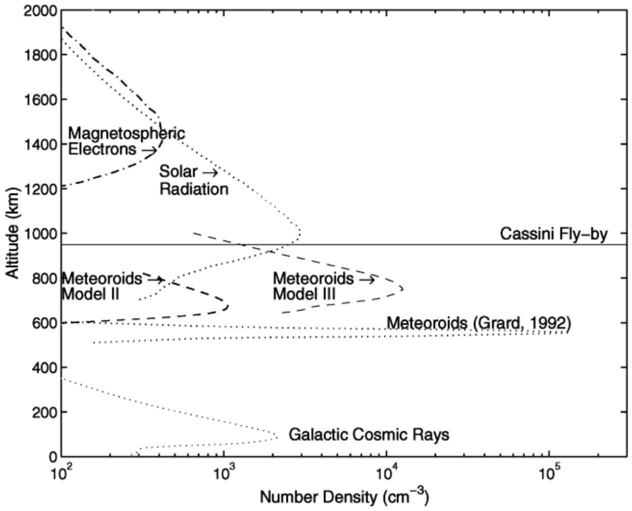

Figure 1.11. *Number density of electrons in the ionosphere of Titan. The electron density due to the different sources is shown separately: magnetospheric electrons, solar radiation, meteoroid Model II (average entry velocity of 18 km s^{-1}, without transport), Model III (average entry velocity of 18 km s^{-1}, with transport and charge exchange), and galactic cosmic-rays [Molina-Cuberos et al., 1999b]. Reproduced from Molina-Cuberos et al. [2001].*

1.5. THESIS AIMS AND OBJECTIVES

The specific aims and objectives of this thesis are listed below along with reference to the relevant chapters:

- Assess the velocity and size distribution of cosmic dust particles entering the Earth's atmosphere (Chapter 2):
    - ➢ Combine three quite different cosmic dust models with CABMOD using a Monte Carlo sampling method.
    - ➢ Determine the ablation rates of Na, K, Fe, Mg and Ca above 60 km.

  - Estimate the accretion rate of cosmic spherules predicted by each model.
  - Compare the absolute ablation fluxes of Na and Fe to observations and models.
  - Analyze model uncertainties.
- Refine and validate CABMOD using a laboratory experimental set-up which enables time-resolved simulations of the melting of IDPs and the evaporation of their major elemental compounds (Chapter 3):
  - Compare and assess experimental and calculated ablation rates of Na, Fe, and Ca.
  - Identify which parameters in CABMOD need to be calibrated according to the laboratory measurements.
  - Develop an improved version of CABMOD.
  - Assess which parts of CABMOD need to be improved in the future.
- Estimate the contribution of each cosmic dust source (JFCs, ASTs, HTCs, and OCCs) to the total influx using the size distribution derived from the Zodiacal Cloud Model [*Nesvorný et al.*, 2010; *Nesvorný et al.*, 2011] and constrained by the COBE (COsmic Background Explorer) and Planck observations of infra-red emission from the zodiacal cloud (Chapter 4):
  - Determine the absolute contributions of each dust source by constraining to the spherule accretion rate, as well as the most recent measurements of the vertical fluxes of Na and Fe atoms above 87.5 km in the atmosphere.
  - Compare the results inferred from IRAS (Infrared Astronomical Satellite) and COBE observations.
- Examine the impact of cosmic dust on the atmospheres of Venus, Mars, and Titan:
  - Assess the contribution of each cosmic dust source to the Venusian and Martian atmospheres.
  - Examine the effect of the near approach to Mars of comet C/Siding Spring A1.
  - Study the impact of cosmic dust in Titan's atmosphere.

This work provides valuable information to answer the main question presented at the start of this chapter, namely: what is the magnitude of the rate of cosmic dust that is entering the Earth's upper atmosphere?

1.6. THESIS LAYOUT

The remainder of the thesis is organized as follows:

Chapter 2: Description, analysis and discussion of three quite different size/velocity cosmic dust distributions.

Chapter 3: Presentation of a novel instrument to measure differential ablation from meteoritic samples.

Chapter 4: Contribution of the different cosmic dust sources to the total mass flux accreted by the Earth.

Chapter 5: Analysis of the meteoric layers of Venus, Mars, and Titan.

Chapter 6: Summary of the results of this thesis, overall conclusions and recommendations for future work.

CHAPTER 2: ON THE SIZE AND VELOCITY DISTRIBUTION OF COSMIC DUST PARTICLES ENTERING THE ATMOSPHERE

2.1. INTRODUCTION

As discussed in Chapter 1, IDPs have their origin in meteor showers and the sporadic background complex. The latter provides a much greater input into the upper atmosphere than meteor showers [*Baggaley*, 2002; *Ceplecha et al.*, 1998]. Essentially, the meteor influx gives rise to the upper atmospheric metallic ion layers observed by radars and lidars, and they are believed to be the source of condensation nuclei, the necessary prerequisite for the formation of noctilucent cloud particles in the polar mesopause region [*von Zahn et al.*, 2002]. For this reason, in order to understand how this flux gives rise to this atmospheric phenomena, accurate knowledge of the global Meteoric Input Function (MIF) is necessary. This function takes account of the directionality, and mass and velocity distributions.

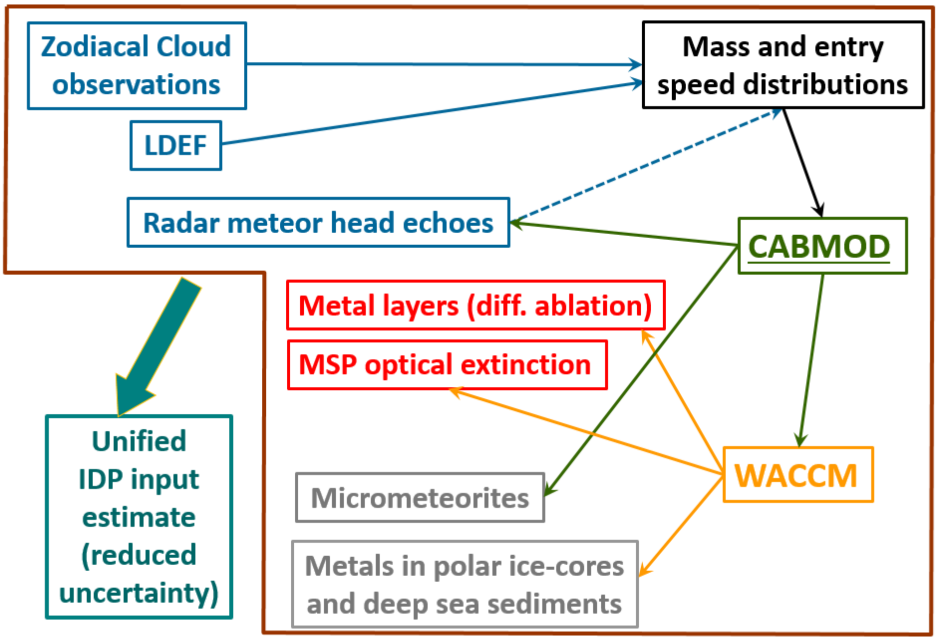

Figure 2.1. *Scheme showing how the mass and velocity distributions are used to derive the global Meteor Input Function.*

Figure 2.1 depicts how the MIF is determined. Different meteor distributions can be combined with CABMOD to determine: 1. The integrated deposition profiles for the most significant metals in the upper atmosphere; 2. The flux of micrometeorites that are deposited on the surface; and 3. An assessment the detectability of meteors by radars. Here we consider the metallic species Fe, Mg, Ca, Na and K. These metals exist as layers of atoms between ~80 and ~105 km and atomic ions at higher altitudes [*Plane*, 2004; *Plane et al.*, 2015]. Below 85 km they form compounds such as oxides, hydroxides, and carbonates which polymerize into nanometer-sized meteoric smoke particles (MSPs). The inclusion of the MIF in the Whole Atmosphere Community Climate Model (WACCM) allows the Na, Fe, Mg, and K layers to be modelled globally [*Feng et al.*, 2013; *Langowski et al.*, 2014; *Marsh et al.*, 2013; *Plane et al.*, 2014].

However, whereas the Carbonaceous Ivuna (CI) chondritic ratios of Na:Fe:Mg are 1:15:17 [*Asplund et al.*, 2009], WACCM requires relative ablation rates of 1:4:1 [*Feng et al.*, 2013; *Langowski et al.*, 2014; *Marsh et al.*, 2013] in order to produce modelled Na, Fe, and Mg layers in agreement with observations. This result indicates that significant differential ablation occurs. *Vondrak et al.* [2008] concluded that if the average meteoroid entry velocity peaks around ~25 km s^{-1}, then about 90% of the incoming mass should ablate. However, this velocity would not explain why a fraction of only ~0.25 of the incoming Fe and Mg ablated relative to Na.

In this chapter three quite different mass/velocity distributions of cosmic dust are evaluated: an astronomical model constrained by observations of IR emission from the Zodiacal Dust Cloud [*Nesvorný et al.*, 2010; 2011]; a model derived from measurements on a space-borne dust detector [*Love and Brownlee*, 1993; *McBride et al.*, 1999]; and an astronomical model describing the portion of the incoming flux measured by meteor head echo detections with High-Power and Large-Aperture (HPLA) radars [*Fentzke and Janches*, 2008; *Pifko et al.*, 2013]. The relative injection rates of the different metals are then compared with those required to model the observed relative abundances of the mesospheric metals. The predicted surface accretion rate of cosmic spherules (i.e., cosmic dust particles which melt but do not completely ablate in the upper atmosphere) is also compared with the measured accretion rate at the bottom of an ice chamber at the Amundsen-Scott base at South Pole [Taylor et al., 1998, 2007] and in the Greenland ice cap [Maurette et al., 1987].

2.2. MODELS OF COSMIC DUST IN THE NEAR-EARTH ENVIRONMENT

The Earth and its atmosphere represent a target for IDPs which allows the incoming objects to be studied directly, if they reach the surface; or indirectly, if they interact with the atmosphere or orbiting spacecraft. The relationship between these samples and their sources depends on the physical and dynamical processes which have characterized their transport to the Earth. Nowadays, there are three different techniques to infer the cosmic dust distribution: 1. Interaction of IDPs on a space-borne dust detector (e.g., LDEF [*Love and Brownlee*, 1993]); 2. HPLA radars [*Mathews et al.*, 2001], which can detect efficiently the small plasma region surrounding and moving with the meteoroid known as the meteor head echo [*Close et al.*, 2002]; 3. Modelling tools which are calibrated against various types of observations (e.g., the Grün Interplanetary Dust Model at 1 AU [*Grün et al.*, 2001], the NASA Orbital Debris Environment Model [*Zhang et al.*, 1997], the European Space Agency meteoroid/debris database (ESABASE) [*Sdunnus et al.*, 1997], the ESA Meteoroid And Space debris Terrestrial Environment Reference (MASTER) model [*Klinrad et al.*, 1997b; *Sdunnus*, 1995], and the Divine Interplanetary Dust model [*Divine*, 1993b]).

In the present chapter, three cosmic dust models are combined with CABMOD in order to get the injection rate profiles for the more important meteoric metals. Two are astronomical models, the Zodiacal Cloud Model (ZCM) [*Nesvorný et al.*, 2010; 2011] constrained by mid-Infrared observations of cosmic dust, and the second is a model developed from HPLA radar observations at Arecibo [*Fentzke and Janches*, 2008; *Janches and Chau*, 2005]. The third is the LDEF model [*Love and Brownlee*, 1993], which is based on measurements made with a space-borne dust detector. The same tests can be applied to MIFs other than the three that are used here as test cases, as well as MIFs developed in the future. At the end of the chapter there is a discussion of the problems associated with reconciling radar observations and global circulation models regarding the nature of the MIF.

2.2.1. The Long Duration Exposure Facility (LDEF).

Considering the anisotropic distributions of meteoroids or space debris particles, one should bear in mind that some spacecraft orbital and attitude geometries directly affect the sampled flux. The LDEF satellite was located in a near circular orbit at a mean altitude of 458 km and an inclination of 28.5º [*McDonnell et al.*, 1993], maintaining an essentially constant geocentric orientation. Hence, the faces on the satellite are often referred to as North, South, East, West, Space and Earth, these being the approximate facing directions with respect to the equatorial plane. Figure 2.2, right panel, shows the LDEF satellite in its orbit: the orbit precesses around the North Celestial Pole (NCP) normal to the orbit, and the ecliptic plane varies with time with a similar period. LDEF was deployed on April

7th 1984 and retrieved in January 1990, so that it experienced a total exposure period of 5.778 years.

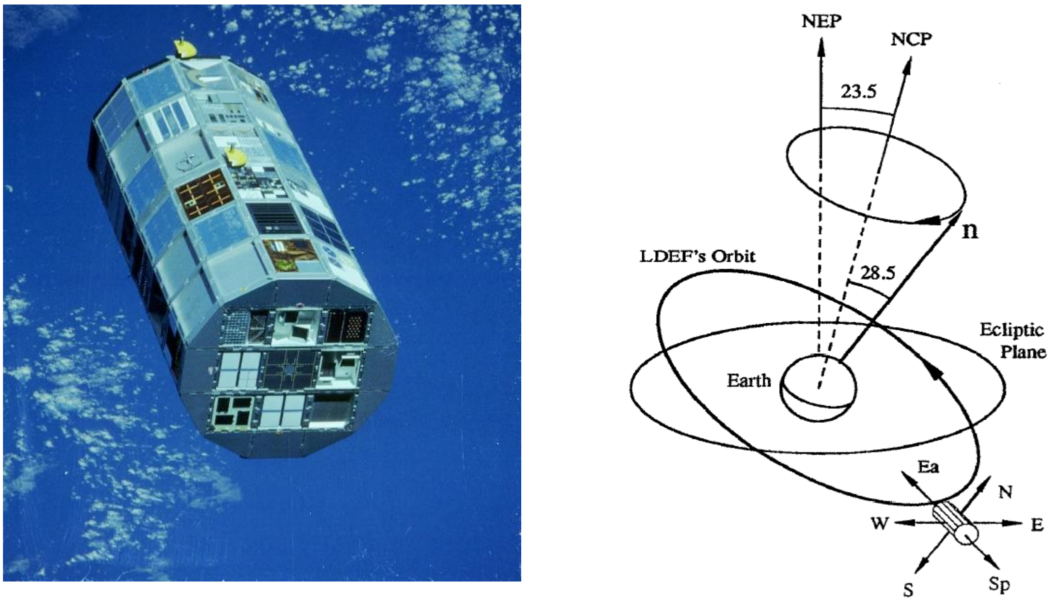

***Figure 2.2**. The LDEF satellite. Left panel: photograph of the space-borne after deployment (https://upload.wikimedia.org/wikipedia/commons/4/40/LDEF_after_deployment.jpeg). Right panel: LDEF's orbit with respect to the Earth and the ecliptic plane (reproduced from McBride et al., 1995). The orbit's normal vector $\vec{n}$ precesses clockwise around the Earth's spin axis (with a period of ~52 days).*

There are a number of factors related to the exposure which make the LDEF data especially suitable for defining the meteoroid influx in the Low Earth Orbit (LEO) environment [*McDonnell et al.*, 1993]. The experiment platforms provide a configuration with a well-defined exposure to primary impactors, preventing contamination of secondary impactors (re-entrant projectiles). Furthermore, the absence of appendages such as solar cells and antennas yields a low expectation of contamination from secondary impactors (see Figure 2.2, left panel).

2.2.1.1. Data sources on LDEF.

There are several panels located on the satellite [*McDonnell et al.*, 1993]:

- The University of Kent's **Microabrasion Package (MAP)**. These panels consist of aluminum foils of various thicknesses between 2.0 μm and 31.0 μm, and brass foils of 5 μm thickness on the East, West, North, South and Space faces of LDEF.
- The **Space Debris Impact Experiment (SDIE)** consisted of over 26 m^2 of 4.8 mm thick aluminum plates situated on all the peripheral faces except the East,

Space and Earth faces. The largest crater found had a diameter of 4 mm. *Humes* [1992] reported an analysis of 532 craters with diameter greater than 0.5 mm.

- The **Interplanetary Dust Experiment (IDE)** recorded the impacts which penetrated semiconductor detectors of 0.4 µm and 1.0 µm thickness on the East, West, North, South, Space and Earth faces during the first year of the LDEF mission. The impact rate was found to be very time-dependant.
- The **Ultra-Heavy Cosmic Ray Experiment (UHCRE)** was protected by thermal blankets consisting of a Teflon A-FEP layer of thickness 127 µm backed with layers of silver, Inconel and paint.
- The **French Cooperative Payload (FRECOPA)** consisted of two experiments on the trailing (West) face of LDEF. The first experiment was composed of a set of thick glass and metallic surfaces which were exposed for the whole mission. The second experiment consisted of thin aluminum and gold foils which were exposed for only nine months.
- The **Chemistry of Micrometeoroids Experiments (CME)**. These panels consisted of approximately 0.8 m^2 of high purity gold sheets of 0.5 mm thickness on the trailing (West) face of LDEF and approximately 1.1 m^2 of aluminum with 3.2 mm thickness. Chemical analysis has revealed that most of the large craters were caused by natural impactors but some man-made debris impacts occurred on LDEF’s trailing edge.
- The **Meteoroid and Debris Special Investigation Group (MD-SIG)** examined the whole LDEF spacecraft during the de-integration procedure and documented all craters with diameters greater than 0.5 mm and all penetration holes with diameters greater than 0.3 mm.

2.2.1.2. Penetration parameters for LDEF impact craters and perforations.

With very few exceptions, it is not possible to know the impact velocities of the particulates responsible for the penetrations on LDEF’s recovered surfaces. It is also not possible to infer the impact angle except within the ±90º limits for the flat detector geometry. The density and the shape of the impacting particulate are also unknown except for general expectations which might accompany their assumed origin as meteoroids or space debris. Nevertheless, experimental impact studies have shown that projectile shape and density are relatively unimportant in determining the size of the crater, so thus the crater volume is basically proportional to the impacting energy [*Cour-Palais*, 1992; *Fish and Summers*, 1965; *McDonnell and Sullivan*, 1992].

The approach to decoding projectile parameters on LDEF was then based on the following factors [*McDonnell et al.*, 1993]:

- **Velocity:** from the flux directionality and modelling of the orbital dynamics of particulates, both bound and unbound.
- **Mass:** from crater depth or diameter or the ballistic penetration limit, but requiring the inferred velocity.
- **Density:** from crater morphology, especially the depth/diameter ratio, but noting that such clues become less useful with increasing velocity.
- **Shape:** variations from crater symmetry, especially in very thin foil perforations.
- **Impact angle:** 1. Variations from craters symmetry, especially the ellipticity and associated lateral displacement in crater development; 2. Deconvolution of the overall angular flux distribution, which is smoothed by the flat geometry for each sampled exposure.

2.2.1.3. Velocity distribution in LDEF.

As discussed above, one of the major sources of uncertainty in the LDEF model is the value of the encounter velocity which is used to adjust the cumulative mass distribution of meteoroids. *Christiansen* [1992] reported laboratory impact experiments of centimeter, millimeter, and micrometer projectiles striking thick aluminum alloy targets at speeds up to 18 km s^{-1}, demonstrating that crater volume under those conditions is nearly proportional to the projectile kinetic energy. *Love and Brownlee* [1993] chose the average meteoroid speed to be 16.9 km s^{-1}, as found by *Erickson* [1969] and *Kessler* [1969] from photographic meteors and supported by crater rate measurements on LDEF.

The most statistically reliable data set comes from the Harvard Radio Meteor Project (HRMP) measurements where ~20,000 meteor observations were taken [*Sekanina and Southworth*, 1975; *Southworth and Sekanina*, 1973]. However, *Taylor* [1995a] identified a numerical error in the original code to reduce the data which resulted in a significant under-estimation of the numbers of fast meteors (especially 50-70 km s^{-1} meteors where the under-estimation is by a factor of ~100). The final corrected velocity distribution of meteoroids encountering the Earth's atmosphere [*Taylor*, 1995a; 1995b] is shown in Figure 2.3, where the mean velocity of this distribution is 17.7 km s^{-1}.

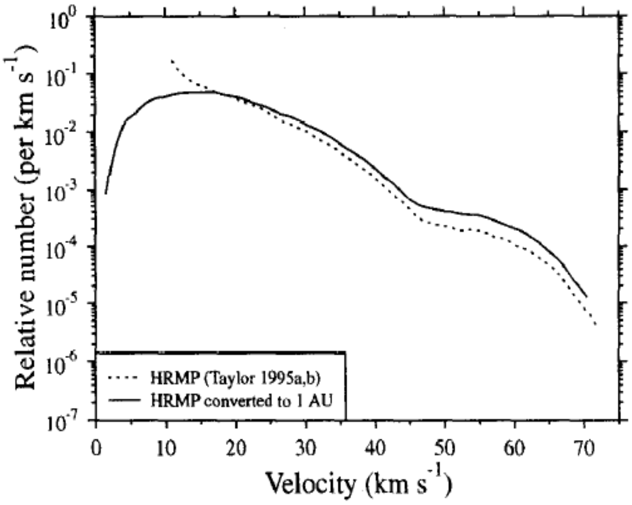

Figure 2.3. *The Harvard Radio Meteor Project meteoroid velocity distribution [Taylor, 1995a]. The distribution is corrected for gravitational enhancements to take the distribution to 1 AU (i.e., as seen from a massless Earth). The dotted curve corresponds to the distribution of meteoroids entering the top of the atmosphere. Reproduced from McBride et al. [1999].*

2.2.2. High Power and Large Aperture Radars.

HPLA radars have been used for micrometeor studies since the 1990's. Although the first measurement was reported by *Evans* [1965] using the Millstone-Hill 440 MHz radar, it was not until the late 1990´s that intense observing programs at the different HPLA facilities around the planet became active [*Close et al.*, 2000; *Mathews et al.*, 1997; *Pellinen-Wannberg and Wannberg*, 1994]. HPLA radars are crucial to the meteor community, since these instruments can detect meteoroid sizes that bridge a gap between traditional meteor radars and dust detectors onboard satellites [*Janches et al.*, 2008].

Both HPLA radars and Specular Meteor Radars (SMR) detect the plasma formed by a meteoroid entering the atmosphere and ablating. However, the peak plasma density and viewing geometry observed by each instrument are quite different [*Baggaley et al.*, 1994; *Brown et al.*, 2005; *Close et al.*, 2007], which may result in disparate velocity distributions. While SMR radars detect the specular reflection of the meteor trail, HPLA radars detect the head reflection from the plasma that moves with the velocity of the meteoroid.

The SMR velocity distributions are derived from the detection of the Fresnel diffraction patterns from the developing trail [*Ceplecha et al.*, 1998]. This technique has several well-known detection biases which are present due to various radar sensitivity effects inherent in this approach. For example, *Galligan and Baggaley* [2004] reported results from 5 years of AMOR meteor observations and presented their results in three forms: 1. A 'direct observed' meteor velocity distribution with no corrections; 2. An 'atmospheric' distribution, which includes atmospheric interaction effects of the meteoroids upon entry and are suggested to be the distribution of the particles that actually do enter the Earth's atmosphere; and 3. A 'space sample' distribution, which has further corrections due to orbital collision probabilities between the meteoroids and the Earth. This last distribution represents the heliocentric meteoroid velocity distribution of the solar system dust cloud regardless of whether these particles will enter the Earth's atmosphere and become meteors.

The most important bias which affects SMR radars is the height ceiling effect [*Olsson-Steel and Elford*, 1987; *Steel and Elford,* 1991]. Thus, meteors with the highest geocentric velocities form plasma higher in the atmosphere because ablation occurs earlier during atmospheric entry [*Jones*, 1997; *Jones et al.*, 2001; *Vondrak et al.*, 2008]. When the trail is formed at higher altitudes, the initial radius of the trail is larger than the radar wavelengths because the mean free path of the atmosphere is large, which translates into a lower electron density and a decrease of the SNR of the returned signal due to destructive interference within the trail. In conclusion, altitude distributions from SMR radars data peak at ~90 km of altitude with few detections above ~110 km [*Galligan and Baggaley,* 2004; *Janches et al.*, 2003], while altitude distributions for HPLA radars peak between 95 and 110 km, depending on the frequency and the radar sensitivity. Most of the events at these high altitudes are due to higher geocentric velocity meteors [*Janches et al.*, 2003; *Vondrak et al.*, 2008].

Since a significant number of meteor velocity distributions measured with HPLA radars have been reported, there have been many discussions about what type of biases these instruments have, such as the minimum detectable Radar Cross-Section (RCS) which provides a metric to characterize the radar system´s ability to detect particles with a given mass and speed, and whether it is possible that the resulting high geocentric velocity distributions are an effect of a bias against slow meteors [*Janches et al.*, 2003]. In fact, HPLA radars are very different instruments when compared one to another. Table 2.1 shows a list of HPLA radars with their signature characteristics. The combination of transmitting peak power, frequency and antenna configuration results in completely different instrument sensitivities.

Table 2.1. *Main characteristics of HPLA radars used for meteor observations. Reproduced from Janches et al. [2008].*

Observatory	**Geographical location**	**Frequency (MHz)**	**Antenna configuration**	**Transmitted power (MW)**
ALTAIR	Kwajalein Atol	160 – 422	46 m single dish with monopulse	6
AMISR	Alaska, USA	440	Phase array of 96 cross dipoles	1.3
Arecibo	Arecibo, Puerto Rico	430	300 m diameter single dish	2
EISCAT	Northern Scandinavia	224 – 930	120 m × 40 m 32 m single dish	2
Jicamarca	Jicamarca, Peru	50	18000 dipoles in a 300 m × 300 m square array	2
Millstone-Hill	Massachusetts, USA	440	47 m and 67 m single dishes	
MU	Japan	46	475 crossed yagi phase array	1
Sondrestrom	Greenland	1290	30 m diameter single dish	3

2.2.2.1. Modelling Meteor distribution using HPLA radars.

This model determines how much, when and where meteoroid mass is deposited in the Earth’s atmosphere. For this purpose, *Janches et al.* [2006] developed a simple model that utilizes Monte Carlo simulation techniques to answer the following questions: given a small volume placed in the MLT, what is the relative number of meteors that would pass through that volume and how does that number depend on the geographical location and time? Figure 2.4a shows a diagram with the basic assumptions made for the Monte Carlo simulation.

1. The volume observed by the radar is assumed to be a cylinder with the bottom placed at 70 km and the top at 140 km of altitude. The radar beam can be approximated as a cylindrical beam of the size of ~300 m diameter dish for the case of Arecibo.

2. *Janches et al.* [2006] and *Fentzke and Janches* [2008] took meteor populations with known radiant distributions, and estimated the contribution from sporadic meteoroid sources on the MIF observed at Arecibo. To simplify the problem, the North and South Apex radiant sources are modeled as a single Apex radiant source with the combined attributes of both sources [*Chau and Woodman*, 2004; *Janches et al.*, 2006].

3. *Fentzke and Janches* [2008] considered a geocentric velocity distribution with a bimodal shape dominated by a fast retrograde component and a slower less dominant prograde velocity component for the Apex source, with ~80% of the population centered at ~55 km s^{-1} and ~20% of the population centered at 17.3 km s^{-1}. The rest of the radiant sources are modeled with Gaussian geocentric velocity distributions with a peak at 30 km s^{-1}.

4. *Fentzke and Janches* [2008] assumed the mass flux reported by *Ceplecha et al.* [1998] as initial global input. The cumulative flux is then converted to estimate the number of meteoroids contained in each mass bin for the whole planet in a year, or per minute per km^2 by a simple time/area product conversion factor.

5. In order to simulate the observed meteor rates, it is necessary to introduce the altitude at which the meteor will be first detected by the radar, which will be a function of its velocity ($h(v)$ in Figure 2.4a).

6. Finally, *Janches and Chau* [2005] have also shown that having a radiant whose elevation angle is above the local horizon is not a sufficient condition for a given meteoroid to be detected by the radar. The authors suggested, from observational results of diurnal rates, that this effect may be caused by the ablation of meteoroids at higher altitudes. That is, if the elevation is too low, the particles might ablate significantly before reaching the Mesosphere and Lower Thermosphere region (MLT). *Janches et al.* [2006] introduced an empirical model with two extreme cases (see Figure 2.4): 1. if the threshold length L is infinity, it implies that any meteoroid whose radiant has an elevation above

the local horizon will penetrate into the MLT and be detected by the radar; 2. if *L* is 0, only meteoroids with vertical trajectories (elevation ~90º) will penetrate into the MLT and be detected by the radar.

However, low-elevation radiant meteors can exhibit a relatively low detectability due to physical processes related with the interaction of the particles with the air molecules. A low elevation particle with a high speed will have a large tangential velocity component (see Figure 2.4b). For example, a particle travelling at 50 km s^{-1} in the tangential direction and through the center of the radar beam will need ~12 ms to cross it. Normally, the inter-pulse period used for the observations is 1 ms [*Janches et al.*, 2003], so the lifetime of the particle within the radar beam is long enough to obtain several samples of such an event. It is reasonable to think that the probability of detecting a meteor will decrease as the travelling time of the meteor through the radar beams decreases. However, as *Janches et al.* [2006] indicated, it is quite unlikely that this effect filters low-elevation meteors.

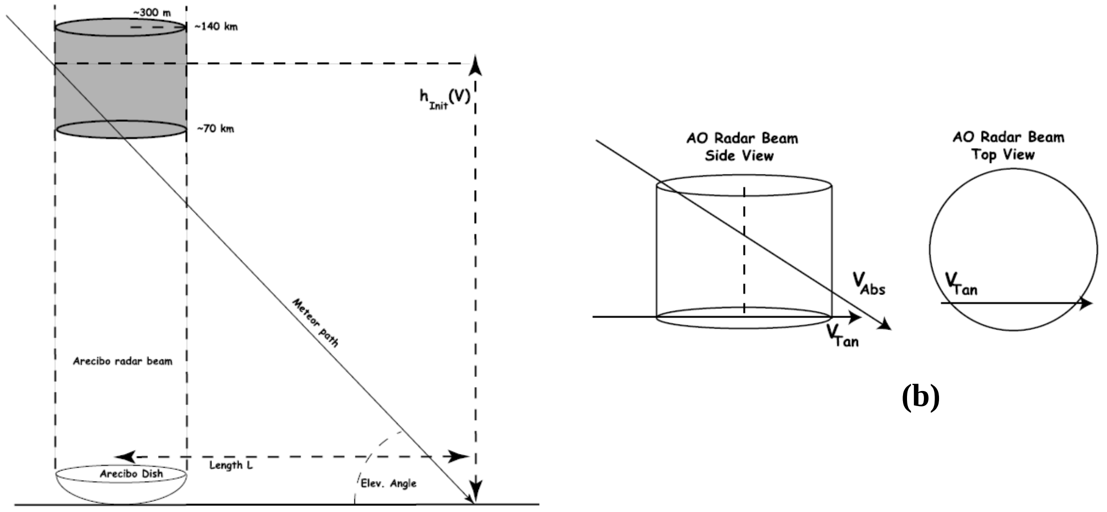

(b)

(a)

Figure 2.4*. Panel a: Diagram showing the basic assumptions made for the Monte Carlo simulation to model the Arecibo radar observations. Panel b: Diagram showing the effect introduced by meteors which have large tangential velocity components while crossing the radar beam. Reproduced from Janches et al. [2006].*

Janches et al. [2006] assumed that the sporadic meteoroid population is distributed among the six known apparent sources: the North and South Apex, the Helion and anti-Helion, and the North and South Toroidal [*Jones et al.*, 1993]. *Fentzke and Janches* [2008] used the observations from Arecibo radar and concluded that the North and South Apex sources represented 33% of meteoroids at 1 AU. The remaining two-thirds of incoming meteoroids was divided among the other apparent sources, with the Helion and anti-Helion sources each contributing nearly 22%, and the North and South Toroidal each providing 11% of the total flux. However, the validation of a radar MIF requires comparison with observations of the meteoroid atmospheric input. *Pifko et al.* [2013] used the MU radar at Japan and reported that the Apex contributed approximately 77% and 87% of the predicted and observed meteors, respectively; these values indicate that the vast majority of the MU-detected meteors originated from the Apex sources, with the remaining sporadic sources representing a minority of the detections. According to *Pifko et al.* [2013], the modeled contribution of the Helion and anti-Helion sources were overestimated significantly, with approximately 20% of the detections predicted to come from these two sources collectively and only about 5% of the observed meteors attributed to them. A summary is shown in Table 2.2.

Table 2.2. *Modeled and observed contributions of the sporadic sources to the meteoroid population detected by the MU radar system. Reproduced from Pifko et al. [2013].*

Source	**MU specific MIF model predictions (%)**	**MU meteor observations (%)**
Apex (fast, slow)	76.6 (99, 1)	86.8 (98, 2)
Helion	8.5	2.8
Anti-Helion	9.0	3.0
North Toroidal	5.6	6.6
South Toroidal	0.3	0.8

2.2.2.2. Detection of differential ablation by radars.

Since radars detect only electrons, it is challenging to understand in detail the ablation process through which these are produced while the micrometeoroid's chemical constituents are deposited in the MLT [*Janches et al.*, 2009]. As mentioned above, the production of electrons depends on the ionization probability of the evaporating constituents [*Jones*, 1997; *Jones et al.*, 2001; *Vondrak et al.*, 2008], which depends both on velocity of the meteoroid and each chemical element. *Janches et al.* [2009] reported the first study which is consistent with differential ablation using observations from the 430 MHz Arecibo radar in Puerto Rico. *Borovicka et al.* [2007] showed that different elements ablate at different points along the train using spectroscopic measurements in normal bright meteors. However, these are relatively large particles.

Janches et al. [2009] estimated the shape and density of the meteor head-echo plasma from the electron line density and meteor velocity as a function of altitude modelled by CABMOD. Figure 2.5 and 2.6 illustrate two examples observed on January 22, 2002 (hereafter these figures will be called Cases 1 and 2, respectively). Panel a in these figures displays the Range-Time-Intensity (RTI) image of the meteor and the white dash-dot line represents the leading edge of the pulse from where the meteor altitude as a function of time is measured [*Janches and ReVelle*, 2005]. For Case 1, the initial observed altitude is 110 km and the final altitude is 103 km. For Case 2, the meteor is observed between 103.5 km and 96 km. The measured instantaneous meteor velocities along the line of sight are displayed in panel b, and they are 35 km s^{-1} for Case 1 and 50 km s^{-1} for Case 2, respectively. The measured head-echo SNR is displayed as a red line in panel c; in both cases striking changes in the measured SNR were observed which can be related to a sudden increase (Case 1) or decrease (Case 2) in the rate of production of electrons giving rise to the meteor head echo plasma (panel e).

For Case 1, panel e shows that the enhancement in the meteor SNR may be produced by the rapid and complete evaporation of Na and K, well before the ablation of the major constituents becomes significant. For Case 2, the scenario is somewhat different. This meteor was much faster, and was detected significantly lower than Case 1, so that the sharp decrease in the production of electrons is likely to have been due to the complete ablation of the main meteoroid constituents.

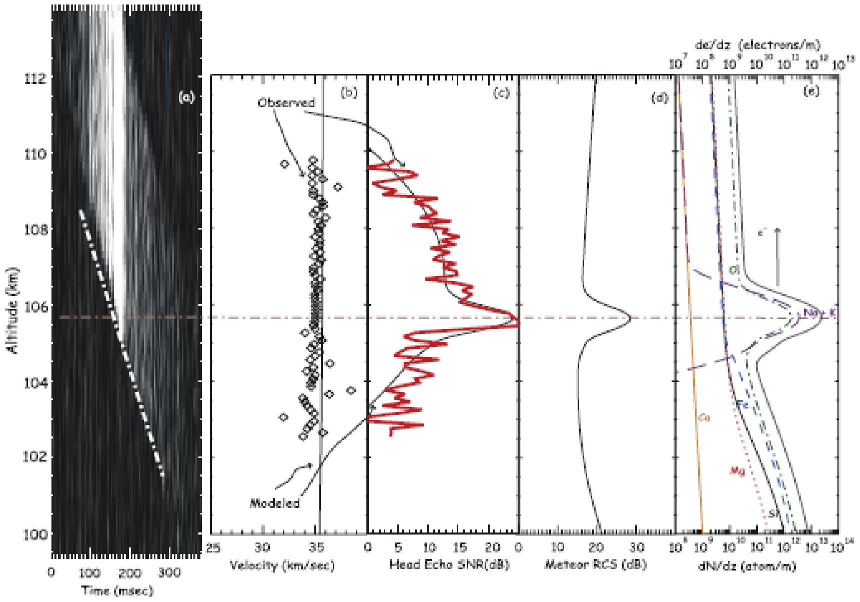

Figure 2.5. *Meteor at 36 km s^{-1} detected by Arecibo (Case 1). (a) Meteor RTI, (b) Modelled line and observed (diamonds) meteor altitude-velocity profile. (c) Modelled (black) and observed (red) meteor SNR. (d) Modelled meteor RCS. (e) Ablation profiles of main elements (bottom axis) and total amount of electrons produced (upper axis). The horizontal line shows the observed enhancement in SNR is due to the rapid ablation of the alkali metals Na and K. Reproduced from Janches et al. [2009].*

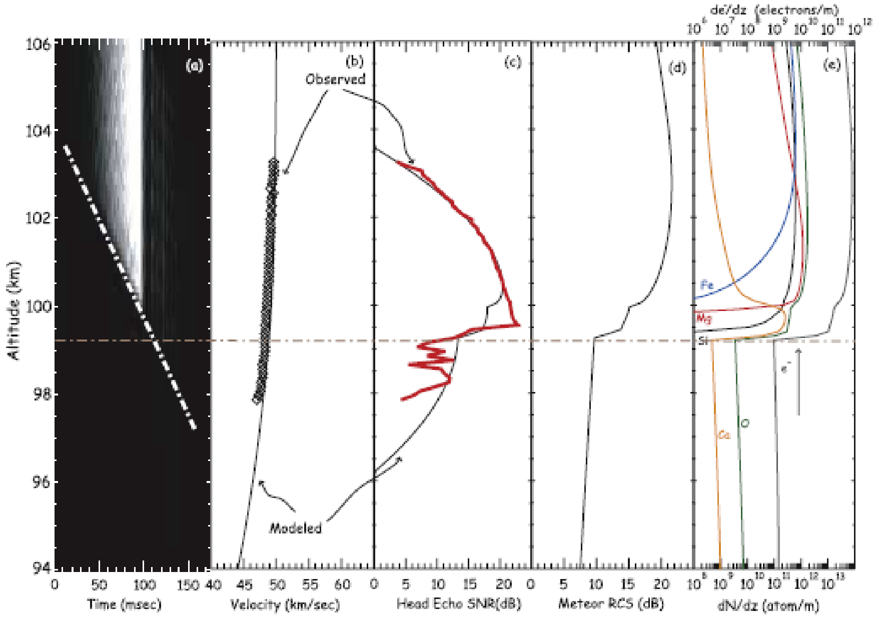

Figure 2.6*. Meteor at 51 km s^{-1} detected by Arecibo (Case 2). (a) Meteor RTI, (b) Modelled line and observed (diamonds) meteor altitude-velocity profile. (c) Modelled (black) and observed (red) meteor SNR. (d) Modelled meteor RCS. (e) Ablation profiles of main elements (bottom axis) and total amount of electrons produced (upper axis). The horizontal line shows the observed enhancement in SNR is due to the rapid ablation of the alkali metals Na and K. Reproduced from Janches et al. [2009].*

2.2.3. The Zodiacal Cloud Model.

The Zodiacal Cloud is a dynamic assembly of meteoroids in bound orbits around the Sun located within about 2 AU of the Earth. The orbits depend on the particle size, location in the cloud, and the type of parent body [*Nesvorný et al.*, 2010]. Traditionally, the Zodiacal Cloud has been described with phenomenological models of dust distributions to explain the amount of scattered light [*Hahn et al.*, 2002; *Hong*, 1985; *Ishiguro et al.*, 1999; *Kneissel and Mann*, 1991], the Doppler shifts of the solar Mg I Fraunhofer line [*Clarke et al.*, 1996; *Hirschi and Beard*, 1987; *Ipatov et al.*, 2008; *Mukai and Mann*, 1993; *Reynolds et al.*, 2004], and the more easily interpretable thermal emission observed in various lines of sight [*Kelsall et al.*, 1998; *Maris et al.*, 2006].

Phenomenological models describe the size, spatial and velocity distributions of dust particles in the solar system [*Dikarev et al.*, 2005; *Divine*, 1993; *Grün et al.*, 1985]. However, these models cannot explain the origin of the Zodiacal Cloud, its temporal brightness variability, and the provenance of IDPs collected at the Earth [*Nesvorný et al.*, 2010]. In fact, there are limitations to linking the detailed laboratory studies of IDPs and MMs to the properties of the parent bodies.

Detailed dynamical models are therefore more useful than phenomenological models for explaining the origin of the Zodiacal Cloud. The physical properties of IDPs, such as density, geometric albedo, elemental composition, mineralogy, tensile strength, heat capacity, etc., are at the root of a dynamical model. Together these properties describe the behavior of the particle in interplanetary space. In dynamical models, the individual particles are tracked by numerical codes as they evolve by various processes from their sources (asteroids, comets, satellites or Kuyper Belt objects) to sinks (e.g., when they sublimate, disrupt, impact or leave the solar system). Most of the dynamical models have been developed assuming that the main belt asteroids are the dominant source of zodiacal dust [*Dermott et al.*, 1984; *Grogan et al.*, 2001; *Grogan et al.*, 1997; *Ipatov et al.*, 2008; *Nesvorný et al.*, 2006; *Reach et al.*, 1997]. *Flynn* [1989] used computer simulations of the entry heating of large micrometeorites, and comparison of the collisional destruction and transport lifetimes of asteroidal dust, to conclude that the zodiacal dust is of asteroidal origin. However, the contributions of each source have remained in doubt. In fact, *Jenniskens* [2008] concluded that JFCs are the main contributor to meteor streams and responsible for the anti-Helion/Helion sources in the sporadic meteor background.

Models of the Zodiacal Cloud must explain the line-of-sight properties, the observed influx of meteors [*Ceplecha et al.,* 1998], and the impact rate of meteoroids on satellites [*Love and Brownlee,* 1993]. Nevertheless, these models use meteoroid velocity distributions derived from meteor observations, and ad hoc meteoroid distributions, avoiding sources and sinks. *Nesvorný et al.* [2010] developed the ZCM model implementing the dynamical characteristics of JFCs, HTCs, long-period OCCs, and ASTs.

Originally, the phenomenon of the zodiacal light was attributed to a smooth, lenticular distribution of cometary debris, centered on the Sun and lying in the plane of the ecliptic [*Giese and Kinateder*, 1986; *Grogan et al.*, 2001]. However, the launch of IRAS in 1983 [*Covault*, 1983] revolutionized our knowledge of the interplanetary medium. In essence, brightness profiles of the ZC became available, clearly showing a level of structure particularly near the ecliptic that could not be explained by the previous paradigm.

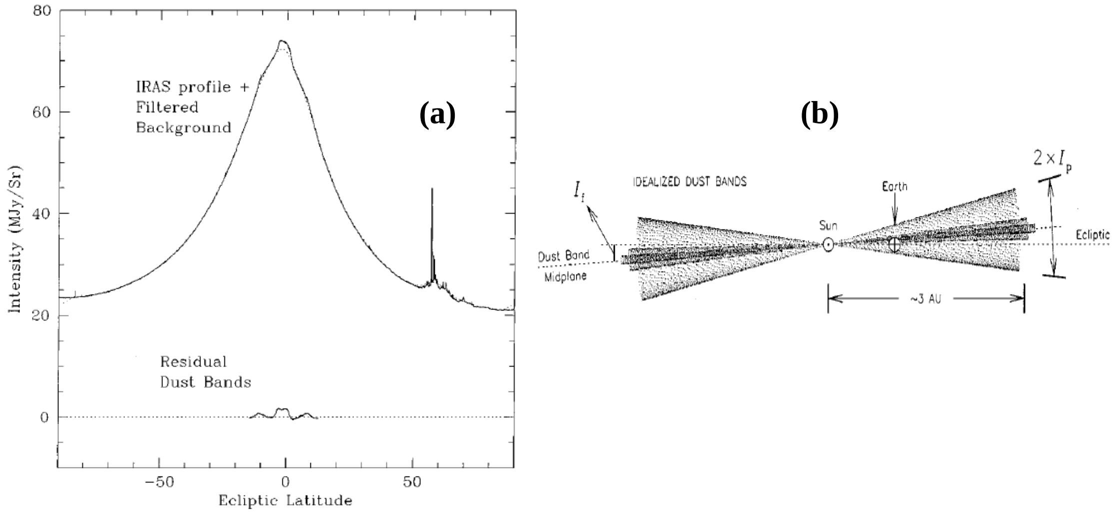

***Figure 2.7**. Panel a: IRAS observation of the Zodiacal Cloud in the* $25\ \mu m$ *waveband (solid curve); the structure around 60° latitude is due to dust in the plane of the Galaxy; by applying a Fourier filter to the IRAS observation, a smooth background profile (underlying dotted curve) is separated from a high-frequency dust band profile (solid lower curve). Panel b: Cross section through idealized dust bands; the angular width of each dust band is twice the proper inclination of its parental asteroid family; the Earth (⊕) is moving around the Sun within the dust bands. Reproduced from Grogan et al. [2001].*

Figure 2.7a shows the brightness profile of the Zodiacal Cloud, along with the results of passing the profile through a fast Fourier filter profile to isolate the near-ecliptic features [*Grogan et al.*, 2001]. The underlying dotted curve in Figure 2.7a represents the background profile, whereas the solid lower curve shows the high-frequency dust band profile. Figure 2.7b shows a schematic diagram of a cross section through a dust band [*Kortenkamp and Dermott,* 1998]. The idealized dust band has a constant forced inclination due to gravitational planetary perturbations which dictate the inclination of the dust band to the ecliptic. *Low et al.* [1984] suggested that these dust bands were traces of collisional debris within the main asteroid belt, based on the determination of their colour temperature. However, other authors [*Dohnanyi*, 1976; *Whipple*, 1967] argued that the traditional source of the IDPs were the debris of short period comets. As discussed below, this argument has been reinforced more recently with the dynamical model developed to explain radar observations of sporadic meteors.

2.2.3.1. Dynamical model for the Zodiacal Cloud and Sporadic Meteors.

The Zodiacal Cloud model developed by *Nesvorný et al.* [2010; 2011] comprises six parts:

1. Definition of the initial orbital distributions of particles of different sizes from different sources. As discussed below, the JFCs are the main contributor to the Zodiacal Cloud and Helion/anti-Helion meteors. The ASTs have low impact speeds and are less likely to be detected by meteor radars, whereas the meteoroids released from long-period comets contribute mainly to the apex source.

2. Tracking the orbital evolution of particles with various sizes from source to sink under the influence of gravitational and radiation forces. Radiation pressure, which particles experience after release from the parent body, is included in the orbital model of *Nesvorný et al.* [2010]. This pressure is proportional to the particle cross-sectional area, albedo and the energy flux of the radiation field which falls off as $1/\delta_S^2$, where δ_S is the distance from the Sun. Consequently, since radiation pressure is a force directed away from the Sun, it opposes the force of gravity, and under certain circumstances pressure on a particle may dominate the gravitational force [*McDonnell*, 1978]. The ratio of the force of radiation pressure to the force of gravity on the particle is given by the β parameter:

$$\beta = 5.7 \times 10^{-5} \frac{Q_{pr}}{\rho R} \; [g \; cm^{-2}] \qquad [2.1]$$

where Q_{pr} is the radiation pressure coefficient, and the particle's radius $R = D/2$ and density ρ are in cgs units; $\beta > 1$ for perfectly absorbing particles, where $Q_{pr} = 1$. *Nesvorný et al.* [2010] set $Q_{pr} = 1$, which corresponds to the geometrical optical limit, where R is much larger than the incident-light wavelength. Equation 2.1 considers only the radial component of the force created by the radiation pressure. Nevertheless, particles have a transverse velocity component, which will be the unique component in particles with a circular orbit. In consequence, the absorbed or reflected photons will tend to slow down the transverse velocity of the particles, since the solar radiation only has a radial component [*Robertson*, 1937]. This effect, known as Poynting-Robertson drag, establishes that for initially circular orbits with radius δ_S, a particle will spiral into the Sun in a time:

$$\tau_{PR} = 7 \times 10^5 R\rho\delta_S^2 v \; [yrs] \qquad [2.2]$$

where R and ρ are the radius (in meters) and density (in kg m^{-3}) of the spherical particle, and δ_S is the initial radius of the circular orbit in AU; v is the fraction of the momentum of the incident (on the particle) light beam transmitted to the particle. For example, assuming R = 500 µm and ρ = 2 g cm^{-3}, the Poynting-Robertson drag lifetime is $\tau_{PR} = 2.5 \times 10^6$ years. Finally, *Nesvorný et al.* [2011] assumed that the solar-wind drag force has the same functional form as the Poynting-Robertson term and contributes ~30% to the total drag intensity.

3. Some solar system meteoroids can be destroyed by collisions with other particles and by heating which can lead to the vaporization of minerals. The remaining grains will then mainly be composed of amorphous silicates and will survive down to very small heliocentric distances. *Nesvorný et al.* [2011] followed the criteria of *Moro-Martin and Malhotra* [2002], *Kessler-Silacci et al.* [2007] and others for which a particle can be thermally destroyed when the grain temperature reaches $T \geq 1500$ K. To simplify, particles can be treated as a black body, so that $T \cong 280/\sqrt{\delta_S}$ K. As a result, there are two extremes: 1. Particles with $D \gtrsim 100$ µm and $T \geq 1500$ K should be removed when reaching $\delta_S \lesssim 0.035$ AU; 2. The smallest particles considered by [*Nesvorný et al.*, 2011], $D \simeq 10$ µm, have T = 1500 K at $\delta_S \simeq 0.05$ AU. Thus, *Nesvorný et al.* [2011] opted for a simple criterion where particles of all sizes were instantly destroyed when they reached $\delta_S \leq 0.05$ AU.

4. The analysis of the effect of disruptive collisions of IDPs is difficult to model using a full collisional cascade in a computer code, due to the exponentially increasing number of particles fragments, which exceeds 10^{25} for D > 30 µm [*Nesvorný et al.*, 2006; *Nesvorný et al.*, 2010], making an N-body integration impractical. In order to simplify the problem, *Nesvorný et al.* [2010] assumed that the collisional lifetime of particles is $\tau_{col}(D)$ and stopped the N-body integration of diameter D particles for $t = \tau_{col}(D)$. They assumed that particles keep the same D for $t < \tau_{col}(D)$ and vanish at $t = \tau_{col}(D)$. Effectively, this is a crude approximation of the real collisional cascade, in which particles can be eroded by small collisions and do not vanish upon disruptive impacts (but produce a range of new particle sizes). *Nesvorný et al.* [2010] chose $\tau_{col}(D)$ based on estimates of satellite impact rates and meteor observations. For example, *Grün et al.* [1985] argued that the collisional lifetime of D = 1 mm particles at 2.5 AU should be ~10^4 yrs. The Poynting-Robertson drag lifetime of these large particles is then significantly longer than $\tau_{col}(D = 1\,mm)$, indicating that they must disrupt before they evolve by Poynting-Robertson drag. In the case of smaller particles with D < 10 µm, $\tau_{PR} \ll \tau_{col}$ due to the lack of small D < 1 µm impactor particles that are blown out of the solar system by radiation pressure [*Dermott et al.*, 2001]. Consequently, since $\tau_{PR} \ll \tau_{col}$ for small particles and $\tau_{PR} \gg \tau_{col}$ for large particles, there must be an intermediate size for which $\tau_{PR} \sim \tau_{col}$. *Grün et al.* [1985] argued that this size must be near 100 µm, and so this size is expected to be very abundant in the Zodiacal Cloud. In fact, this is consistent with the LDEF measurements which estimate a dominant population with D ~ 200 µm at δ_S = 1 AU [*Love and Brownlee*, 1993].

5. Particles were assumed to be isothermal and rapidly rotating spheres. They emit thermal radiation from a surface of area $4\pi R^2$, and absorption was assumed to occur with an effective cross section πR^2. *Nesvorný et al.* [2010] set the emissivity at a wavelength of 25 µm to be 1 and fitted the emissivities at 12 µm and 60 µm. They found that the relative emissivities at 12 µm and 60 µm that match the data best are 0.70-0.75 and 0.95-1, respectively. For those estimates, they assumed silicate particles with some carbon content.

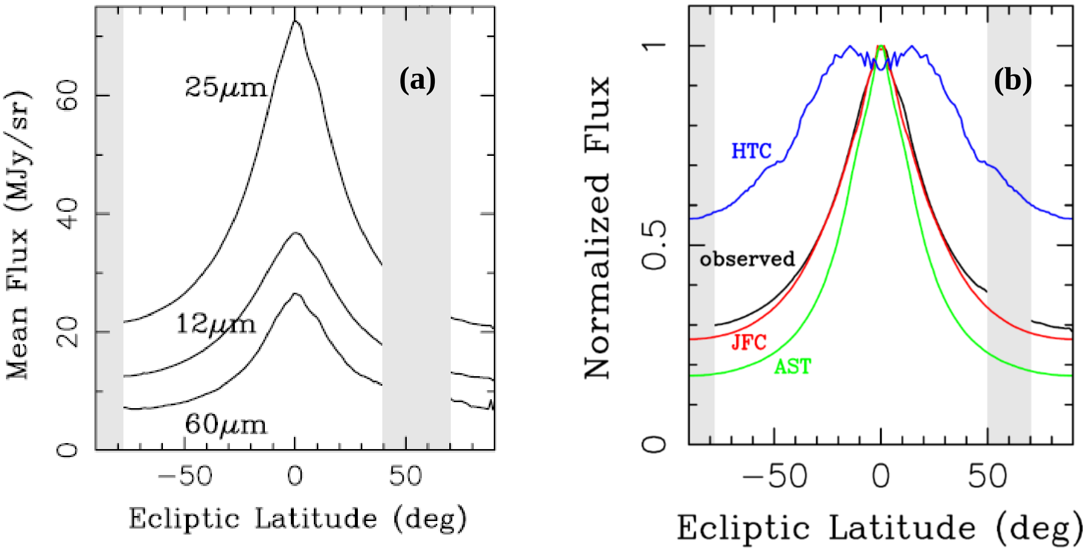

Figure 2.8. *Panel a: Mean IRAS profiles at 12, 25, and 60 μm wavelengths; the selected IRAS scans were centered at the ecliptic. Panel b: Comparison of the 25 μm profiles produced by different sources with IRAS observations; the coloured lines show profiles expected from different source populations: asteroids (green), JFCs (red), and HTCs (blue). Reproduced from Nesvorný et al. [2010].*

The thermal radiation of the particles is detected by a telescope observing at mid-infrared wavelengths. To compare the results with the IRAS observations shown in Figure 2.8a, *Nesvorný et al.* [2010] modelled the orbitally envolving particles and produced infrared fluxes that a space-borne telescope would detect depending on its location, pointing direction and wavelengths. Figure 2.8a shows the mean fluxes at 12, 25, and 60 μm wavelengths as a function of ecliptic latitude. As indicated above, the model is constrained by the IRAS observations of thermal emission.

6. A small fraction of the particle population is accreted by the Earth, producing meteors. To estimate the terrestrial accretion rate of meteoroids, *Nesvorný et al.* [2010] took the *Bottke et al.* [2005] model based on Greenberg's formalism [*Greenberg*, 1982]. In essence, these models use Öpik's theory [*Öpik*, 1951] to assess the accretion rate. The model used by *Nesvorný et al.* [2011] evaluates the radiants of the impacting particles, accounting for all impact configurations as well as weighting the results by the probability with which each individual configuration occurs, including focusing. The radiants are calculated before applying the effect of gravitational focusing.

As discussed in more detail in the next section, *Nesvorný et al.* [2010; 2011] found that JFCs are the are the main source of the meteors arriving at the Earth from the Helion/anti-Helion directions. To match the radiant and orbit distributions, as measured by the CMOR (Canadian Meteor Orbit Radar) and AMOR radars, their model implies all cometary particles must frequently disintegrate when reaching orbits with low perihelion distances.

2.2.3.2. Contribution of cosmic dust sources to the Zodiacal Cloud.

Estimates of the source contributions to the ZC from several studies are summarized in Table 2.3. These estimates were based on the IRAS satellite and COBE observations, on cratering rates, shape of microcraters, etc., and depend strongly on the assumed particle size of migration of IDPs produced by different small bodies. *Ipatov et al.* [2008] considered a wide range of particle masses, whereas other authors used results of calculations for one or two sizes of particles. *Liou et al.* [1995] considered 9 µm diameter dust particles, and studies by *Gorkavyi et al.* [2000] and *Ozernoy* [2001] were based on 1 and 5 µm particle modelling. A significant fraction of cometary dust in near-Earth space has been proposed by *Southworth* [1964], *Liou et al.* [1995], *Zook* [2001] and *Nesvorný et al.* [2010; 2011]. Based on cratering from an ensemble of Earth- and Lunar-orbiting satellites, *Zook* [2001] reported a cometary contribution of ~75%. *Grogan et al.* [2001], *Dermott et al.* [2001] and *Wyatt* [2005] suggested that at least 30% of the IDPs comes from the break-up of the asteroids, whereas *Dermott et al.* [2002] concluded that Earth accretes mainly asteroid dust.

Figure 2.8b shows the 25 µm wavelength emission flux of particles with D = 100 µm by different source populations and, as discussed by *Nesvorný et al.* [2010], these profiles do not depend significantly on the size of the particle. The ASTs profile presents a very sharp peak centered at ecliptic. If this profile is compared with the observed one, it can be concluded that a broader distribution of orbital inclinations is apparently needed to match the IRAS measurements.

The profile produced by the HTC particles is broader than the observed one (Figure 2.8b). Dust released by HTCs is expected to be concentrated along certain locations on the sky making it difficult to explain the smooth profile of the zodiacal dust. In Figure 2.8b does not represent the OCC particles, since they have a nearly isotropic inclination distribution. In conclusion, AST, HTC, and OCC particles cannot match the observed profile of the Zodiacal Cloud.

Table 2.3. *Fractions of cometary, asteroidal, and trans-neptunian particles among the Zodiacal Cloud, constrained by different observations. Adapted from Ipatov et al. [2008].*

References	**Observations used**	**Fraction of cometary dust**	**Fraction of asteroid dust**	**Fraction of trans-Neptunian dust**
Zook [2001]	Cratering rates from Earth- and Lunar-orbiting satellites	0.75		
Liou et al. [1995]	IRAS observations of the shape of the Zodiacal Cloud	0.67-0.75		
Gorkavyi et al. [2000]; *Ozernoy* [2001]	COBE/DIRBE observations of the brightness vs latitude	0.36	0.3	0.34
Grogan et al. [2001]; *Dermott et al.* [2001]; *Wyatt* [2005]	Dust bands		>0.3	
Dermott et al. [2002]	Dust bands		Most	
Brownlee et al. [1993]; *Vedder and Mandeville* [1974]; *Fechtig et al.* [2001]	Shape of microcraters		>0.7	
Nesvorný et al. [2006]	IRAS observations of dust bands	Dominated for high speed cometary particles	0.05-0.09 for Karin/Veritas particles	
Ipatov et al. [2008]	WHAM observations and observations of number of density	0.4-0.7	0.3-0.5	≤0.1
Nesvorný et al. [2010]	IRAS observations of dust bands	0.85-095 for JFC particles		
Rowan-Robinson and May [2013]	IRAS and COBE observations of mid-IR emissions of the zodiacal dust	0.6-0.80	0.2-0.4	
Yang and Ishiguro [2015]	Optical properties, albedo, and spectral gradient of zodiacal light	0.94	0.60	

Finally, the width and the shape of the modelled JFC emission flux profile in Figure 2.8b closely matches the observations. A slight difference is apparent for large ecliptic latitudes where, shown here for D = 100 µm and $\tau_{JFC} = 12{,}000$ yr, the model flux is slightly weaker than the one measured by IRAS. This difference could be explained if: 1. Slightly smaller JFC particles were used, and/or 2. The Zodiacal Cloud has a faint isotropic component. Consequently, this close resemblance of the modelled JFC profile with IRAS data is a strong indication that JFCs are the dominant source of particles in the Zodiacal Cloud.

2.3. MODELING ABLATION AND COSMIC SPHERULE PRODUCTION

Figure 2.9a shows a histogram of the particle mass distributions for each of the three models considered here. The mass distribution is expressed in terms of mass flux per decade versus the mass range from 10^{-9} to 0.1 g, which covers the bulk of the incoming daily material [*Ceplecha et al.*, 1998]. For the LDEF and HPLA radar distributions (hereafter d-MIF and r-MIF), the median input mass of the incoming dust particles is ~10 µg, with a total input rate of 110 ± 55 t d^{-1} [*Love and Brownlee*, 1993] and 14 ± 3 t d^{-1} [*Fentzke and Janches*, 2008; *Janches et al.*, 2014], respectively. For the Zodiacal Cloud model (hereafter z-MIF), the mass distribution is shifted to smaller mass ranges with a median input mass of ~1 µg. The total input rate in the z-MIF model is 34 ± 17 t d^{-1}, although there may be 30-50% of additional mass input from ASTs and Long-Period Comets (LPCs). This aspect will be discussed in Chapter 4.

Figure 2.9b depicts the entry velocity distributions of the three models. The velocity ranges from 11.5 km s^{-1} for particles in a prograde orbit to 72.5 km s^{-1} for those in a retrograde orbit. The z-MIF velocity distribution is sharply peaked to low velocities (average = 14 km s^{-1}), since the majority of particles are predicted to be in near-prograde orbits originating from the Helion and anti-Helion sporadic sources [Nesvorný et al., 2011].

In contrast, the r-MIF velocity distribution depends strongly on the mass range. For masses $\geq$ 0.1 µg, the velocity distribution follows a bimodal trend where the dominant peak is located at 30 km s^{-1} and there is a secondary maximum at 55 km s^{-1}. Meanwhile, there is a single peak at 55 km s^{-1} for masses < 0.1 µg, because the r-MIF takes into account only the portion of the incoming flux that is detectable by the radar [*Fentzke and Janches*, 2008]. In the case of the d-MIF, the LDEF velocity distribution (Figure 2.9b) is taken from *McBride et al.* [1999] and has an average of 18 km s^{-1}.

We assume the particles have an ordinary chondrite composition (essentially $MgFeSiO_4$ with small amounts of other metal oxides) with a melting point of 1800 K, as discussed in chapter 1. This is supported by the analysis of Comet 81P/Wild 2 dust samples [*Gainsforth et al.*, 2015] and the observation that S-type asteroids, the probable parent bodies of ordinary chondrites, are the dominant group between 1 and 2.4 AU [*McSween*, 1999]. The particles are also assumed to be fully mixed with a particle density of 2 g cm^{-3} [*Vondrak et al.*, 2008].

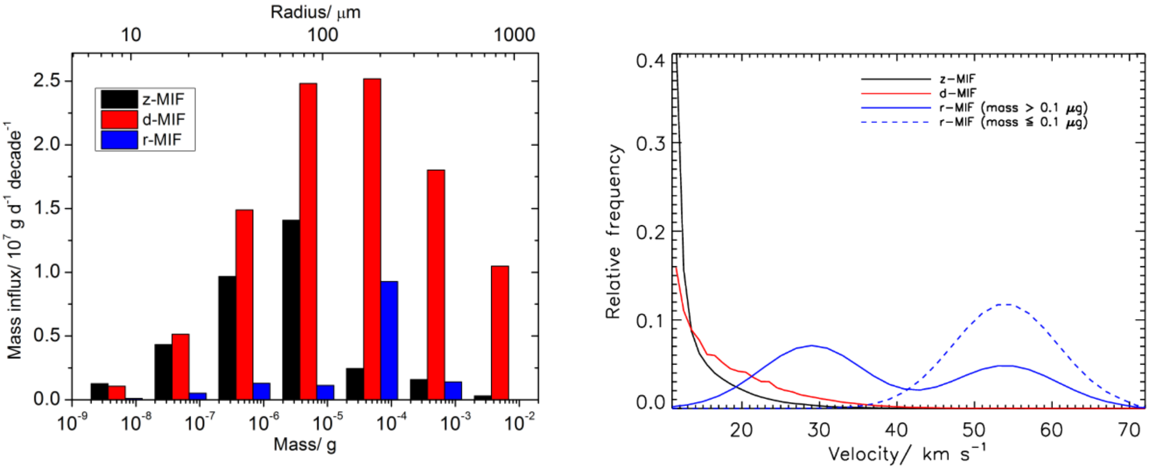

Figure 2.9. *Panel a: Histogram of the particle mass distribution. Panel b: entry velocity distributions for the z-MIF (black), d-MIF (red), and r-MIF (blue). Reproduced from Carrillo-Sánchez et al. [2015].*

CABMOD predicts the ablation rate profiles of Na, K, Fe, Mg, Si, Ca, Al, and Ti. If the meteoroid has not ablated completely, then the model determines whether the particle melted at any point along the trajectory and thus became a cosmic spherule, or survived entry unchanged to become an unmelted micrometeorite (UMM). Complete melting of the particle, and hence formation of a spherule if only partial evaporation of the particle subsequently occurs, is assumed to occur if the meteoroid temperature reaches 1800 K [*Vondrak et al.*, 2008]. Solidified spherules are denser than cosmic dust particles; here we use a mean density of 3.2 g cm^{-3} [*Kohout et al.*, 2014] to estimate the spherule size for comparison with measurements.

For simplicity, CABMOD was run with a constant atmospheric density profile (March, 40°N), assuming a CI chondrite composition (see *Vondrak et al.* [2008] for more information). Each meteoroid in the r-MIF and z-MIF models has a specified mass, velocity, and entry angle. These models contain 2.7×10^7 and 6.7×10^6 individual IDPs, respectively. In view of these very large numbers, the following procedure was adopted to integrate efficiently across the mass/velocity/entry angle distributions. Each mass decade in the distribution was divided into five bins. A Monte Carlo procedure was used to sample the particle velocity and entry angle distributions of particles within each bin, and the resulting elemental ablation profiles and residual particle masses were co-added. The results for each bin were then summed to yield the integrated ablation profiles.

Figure 2.10 shows how the CABMOD model has been combined with a Monte Carlo technique to sample the particle velocity and entry angle for a specified mass. For each particle, CABMOD predicts the changes in velocity, altitude, temperature and mass until either the minimum temperature/mass or the lower limit altitude is reached. After integrating, we evaluate either if the meteoroid has evaporated completely or if there is a final residual mass. In this sense, cosmic spherules will be those micrometeorites which have experienced alteration by frictional heating when they pass through the atmosphere, whereas UMMs can have been thermally metamorphosed but not melted. Finally, the total ablated mass for each individual particle is added to get the distribution of elemental ablation profile for all metallic species.

In order to determine the minimum number of particles that should be sampled in each bin, the ratios of the integrated ablation profiles for each metal relative to Na were compared for different sample sizes. No significant improvement was observed when increasing the sample size above 200. For instance, for the z-MIF model, the ablation ratios for a sample size of 200 were Fe:Na = 5.9 ± 0.2, Mg:Na = 4.0 ± 0.2, and Ca:Na = $(6.1 \pm 0.5) \times 10^{-2}$, compared with Fe:Na = 5.9 ± 0.1, Mg:Na = 4.0 ± 0.1, and Ca:Na = $(6.2 \pm 0.3) \times 10^{-2}$ for a sample size of 500. The total numbers of particles sampled were then 9500, 8600, and 11,200 for the z-MIF, r-MIF, and d-MIF, respectively. In the case of the d-MIF model where the entry angle is not specified, a constant value of 35° was used since the integrated ablation rates are relatively insensitive to this parameter [*Vondrak et al.*, 2008].

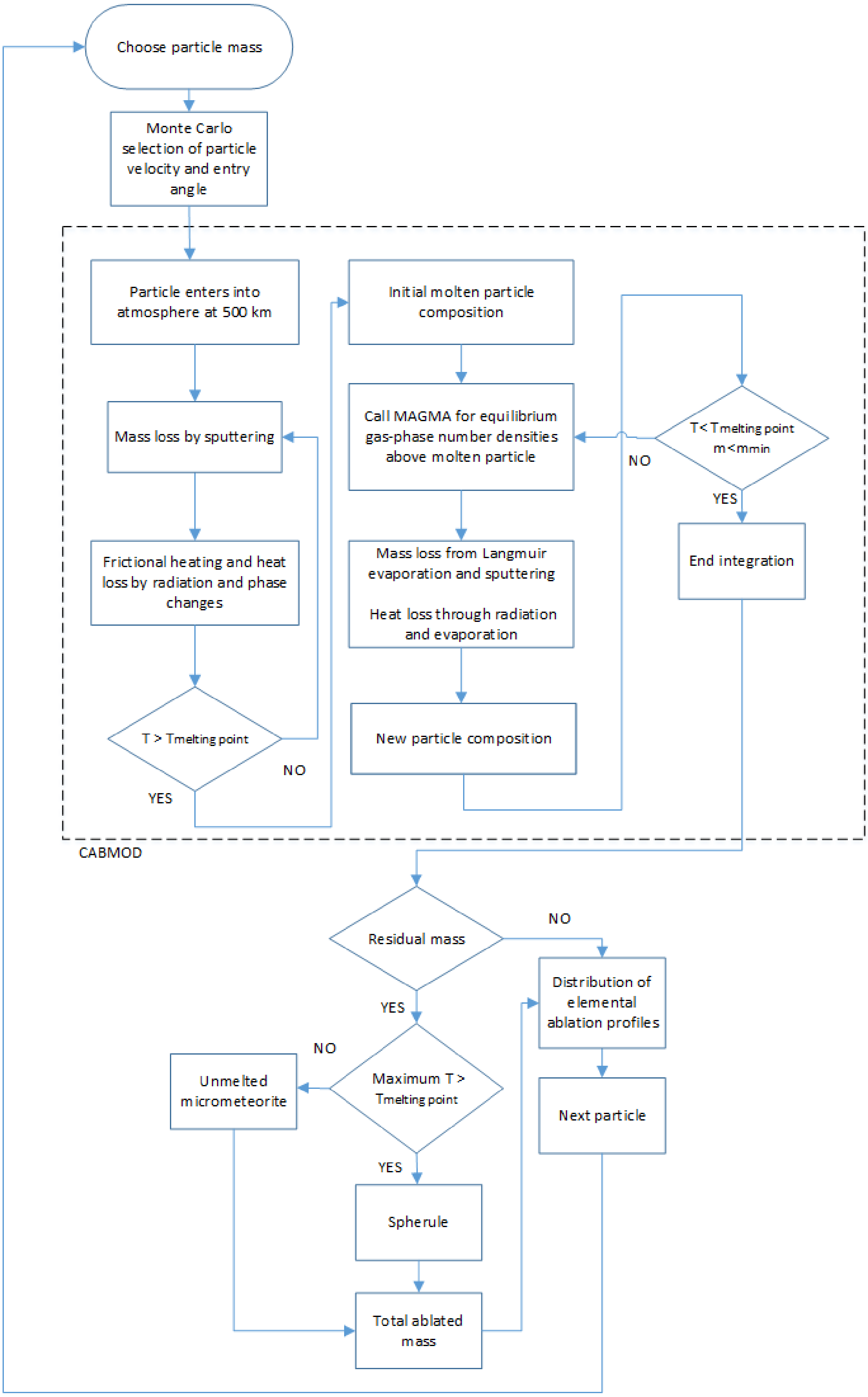

Figure 2.10*. Flow chart illustrating how the CABMOD model determines the ablated mass loss and the residual melted and unmelted mass of an individual cosmic dust particle entering into the Earth atmosphere.*

2.4. RESULTS AND DISCUSSION

2.4.1. Differential Ablation.

The elemental ablation rate profiles for the three models are plotted in the panels of Figure 2.11. These profiles are integrated over the meteoroid velocity, zenith angle (in the case of the z-MIF and r-MIF), and mass distributions to yield the total ablation rates of the individual elements. In all cases, the most volatile elements (Na and K) ablate 10-15 km higher than the main constituent elements (Fe, Mg, and Si), which in turn ablate a few kilometers higher than the most refractory elements (Ca, Al, and Ti). As expected, the ablation profiles for the r-MIF model are 10-20 km higher than the corresponding profiles for the z-MIF and d-MIF models because of the much faster velocity distribution (Figure 2.9b). As a result, sputtering is also more important in the r-MIF model. Note that although the velocity distribution for the d-MIF model is shifted to somewhat higher velocities than the z-MIF (Figure 2.9b), the larger particles in the d-MIF distribution (Figure 2.9a) take longer to reach melting point with the result that ablation persists to lower altitudes than in the z-MIF.

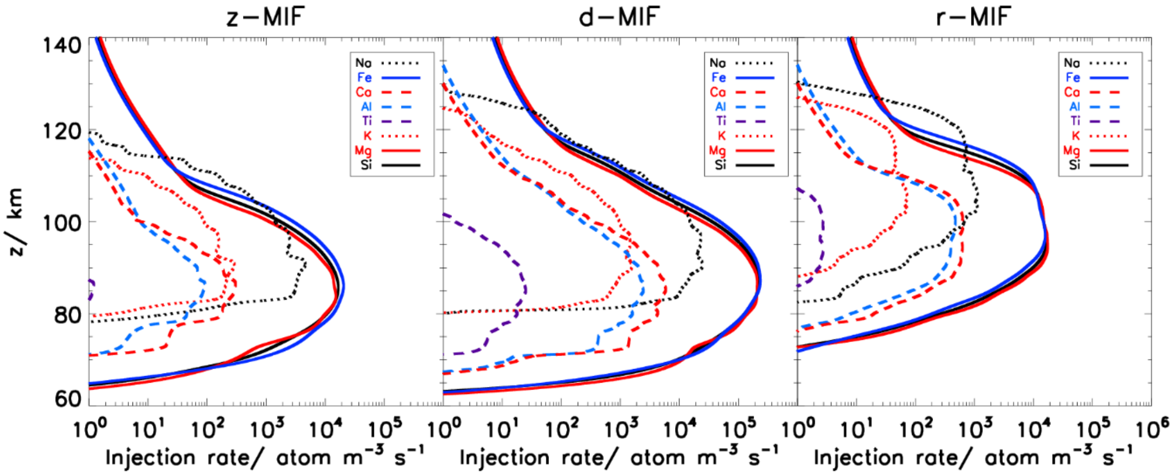

Figure 2.11. *Ablation rate profiles for individual elements, integrated over the available mass ranges of the z-MIF, d-MIF, and the r-MIF models. The meteoroid mass covers the mass range 10^{-9}-10^{-3} g (z-MIF and r-MIF) and 10^{-14}-10^{-3} g (d-MIF). Reproduced from Carrillo-Sánchez et al. [2015].*

Table 2.4 lists the global mass balance for each model: that is, how the incoming mass is partitioned between UMMs, cosmic spherules, and the ablated mass. The ablated mass is then broken down by element (the percentage of each element which ablates from the incoming total is also listed). The z-MIF and the r-MIF models are at opposite extremes: 91% of the total mass ablates in the r-MIF model compared with only 12% of the mass in the z-MIF. This significant difference largely arises because of the fast velocity distribution of the r-MIF. The differences between the models are even more dramatic when considering the comparative ablation rates of individual elements. Starting with Na, which is a relatively volatile metal and therefore ablates efficiently, 40% of the total incoming Na ablates in the case of the z-MIF model compared with 95% for the r-MIF. In fact, the Na ablation rates are almost the same for both models (0.1 t d^{-1}), because the smaller total mass input of the r-MIF is compensated by the higher ablation fraction of Na. For more refractory metals, the dust velocity distribution becomes more critical. Taking Ca as an extreme case, only 2% of the incoming Ca ablates for the z-MIF, compared with 52% for the r-MIF. The differential ablation ratio (DAR)[4] is defined as a departure from the chondritic ratio of two elements. The chondritic Na:Ca ratio is 0.96 [*Asplund et al.*, 2009]. For the r-MIF, the Na:Ca ratio increases slightly to 1.5. In contrast, the z-MIF exhibits pronounced differential ablation with a Na:Ca ratio of 16.1.

Table 2.4. *Global mass balance of the z-MIF, d-MIF, and r-MIF models. Note that the mass flux of ablated atoms is broken down by element in the italicized sub-table, where the number in parenthesis shows the percentage fraction of each element that ablates from its total atmospheric input. Reproduced from Carrillo-Sánchez et al. [2015].*

Mass flux	**z-MIF (t d^{-1})**	**d-MIF (t d^{-1})**	**r-MIF (t d^{-1})**
Unmelted micrometeorites	22.0	23.2	0.3
Cosmic spherules	8.1	35.4	1.2
Ablated atoms	3.9	51.4	12.5
Na	*0.1 (40%)*	*0.7 (83%)*	*0.1 (95%)*
K	*0.01 (36%)*	*0.07 (76%)*	*0.01 (86%)*
Fe	*1.5 (16%)*	*17.2 (56%)*	*3.7 (94%)*
Si	*0.6 (11%)*	*7.9 (45%)*	*2.0 (90%)*
Mg	*0.4 (8%)*	*6.6 (41%)*	*1.8 (88%)*
Ca	*0.01 (2%)*	*0.3 (20%)*	*0.1 (52%)*
Al	*$2.4\cdot10^{-3}$ (0.5%)*	*0.08 (6%)*	*0.05 (28%)*
Ti	*$5.4\cdot10^{-5}$ (2%)*	*$1.4\cdot10^{-3}$ (18%)*	*$6.5\cdot10^{-4}$ (65%)*
O	*1.3 (10%)*	*18.5 (45%)*	*4.6 (87%)*
Total	34	110	14

The velocity distribution of the d-MIF is only slightly faster than the z-MIF (Figure 2.9b). Thus, similar ablation behavior might be expected. However, the d-MIF mass

---

[4] The differential ablation ratio (DAR) of a metal *x* relative to Na is defined as:

$$DAR_x = \frac{atomic\ mixing\ ratio\ of\ metal\ x\ released}{atomic\ mixing\ ratio\ of\ Na\ released}$$

distribution is shifted to much heavier particles (Figure 2.9a), which exhibit less differential ablation because they reach higher temperatures during atmospheric entry, so that a higher fraction of the refractory elements ablate (Figure 12 in *Vondrak et al.* [2008]). Thus, the Na:Ca ratio for the d-MIF model is only 4.6.

The differential ablation ratios of Fe, Ca, Mg, and K relative to Na are shown in Figure 2.12 for the three models. The abscissa is the ablation ratio required to match the modeled mesospheric metal layers, within the framework of the WACCM model, against observations by lidar and satellite [*Feng et al.*, 2013; *Langowski et al.*, 2014; *Marsh et al.*, 2013; *Plane et al.*, 2014; *Vondrak et al.*, 2008]. The ordinate axis represents the ablation ratios from Table 2.4. The black points show the relative CI chondritic ratios used in the CABMOD model [*Vondrak et al.*, 2008] and so illustrate the ratios corresponding to an absence of differential ablation.

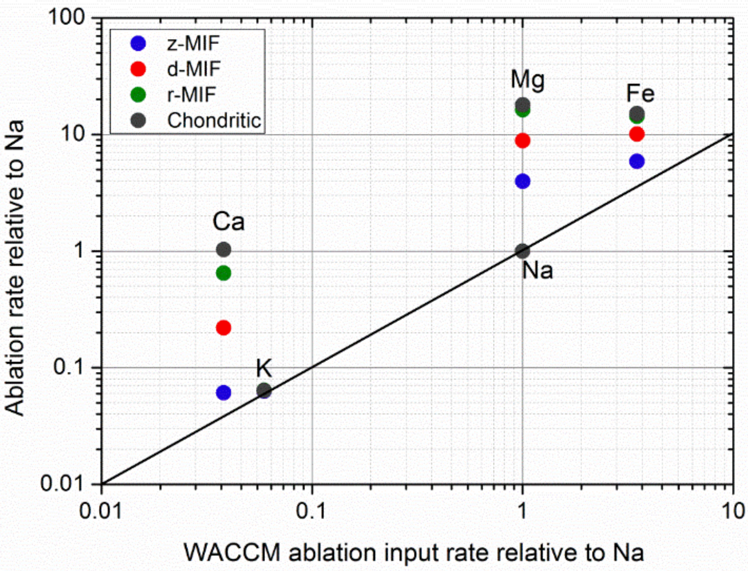

Figure 2.12. *Ablation rates for Fe, Ca, Mg, and K relative to Na, produced by the z-MIF, d-MIF, and r-MIF models, plotted against the relative input rates required to model the global metal atom layers in the MLT. The solid line is the 1:1 correlation line. Reproduced from Carrillo-Sánchez et al. [2015].*

Because Na ablates very efficiently, differential ablation of other elements leads to points vertically below the black points on the Figure 2.12. The further the points lie above the line of 1:1 correspondence, then the smaller the degree of differential ablation that the cosmic dust model is producing. Inspection of Figure 2.12 shows that Na and K ablate essentially in their chondritic ratio; hence, the points for all three models lie on top of each other. In contrast, as the elements become more refractory, a larger degree of differential ablation is exhibited. The r-MIF produces very little differential ablation for Fe, Mg, or Ca, whereas the z-MIF produces a Ca:Na ratio that is close to that required by WACCM. However, even the z-MIF does not produce sufficient differential ablation of Mg and Fe, one possible explanation for this is that Na is enriched in cometary particles, compared to the CI ratio. Indeed, Na enrichments in cometary particles have been reported recently [*Gainsforth et al.*, 2015; *Schulz et al.*, 2015].

2.4.2. Accretion of Cosmic Spherules.

Cosmic spherules have been found in a multitude of terrestrial environments: in the swamps of Siberia [*Krinov*, 1959], in desert sands [*Fredriksson and Gowdy*, 1963], in beach sand [*Marvin and Einaudi*, 1967], in deep sea sediments [*Brownlee et al.*, 1977], in lithified abyssal sediments exposed on land [*Czajkowski et al.*, 1983; *Jehanno et al.*, 1987; *Taylor et al.*, 1991], in Greenland's melt-water drainage basins [*Maurette et al.*, 1987; *Maurette et al.*, 1986], in Antarctic sediments [*Hagen*, 1988; *Koeberl and Hagen*, 1989], and in ices cores [*Yiou and Raisbeck,* 1990].

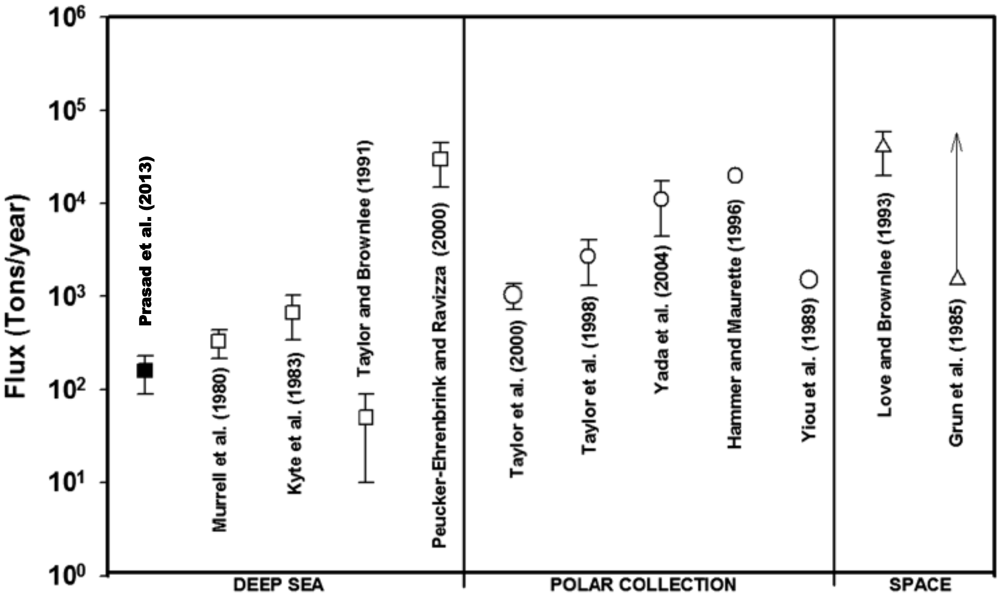

***Figure 2.13**. Fluxes of micrometeorites estimated from different collections in deep sea sediments and polar collections. Reproduced from Prasad et al. [2013].*

Figure 2.13 illustrates fluxes of MMs and IDPs estimated from different sources [*Prasad et al.*, 2013]. It is evident that the fluxes from the deep sea regions are much lower than those from the polar regions. The main reason of this significant difference is that measurements of deep sea sediments is made by measurements of Os and Ir concentrations, whereas ice core estimates are based on particulate counts.

The South Pole Water Well (SPWW) is a 24-m-diameter by 15-m-deep melt pool 100 m below the surface. It supplies potable water to the Amundsen-Scott South Pole Station. Owing to the large volume of ice melted, the well is the largest source of MMs yet discovered. In principle, the compressed-snow polar ice preserves a record of melted and unmelted MMs in an environment low in terrestrial debris. Because contamination of the well by fuel is a major concern, a low-temperature EPDM (ethylene propylene dienemonomer mat) surrounds the wellhead and extends out 7m. In the present thesis the flux of spherules for the d-MIF, r-MIF, and z-MIF distributions have been calculated and then compared with the spherule global flux estimated by *Taylor et al.* [1998], 4.4 ± 0.8 t d^{-1}, which was estimated a using a collection of thousands of well-preserved cosmic spherules in the size range of 50-700 µm.

The flux of spherules in this size range for the z-MIF model is 6.8 ± 3.4 t d^{-1}, which is in good agreement with the South Pole measurement. In contrast, the spherule flux is only 0.5 ± 0.1 t d^{-1} for the r-MIF, and the d-MIF model produces a much higher flux of 29.7 ± 14.9 t d^{-1}. The spherule flux estimated from the z-MIF model also falls within the range of 1.4-19.2 t d^{-1} from the deep-sea sediment record [*Peng and Lui*, 1989]. Lastly, *Maurette et al.* [1987] reported a spherule flux of 6.0 t d^{-1} within the size range 50-300 µm, from micrometeorites collected in the Greenland ice cap. The z-MIF model again provides the best agreement with a flux in this size range of 6.2 ± 3.1 t d^{-1}, compared with 0.4 ± 0.1 t d^{-1} and 25.9 ± 13.0 t d^{-1} for the r-MIF and d-MIF models, respectively.

2.4.3. Input Fluxes of Na and Fe.

We now compare the absolute ablation fluxes of Na and Fe to observations and models. Na and Fe resonance wind-temperature lidars have recently been used to measure the vertical fluxes of these metals in the MLT. Gardner and coworkers have reported two estimates for the global Na input flux of 0.28 ± 0.05 t d^{-1} [*Gardner et al.*, 2014] and 0.30 ± 0.05 t d^{-1} [*Huang et al.*, 2015], which are a factor of 2.8-3.0 times higher than the z-MIF model. In the case of Fe, the lidar-based estimate of 4.29 ± 0.75 t d^{-1} [*Huang et al.*, 2015] is a similar factor of 2.9 times larger than the z-MIF. Given that the stated uncertainty in the z-MIF is a factor of 2 [*Nesvorný et al.*, 2011], this discrepancy may not be as significant as it appears.

HPLA radars mostly observe a different group of relatively fast particles, as evidenced by the completely different velocity distributions in Figure 2.9b [*Janches et al.*, 2014]. Thus, to a first approximation, the r-MIF can be added to the z-MIF, yielding (from Table 2.4) Na and Fe fluxes of 0.2 and 5.2 t d^{-1}, which are reasonably close to the lidar-based estimates. Interestingly, this Fe flux is in sensible accord with the accretion rate of meteoric smoke particles in polar ice, which indicates a global Fe ablation flux of around 8 ± 4 t d^{-1} [*Dhomse et al.*, 2013]. However, it should be noted that although the cosmic spherule flux would be little altered by adding the two MIFs together (since the r-MIF produces relatively few spherules—Table 2.4), the degree of differential ablation for Ca, Mg, and Fe would be worse than for the z-MIF alone.

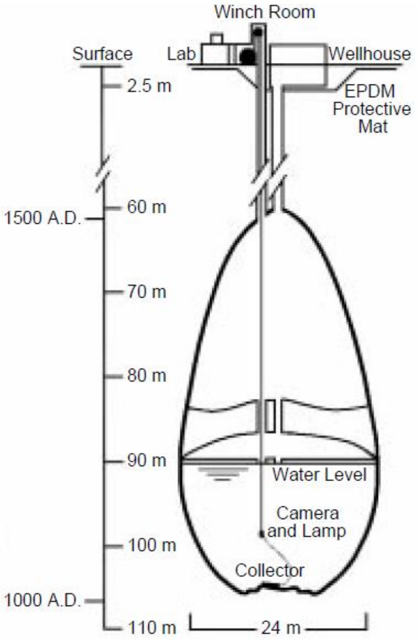

***Figure 2.14**. Approximate size and shape of the South Pole Water Well (SPWW) in December 1995. Reproduced from Taylor et al. [1998].*

2.4.4. Model uncertainties.

One parameter in CABMOD to which there is significant sensitivity is the melting point of the particle [*Vondrak et al.*, 2008]. This is set to 1800 K, as mentioned above, which is typical for olivine $Mg_{2x}Fe_{2(1-x)}SiO_4$ of composition $x = 0.5$ (that is, a Mg/Fe ratio ~1, as found in both S-type asteroidal and cometary particles). We have rerun the model with the melting point varied from 1700 K (x = 0.25) to 1900 K (x = 0.75). For the z-MIF, which is most sensitive to this parameter, the cosmic spherule production rate decreases from 9.4 t d^{-1} to 6.9 t d^{-1}, which is only ±16% from the standard model. The effect on the ablation ratios is also small (Figure 2.12 and Table 2.5). For example, the Fe:Na ratio increases from 6.13 to 7.30 and the Ca:Na ratio from 0.06 to 0.07.

The metal atom injection rates in WACCM are optimized to yield the best fits to metal layer observations [*Feng et al.*, 2013; *Langowski et al.*, 2014; *Marsh et al.*, 2013]. The uncertainty in the absolute metal atom concentration measured by lidar is typically ±30%, similar to satellite measurements of Mg [*Langowski et al.*, 2014]. The uncertainty in the measured metal atom:Na ratio is thus ±42%. In WACCM, the transport (residual circulation and diffusion) and concentration fields of the neutrals (O, H, O_3, etc.) and charged species (NO^+, O_2^+, and electrons) affect all metal species in the same way and should not contribute to the uncertainty in the metal atom ratios. Of course, there is uncertainty in the metal chemistry, both in individual rate coefficients (~30 reactions per metal [*Plane et al.*, 2015]) and the possibility of unknown reactions. However, a fairly strict test of the completeness of the chemistry of a particular metal is that the modeled metal atom layer satisfactorily reproduces the peak height, width, top and bottom scale heights, and diurnal/seasonal variations [*Plane et al.*, 2015]. Thus, the additional uncertainty in the chemistry is likely to be comparatively small, and so the uncertainties in the metal:Na ablation ratios required by WACCM (abscissa in Figure 2.12) are probably no more than ±60%.

Table 2.5. *Global mass balance for z-MIF with the melting point varied from 1700 K and 1900 K. As can be seen, there is only a modest change in the cosmic spherule production rate.*

Mass Flux	1700 K	1800 K	1900 K
Unmelted MMs [t d^{-1}]	20.0	22.0	22.4
Spherules [t d^{-1}]	9.4	8.1	6.9
Ablated Mass [t d^{-1}]	4.6	3.9	4.7

2.5. SUMMARY OF THE CHAPTER

This study shows that a significant fraction of the cosmic dust entering the Earth's atmosphere needs to consist of small (< 5 µg) and slow (< 15 km s^{-1}) particles in order to explain the measured accretion rate of cosmic spherules at the surface, as well as the significant differential ablation of the more refractory meteoric metals with respect to Na in the MLT. Of the three MIFs selected for this study, the Zodiacal Dust Cloud model (z-MIF) seems to do best when judged against these criteria.

However, there are at least two unresolved issues. First, *Janches et al.* [2014] have shown that the z-MIF predicts a flux of relatively fast particles (> 15 km s^{-1}) which are not observed by HPLA radars; this suggests that further refinements to the JFC component of the z-MIF are required, even before other components (asteroidal, long-period comets) are added. Second, the metal ablation rates required to model the Fe and Na layers in WACCM [*Feng et al.*, 2013; *Marsh et al.*, 2013] are factors of 3-5 times smaller than the z-MIF (Table 2.4) and 10-14 times smaller than lidar-based estimates [*Huang et al.*, 2015]. One implication is that additional vertical transport in the upper mesosphere is required to accommodate increased metal ablation rates and produce metal layers which still match observations. This would have wider implications in the increased downward transport of heat and chemical constituents such as atomic O and NO.

CHAPTER 3: A NOVEL INSTRUMENT TO MEASURE DIFFERENTIAL ABLATION OF METEORITE SAMPLES AND PROXIES: THE METEORIC ABLATION SIMULATOR (MASI)

3.1. INTRODUCTION

The Meteor Ablation Simulator (MASI) has been developed at the University of Leeds to improve and benchmark CABMOD predictions with experimental Na, Fe and Ca ablation rate profiles. MASI is the first laboratory experimental set-up that allows simulations of atmospheric ablation to be conducted under realistic time-resolved conditions. The comparison of homogeneous, single mineral CABMOD simulations to the MASI experimental data using meteoritic IDP analogues highlights the complexity of the process of melting and evaporation of IDP mineral assemblages, but also the usefulness of CABMOD for calculating elemental yields of volatile (e.g. Na) and moderately refractory (e.g. Fe) elements.

An important assumption in CABMOD is the mineralogy of IDPs. The composition and origin of IDPs has been debated for decades e.g. *Mackinnon and Rietmeijer* [1987]. The current view is that IDPs are mainly of cometary origin and related to carbonaceous chondrites [*Noguchi et al.*, 2015; *Taylor et al.,* 2012], in contrast to the terrestrial meteorite record, composed mostly of ordinary chondrites. About 75% of IDPs are estimated to be CI and CM-like fine-grained aggregates containing a variety of anhydrous and hydrated silicate minerals [*Taylor et al.*, 2012]. Hydrated silicates undergo chemical and mineralogical reactions above 900 K [*Greshake et al.,* 1998] and the melting points of anhydrous minerals span a range of temperature between ~1400 and 2200 K. The uncertainties about the most frequent IDP composition and the technical challenge of modelling melting and evaporation of multiphase aggregate particles have imposed the current working assumption in CABMOD of single mineral (olivine) IDPs, justified by the high recurrence of this mineral phase in IDPs and by the evolution of hydrated silicates into anhydrous silicates at temperatures well below melting during atmospheric entry [*Greshake et al.,* 1998; *Sandford and Bradley,* 1989]. It is important to note that in a single phase monolithic olivine particle, trace volatile constituents can only evaporate after the melting point of Mg-rich olivine has been reached ($T > 1800$ K), since diffusion in the solid phase is slow [*Capek and Borovicka,* 2009]. Moreover, the evaporation of refractory elements such as Ca can only occur once Mg and Si have been lost [*Alexander et al.*, 2002], which implies that their evaporation is extremely dependent on mineralogy.

In order to reduce uncertainties in ablation modelling it is clearly necessary to set CABMOD on solid experimental ground. The first objective of this study was to refine and validate CABMOD using a laboratory experimental set-up which, for the first time, enables time-resolved simulations of the melting of IDP analogues and the subsequent evaporation of their major elemental constituents under conditions of atmospheric entry. Specifically, the assumptions of monolithic IDPs with a single mineral composition and of Langmuir evaporation need to be tested. The second, related, objective is to test the CABMOD prediction of differential ablation of Fe and Ca with respect to Na.

There have not been many attempts to simulate micrometeoroid ablation in laboratory experiments. Most previous studies have focused on understanding the thermal processing of micrometeorites retrieved on the ground both from a textural and compositional perspective, in order to infer their origin [*Greshake et al.*, 1998; *Sandford and Bradley*, 1989; *Toppani et al.*, 2001]. More recent experiments using pyrolysis and gas-phase infrared spectroscopy have also attempted to quantify the yield of sulphur, CO_2 and H_2O in order to estimate the potential impact of micrometeoroids on planetary atmospheres [*Court and Sephton*, 2009; 2011].

The MASI instrument has been developed to study meteoric ablation in the laboratory. The instrument is designed to test the various assumptions in a model like CABMOD: in particular, the melting and evaporation rates of the elemental constituents. IDP analogs (for example, ground-up meteorite particles) of radius 9 to 150 μm are heated to high temperatures (2900 K) in just a few seconds, thus mimicking their heating profiles during atmospheric entry. During this time the time-resolved ablation of the metallic constituents is detected by laser-induced fluorescence (LIF). From these measurements, it is possible to test both the thermodynamic model within CABMOD as well as the use of the Hertz-Knudsen relation to describe evaporation.

3.2. EXPERIMENTAL SETUP

3.2.1. System description.

The MASI system consists of a filament mounted in a central chamber, pumped down to ~15 Pa. The chamber has 8 horizontal flanges as well as larger flanges at the top and the bottom of the chamber (Figure 3.1). These 10 ports allow: 1. Access to the filament; 2. The electrical feedthrough for the filament; 3. Two detection lasers; 4. Perpendicular to them, two photomultipliers; 5. A viewport for the pyrometer; and 6. An exhaust outlet

(Figures 3.1 and 3.2). The filament is a tungsten ribbon (Sigma Aldrich) 25 mm in length, 1 mm wide and 0.025 mm thick. It is typically mounted such that there is a flat surface in the middle on which the particles are placed (Figure 3.1b). It is mounted on a terminal block of an electrical feedthrough which is connected to a DC power supply (Delta Elektronica ES 015-10). The currents used range from 0 to 5 A (0 to 1.7 V); at the maximum current, filament temperatures in excess of 2873 K are produced. A typical filament might last for 100 or so heating profiles. Filament lifetime can be extended by not overloading the filament with sample and using the lowest temperatures and less rapid heating ramps possible to limit the heating rate of the sample.

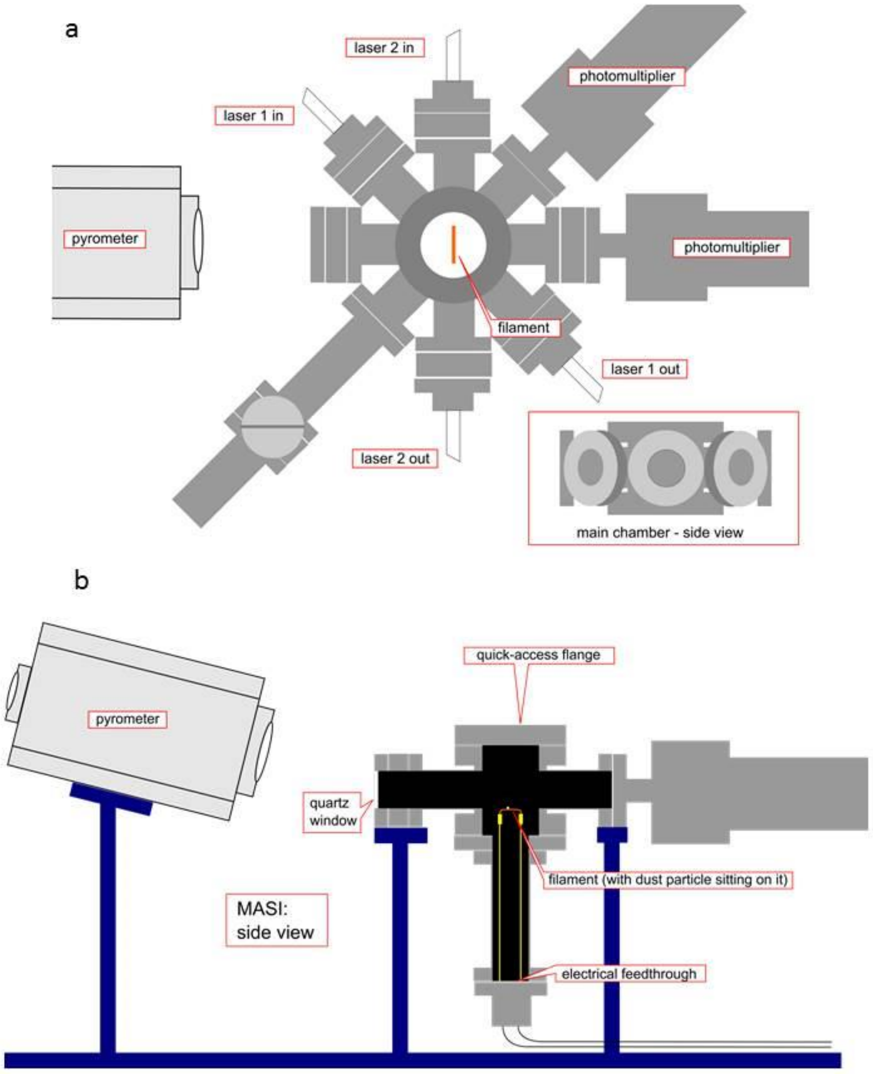

Figure 3.1. *Top (a) and side (b) views of MASI. Reproduced from Bones et al. [2016].*

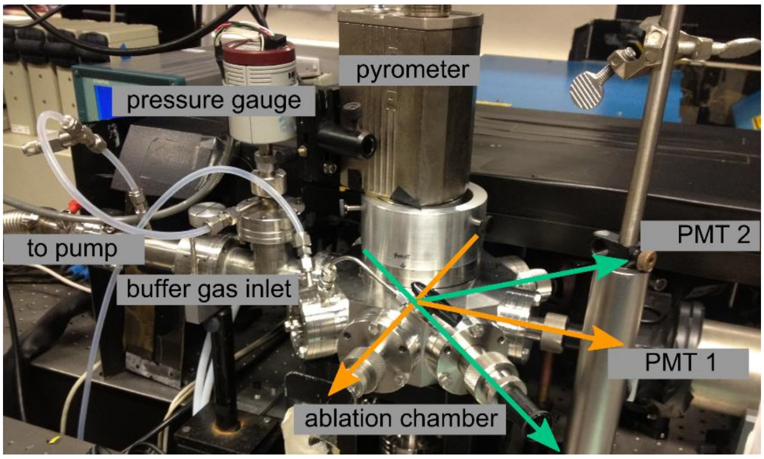

Figure 3.2. *Photograph of the MASI set up. The directions of the laser beams and the orthogonal fluorescence detection directions are highlighted in yellow (sodium LIF detection) and green (other metal LIF detection). All laser beams are on the horizontal plane. In this set up, the pyrometer is mounted vertically above the MASI chamber. Reproduced from Bones et al. [2016].*

The filament temperature is measured with a rapid response pyrometer (System 4, R1 ratio thermometer, Land Instruments). This ratio pyrometer is capable of measuring the temperature of objects less than 1 mm wide with a stated time resolution of 1 ms. Its operating temperatures are 1273-2873 K. This temperature range proves sufficient to recreate temperature profiles for ablation of small particles (radius 9-150 μm) entering the Earth's atmosphere at moderate velocities (14-31 km s^{-1}). Accurate temperature readings rely on the pyrometer being focused on the filament, close to the point where the particles are. The pyrometer calibration was checked by heating an iron filament to melting point (1811 K), whereupon the filament melted.

Metal atoms ablated from the IDP analog particles are detected with the LIF instrument. At the time of writing, the system has been configured to measure the ablation of sodium, iron and subsequently calcium. In principle any combination of metals would be possible. In general, it is intended to retain sodium as the reference element and vary the second metal. Sodium is also used as a reference metal in atmospheric measurements because it is easily detectable by lidar [*Plane et al.*, 2015].

In order to record systematically the particle melting and any movement on the filament, a video camera was installed (a modified Microsoft LifeCam Cinema web cam). This camera has a CMOS detector with a maximum resolution of 1280 × 800 pixels at 25 Hz. The camera either utilizes the pyrometer optics, positioned behind the eyepiece of the pyrometer, or images the filament directly from above (port 1).

3.2.2. Particle preparation.

A very important aspect of these experiments is the selection of representative IDP analogues. Unmelted IDPs (R > 50 μm) collected in different studies consist of fine-grained aggregates and are similar to the matrix of carbonaceous chondrites, with a minor population of ordinary chondritic aggregates and anhydrous minerals [*Dobrica et al.*, 2009; *Taylor et al.*, 2012]. Carbonaceous porous IDPs with R < 50 μm have also been retrieved both from the stratosphere [*Zolensky and Lindstrom*, 1992] and the polar icecaps [*Noguchi et al.*, 2015]. In order to account for some of the properties of these populations, samples of the Allende [*Krinov*, 1970] (CV3), Murchison [*Fuschs et al.*, 1973] (CM2) and Chergach [*Wieisberg et al.*, 2008] (H5) meteorites, and of terrestrial Mg-rich olivine and Na-rich and Ca-rich plagioclases have been used.

The IDP analogues are prepared by grinding pieces of each meteorite/mineral and separating them in six size classes or bins with radii <19, 19-53, 53-75, 75-125, 125-177, >177 μm (Figure 3.3, panel a), encompassing the IDP size range (R < 200 μm) that makes the largest contribution to the atmospheric input [*Love and Brownlee*, 1993; *Nesvorný et al.*, 2011]. The samples have been carefully characterized to determine their size distributions, mineralogy and elemental compositions. Figure 3.3, panels b-d, show examples of IDP analogues employed in this study, and illustrate the differences between IDPs and meteoritic fragments used as IDP analogues. Ordinary chondrite (OC) fragments consist of compact aggregates (Figure 3.3b), while the carbonaceous chondrites are very heterogeneous, showing porous fine-grained aggregates (Figure 3.3c) not too different from the IDP assemblages [*Jessberger et al.*, 2001] as well as coarse grains (Figure 3.3d).

Figure 3.4 shows compositional maps of an OC H5 particle, which illustrates the heterogeneous distribution of elements in these meteoritic aggregates, analogous to what is usually found in IDPs [*Zolensky and Lindstrom*, 1992] and cometary material [*Brownlee et al.*, 2006]. The particle in Figure 3.4 has a Mg-rich silicate backbone with major Na-plagioclase and metallic Fe or iron sulphide (FeS) inclusions, and minor K and Ca-rich domains. Note that Mg is missing in those domains where other elements are enriched. This heterogeneous distribution of elemental constituents is also found in the carbonaceous analogues (Figure 3.5).

The particles are suspended in ethanol and delivered to the tungsten filament using a glass pipette. A few particles (normally 5 or less) are deposited in the filament for the four largest size bins. For the two smallest size bins tens of particles are deposited. This implies that the ablation curves recorded in each experiment are generally averages of the ablation profiles of a few particles within the size distributions shown in Figure 3.13.

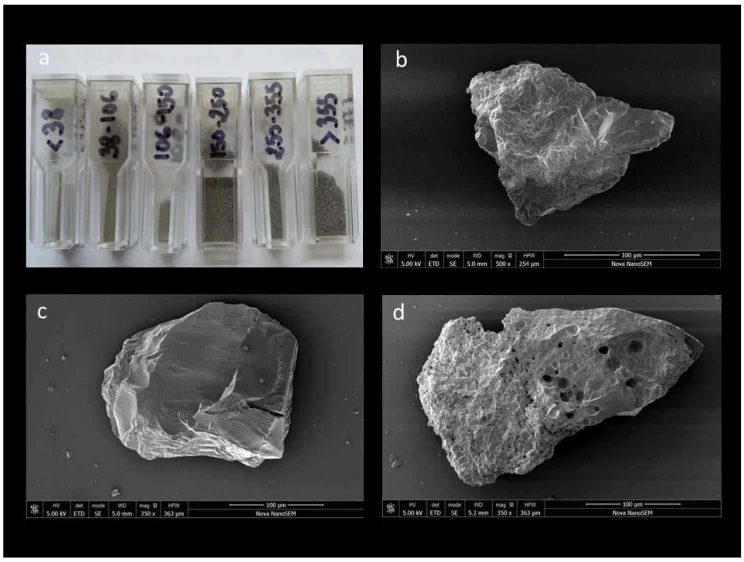

Figure 3.3. *IDP analogues. Panel a: cuvettes containing ground meteorite particles segregated according to mesh size. Panel b: Scanning Electron Microscopy (SEM) micrograph of an example Chergach IDP analogue. Panels c and d: Allende IDP analogues. Reproduced from Gómez-Martín et al. [2016].*

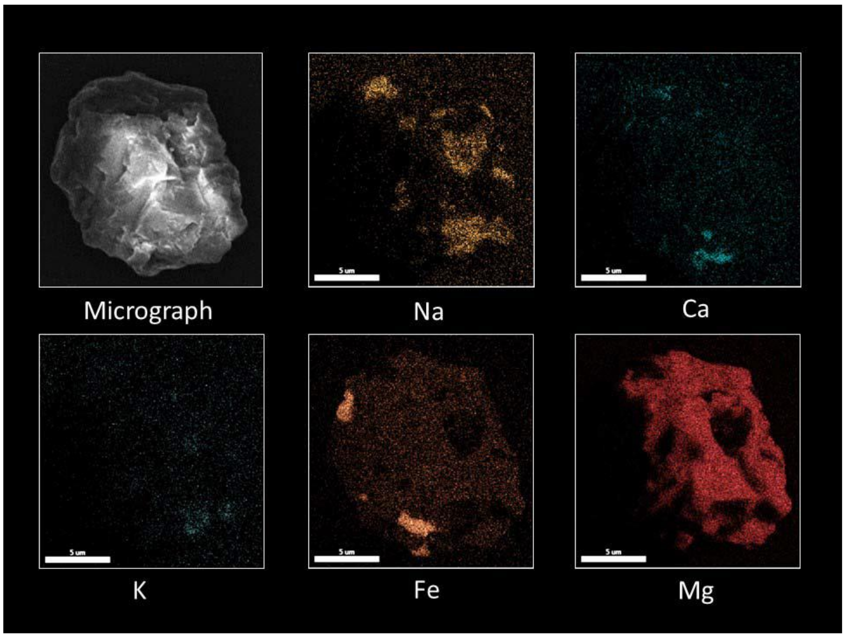

Figure 3.4. *Energy-dispersive X-Ray (EDX) analysis of an IDP analogue (Chergach, OC, H5), showing the spatial distribution of Na, Ca, K, Fe and Mg in the particle. Reproduced from Gómez-Martín et al. [2016].*

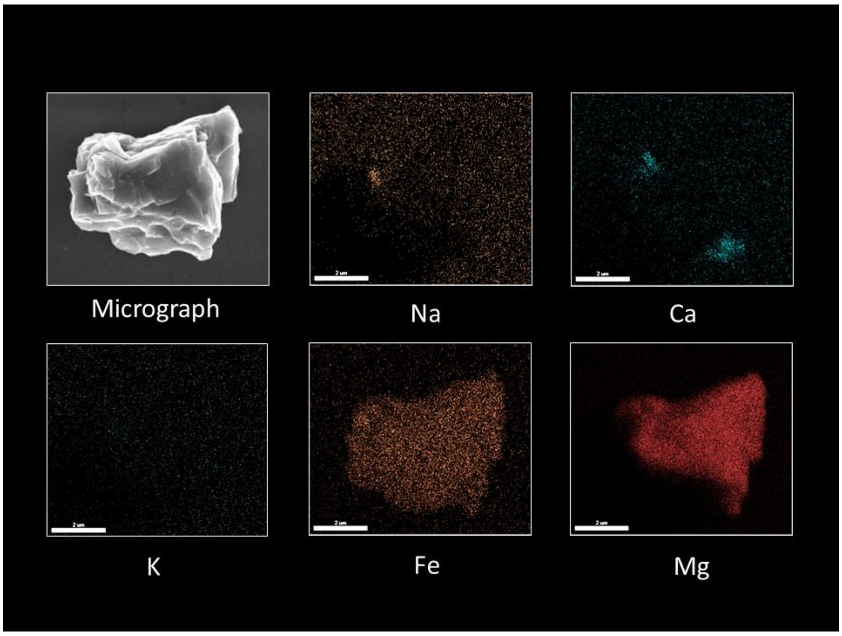

Figure 3.5. *Energy-dispersive X-Ray (EDX) analysis of an Allende IDP analogue, showing the spatial distribution of Na, Ca, K, Fe and Mg in the particle. Reproduced from Gómez-Martín et al. [2016].*

A problem encountered in these experiments is electro-migration [*Kumar et al.*, 2014], which causes the particle to move on the surface of the filament, and it is particularly critical for studying the ablation of refractory elements. In order to maintain the particles within the homogeneous temperature region of the filament (away from the electrodes), the surface needs to be roughened by carrying out several preparatory ablation experiments. Also, the video-camera is used to demonstrate that the particles ablate within the region at the temperature measured by the pyrometer, approximately at the center of the filament.

3.3. ABLATION PROFILES FOR SODIUM, IRON AND CALCIUM

3.3.1. Temperature profiles.

In order to study the influence of particle morphology and composition on melting and evaporation, simple analytical temperature profiles such as linear ramps may be applied. These can then be used to convert the time axis into a temperature axis, allowing direct visualization of the temperatures of ablation onset, the peak ablation temperatures, and the Full Width at Half Maximum (FWHM) of ablation pulses required for the benchmarking of CABMOD. To achieve full ablation of more refractory species such as Fe and Ca, linear profiles may be run several times, or high temperature step functions may be considered.

The atmospheric entry temperature profiles were calculated from the meteor physics module of CABMOD. The profiles of temperature as a function of time are then interpolated by a standalone LabVIEW program into the corresponding pyrometer current with a time resolution of 4 ms to match the resolution of the MASI. The maximum profile length is 12 seconds or 3000 data points. Profiles of 8 seconds are commonly used for the meteoric profiles.

The results of typical series of experiments with Chergach and Allende samples are shown in Figure 3.6 (Na and Fe) and Figure 3.7 (Na and Ca). Inspection of these figures reveals that Na, Fe and Ca ablate differentially, that is, evaporate at different times during the heating program. In this first group of experiments, a linear temperature ramp between 1400 and 2700 K is used in order to facilitate identification of major trends and simplify comparison to CABMOD simulations ($T = c_1 + c_2 t$, with $c_1 = 1375$ K and $c_2 = 138$ K s^{-1}). In the Ca experiments, the ramp typically ends in a plateau at 2400 K to limit the electro-migration of particles. Examples of ablation curves of Na, Fe and Ca for all the meteorites and minerals considered in this study are shown in Figure 3.8 ($53\ \mu m < R < 75\ \mu m$). For each element, there is a clear correspondence of the signal onset in experiments with the meteoritic analogues and the onset in experiments with minerals which are rich in a particular element.

3.3.2. Sodium and Iron.

CABMOD assumes that particles have an olivine-based composition, and therefore the melting point of olivine is used as a reference in these experiments, assuming an olivine with the Mg/(Mg+Fe) ratio measured for each meteoritic analogue. Figure 3.6 shows that both Na and Fe start evaporating below the melting point of Fo_{80} olivine (1930 K) and even below Fo_{50} olivine (1800 K), and that the Na pulse appears at lower temperatures than Fe. The figure also indicates that the onset of evaporation of both Na and Fe increase with particle size (Figure 3.9 shows average onsets for all the experiments carried out in this study).

The respective Na and Fe onsets for the albite (Ab_{95}) and forsterite (Fo_{90}) are close to the melting point corresponding to their respective stoichiometry. The Na onset in Chergach is the same as for albite, and the Fe onset is consistent with metallic Fe (both known constituents of H5 meteorites). In Allende (CV3) and Murchison (CM2) the onsets of Na and Fe are consistent with sodic feldspathoids and metallic Fe, respectively. The slightly higher Fe onset in Allende is probably due to the lower amount of metallic Fe in carbonaceous chondrites. The temperature onset of the small but detectable Na content in the Fo_{90} sample shows size dependence and tends towards the melting point of forsterite.

Another way of visualising the varying evaporation onsets is calculating the fraction of evaporated Na and Fe below a certain reference temperature, e.g. the melting point of Fo_{50} and Fo_{80} olivine. The ratio Fe(T < 1930 K)/Fe(total) for Chergach reaches 15% for the smallest sizes. Chergach contains magnesium rich olivine (Fo_{83}), but as an H5 meteorite it also contains substantial amounts of metallic Fe, which explains why Fe evaporates below 1930 K. The ratio Fe(T < 1800 K)/Fe(total) is smaller than ~5% for all particle sizes. Na(T < 1930 K)/Na(total) is very significant for the three smallest size bins, which is an indication of low melting point Na-bearing minerals such as Albite, Sodalite or Nepheline.

There is a strong size-dependence of the fraction ablated below the forsterite melting temperature. Some experiments were carried out with samples of Chergach prepared from reground large particles ($R > 177$ μm), which were subsequently segregated into the same size bins. For these, the fraction Na(T < 1930 K)/Na(total) is smaller, which indicates preferential accumulation of the sodium-containing mineral in the smallest size bins during the primary size segregation.

A caveat to the interpretation of the ablation curves in Figure 3.6, Figure 3.7 and Figure 3.8 is that the size bins employed in this study have relatively broad, overlapping size distributions. This implies that when running many experiments for a single size bin, the characteristics of the pulses such as their onset, temperature at the peak ablation and FWHM will show some scatter, as can be seen in Figure 3.12 and 3.13. This is advantageous because experiments frequently involve the ablation of several particles (see above), which has an averaging effect. On the other hand, there is some ambiguity in the assignment of the pulse FWHM, especially for minor elements such as Na and Ca.

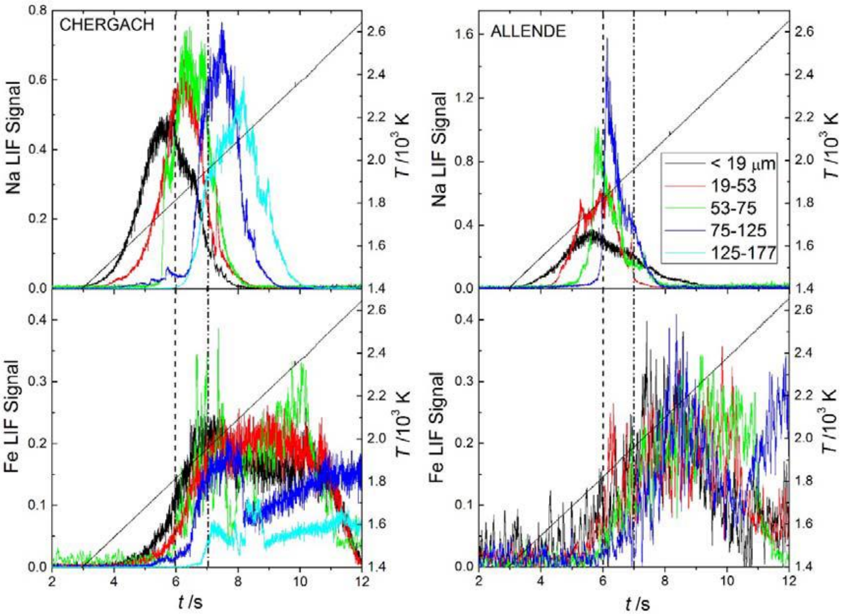

Figure 3.6. *Laser Induced Fluorescence signal of Na (top panels) and Fe (bottom) for different particle size bins (radii indicated in the legend) of the Chergach (right) and Allende (left) meteoritic IDP analogues. The temperature ramp (black line) is plotted in the right hand side axes of each panel. The dashed and dash-dotted vertical black lines mark the 1800 K (Fo_{60}) and 1950 K (Fo_{80}) temperature thresholds. Reproduced from Gómez-Martín et al. [2016].*

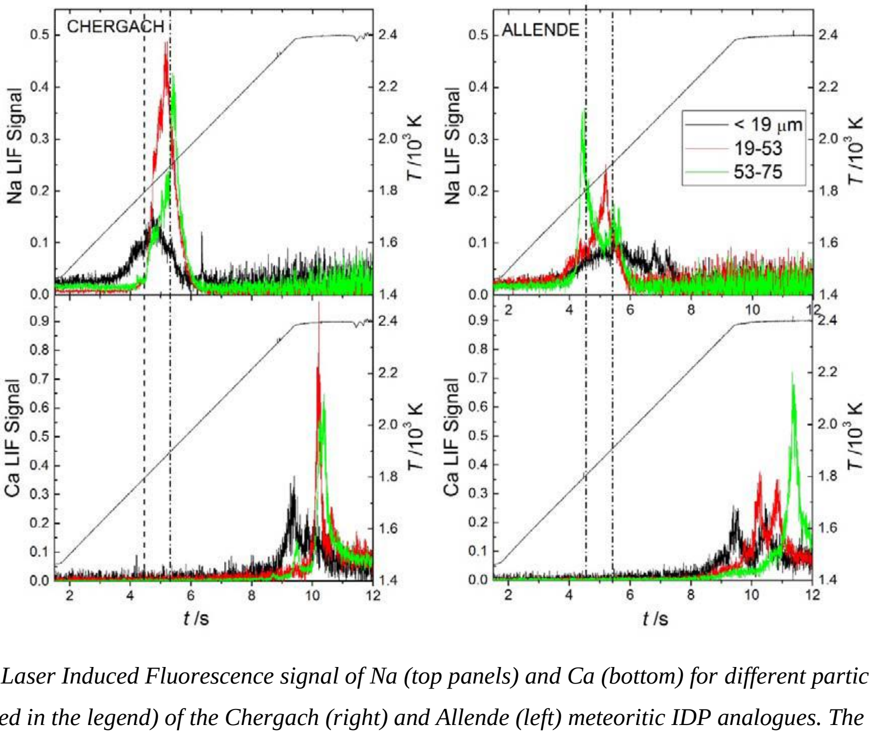

Figure 3.7*. Laser Induced Fluorescence signal of Na (top panels) and Ca (bottom) for different particle size bins (radii indicated in the legend) of the Chergach (right) and Allende (left) meteoritic IDP analogues. The temperature ramp (black line) is plotted in the right hand side axes of each panel. The dashed and dash-dotted vertical black lines mark the 1800 K (Fo_{60}) and 1950 K (Fo_{80} and An_{90}) temperature thresholds. Reproduced from Gómez-Martín et al. [2016]*

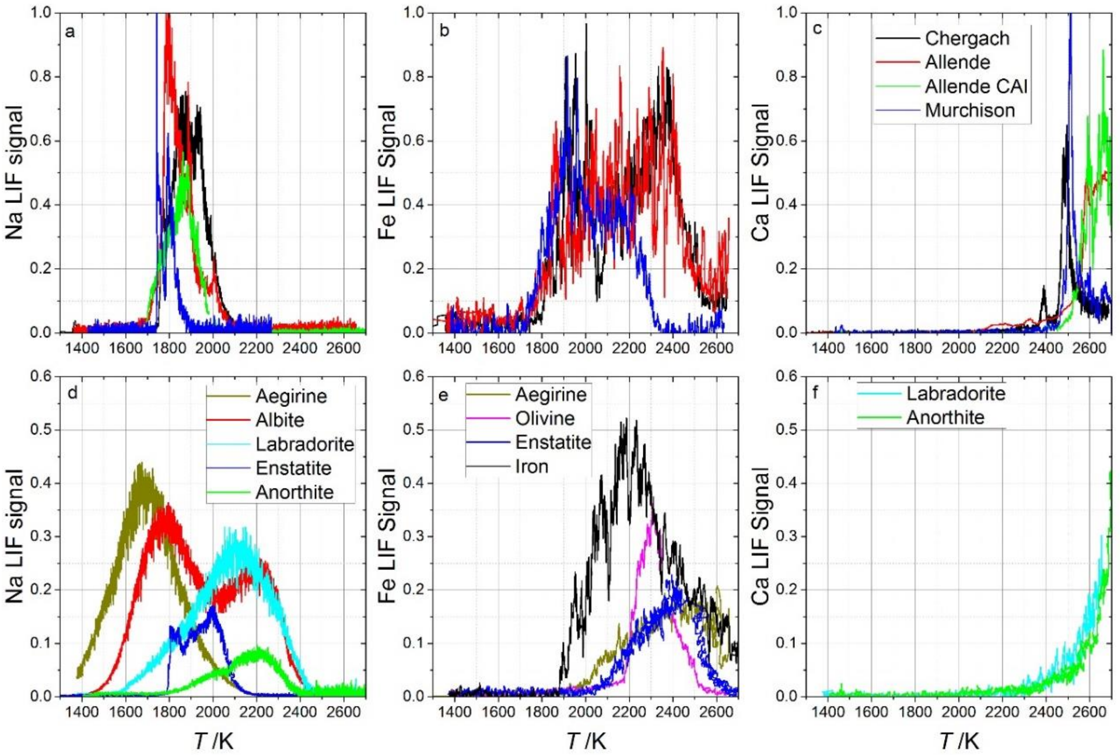

***Figure 3.8**. Selection of experiments for the size bin 53 µm < R < 75 µm with all the samples employed in this study. Top panel row (a-c): meteorites, including a run with white aggregate inclusions (CAIs) separated from Allende's black matrix. Bottom panel row (d-f): minerals: aegirine (dark yellow), albite (red), labradorite (cyan), enstatite (blue), anorthite (green), iron (black) and olivine (pink). Left column (panels a and d): Na signal; Central column (panels b and e): Fe signal; Right column (panels c and f): Ca signal. Reproduced from Gómez-Martín et al. [2016].*

The Na pulses frequently consist of a superposition of different peaks, which one may assign to different particles. However, it turns out that one single particle (as registered by the video camera) may also produce composite pulses, as shown in Figure 3.9, panel b. The reason for this is related to the Na-rich domains. Figure 3.10, panel b, shows an example for Allende where the Na pulses from several particles overlap (the video shows more particles than Na pulses in this case), while panel a shows a mixture of narrow and broad peaks which possibly result from several particles with several Na-rich grains. Figure 3.10b shows an example with an ordinary Allende sample and with a white aggregate sample (calcium-aluminum inclusions, or CAI) (separated by hand using a microscope from the rest of the Allende fragments). The normal samples show lower evaporation onsets for Na. Figure 3.11, shows ablation examples for Murchison where (a) one or (b) two particles released Na. In Figure 3.11b the video revealed two particles very close to each other, but never in contact.

The strategy followed for Na has been to fit multiple peaks when the Na pulse is obviously a superposition and use the FWHM of the largest peak. The average results for a specific temperature ramp are shown in Figure 3.12, and indicate narrower Na peaks for Murchison, although the number of measurements is much smaller due to the limited amount of sample available. It is important to note that for the smallest size bin it is impossible to deposit just a handful of particles. In fact, tens of particles are deposited at least, which upon melting end up coalescing under the influence of electro-migration.

In the case of Fe, the situation is complicated by the obvious presence of a lower and a higher temperature phase, which cause the broad pulses in panels a of Figure 3.9, Fig 3.10 and Figure 3.11. The Fe signal can be fitted as superposition of two peaks of roughly the same width. Generally, the low temperature peak is narrower, but not always (e.g. Figure 3.11), and the onset of the high temperature peak is broadly consistent with forsteritic olivine. In this case the FWHM in Figure 3.12, panel b, is taken directly from the observed signal. A low temperature Fe-bearing phase is not considered in CABMOD.

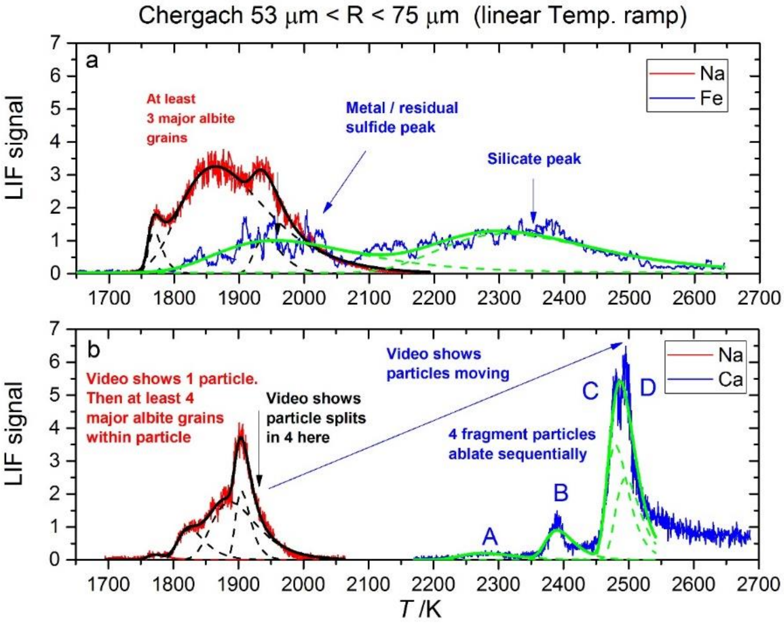

Figure 3.9. *Panel a: detection of Na (red) and Fe (blue) in an experiment with Chergach analogues of the 53 μm < R < 75 μm size bin for a 138 K s*$^{-1}$ *linear heating ramp. Multi-peak fits of Na (black) and Fe (green) are shown. The individual fitted peaks are shown by dashed lines. Panel b: the same for another experiment where Na (red) and Ca (blue) were detected. This particular example corresponds to a single particle experiment. Reproduced from Gómez-Martín et al. [2016].*

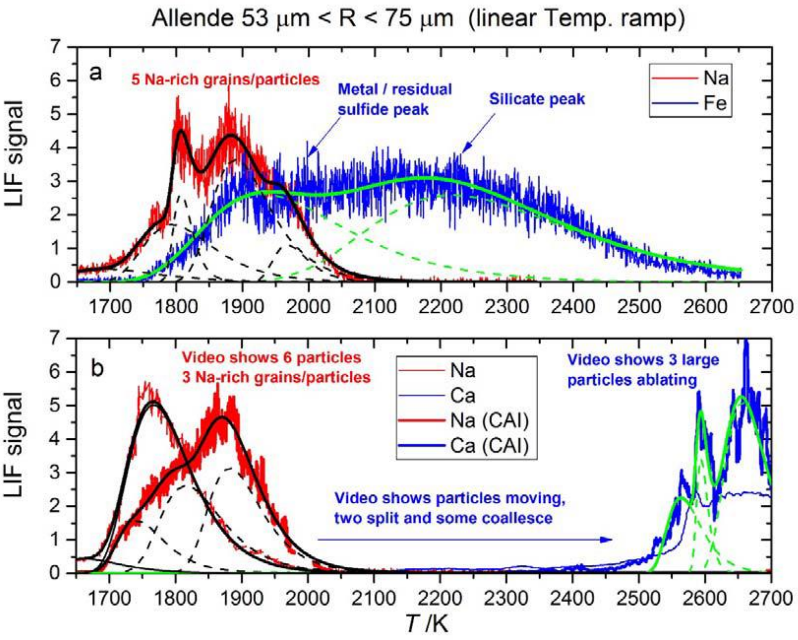

Figure 3.10. *Panel a: detection of Na (red) and Fe (blue) in an experiment with Allende analogues of the 53 μm < R < 75 μm size bin for a 138 K s^{-1} linear heating ramp. Multi-peak fits of Na (black) and Fe (green) are shown. The individual fitted peaks are shown by dashed lines. Panel b: the same for another experiment where Na (red) and Ca (blue, 10 point moving average) were detected. This example corresponds to an experiment with several particles. Reproduced from Gómez-Martín et al. [2016].*

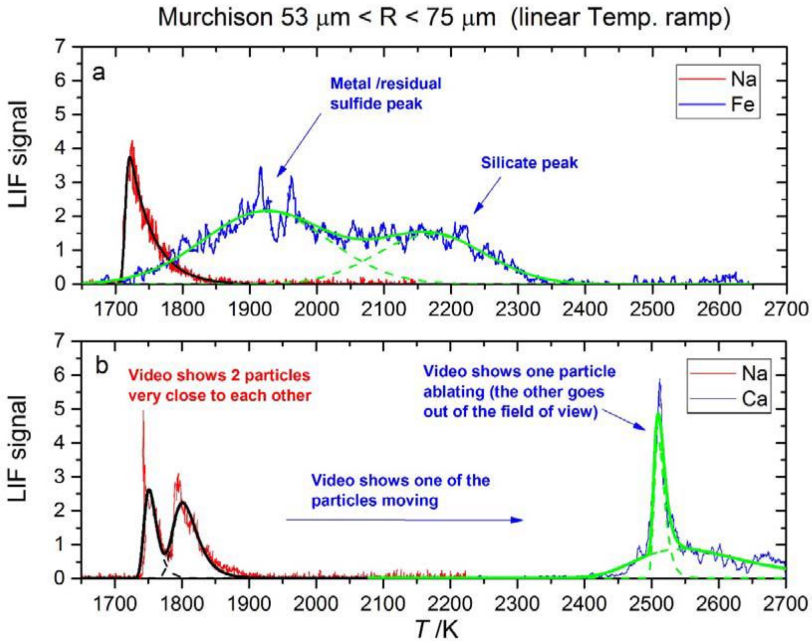

Figure 3.11. *Panel a: detection of Na (red) and Fe (blue, 10 point moving average) in an experiment with Murchison analogues of the 53 μm < R < 75 μm size bin for a 138 K s^{-1} linear heating ramp. Multi-peak fits of Na (black) and Fe (green) are shown. The individual fitted peaks are shown by dashed lines. Panel b: the same for another experiment where Na (red) and Ca (blue) were detected. Reproduced from Gómez-Martín et al. [2016].*

3.3.3. Calcium.

As a refractory element, Ca presents a big experimental challenge. There is a risk of particles moving out of the high temperature region of the filament due to electro-migration before they ablate completely. This has been addressed by roughening of the filament surface [*Kumar et al.*, 2014] and by employing a video camera to screen out invalid experiments where particles move too far away from the centre. Figure 3.7 shows examples of Na and Ca ablation profiles obtained for the Chergach and Allende analogues for 3 size bins. The dashed and dash-dotted vertical black lines mark the 1800 K (Fo_{60}) and 1950 K (Fo_{80} and An_{90}) melting temperatures. It can be seen that for meteorite analogues, Ca starts evaporating not far from the onset in experiments with labradorite and anorthite (Figure 3.8). The average Ca evaporation onset for labradorite is 2400 ± 120 K (n = 12) while the average Ca evaporation onsets for Chergach and Allende are respectively 2280 ± 120 K (n = 29) and 2210 ± 50 K (n = 9).

Multiple ablation peaks are usually observed, which is reminiscent of the Na behaviour, although the individual peaks are generally narrower (with FWHM of the order of 20 K for the 138 K s^{-1} ramp). Figure 3.14 shows 4 snapshots of the video corresponding to the experiments with the Chergach analog shown in Figure 3.9, panel b. This sequence shows how the four particles present on the surface of the filament in this experiment melted and moved a few millimetres before ablating. The movement took place within the 'safe' region where there are no temperature gradients. Single particles have been observed to split after melting, which is the case of the experiment illustrated in Figure 3.9, panel b. In a frame previous to the frame1 in Figure 3.14, a single particle is observed to split in two small and two large particles, which then migrate and ablate sequentially in the order of smallest to largest. More frequently, several of the particles originally deposited ablate individually, as is the case of the experiment in Figure 3.10, panel b, for which the video recording shows 3 particles disappearing.

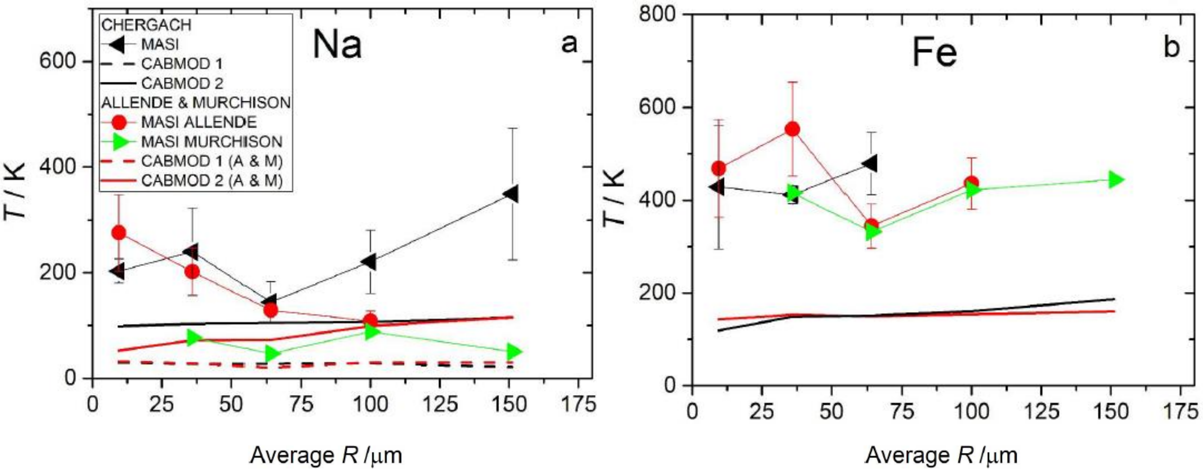

***Figure 3.12**. Widths (FWHM) of the Na and Fe ablation pulses (panels a and b respectively) for two IDP analogues (Chergach in black and Allende in red). The FWHM of the ablation pulses is specific of the heating ramp. The FWHMs in this figure corresponds to pulses resulting from the heating curves in the form $T = c_1 + c_2t$, with $c_1 = 1375$ K and $c_2 = 138$ K s^{-1}. Dashed lines: predictions of the previous version of CABMOD [Vondrak et al., 2008]. Solid lines: predictions of the current version of CABMOD, with updated Na thermodynamics and wider sigmoid temperature dependence of the sticking coefficient γ (see text for details). Reproduced from Gómez-Martín et al. [2016].*

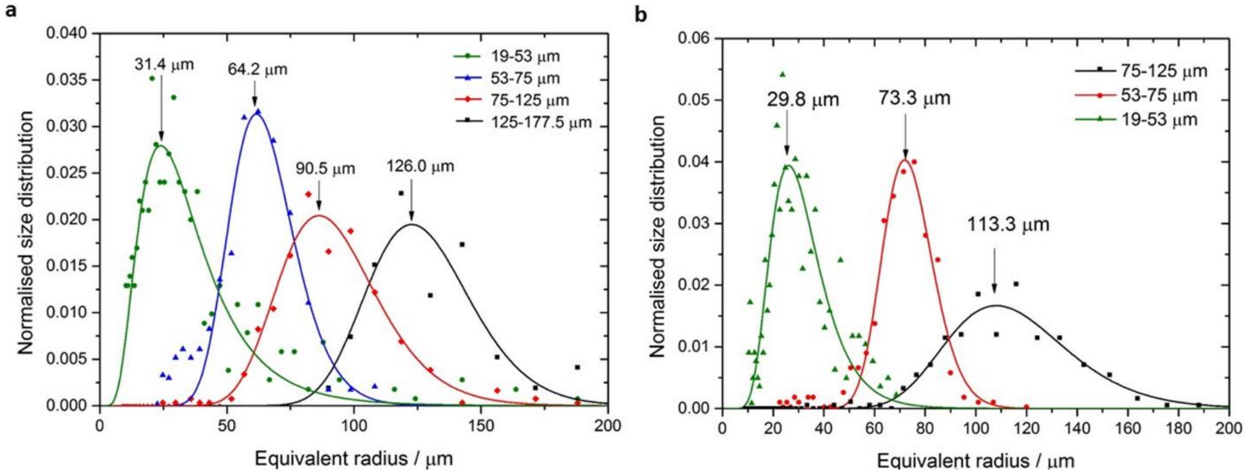

***Figure 3.13**. Size distributions of Chergach (a) and Allende (b) sample bins as measured by optical microscopy. Data have been normalized to give probability density functions for each distribution. The mean radius of each distribution is also marked. Reproduced from Gómez-Martín et al. [2016].*

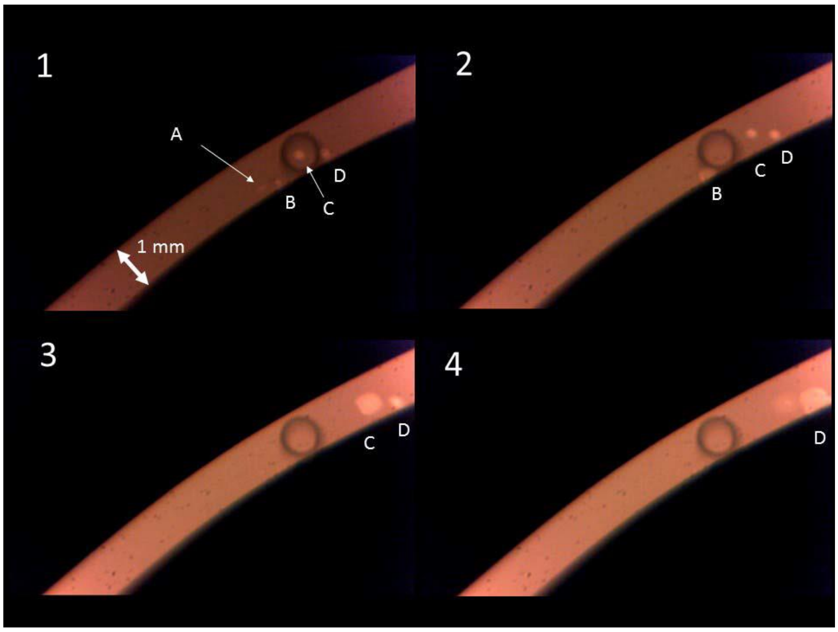

Figure 3.14. *Snapshots of a video corresponding to the experiment in Figure 3.9, panel c. Frame 1 shows four particles around the center of the filament, where the circular target of the pyrometer is positioned. At this point all the sodium has been already shed by the particles. Particle A is ablating at this point. Frame 2 shows the ablation of particle B while particles C and D have moved past the target. In Frame 3 particles C ablates and particle D is starting to ablate. In Frame 4 particles D ablates and to its left a remnant of C is still visible. Reproduced from Gómez-Martín et al. [2016].*

3.3.4. Atmospheric entry profiles and Fe and Ca yields.

Experiments performed using mass-specific entry heating profiles obtained from the CABMOD energy and momentum balance calculations [*Vondrak et al.*, 2008] are shown in Figure 3.15 (for Fe and Na). The experiments simulate the entry of ordinary and carbonaceous chondrite particles with an average radius of 64 μm, speeds of 14, 17 and 21 km s^{-1} and entry angle of 35°. Here, instead of plotting signal vs. time, the correspondence between time and altitude calculated by the model is used to provide a more intuitive representation of the atmospheric injection of Na and Fe by meteoric ablation. These plots provide a useful visualization of the process of atmospheric differential ablation: while the Na ablation rate does not follow the temperature profile in any of the cases presented (it ablates completely before reaching the peak particle temperature), the iron ablation rate follows closely the temperature profile for the 14 km s^{-1} experiments. In this case evaporation stops because the temperature decreases, not because Fe is consumed. By contrast, for an entry speed of 21 km s^{-1}, Fe ablation ends before the temperature starts decreasing, meaning that it has completely ablated from the particle.

In these experiments, the remaining Na and Fe (and Ca) in the unablated material were determined by heating the tungsten filament at a high temperature to completely vaporize the residual as shown in Figure 3.16, panels b and d. For the particular experiments in Figure 3.15 with Allende (bottom row of panels), it is observed that full ablation of Na occurred in the 3 cases, while 20%, 80% and 100% of Fe ablated with increasing speed. The average yields (i.e. the ablated fraction) of Na and Fe from 47 ablation profiles for different combinations of particle mass and velocity (all for 35° entry angle) and using the Allende meteorite analogues have been calculated from the experimental data and from the model predictions (Table 3.1). The yields of Ca from atmospheric entry simulations have been also calculated from a set of 36 experiments for Allende (Table 3.2) and 22 for Chergach.

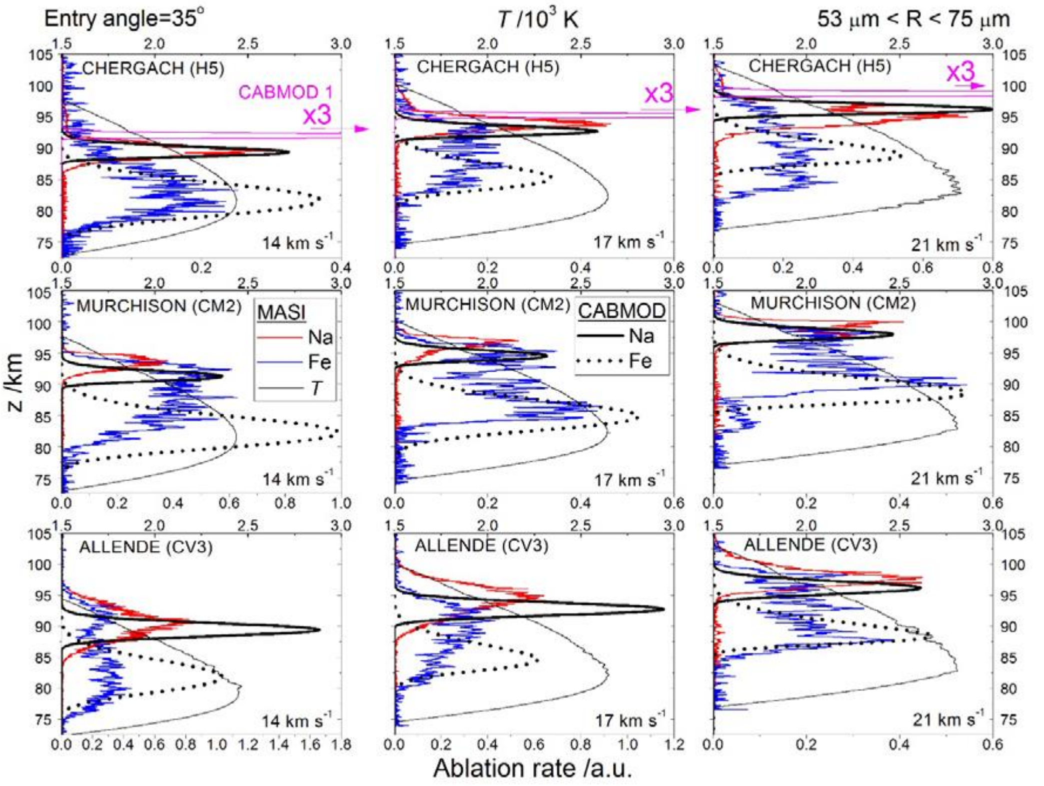

Figure 3.15. *Atmospheric ablation vertical profiles for R_{avg} = 60 μm particles at three different speeds and three different IDP analogues. Red lines are for observed Na LIF, blue lines for observed Fe LIF (bottom axes) and black lines for measured temperature (top axes). The Na and Fe ablation rates obtained from the updated version of CABMOD are the thick black solid and dotted lines, respectively. The observed and modelled Na (Fe) profiles are normalized to the same area. Pink dashed lines indicate the modelled Na ablation rate with the previous version of CABMOD (Na profiles are out of scale as indicated). Reproduced from Gómez-Martín et al. [2016].*

Table 3.1. *Fe and Na yields (Φ = Ablated/Total) and Differential Ablation Coefficients (DAC = Φ_{Fe}/Φ_{Na}) from experiments with the Allende IDP analogues, and from CABMOD calculations (entry angle 35°). Reproduced from Gómez-Martín et al. [2016].*

R^a /µm	**m^b /µg**	**v /km s^{-1}**	**n^c**	**Φ_{Na}^{MASI}**	**σ^d**	**Φ_{Na}^{CABMOD}**	**Φ_{Fe}^{MASI}**	**σ**	**Φ_{Fe}^{CABMOD}**	**DAC MASI ^{e}**	**σ**	**DAC CABMOD**	**v weight^f**	**DAC MASI ^{g}**	**DAC CABMOD**	**m weight^f**	**DAC MASI ^{h}**	**DAC CABMOD**
9	0.01	14	2	0.01	0.01	0.00	0.00	0.02	0.00	0		0.0	0.15	**0.44**	**0.09**	0.45		
		17	4	0.14	0.03	0.01	0.00	0.02	0.00	0		0.0	0.075					
		21	3	0.85	0.06	1.00	0.46	0.20	0.02	20	9	0.8	0.025					
		31	2	0.95	0.03	1.00	0.80	0.13	1.00	31	5	37.4	0.0025					
36	0.57	14	5	0.90	0.09	1.00	0.52	0.08	0.05	21	4	1.9	0.15	**8.46**	**5.08**	1		
		17	5	0.95	0.05	1.00	0.41	0.28	0.60	16	11	22.5	0.075					
		21	4	0.97	0.01	1.00	0.52	0.19	1.00	20	7	37.4	0.025					
		31	2	0.94	0.00	1.00	0.67	0.45	1	27	18	37.4	0.0025					
64	3.18	14	5	0.95	0.07	1.00	0.58	0.17	0.49	23.0	7	18.3	0.15	**6.11**	**5.79**	0.52		
		17	4	0.97	0.03	1.00	0.88	0.16	1.00	34	6	37.4	0.075					
		21	5	0.97	0.02	1.00	0.88	0.14	1	34	5	37.4	0.025					
100	12.15	14	3	0.95	0.09	1.00	0.91	0.05	1	36	4	37.4	0.15	**5.67**	**6.53**	0.37		
		17	3	0.99	0.03	1.00	0.95	0.04	1	36	2	37.4	0.075					
Mass- and velocity-weighted Fe DAC relative to Na, Allende (entry angle α=35°)																	**20.7 ± 2.1**	**17.5**
Mass- and velocity-weighted Fe DAC relative to Na, normalized to CI (entry angle α=35°)																	**8.4**	**7.1**
Mass- and velocity-weighted Fe DAC relative to Na, normalized to CI, 1.5 Na enrichment (entry angle α=35°)																	**5.6**	**4.7**
CABMOD (previous version [*Carrillo-Sánchez et al.*, 2015]) integrated DAC **for all possible m, v and α**																		5.9
CABMOD (updated version, this work) integrated DAC **for all possible m, v and α**																		6.9
DAC derived from lidar observations (chemistry effects accounted for) [*Carrillo-Sánchez et al.*, 2015]																		3.5

---

[a] Average radius. [b] Average mass assuming spherical particles with density 3 g cm^{-3} [c] Number of measurements for each (v, m) combination. [d] Standard deviation. [e] DACs for each (m, v) combination. [f] Weighting factors from the Zodiacal Cloud mass and velocity distributions [*Nesvorný et al.*, 2010; *Nesvorný et al.*, 2011]. [g] Velocity-weighted DACs for each mass bin. [h] Overall DACs.

Table 3.2. *Ca and Na yields (Φ = Ablated/Total) and Differential Ablation Coefficients (DAC = Φ_{Ca}/Φ_{Na}) from experiments with the Allende IDP analogues, and from CABMOD calculations (entry angle 35°). Reproduced from Gómez-Martín et al. [2016].*

R^a /μm	m^b /μg	v /km s^{-1}	n^c	$\Phi^{\text{MASI}}_{\text{Na}}$	σ^d	$\Phi^{\text{CABMOD}}_{\text{Na}}$	Φ^{MASI}_{Ca}	σ	$\Phi^{\text{CABMOD}}_{\text{Ca}}$	**DAC** MASI [e]	σ	**DAC** CABMOD	v **weight**[f]	**DAC** MASI [g]	**DAC** CABMOD	m **weight**[f]	**DAC** MASI [h]	**DAC** CABMOD
9	0.01	14	4	0.89	0.05	0.000	0.16	0.17	0.000	0		0	0.15	**0.00**	**0.00**	0.45		
		17	1	1.00		0.008	0.02	0.00	0.000	0		0	0.075					
		21	1	1.00		1.000	0.02	0.00	0.000	0		0	0.025					
		31	3	0.84	0.12	1.000	0.01	0.03	0.027	0.6	0.7	0.1	0.0025					
36	0.57	14	4	0.83	0.23	1.000	0.13	0.16	0.000	0.08		0	0.15	**0.03**	**0.01**	1		
		17	1	1.00		1.000	0.01	0.00	0.000	0.06		0	0.075					
		21	7	0.80	0.15	1.000	0.01	0.01	0.003	0.05	0.11	0	0.025					
		31	6	0.79	0.08	1.000	0.06	0.07	0.924	0.6	0.7	3.3	0.0025					
64	3.18	14	3	0.97	0.00	1.000	0.32	0.18	0.000	0.04	0.00	0	0.15	**0.01**	**0.03**	0.52		
		17	4	0.89	0.05	1.000	0.16	0.17	0.001	0.05	0.05	0	0.075					
		21	1	1.00		1.000	0.02	0.00	0.361	0.3	0.3	1.3	0.025					
100	12.15	14	1	1.00		1.000	0.02	0.00	0.000	1.2	0.7	0	0.15	**0.19**	**0.00**	0.37		
Mass- and velocity-weighted Ca DAC relative to Na, Allende (entry angle α=35°)																	**0.2 ± 0.2**	**0.04**
Mass- and velocity-weighted Ca DAC relative to Na, normalized to CI (entry angle α=35°)																	**0.07**	**0.01**
Mass- and velocity-weighted Ca DAC relative to Na, normalized to CI, 1.5 Na enrichment (entry angle α=35°)																	**0.05**	**0.01**
CABMOD (previous version) integrated DAC **for all possible *m*, *v* and α**																		0.06
CABMOD (updated version, this work) integrated DAC **for all possible *m*, *v* and α**																		0.08
DAC derived from lidar observations (chemistry effects accounted for) [*Carrillo-Sánchez et al.*, 2015]																		0.04

[a] Average radius. [b] Average mass assuming spherical particles with density 3 g cm^{-3} [c] Number of measurements for each (v, m) combination. [d] Standard deviation. [e] DACs for each (m, v) combination. [f] Weighting factors from the Zodiacal Cloud mass and velocity distributions [*Nesvorný et al.*, 2010; *Nesvorný et al.*, 2011]. [g] Velocity-weighted DACs for each mass bin. [h] Overall DACs.

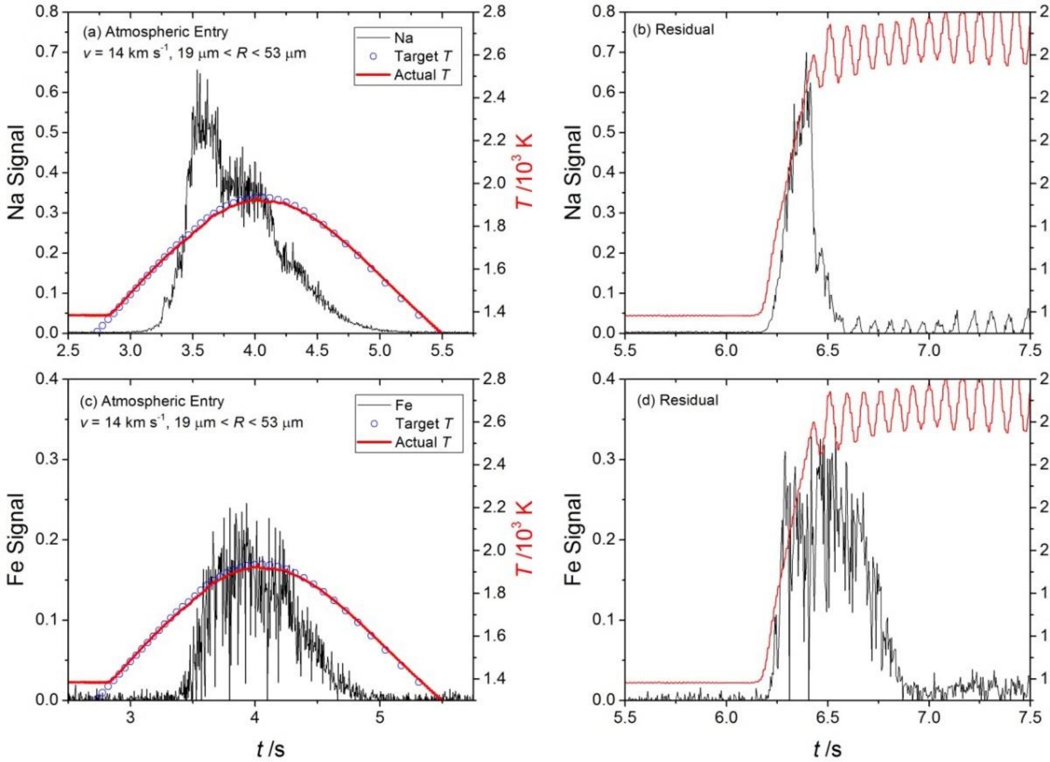

Figure 3.16. *Example of experiment designed to determine the yield of Na and Fe from an atmospheric entry heating profile (panels (a) and (c)) corresponding to a 0.5 μg particle (size bin with radii between 19 and 53 μm) entering the atmosphere at 14 km s^{-1}. The lower limit of the pyrometer range (1300 K) impedes reproducing the full temperature profile from low temperature. However, the temperatures relevant for Na and Fe ablation are within the accessible range. Panels (b) and (d) show the complete ablation of the residual Na and Fe remaining in the material unablated in the atmospheric entry using a high temperature step function. The oscillations in high temperature profile are due to the difficulty of controlling temperature close to the upper limit of the pyrometer range (~3000 K). However, these oscillations do not have any influence on the result since the only requirement is that the residual particle fully ablates. Reproduced from Gómez-Martín et al. [2016].*

3.3.5. Interpretation of the ablation profiles.

Inspection of Figure 3.4 and Figure 3.5 sheds some light into the size dependence of the temperature onsets. Na appears in localized domains in both meteoritic samples. Small Fe-rich domains are also present in Chergach. Loose Na-rich plagioclase grains (~20 μm [*Wieisberg et al.*, 2008]) present in the matrix of ordinary chondrites (Albitic Feldspar [*Bryan and Kullerud*, 1975] with melting point at ~1400 K [*Bowen*, 1913]) most likely accumulate in the smallest size bins, while the largest bins are dominated by coarser grained minerals. The preferential accumulation of fine grains of plagioclase in the small size bins is confirmed by the smaller Na(T < 1930 K)/Na(total) observed for samples prepared from reground large particles (Figure 3.8).

The onsets for the smallest size bins are similar to those observed with albite, because the loose albite grains are free to melt and evaporate following the plagioclase phase diagram. Plagioclase grains still exist in larger size bins, but they are embedded in larger particle aggregates, and considering the low porosity of H5 meteorites [*Wilkinson and Robinson*, 2000] the whole particle probably needs to melt in order to release the inner sodium-rich pockets, which likely causes the observed delayed evaporation for larger size particles.

A recent study of unmelted and partially melted micrometeorites collected at the Earth's surface shows that the porosity of partially melted particles is higher, which is likely an indication of low temperature melting and evaporation of volatile mineral phases creating empty pockets within the IDP grainy aggregates [*Kohout et al.*, 2014]. The higher porosity of Allende [*Macke et al.*, 2011] could be an explanation of the somewhat weaker size dependences observed. The Na onsets from Murchison and Allende are higher than for Chergach, which reflects the higher melting temperature of nepheline, which is the major Na-bearing feldespatoid in carbonaceous chondrites. The limited number of experiments carried out with Murchison samples show well defined, narrower and sharper profiles than in Allende.

The Fe-rich distinct grains shown in Figure 3.4 are probably subjected to a similar mechanism as the Na-rich grains, which would explain the size dependence of the Fe signal onsets. The abundance of Fe also makes the ablation profiles somewhat more regular and smoother, but the presence of lower and higher temperature phases produces the very long melting curves shown in Figures 3.9–3.11. Chondritic materials are assemblages of different metal alloys and minerals, such as Fe-Ni metal grains, troilite (FeS), and silicates of varying Fe content. Thus, it is not surprising that the onset temperature of Fe ablation is not far from the melting point of metallic Fe (~1800 K), and ablation continues for the rest of the temperature ramps. Figure 3.8 shows that, in contrast, Mg-rich olivine samples Fo_{80} display onsets around 200 K higher than the meteoritic analogues, and that the later can be better understood as a superposition of the metallic Fe and Fo_{90} ablation curves. Possibly, the presence of residues of molten sulphide material also help to lower the onset of the Fe signal. It is also noticeable that the fraction of Fe ablated below the melting point of the corresponding Mg-rich olivine is higher for Chergach, which is consistent with the higher content of metallic Fe in H-type ordinary chondrites.

Pure Fe, albite, labradorite and olivine show Na or Fe evaporation onsets not far from their corresponding melting points. As a consequence, Na and Fe evaporation onsets in IDP meteoritic analogues can be understood in terms of the melting point of common mineral phases included in the meteoritic aggregates. Ca on the other hand appears at a higher temperature than the melting point of labradorite in IDP analogues, for which it starts evaporating after all Na has been released. The evaporation onset of Ca in labradorite and anorthite is similar to the onset in both analogues (e.g. Figure 3.8), which is consistent with the Ca-bearing phase being Ca-rich feldspar, commonly found in chondrites [*Bryan and Kullerud*, 1975; *Clarke et al.*, 1971; *Fuschs et al.*, 1973]. It should be noted that the partitioning of Ca in a melt is extremely dependent on the concentration of major "pseudo-species" such as MgO and SiO_2 [*Fegley and Cameron,* 1987]. The distribution of Ca between the different pseudospecies in the melt depends on the thermodynamic activities of MgO, SiO_2 and Al_2O_3, because the major Ca pseudo-species are $CaSiO_3$, $CaMgSi_2O_6$, $CaAl_2Si_2O_8$, and other Ca silicates. Changes in the calculated activities of MgO, SiO_2 and Al_2O_3 also affect Ca chemistry, whether or not all Ca is found as $CaMgSi_2O_6$. The MgO activity affects SiO_2 via $MgSiO_3$ and Mg_2SiO_4, for example. Therefore the evaporation of Ca is very dependent on the composition of the melt, and not only on the Van't Hoff parameters of CaO.

3.4. ASSESSMENT OF CABMOD RESULTS

The simulation of the melting of an assemblage of many grains of different minerals is an extremely challenging task. Clearly, the assumption of a single mineral constituent is simplistic and leads to inaccuracies, especially regarding minor elemental constituents. Firstly, the phase diagram of the silicate constrains the evaporation of the minor volatile elemental constituents and secondly, the over-abundance of scavenging species in the single melt (such as MgO and SiO_2) delays significantly the release of refractories such as Ca. Furthermore, other physical effects observed in the MASI experiments such as delayed release from larger particles and multiple pulses cannot be accounted for presently by CABMOD.

A version of CABMOD has been adapted to model the MASI experiments, where the momentum and energy balance calculations and the non-thermal ablation module are bypassed. This laboratory version of CABMOD instead directly uses the temperature profiles measured by the pyrometer. The model is then run with the specific elemental composition, density, etc. of the different IDP analogues employed. Figure 3.17 shows a comparison between the MASI Na, Fe and Ca ablation curves obtained for one particular size bin (53 µm < *R* < 75 µm) for Chergach and Allende with a linear temperature ramp and the corresponding predictions using the original version of CABMOD with melting points corresponding to the Fe to Mg ratio in their silicates (2000 K for Chergach and 1800 K for Allende and Murchison, indicated by thick black lines on each panel). The original version of the model (hereafter CABMOD 1, in blue) is unable to reproduce the onset and the width of the pulses. The dependence on particle size (average radius of the corresponding size bin) of the FWHM and the temperature at the peak ablation calculated with CABMOD 1 are plotted in Figure 3.12. The Na and Fe pulses are narrower than the observations, particularly in the case of Na, and the release of Ca in CABMOD is delayed.

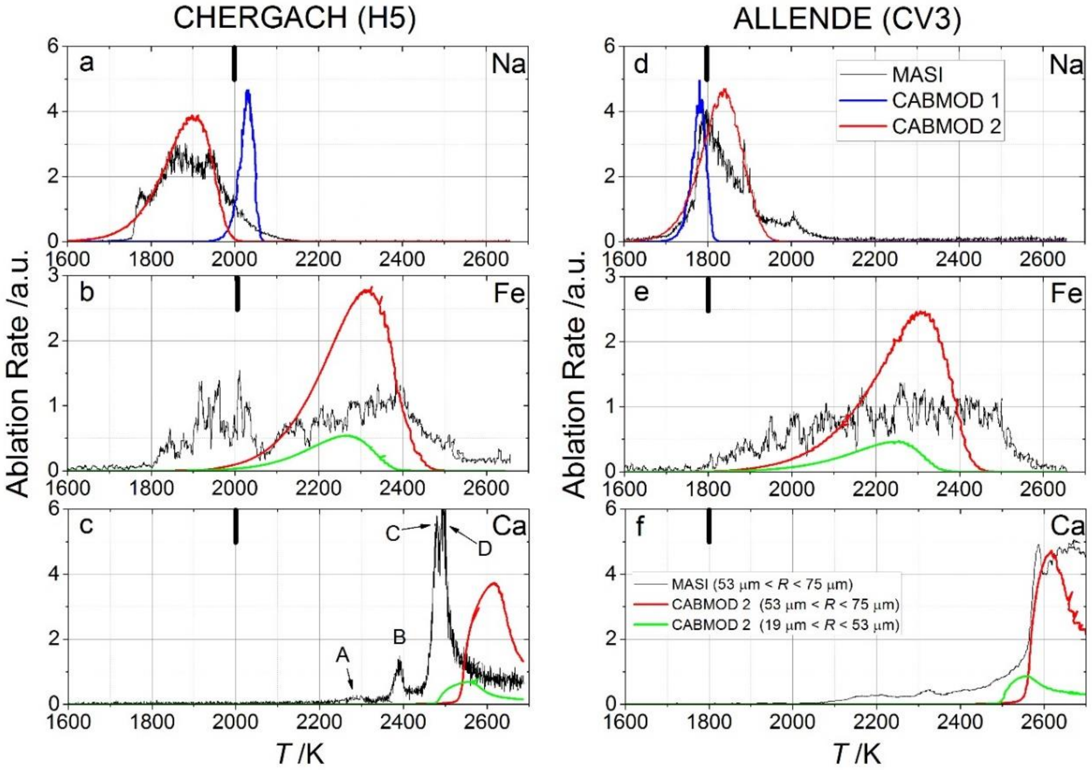

***Figure 3.17**. Na, Fe and Ca ablation rates vs. temperature (138 K s^{-1} ramp) for the 53 µm < R < 75 µm size bin. The left column shows data for Chergach (panels a, b and c) and the right column data for Allende (panels d, e and f). Each row shows data for one element: Na (panels a and d), Fe (panels b and e) and Ca (panels c and f). The ablation rate in arbitrary units is on the left axis and the temperature of the filament on the right axis of each panel. The black vertical lines indicate the melting temperatures of Fo_{80} and Fo_{60}. The prediction of the original version of CABMOD appears in blue, and the red lines show the results with the new version with updated Na thermodynamics and wider sigmoid function γ(T). The green lines correspond to a calculation for the next smallest size bin with the same ramp. Reproduced from Gómez-Martín et al. [2016].*

Implementing a multi-phase aggregate in CABMOD is beyond the scope of this work. Here our objective is to identify shortcomings of the model and advance some possible solutions, as well as assess its performance in predicting integrated injection rates. Another objective is to produce the best possible Na ablation profiles, given the importance of Na ablation and subsequent impact ionization in determining the radar detectability of slow/small meteoroids where Na may be the only element that ablates [*Carrillo-Sánchez et al.*, 2015; *Janches et al.*, 2014; *Janches et al.*, 2015].

In a first attempt to improve the agreement between CABMOD and MASI, the model was upgraded with the latest version of the MAGMA code, which includes revised data for Na and K alumino-silicates [*Holland and Powell*, 2011]. Revision of the thermodynamics of Na resulted in lower equilibrium vapour pressures and thus in a lower evaporation rate, which fits better the high temperature tail of the Na pulses. Note that the effective evaporation coefficient can also be modified to vary between $\gamma_i = 0$ and $\gamma_i \leq 1$ (rather than $\gamma_i = 1$) below and above the melting point, respectively, which would have the same effect as a decrease in the equilibrium vapour pressure. A unity evaporation coefficient for Na seems like a reasonable result from the comparison of the theory and the experiment.

In order to account for the lower onset of the Na signal, the sigmoidal temperature dependence of γ_i in the phase transition can be made smoother so that it extends over a wider temperature range, which is equivalent to relaxing the constraint imposed by the very high melting temperature of the assumed Mg-rich olivine composition. Thus, the problem of the simplistic description of the composition of the particle can be provisionally addressed for Na by allowing for a range of melting temperatures, which acknowledges the presence of more volatile mineral phases.

The comparison between model runs for Na and observations shown in Figure 3.17, although still far from perfect, highlights the fact that the Na ablation rate is significantly slower than previously assumed. A narrower sigmoid performs a better fit with Allende Na profiles, which is perhaps an indication of the higher porosity of this meteorite compared to Chergach. For the test linear temperature ramp employed throughout this work, the FWHM of the modelled pulses is 2-3 times higher than with CABMOD 1 and in reasonable agreement with the MASI results for the three most important size bins for Allende (Figure 3.13b). In the new developed version of CABMOD (hereafter CABMOD 2), calculations of Na ablation rates from micrometeorite entries are in reasonable agreement with the MASI simulations in Figure 3.17, where the experimental and calculated curves are normalized to the same area.

Given that 75% of IDPs are estimated to be carbonaceous [*Taylor et al.*, 2012] the Allende sigmoid width is employed for calculations of realistic atmospheric ablation profiles with CABMOD 2 which are then used to derive Fe and Ca yields relative to Na. It is thought that CM chondrites such as Murchison are mineralogically closer to IDPs.

The FWHM of the Fe pulses modelled with CABMOD is approximately half of the FWHM of the MASI Fe pulses (Figure 3.12, panel b), which is in line with the 'silicate Fe peaks' fitted in Figures 3.9–3.11. Figure 3.17 illustrates that CABMOD does a slightly better job in reproducing the Fe profile shapes for Allende than for Chergach, which is most likely due to the lower metallic content in carbonaceous meteorites. The modification of the sigmoid function in CABMOD does not have an impact in the Fe simulated curves, because the equilibrium vapour pressure of Fe above olivine is very small below the melting point. CABMOD does not predict significant particle size effects (pulse onset or width changing with size) besides the dependence on total Fe due to particle mass (the red and the green curves correspond to the size bin of the experimental curves shown in black, and to a smaller size bin, respectively). Improved prediction of the Fe (and Ca) ablation rates can only be achieved by a more complex treatment of the mineral aggregates in CABMOD.

Figure 3.17 shows the CABMOD prediction for Ca (panels c and f). It can be seen that the model fails to replicate the onset and the shape of the curves, but the calculation for the smaller size bin replicates qualitatively the sequence of the observed peaks (the particle fragments A and B are smaller than C and D, and similarly the smaller particle shows a lower temperature onset for calcium in the simulations). No ad hoc modification of the model to better match the Ca ablation rate has been introduced. Similarly, a multiphase treatment of IDPs is the only way of dealing at once rigorously and simultaneously with all the ablation features observed in the present study.

Despite the poor agreement between simulated and observed Ca ablation profiles using linear ramps, it is worth noting that for steeper heating ramps the difference between the observed and the modelled Ca signal onset is less severe, to the point that the shape of the experimentally simulated and calculated atmospheric injection profiles of Ca are very similar. This can be seen for example in Figure 3.18, where the position of the Ca peak in an atmospheric ablation experiment is well matched by the model prediction. The yield of Ca, however, is a matter of concern, as will be shown below.

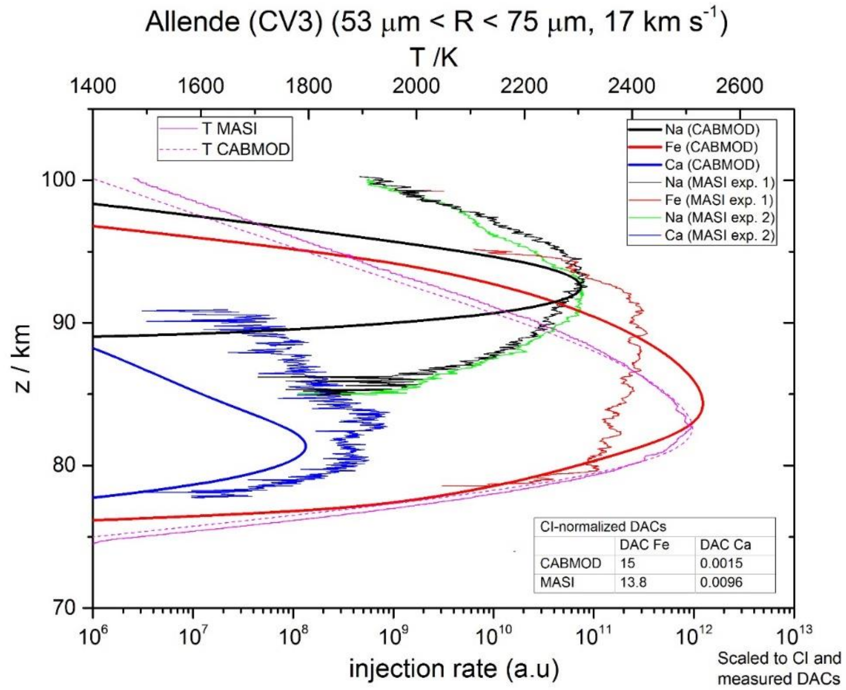

Figure 3.18. *Ablation rates for Allende particles at 17 km s^{-1} for Na (black and green), Fe (red) and Ca (blue). Experimental curves are the thin lines and CABMOD 2 simulations are thick lines. The Fe and Ca profiles cannot be obtained simultaneously, so the two corresponding Na profiles are plotted to demonstrate reproducibility. The target (dashed line) and measured (solid line) temperature profiles are shown in pink. The observed and modelled curves are scaled to their relative differential ablation coefficients for this particle mass and velocity. Reproduced from Gómez-Martín et al. [2016].*

The experimentally-determined yields of Fe and Na for a selection of velocity- and mass-specific calculated heating profiles are shown in Table 3.1. The data shows some scatter, and there are some disagreements which are possibly related to the higher yield of Fe at lower temperatures due to low melting point of Fe-containing mineral phases. Nevertheless, the model reproduces correctly the trend of greater Fe ablation with increasing particle speed and mass, as shown by the differential ablation coefficients plotted in Figure 3.19. Thus CABMOD provides a reasonable estimate of the differential ablation of Na and Fe for different combinations of mass and size, even if the detailed physics of melting of a complex aggregate of mineral grains is not described in the model.

It is actually possible to derive a mass and velocity distribution-weighted DAC from the data plotted in Figure 3.19 by using the ZCM [*Nesvorný et al.*, 2011] (velocity and mass weighting factors included in Table 3.1). This results in CI-normalized values of 8.4 and 7.1 for MASI and CABMOD respectively. This good agreement arises because most of the mass in the Zodiacal Cloud mass distribution is in the 36 and 64 μm radius bins. Because most of the Na and Fe are released in the range of masses and velocities considered, the results are not too far from the Fe/Na DAC derived from CABMOD 2 considering the full ZCM mass and velocity distributions, which is 6.9.

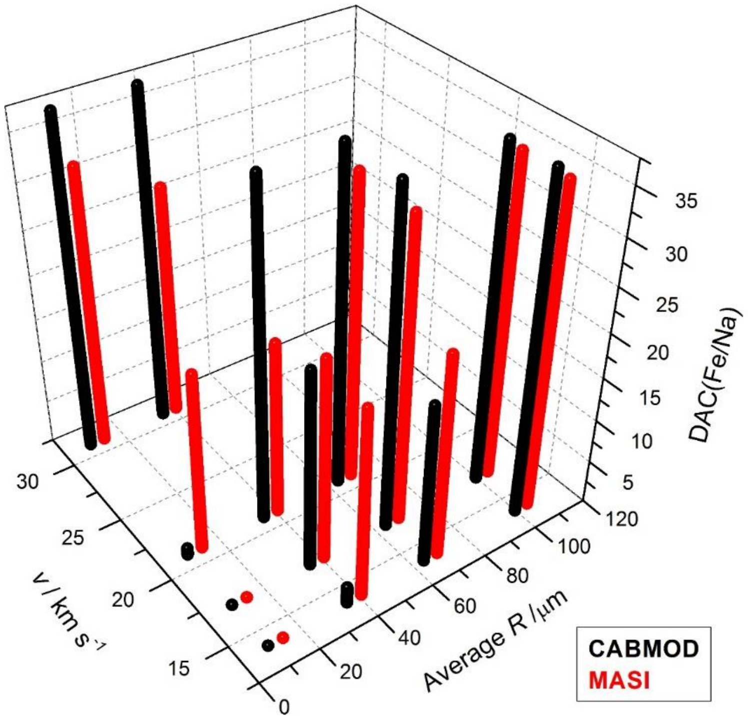

Figure 3.1*9. Differential ablation coefficients (ratio of the fraction of ablated Fe to the fraction of ablated Na) for different combinations of size and entry velocity using the Allende IDP analogues. MASI results are shown in red and CABMOD predictions in black. Note that for complete ablation of Na and Fe (high speed/large particles) the DAC tends to the Fe/Na ratio in the Allende meteorite (~37). Reproduced from Gómez-Martín et al. [2016].*

It is worth noting here that global modelling of the lidar-observed sodium and iron layers in the terrestrial mesosphere requires a Fe/Na DAC of 3.5 [*Carrillo-Sánchez et al.*, 2015]. The MASI results indicate that complete Na ablation occurs for almost all combinations of mass and speed. Moreover, it seems that Fe ablates slightly more efficiently than expected due to the low temperature phase unaccounted for by CABMOD. Therefore, the remaining difference between the CABMOD predicted DAC and that derived from lidar observations and modelling [*Carrillo-Sánchez et al.*, 2015] requires both differential ablation and enrichment of Na in meteoroids relative to CI, as suggested in previous studies [*Trigo-Rodriguez and Llorca*, 2007] and observed in cometary material [*Schulz et al.*, 2015].

The large difference between the CABMOD Ca DAC for the full velocity and mass distributions (0.08) and the CABMOD Ca DAC for the set of selected mass and velocity combinations used in the experiments (0.01) is essentially due to the absence of large masses and velocities from the reduced set (Table 3.2). The heating profiles corresponding to the missing tail of speeds and masses reach the highest temperatures, and therefore are those for which the largest yields of Ca occur. It is therefore significant that the experimental DAC for the limited set of low speeds and masses considered is 0.07, not far from the full distribution modelled result.

The poor agreement for Allende (~0.01 CABMOD vs 0.07 MASI) can be explained by noting that ablation of Ca is more efficient than predicted by the model owing to the specific composition of the Ca-containing minerals, which essentially lack Mg and have a smaller Si/Ca ratio than in the elemental composition assumed for the whole particle in CABMOD. The scatter of the experimental Ca yields from Allende is large (±100%), but this most likely reflects the presence of different Ca-bearing phases which are heterogeneously distributed, as discussed by *Clarke et al.* [1971]. Since the Ca-rich minerals are abundant in CAIs, some experiments were carried out with hand-picked CAI fragments in order to check for differences in the evaporative behaviour of Ca, but the results were inconclusive (e.g. Figure 3.10), possibly because of the presence in the non-separated samples of chondrule fragments, which also contain minerals with low Si/Ca ratio. By contrast, the Ca yield from the Chergach analogues are significantly smaller.

The design of MASI requires prescribing modelled atmospheric heating profiles to the particles. The modelled atmospheric heating profiles depend on the free molecular drag and the free molecular heat transfer coefficients [*Vondrak et al.*, 2008], which can only be studied in an experimental arrangement where particle heating results from aerobraking [*Thomas et al.*, 2016]. Therefore, uncertainties propagating from these parameters or from the simplifications involved in the energy and momentum balance equations are not taken into account in the calculation of yields. Non-thermal mass loss (sputtering) cannot be studied with MASI either, although it has been shown [*Vondrak et al.*, 2008] that this mechanism is negligible for meteoroids with velocities up to 45 km s^{-1} and heavier than 10^{-5} μg [*Vondrak et al.*, 2008], which encompasses most of the IDP population and in particular the mass bins and speeds that can be studied with the MASI apparatus.

3.5. SUMMARY OF THE CHAPTER

A novel experimental set up has been constructed to test the description of meteor ablation in the state-of-the-art chemical ablation model CABMOD. Figure 3.18 shows experimental and calculated ablation rates (arbitrary units) of Na, Fe and Ca, scaled to their respective DACs relative to Na (Na=1). CABMOD reproduces general features of the MASI experiments, such as the relative position of the ablation curves and the position of the peak ablation of Na and Ca. CABMOD also reproduces well the differential ablation of Fe:Na. The current version of CABMOD 2 produces reliable results for the integrated differential ablation of Fe and of the other major elemental constituents of similar volatility such as Mg and Si, which will be the subject of future research with the MASI. On the other hand, the integrated differential ablation of Ca is not well described. CABMOD cannot reproduce the large experimental yields of Ca from Allende. However, the much smaller Ca yields from Chergach indicate that the mineralogy of the simulated particles is key to simulating atmospheric ablation profiles of Ca. A suitable analogue, representative of the average Ca distribution in IDPs needs to be used for this purpose.

CABMOD does not reproduce efficiently the width of the Na and Fe peaks, and the magnitude of the Ca ablation relative to Na, i.e. instantaneous properties of single meteors that may be important for radar detection. Consequently, a solution is to increase the width of the temperature dependence of the sticking coefficient in the transition between the liquid and solid phase of the Na profile. This could help in the current efforts to better model radar head echoes and reduce uncertainties in the simulation of observed radar meteor rates. Due to its low ionization potential and high volatility, ablated Na is a major contributor to radar detectability of meteors. A decrease of the peak number of head echo electrons due to the slower Na ablation would correspond to a quadratic decrease of the radar cross section, which would reduce the radar detection limit [*Janches et al.*, 2014; *Janches et al.*, 2015]. These calculations are relevant to quantifying the input rate of cosmic dust into the Earth’s atmosphere, as well as the injection rate of ablated metals.

The major shortcoming of the model is its poor physical description of the particles. Further developments need to address the complexity of IDP composition and morphology and resolve the influence of these on differential ablation rates.

CHAPTER 4: SOURCES OF COSMIC DUST IN THE EARTH'S ATMOSPHERE

4.1. INTRODUCTION

As discussed in Chapters 1 and 2, the principal sources of the Zodiacal Cloud are JFCs, ASTs, HTCs, and LPCs. Observations of the mid-infrared spectra of the Zodiacal Cloud reveal that particles in the bands are larger than those in the Diffuse Cloud [*Ade et al.*, 2014; *Fixsen and Dwek*, 2002; *Nesvorný et al.*, 2010]. In fact, this is not unexpected. The composition of the Diffuse Cloud is often claimed to be both asteroidal and cometary [*Nesvorný et al.*, 2010], whereas the bands are understood to be mainly asteroidal debris [*Sykes and Greenberg*, 1986]. In the 1990s, it was assumed that gravitational focusing of relatively slow-moving AST particles would enhance their contribution to the Zodiacal Cloud and the terrestrial input [*Dermott et al.*, 1996; *Durda and Dermott*, 1997; *Flynn*, 1989; *Flynn and McKay*, 1990]. *Öpik* [1951] analyzed the capturing probability of a small particle on an intersecting orbit with a planet. The gravitational enhancement (η_e) is defined as the ratio between the effective cross section (σ_e) for capture of a particle by a planet and the physical cross section (πR^2) of the particle:

$$\eta_e = \frac{\sigma_e}{\pi R^2} = 1 + \frac{v_\infty^2}{v^2} \qquad [4.1]$$

where v_∞ is the escape velocity from the surface of the planet, 11.2 km s^{-1} in the case of the Earth, and v is the geocentric speed of the particle. Consequently for fast particles with $v > v_\infty$, the gravitational enhancement approaches to unity. In contrast, η_e tends to infinity as $v \to 0$. If we assume the average entry velocity for the JFCs, ASTs and HTCs populations from the ZCM are 14.5, 12.0 and 34.4 km s^{-1}, respectively [*Nesvorný et al.*, 2010; *Nesvorný et al.*, 2011] , then the gravitational enhancement factors for these sources are 1.6, 1.9 and 1.1, respectively. This result shows that theoretically, for a given size, the Earth accretes particles from the AST with an efficiency 1.7 times greater than cosmic dust from the HTCs. Accordingly, the IDPs and MMs entering the Earth's atmosphere are expected to be dominated by the main belt asteroidal particles [*Flynn*, 1989; *Flynn and McKay*, 1990].

As discussed in Chapter 2, *Nesvorný et al.* [2010] concluded that the dominant source of cosmic dust is JFCs, with a contribution of 85-95%. This is because the profile of the mid-Infrared emission across the plane of the ecliptic matches that expected from JFC particles, whereas HTC particles should have a broader profile and the AST profile should be narrower (Figure 2.7b). More recently, *Yang and Ishiguro* [2015] combined observations of the albedo and spectral gradient of the Zodiacal Cloud to show that cometary dust (perhaps including D-type asteroids) contributes ~94% of the Zodiacal Cloud, with the remaining ~6% from C-type, X-type, and B-type asteroidal particles.

In this Chapter a completely different approach to this problem is employed. The absolute contributions of each of these dust sources to the global input of cosmic dust is constrained by the cosmic spherule accretion rate at the bottom of an ice chamber at the Amundsen-Scott base at South Pole [*Taylor et al.*, 1998], together with recent measurements of the vertical fluxes of Na and Fe atoms above 87.5 km in the atmosphere [*Gardner et al.*, 2016; *Gardner et al.*, 2014; *Huang et al.*, 2015]. Two different mass distributions for the JFCs are compared: the first derived from IRAS observations, and the second inferred from the most recent analysis provided by the Planck satellite.

4.2. METEOR SOURCES IN THE ZODIACAL CLOUD

4.2.1. Mass and velocity distributions of dust from different sources.

In the ZCM model [*Nesvorný et al.*, 2010; *Nesvorný et al.*, 2011], sub-mm particles from the different dust sources are launched and tracked as their orbits evolve under the influence of solar radiation pressure, Poynting-Robertson drag and planetary perturbations (see Section 2.2.3.1 for more details). The size distribution of cosmic dust particles was assumed to be represented by a broken power law (eq. 4.2) with a differential index k_1 between -2 and -3 below the break diameter D_b, and a differential index k_2 between -4 and -5 above D_b [*Fixsen and Dwek*, 2002]:

$$\frac{f(D)}{f_0} = \begin{cases} (D/D_b)^{k_1}, \ D \leq D_b \\ (D/D_b)^{k_2}, \ D > D_b \end{cases} \qquad [4.2]$$

where f_0 represents the pre-exponential factor. The observations made by the FIRAS (Far Infrared Absolute Spectrophotometer) instrument abroad the COBE satellite indicate that D_b lies between 30 µm and 60 µm, which is supported by measurements of weak Zodiacal Cloud emission at sub-mm wavelengths by the Planck telescope launched in 2009 [*Ade et al.*, 2014]. In the present study, we assume D_b = 36 µm, which corresponds to a dust composition in between amorphous carbon (D_b ~28 µm) and silicate (D_b ~64 µm) [*Fixsen and Dwek*, 2002]. The cumulative size distributions for IRAS and Planck are shown in Figure 4.1. As discussed in chapter 2, the IRAS observations suggests D_b ~100 µm

[*Nesvorný et al.*, 2010]. According to Figure 4.1, the Planck distribution has a differential index of -1.4 ± 0.3 below the break diameter, and a differential index of -4.3 ± 0.1 above D_b. In contrast, the IRAS distribution exhibits differential indices of -2.7 ± 1.8 and -4.8 ± 0.1 below and above the break diameter, respectively.

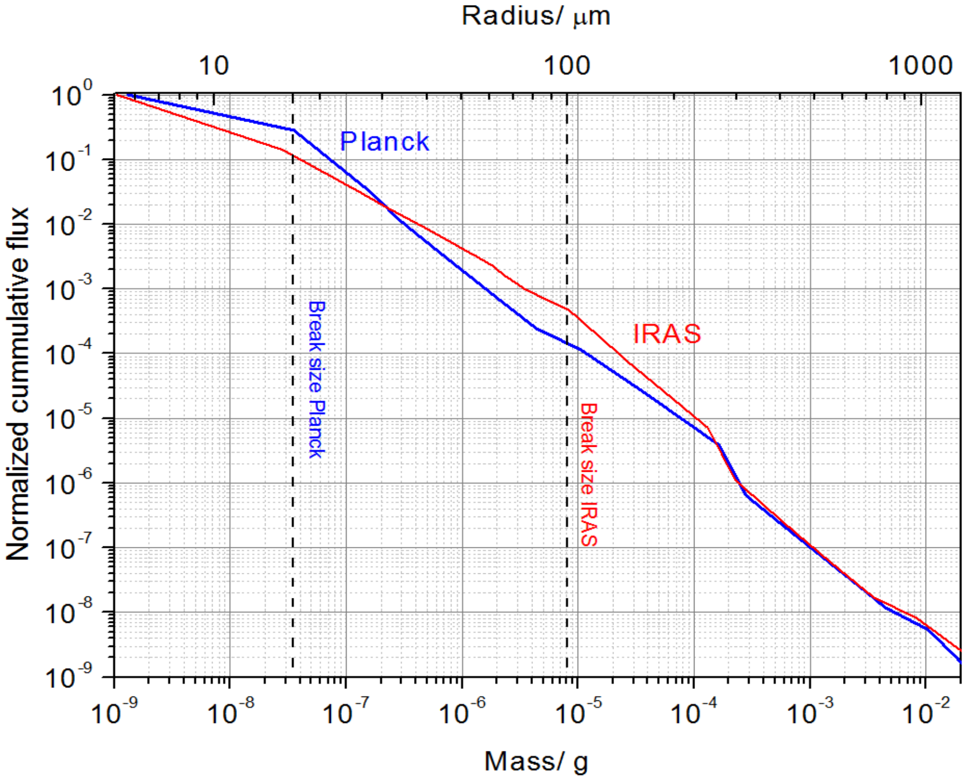

Figure 4.1. *Cumulative size/mass distributions of JFC particles inferred from observations of emission from the Zodiacal Cloud by the Planck (blue) and IRAS (red) satellites. Reproduced from Carrillo-Sánchez et al. [2016].*

Figures 4.2a and 4.2b are histograms of the particle mass distributions for the four cosmic dust sources accreted at the Earth derived from the Planck and IRAS observations, respectively. These distributions are shown as mass flux per decade over the mass range 10^{-9}-10^{-2} g, i.e., with a radius between 5 μm and 1 mm, assuming a particle density of 2.2 g cm^{-3} [*Consolmagno et al.*, 2008]. The mass influx of each source has been weighted according to the fitting procedure described in Section 4. As discussed above, the JFCs were modelled using either the Planck or IRAS distributions (these are termed JFC-IRAS and JFC-Planck particles, respectively). Figures 4.1a and 4.1b show that the JFCs-Planck mass distribution peaks around 0.01 μg, whereas the largest mass contribution of accreted JFC-IRAS, HTC and OCC particles is from particles of ~1 μg, and the AST peak is ~10 μg. Following from the conclusion that most of the Zodiacal Cloud emission is from JFC particles, the IRAS and Planck observations indicate a global input of 34 ± 17 t d^{-1} of JFC-IRAS particles [*Carrillo-Sánchez et al.*, 2015] or 30 ± 15 t d^{-1} of JFC-Planck particles

[*Janches et al.*, 2015] into the atmosphere. Meanwhile, the total mass input rates of the AST, HTC and OCC sources are arbitrarily set to 10 t d^{-1} in the ZCM, because the Zodiacal Cloud observations cannot be used to calibrate these mass distributions. In Section 4 the absolute magnitudes of all four dust sources are optimized to get an estimate of the Total Input Mass (TIM).

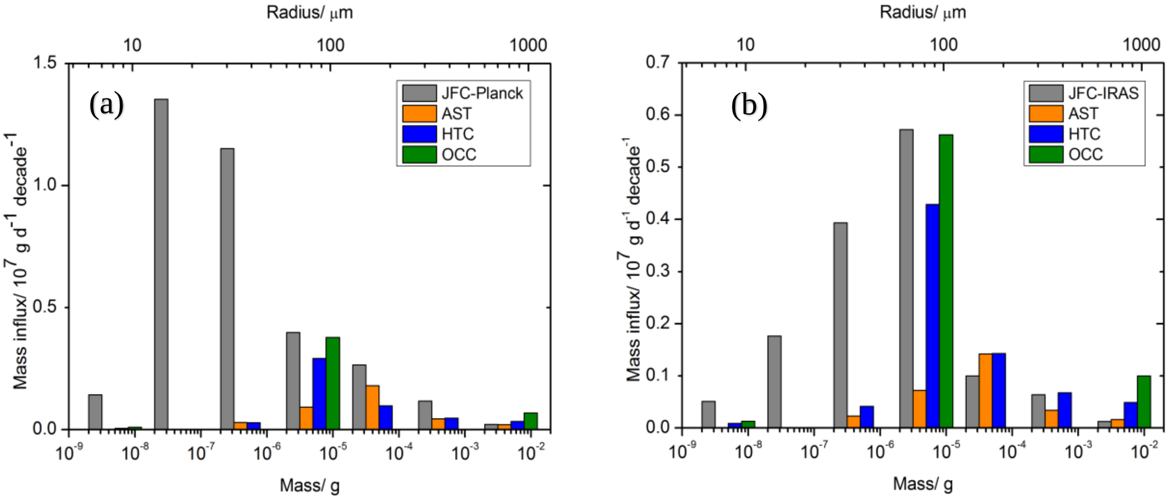

Figure 4.2. *Histograms of the particles mass distribution with each dust source weighted with the corresponding coefficients α, β, and γ, where JFC is represented in grey, AST in orange, HTC in blue, and OCC in green. Panel a: Mass distribution assuming JFC-Planck observations. Panel b: Mass distribution based on JFC-IRAS measurements. Reproduced from Carrillo-Sánchez et al. [2016].*

Figures 4.3a and 4.3b show the entry velocity distributions of the different populations, modeled by the ZCM. The slowest particles tend to be JFC and AST particles, and the fastest particles are HTC and OCC particles from long-period comets (the velocity ranges are between 11.5 km s^{-1} for particles in a prograde orbit and 72.5 km s^{-1} for those in a retrograde orbit). The average entry velocity of the JFCs and the ASTs is 14.5 km s^{-1} and 12.0 km s^{-1}, respectively, which means that most of these particles are in prograde orbits with radiants in the Helion and anti-Helion sporadic sources [*Nesvorný et al.*, 2010; *Nesvorný et al.*, 2011].

The velocity distribution for the HTC and OCC particles is shown in Figure 4.3b. The HTC distribution depends on the mass range: for masses < 1 μg, the distribution follows a bimodal trend with a dominant peak at 26 km s^{-1} and a second maximum at 57 km s^{-1}. For masses > 1 μg there is a single peak at 26 km s^{-1}. The OCC distribution exhibits a single peak at 58 km s^{-1}. Most of these particles are in a retrograde orbit and they likely have radiants in the north and south apex sources.

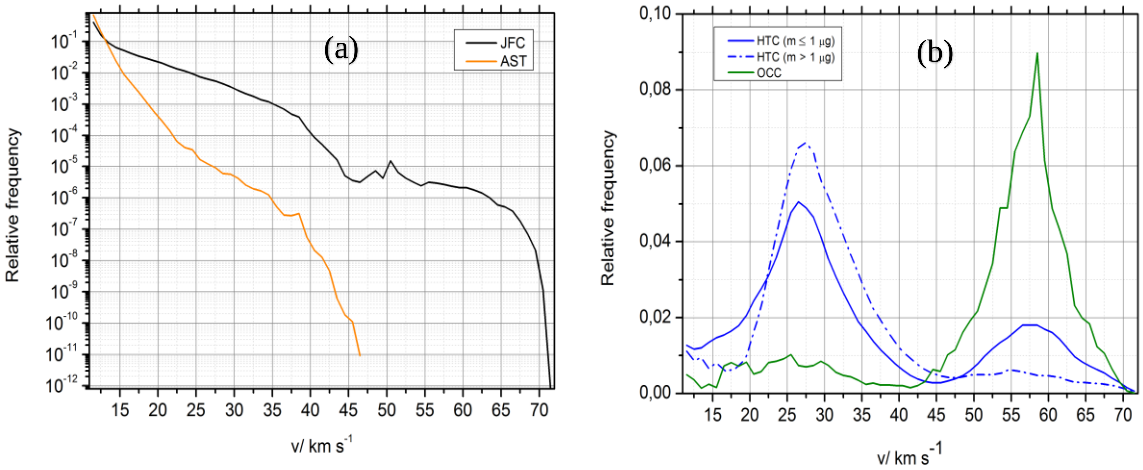

***Figure 4.3**. (a) and (b) Velocity distributions for JFC (grey), AST (orange), HTC (blue), and HTC (green). Note the dependence of the HTC distribution with the mass. Reproduced from Carrillo-Sánchez et al. [2016].*

4.2.2. Meteoric ablation modelling.

Owing to the large number of particles from each cosmic dust source that are produced by the ZCM (6.7×10^6 for JFC-IRAS, 9.3×10^6 for JFC-Planck, 1.5×10^6 for ASTs, 3.3×10^6 for HTCs, and 1.9×10^5 for OCCs), we have used a Monte-Carlo sampling procedure described by *Carrillo-Sánchez et al.* [2015] (see Section 2.3 for more details). Only particles smaller than 500 μm in radius (< 10^3 μg) are considered to ensure isothermal heating of the particles in CABMOD [*Vondrak et al.*, 2008]. Furthermore, this is a reasonable approximation because the very large particles do not represent a significant share of the total influx. As shown in Figures 4.2a and 4.2b, this is not a significant constraint. Each mass decade is divided into five bins, and the velocity and zenith angle distributions are Monte-Carlo selected. The resulting atmospheric ablation profiles are then co-added. Finally, the results for each mass bin are summed to obtain the integrated injection rate profiles for each metallic element (see Figure 2.10). The total number of sampled particles is 15,500 for each source, assuming a sample size of 500 particles per mass and 5 bins per decade in the mass range between 10^{-3} and 10^3 μg. For simplicity, we have used a constant atmospheric density profile (40ºN in March).

The injection rate profiles for individual elements from the different sources are shown in Figure 4.4. Note that these ablation profiles have been weighted following the fitting procedure in Section 4.2.3, in order to show their absolute contributions to the total input of each element. The top panels illustrate the contributions of JFC-Planck, AST and HTC particles. The lower left panel shows the elemental ablation rate profiles for JFC-

IRAS, and the final two panels show the total inputs for IRAS and Planck. In all cases, the most volatile elements (Na and K) ablate 10-15 km higher than the main constituent elements (Fe, Mg and Si), which turn in ablate higher than the most refractory elements (Ca, Al and Ti). As expected, the ablation profiles for the ASTs are about 10-20 km below the corresponding profiles for the JFCs and HTCs. This is caused by their slower velocity distribution (Figure 4.3) and the larger particles in the AST population taking longer than the JFCs to reach the melting point. The ablation profiles for the HTCs represent the opposite extreme, and are quite similar to the distribution of meteor trails observed by HPLA radars; this may indicate that most of the meteors observed by these radars are either HTC or OCC particles. The ablation profiles for the OCCs are very similar to those produced by the HTC particles, and so are not shown in Figure 4.4.

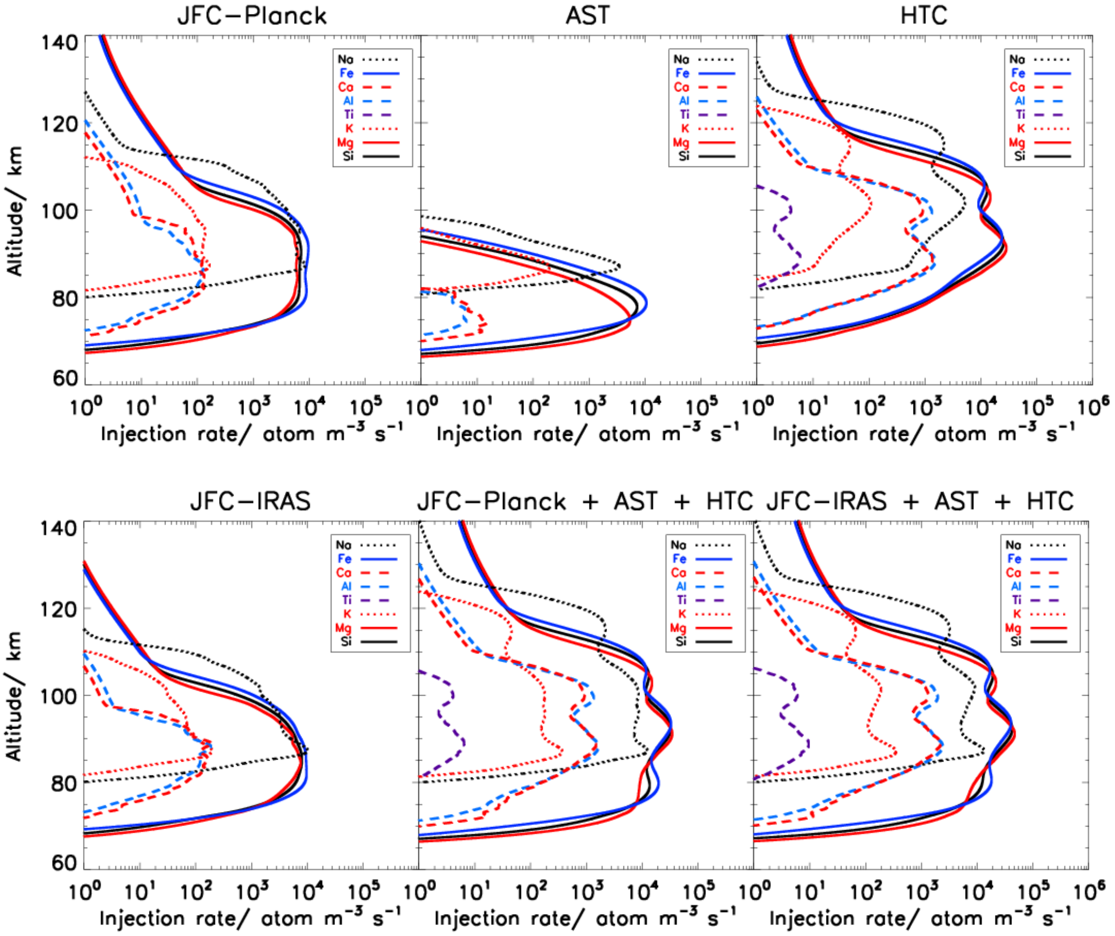

***Figure 4.4**. Ablation rates profiles for individual elements integrated for the JFC (constrained with the Planck and IRAS observations), AST and HTC populations. The last two plots show the overall injection rates. Reproduced from Carrillo-Sánchez et al. [2016].*

4.2.3. Determining the contribution of each cosmic dust source.

Three observations are used to constrain the relative contributions of each of these dust sources. First, the analysis of cosmic spherules at the South Pole indicates a global accretion rate of 4.4 ± 0.8 t d^{-1}, for spherules with diameters between 50 and 700 µm [*Taylor et al.*, 1998]. Second, the global input rate of Na atoms from meteoric ablation above 87.5 km is estimated to be 0.30 ± 0.06 t d^{-1}, by taking the annual mean vertical flux of Na atoms at 87.5 km (16700 ± 1800 atom cm^{-2} s^{-1}) measured at the Starfire Optical Range (SOR) at 35^{o}N [*Gardner et al.*, 2014]; assuming that this can be extrapolated globally [*Gardner et al.*, 2016], though we (arbitrarily) double the error to allow for uncertainty in this extrapolation; and multiplying the flux by a factor of 1.03 to obtain the total Na input by including the other forms of Na modeled to be present at 87.5 km [*Marsh et al.*, 2013]. Third, the global input rate of Fe atoms above 87.5 km is estimated to be 2.29 ± 1.05 t d^{-1}, by taking the ratio of the Fe to Na atom fluxes measured at the Table Mountain Lidar Facility (40^{o}N) to be 2.36 (Figure 4.5), and multiplying by a factor of 1.38 [*Feng et al.*, 2013] to obtain the total Fe input.

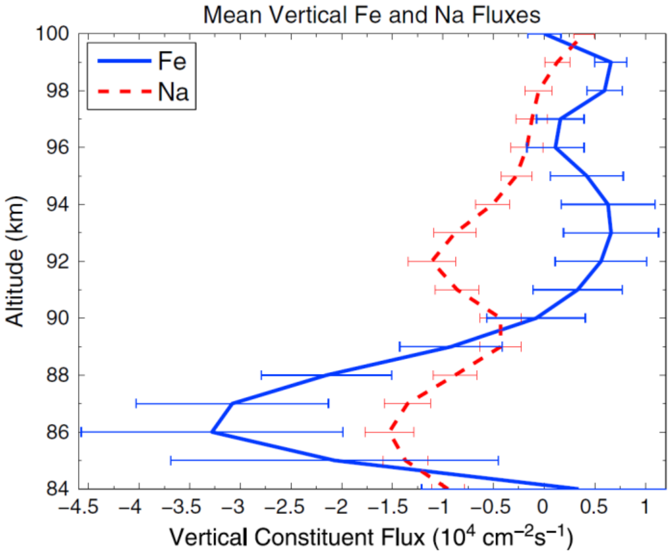

Figure 4.5*. Profiles of the mean vertical fluxes of atomic Fe (blue solid line) and Na (red dashed lines) measured at the Table Mountain Lidar Facility in August-September 2010. Reproduced from Huang et al. [2015].*

The ablation profiles of Na and Fe from each cosmic dust source (Figure 4.3) can now be integrated above 87.5 km to produce an ablation flux, which is then multiplied by the global surface area of the atmosphere at 87.5 km to produce a global input rate. This assumes that the flux is globally isentropic, which should be the case when integrated over a year [*Feng et al.*, 2013]. The cosmic spherule flux predicted by CABMOD for each dust source can similarly be converted into a global accretion rate.

We now have three simultaneous equations of the form in equation [4.3]:

$$\psi_{Total} = \alpha\psi_{JFC} + \beta\psi_{AST} + \gamma\psi_{LPC} \qquad [4.3]$$

where ψ_{Total} is the global mass accretion rate of either Na atoms, Fe atoms or cosmic spherules; ψ_{JFC}, ψ_{AST} and ψ_{LPC} are the global mass accretion rates of Na, Fe or spherules from the different sources; and α, β and γ are the coefficients which weight the contribution from each source. LPC in equation [4.3] refers to Long Period Cometary particles. This covers both HTCs and OCCs, which cannot be distinguished using our three criteria (see below). In the following discussion, the LPC particles are treated as HTCs unless otherwise stated.

Since there are three simultaneous equations and three unknowns (α, β and γ), the solution is in principle unambiguous. However, one constraint on the solution is the elemental abundance ratio of Na to Fe in the cosmic dust particles. The measured Fe and Na atom fluxes above 87.5 km [*Huang et al.*, 2015] correspond to a Fe:Na ratio of ~3.16, which is similar to the ratio of 3.6 required in a global model of the Na and Fe layers [*Feng et al.*, 2013]. However, if the Fe:Na ratio in the cometary particles is the carbonaceous CI ratio of 15.5 [*Asplund et al.*, 2009], then CABMOD predicts the Fe:Na ablation flux above 87.5 km would be either 3.4, 13.2 or 14.6 for the JFC, HTC and OCC sources, respectively. Thus, even if the LPC particles make up a small proportion of the total input [*Nesvorný et al.*, 2010; *Yang and Ishiguro*, 2015], because they ablate relatively efficiently this implies that the cometary particles must be enriched in Na. There is in fact strong evidence for Na overabundance compared to Fe: an enrichment factor of 3.2 from the VEGA-1 mission to comet 1P/Halley [*Jessberger et al.*, 1988]; 2.0 from the Stardust mission to comet 81P/Wild 2 [*Gainsforth et al.*, 2015]; ~2 from meteor spectroscopic analysis during the Perseid and Leonid showers [*Trigo-Rodriguez and Llorca*, 2007]; and most recently, 4.8 ± 3.7 from the Rosetta mission to 67P/Churyumov–Gerasimenko [*Hilchenbach et al.*, 2016]. The average enrichment factor is thus 2.9 ± 1.3. The additional Na appears to be contained in interstitial material that binds together mineral grains in the particles.

The optimal fits using the JFC-Planck particles (termed the ZCM-Planck model) are: Na enrichment factor = 2.5, $\alpha = 1.17 \pm 0.47$, $\beta = (3.46 \pm 1.96) \times 10^{-2}$, and $\gamma = (4.99 \pm 2.72$

)×10^{-2}. These values and their stated uncertainties were estimated by using Monte Carlo selection (assuming a top-hat distribution) to choose the cosmic spherule, Na and Fe fluxes within their quoted uncertainties, and then solving the simultaneous equations for new values of α, β and γ. Trials which generated negative values of any of these parameters were rejected. A Na enrichment factor of 2.5 gave the highest number of successful trials (71%). The values and their uncertainties are then the mean and standard deviations of 10^5 trials. In terms of the global mass input rate, the contributions of the JFC, AST and LPC particles are 34.6 ± 13.8 t d^{-1} (80%), 3.7 ± 2.1 t d^{-1} (8%), and 5.0 ± 2.7 t d^{-1} (12%), respectively.

The corresponding results for the JFC-IRAS distribution (termed the ZCM-IRAS model) are: $\alpha = 0.41 \pm 0.17$, $\beta = (2.73 \pm 2.00) \times 10^{-2}$, $\gamma = (6.78 \pm 1.72) \times 10^{-2}$. In terms of the global mass input rate, the contributions of the JFC, AST and LPC particles are 13.7 ± 5.7 t d^{-1} (57%), 2.9 ± 2.1 t d^{-1} (13%) and 7.4 ± 1.9 t d^{-1} (30%), respectively. The TIM for the ZCM-IRAS model is 24.0 ± 6.4 t d^{-1}. In this case, the number of successful trials assuming a Na overabundance of 2.5 is 23%.

4.3. RESULTS

Tables 4.1 and 4.2 (top four rows) illustrates the partitioning of the accreted mass between un-melted micrometeorites, cosmic spherules, and ablated atoms, for the JFC (Planck and IRAS), AST and LPC (=HTC) dust sources. The fourth column shows the total from the three sources. The bottom part of Tables 4.1 and 4.2 show the ablated mass of each element for each of the dust sources. The final column shows the fate of the OCC particle population, which was calculated by setting LPC = OCC instead of HTC in the fitting procedure (minor changes to the JFC and AST outcomes are not shown in the Tables). Because the HTCs and OCCs are relatively fast particles (Figure 4.3), Table 4.1 shows that 88% of the HTC mass input, or 98% of the OCC mass input, ablates. As a consequence, these dust populations make an insignificant (6% and 1% for HTC and OCC, respectively) contribution to the cosmic spherule flux. They also produce very similar Fe:Na ablation ratios (5.7 and 5.9, respectively, with a Na enrichment factor of 2.5). This explains why solving equation 4.3 does not distinguish between HTCs and OCCs.

We now consider why the fitting procedure yields such a high relative input of JFCs. The ratio of the Na mass input measured by lidar above 87.5 km [*Gardner et al.*, 2016;

Gardner et al., 2014; *Huang et al.*, 2015] to the cosmic spherule flux [*Taylor et al.*, 1998] is $Na|_{87.5\ km}\colon\psi_{sp} = 0.07$. For Fe, the corresponding ratio is $Fe|_{87.5\ km}\colon\psi_{sp} = 0.52$. These ratios can be compared with the corresponding ratios for the different sources in Tables 4.1 and 4.2. The JFCs produce the closest ratios to the measurements in both Planck and IRAS. For JFC-Planck, $Na|_{87.5\ km}\colon\psi_{sp} = 0.08$ and $Fe|_{87.5\ km}\colon\psi_{sp} = 0.42$. In contrast, the ASTs and LPCs represent lower and upper limits, since these sources are at the opposite extreme in the production of ablated atoms and spherules. For the ASTs, where there is a low average velocity, there is a significant production of spherules compared to ablated atoms, so that $Na|_{87.5\ km}\colon\psi_{sp} = 0.01$ and $Fe|_{87.5\ km}\colon\psi_{sp} = 0.18$. For the LPCs, where there is a high average velocity, the situation is reversed: $Na|_{87.5\ km}\colon\psi_{sp} = 0.30$ and $Fe|_{87.5\ km}\colon\psi_{sp} = 4.33$. Consequently, the fitting procedure determines a minor contribution from both ASTs and LPCs.

Table 4.1. *Global mass input from the four cosmic dust sources for the JFC-Planck fit. Elemental ablation inputs are italicized; the percentages in parentheses show the fraction of each element that ablates from its total atmospheric input from each source. Reproduced from Carrillo-Sánchez et al. [2016].*

Mass flux	**JFC (t d^{-1})**	**AST (t d^{-1})**	**LPC=HTC (t d^{-1})**	**Total (t d^{-1})**	**LPC=OCC (t d^{-1})**
Unmelted micrometeorites	27.4	1.2	0.3	28.9	0.04
Cosmic spherules	4.4	1.8	0.3	6.5	0.06
Ablated atoms	2.8	0.7	4.4	7.9	4.4
Cosmic spherules [†]	2.4	1.7	0.3	4.4	0.05
Unmelted ($D > 50\ \mu m$)	3.0	1.1	0.2	4.3	0.03
Na	*0.2 (28%)*	*0.02 (75%)*	*0.09 (99%)*	*0.3 (40%)*	*0.09 (100%)*
K	*7.7×10^{-3} (27%)*	*2.2×10^{-3} (74%)*	*4.0×10^{-3} (97%)*	*0.01 (28%)*	*3.8×10^{-3} (100%)*
Fe	*1.0 (10%)*	*0.3 (28%)*	*1.3 (90%)*	*2.6 (21%)*	*1.2 (98%)*
Si	*0.4 (6%)*	*0.1 (17%)*	*0.7 (87%)*	*1.2 (17%)*	*0.7 (97%)*
Mg	*0.3 (5%)*	*0.06 (11%)*	*0.6 (85%)*	*1.0 (16%)*	*0.6 (97%)*
Ca	*7.0×10^{-3} (1%)*	*1.8×10^{-4} (0.4%)*	*0.05 (70%)*	*0.06 (10%)*	*0.06 (93%)*
Al	*3.7×10^{-3} (0.8%)*	*5.5×10^{-5} (0.1%)*	*0.04 (59%)*	*0.04 (7%)*	*0.05 (88%)*
Ti	*3.6×10^{-5}(2%)*	*1.7×10^{-6} (0.8%)*	*2.5×10^{-4} (84%)*	*2.9×10^{-4} (11%)*	*3.0×10^{-4} (100%)*
O	*0.9 (7%)*	*0.2 (18%)*	*1.6 (90%)*	*2.7 (17%)*	*1.7 (100%)*
Total	**34.6**	**3.7**	**5.0**	**43.3**	**4.5**
$\%Na|_{87.5\ km}$ [††]	86%	46%	99%	**87%**	100%
$\%Fe|_{87.5\ km}$ [††]	52%	0.9%	92%	**65%**	98%

[†] Spherules in the size range $50\ \mu m \leq D \leq 700\ \mu m$ corresponding to measurements at South Pole [*Taylor et al.*, 1998].

[††] Fraction of Na and Fe ablated above 87.5 km.

A significant result of the present study is that the JFC-Planck particles contribute (80 ± 17)% of the mass input to the terrestrial atmosphere. This is consistent with the conclusions of *Nesvorný et al.* [2010], *Yang and Ishiguro* [2015], and *Rowan-Robinson and May* [2013] (see Section 4.1). In contrast, although the JFC-IRAS is still the dominant source, its contribution is estimated to be only (57 ± 19)%. It should be noted, as pointed out by *Yang and Ishiguro* [2015], that the analysis of Antarctic micrometeorites and cosmic dust particles collected in the stratosphere has found that less than 50% are "chondritic porous" particles, which are taken to be of cometary origin [*Noguchi et al.*, 2015]. In contrast, the present study indicates ZCM-Planck that for 63% of un-melted micrometeorites and cosmic spherules with diameters > 50 μm (the lower limit for measurements) should be cometary. This may indicate that some of the "chondritic smooth" particles, assumed to be asteroidal, are wrongly assigned. Because the JFC-Planck particle mass distribution peaks around 0.01 μg (Figure 4.2a) there is only significant ablation of the high-mass tail of the distribution, so that 67% of the TIM does not melt during entry.

Table 4.2. *Global mass input from the four cosmic dust sources for the JFC-IRAS fit. Elemental ablation inputs are italicized; the percentages in parentheses show the fraction of each element that ablates from its total atmospheric input from each source. Reproduced from Carrillo-Sánchez et al. [2016].*

Mass flux	**JFC (t d^{-1})**	**AST (t d^{-1})**	**LPC=HTC (t d^{-1})**	**Total (t d^{-1})**	**LPC=OCC (t d^{-1})**
Unmelted micrometeorites	8.5	1.0	0.4	9.9	0.07
Cosmic spherules	3.1	1.4	0.6	5.1	0.1
Ablated atoms	2.1	0.5	6.4	9.0	6.5
Cosmic spherules †	2.8	1.4	0.4	4.6	0.08
Unmelted ($D > 50\ \mu m$)	2.4	0.9	0.3	3.6	0.04
Na	*0.1 (45%)*	*0.02 (75%)*	*0.1 (99%)*	*0.2 (48%)*	*0.1 (100%)*
K	*4.9×10^{-3} (44%)*	*1.8×10^{-3} (74%)*	*5.9×10^{-3} (97%)*	*0.01 (51%)*	*5.6×10^{-3} (100%)*
Fe	*0.8 (20%)*	*0.2 (28%)*	*1.9 (90%)*	*2.9 (43%)*	*1.9 (98%)*
Si	*0.3 (13%)*	*0.08 (16%)*	*1.0 (87%)*	*1.4 (37%)*	*1.0 (97%)*
Mg	*0.2 (11%)*	*0.05 (11%)*	*0.9 (85%)*	*1.1 (31%)*	*0.9 (97%)*
Ca	*6.2×10^{-3} (3%)*	*1.4×10^{-4} (0.4%)*	*0.07 (70%)*	*0.08 (27%)*	*0.08 (93%)*
Al	*3.4×10^{-3} (2%)*	*4.3×10^{-5} (0.1%)*	*0.06 (59%)*	*0.06 (19%)*	*0.08 (88%)*
Ti	*3.2×10^{-5}(4%)*	*1.4×10^{-6} (0.8%)*	*3.7×10^{-4} (84%)*	*4.0×10^{-4} (28%)*	*4.5×10^{-4} (100%)*
O	*0.7 (14%)*	*0.2 (18%)*	*2.4 (90%)*	*3.3 (38%)*	*2.4 (99%)*
Total	**13.7**	**2.9**	**7.4**	**24.0**	**6.7**
$\%Na\vert_{87.5\ km}$††	76%	46%	99%	**86%**	100%
$\%Fe\vert_{87.5\ km}$††	39%	0.9%	92%	**70%**	98%

† Spherules in the size range $50\ \mu m \leq D \leq 700\ \mu m$ corresponding to measurements at South Pole [*Taylor et al.*, 1998].

††Fraction of Na and Fe ablated above 87.5 km.

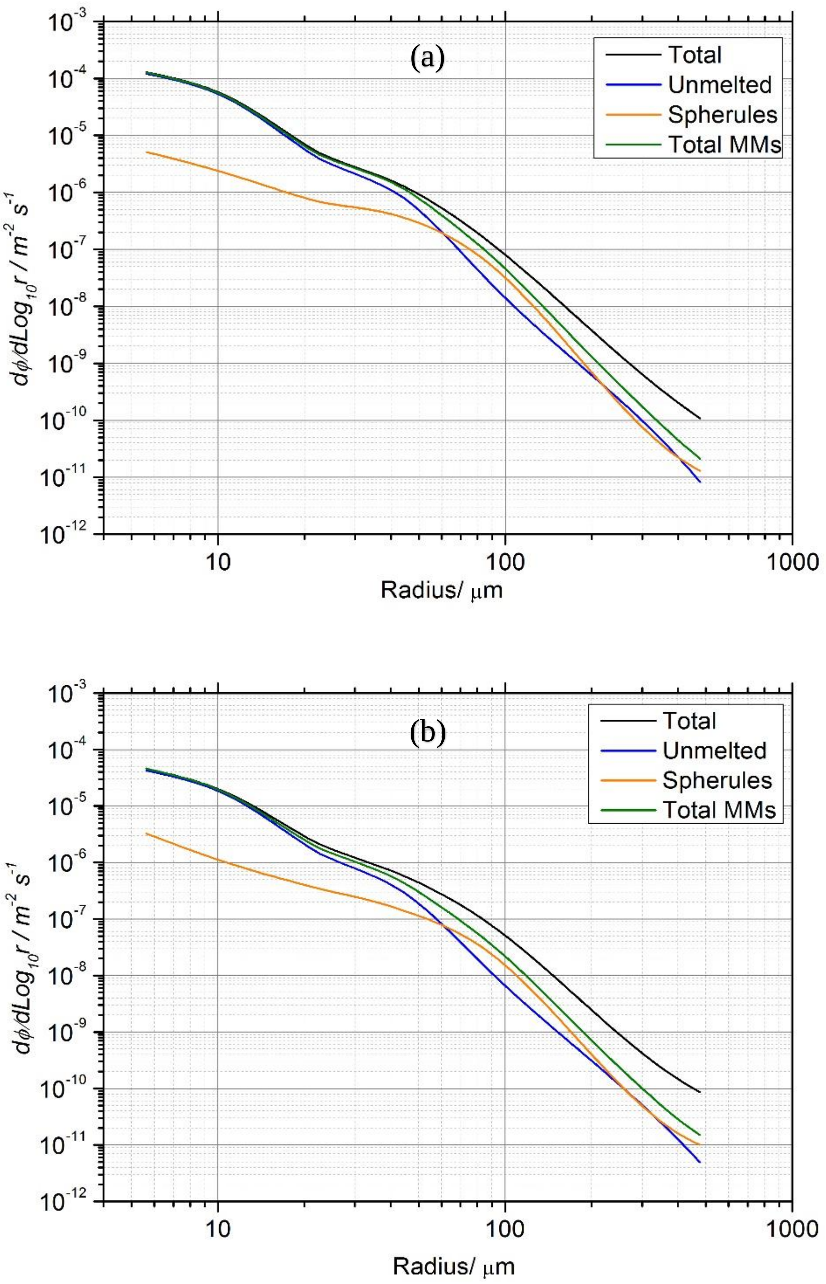

Figure 4.6. *Differential flux of cosmic dust particles against the radius for the (a) Planck and (b) IRAS distributions. The total flux made up of particles from Jupiter family comets, the asteroid belt, and Halley type comets (black line), particles which form cosmic spherules (orange), and unmelted micrometeorites (blue).*

Tables 4.1 and 4.2 show that there are striking differences in the ablation efficiencies of individual elements for the different dust sources. In the case of Na, the ablation efficiency from JFC-Planck particles is 28%, compared with 99% for LPC particles. For the highly refractory elements, the differences are even more extreme: for Ca, the ablation efficiency is 1%, compared with 70% for the LPCs. Note that even though the average velocity of ASTs is lower than JFCs (Figure 4.2a), the ablation efficiencies are higher for all the elements apart from the most refractory (Ca, Al, Ti) because the particle mass distribution is shifted to larger particles which tend to reach higher temperatures during atmospheric entry.

Figure 4.6 illustrates the differential flux of particles for ZCM-Planck and ZCM-IRAS. The gradual fall-off in the differential flux is expected because solar radiation pressure ejects very small particles from the Solar System [*Nesvorný et al.*, 2010]. Spherules become the major form of residual meteoroids for R > 60 μm for both, ZCM-Planck and ZCM-IRAS, although more of these larger particles enter at high enough speeds to ablate completely.

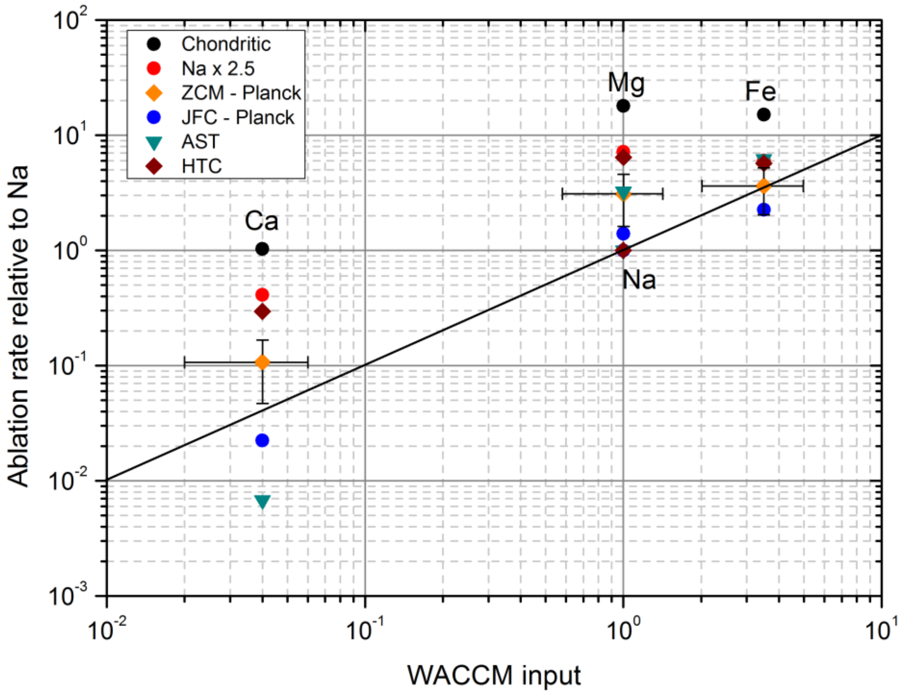

Figure 4.7. *Ablation rates for Ca, Fe and Mg relative to Na produced for the ZCM-Planck, and all cosmic dust populations given the Planck distribution. The abscissa represents the relative input rates required to model the global metal atoms in the MLT. The solid line is the 1:1 correlation line. The horizontal error bars show the uncertainty in the measured ratios used in WACCM, whereas the vertical error bars correspond to the uncertainties associated to the estimate of the contribution of each dust source. The black points show the relative CI chondritic compositions, and the red points are the CI composition with a Na enrichment factor of 2.5. Reproduced from Carrillo-Sánchez et al. [2016].*

Figure 4.7 correlates the ablation efficiencies of Fe, Mg and Ca relative to Na (data taken from Table 4.1) against the relative ablation rates of these elements required to produce good agreement between WACCM and lidar and satellite observations of the mesospheric metal atom layers [*Carrillo-Sánchez et al.*, 2015]. The black circles show the CI chondritic ratios [*Asplund et al.*, 2009], and the red circles represent the ratios with a Na enrichment factor of 2.5. These points represent the case where there is no differential ablation i.e. complete ablation of all elements, and are well above the line of 1:1 correspondence. However, when differential ablation is included, ZCM-Planck (orange diamonds) produces much improved correlation with the modeled observations. Figure 4.7 also shows the differential ablation ratios for the JFC, AST and HTC particles in the ZCM-Planck model, where the HTCs essentially ablate in their chondritic ratios for all metals. In contrast, the ASTs exhibit such a high degree of differential ablation for the refractory elements that the Ca:Na ratio is well below the line of 1:1 correspondence. The corresponding ablation rates of Fe, Mg, and Ca relative to Na for ZCM-IRAS exhibit a similar behavior to that shown in Figure 4.7.

4.4. SUMMARY OF THE CHAPTER

In this chapter the absolute inputs of cosmic dust particles from four different sources – JFCs, ASTs, HTCs and OCCs – to the Earth's atmosphere were constrained using the measured vertical Na and Fe fluxes above 87.5 km, and the accretion rate of cosmic spherules at South Pole. Because HTCs and OCCs are characterized by high entry velocities, it is not possible to distinguish between them in terms of these constraints. Taking a JFC mass distribution determined recently from observations of the zodiacal light by the Planck satellite, JFCs are shown to contribute (80 ± 17)% of the total input mass of 43 ± 14 t d^{-1}, assuming a Na to Fe enrichment of 2.5 which is close to the average enrichment measured in cometary particles. Finally, the differential ablation of Ca and Fe, with respect to Na, is now large enough to model the respective metal atom layers in the upper mesosphere.

CHAPTER 5: METEORIC ABLATION IN THE ATMOSPHERES OF VENUS, MARS, AND TITAN

5.1. INTRODUCTION

As discussed in Chapters 2 and 4, the ablation of a continuous flux of extraterrestrial material in the atmosphere gives rise to permanent layers of free neutral and ionized metal atoms. Mg, Fe, Na and Si are the most abundant metallic species in the atmosphere, whereas other species such as K, Al and Ca are present at concentrations at least one order of magnitude lower (see Figures 2.11 and 4.4). Meteor showers may increase the concentration of these metals by a factor of 2-3, although this fact has been hard to verify because meteor showers are normally well below the activity of the sporadic backround [*Grebowsky et al.*, 1998; *Kopp*, 1997]. As discussed in Chapter 1, the radio occultation technique has been used to sound planetary atmospheres since the 1960s. These measurements have shown that the daytime ionosphere exhibits a major peak produced by solar radiation and photoelectrons (see Figure 1.10), and below this main peak one or more secondary peaks can occur, which may be caused by meteoric ablation.

Pioneer Venus measured the electron density profile in the nightside ionosphere of Venus [*Kliore et al.*, 1979] which shows low altitude layers below the main ionospheric layer (see Figure 1.10, top panel). The main peak is located at an altitude of 142.2 ± 4.1 km, with a peak electron density varying between 23×10^{3} and 40×10^{3} cm^{-3}. Below this main peak, there is an intermittent double peak around 120 km, which is close to the ablation peak of meteoric ablation (see below), although other phenomena such as direct ionization by electron precipitation or protons in the nightside could explain the occurrence of this layer [*Kliore et al.*, 1979; *Molina-Cuberos et al.*, 2008].

The atmosphere of Mars has been sounded in more detail than other planets. *Fjeldbo et al.* [1966] analyzed the data provided by Mariner IV and found that the daytime ionosphere is characterized by a main layer produced by solar radiation at an altitude of 140 km with a number density of the order of $\sim10^{4}$ cm^{-3}. Another two layers were found below this main peak. *Fjeldbo et al.* [1966] reported a secondary layer at around 100 km with a density approximately one order of magnitude lower than the main peak, and *Savich et al.* [1976] found a secondary layer at ~80 km during nighttime using the Soviet spacecraft Mars 4 and Mars 5. Some years later, these layers were confirmed by Mars Express (see Figure 1.10, bottom panel) that found a sporadic layer between 65 and 110 km in altitude in 10 of 120 ionospheric electron concentration profiles [*Patzold et al.*, 2005]. More recently, metallic ion layers produced by the meteor storm event following the close encounter between Comet Siding Spring (C/2013 A1) and Mars were identified by the Imaging Ultraviolet Spectrograph (IUVS) aboard the Mars Atmosphere and Volatile Evolution (MAVEN) spacecraft [*Schneider et al.*, 2015].

Finally, Titan is the only moon in the solar system with a thick atmosphere. *Bird et al.* [1997] concluded that the main ionospheric peak was located at an altitude of 1180 ± 150 km using the Voyager I fly-by observations. However, no evidence of a lower secondary peak below the main ionospheric layer has been found, although this has been predicted by some theoretical models of Titan's atmosphere [*English et al.*, 1996; *Molina-Cuberos et al.*, 2001].

In this chapter, the process of meteoric ablation in these three solar system bodies is examined. CABMOD 2 [*Vondrak et al.*, 2008] is combined with the ZCM [*Nesvorný et al.*, 2010; *Nesvorný et al.*, 2011] extended to Mars and Venus and constrained by the IRAS observations, to model: 1. The meteoroid metal layers deposited in the atmospheres of each planet; 2. The global mass influx accreted by Mars and Venus, and 3. What portion of the TIM ablates completely or remains unmelted. In the case of Venus, the ablation process and the distribution of metal layers is studied for both the noon and midnight sides because of the significant differences that are caused by the slow rotational period of the planet [*Hedin et al.*, 1983; *Keating et al.*, 1985]. Finally, the ablation of cosmic dust in Titan's atmosphere is examined. Owing to the lack of knowledge regarding the meteoroid distribution for the outer solar system bodies, where the major contributor of IDPs is the Edgeworth-Kuiper Belt (EKB) [*Landgraf et al.*, 2002], is not possible to model a complete MIF for Titan's atmosphere. Consequently, the present work explores if the ablation process is relevant in Titan's atmosphere, since unablated particles with small sizes (R < 10 μm) may contribute significantly to the available surface area for heterogeneous chemistry, whereas larger particles sediment very rapidly through Titan´s atmosphere [*Frankland et al.*, 2016].

5.2. ABLATION MODELLING OF THE ATMOSPHERES OF VENUS, MARS, AND TITAN

5.2.1. Meteoric Ablation in the Martian Atmosphere.

In order to model Mars' atmosphere, CABMOD uses the Mars Climate Database [*Lewis et al.*, 1999] (http://www-mars.lmd.jussieu.fr/mcd_python/). Figure 5.1 (left panel) shows the atmospheric density profiles for Earth – conditions of March 40ºN (http://ccmc.gsfc.nasa.gov/modelweb/models/msis_vitmo.php) – and Mars at two different latitudes in winter, 40ºN and 80ºN. Mars' atmosphere is markedly less dense than the terrestrial atmosphere below 100 km, so that meteoric ablation occurs at a lower altitude on Mars. Moreover, it is noticeable that the atmospheric density is significantly lower at higher latitudes.

Figure 5.1 (right panel) shows height profiles of the main atmospheric constituents in Mars' atmosphere, which have been used in CABMOD. Note that the main constituent is CO_2 between 50 and 250 km. Atomic O is more abundant than O_2 above 75 km, although its concentration is about $\sim 2\times10^{10}$ cm^{-3}, more than one order of magnitude lower than the concentration of O in the terrestrial atmosphere at 100 km, which makes the contribution of metallic ions to the Mars third ion layer around 80 km seem less likely because O plays an important role in reducing metal oxide ions back to atomic ions (e.g. $MgO^+ + O \rightarrow Mg^+ + O_2$, although the analogous reaction with CO is also important because of the relatively high CO concentrations (Figure 5.1) [*Whalley and Plane*, 2010].

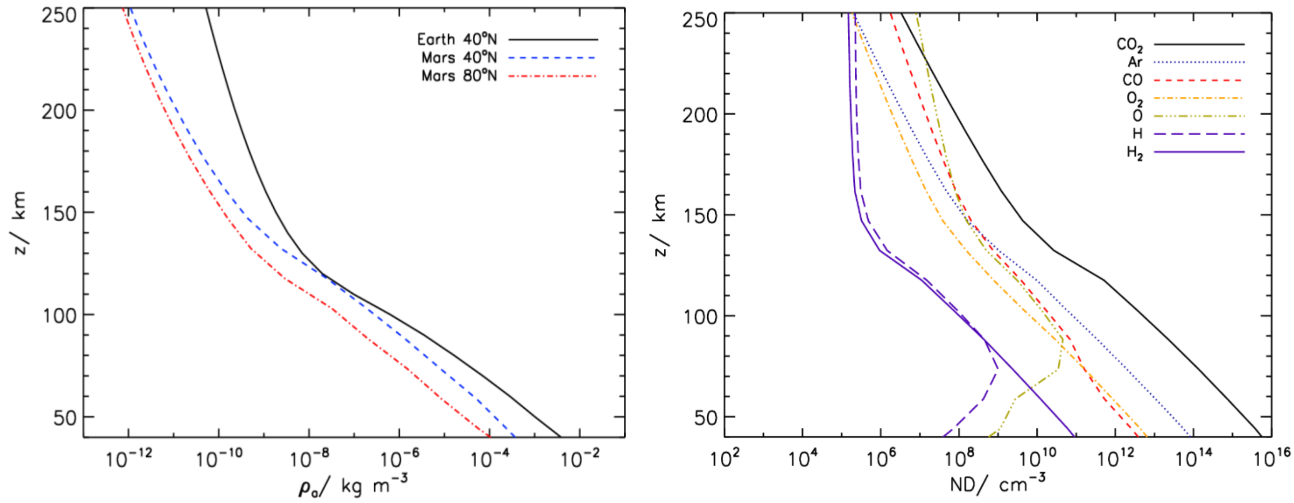

***Figure 5.1**. Left panel: atmospheric density profiles for Earth (40ºN) (http://ccmc.gsfc.nasa.gov/modelweb/models/msis_vitmo.php) and Mars winter (40ºN and 80ºN). Right panel: vertical profiles of main compounds in the Martian atmosphere which have been used in CABMOD. The Martian atmosphere has been modelled in CABMOD using the Mars Climate Database (http://www-mars.lmd.jussieu.fr/mcd_python/).*

Figure 5.2 (left panel) compares the ablation profiles for a 5 µg meteoroid that enters into the atmospheres of Earth and Mars with an entry velocity of 20 km s^{-1} and a zenith angle of 35º. The latitude, 40°N, is the same for both planets. These results reveal that the ablation process at Mars occurs roughly 10 km lower than Earth. The ablation peak for the more volatile elements, Na and K, is located at 94 km in Mars, compared with ~100 km in the case of the Earth. Figure 5.2 (right panel) shows the effect of the latitude. The ablation peak of different metals at 80ºN are located 15 km lower than at 40ºN.

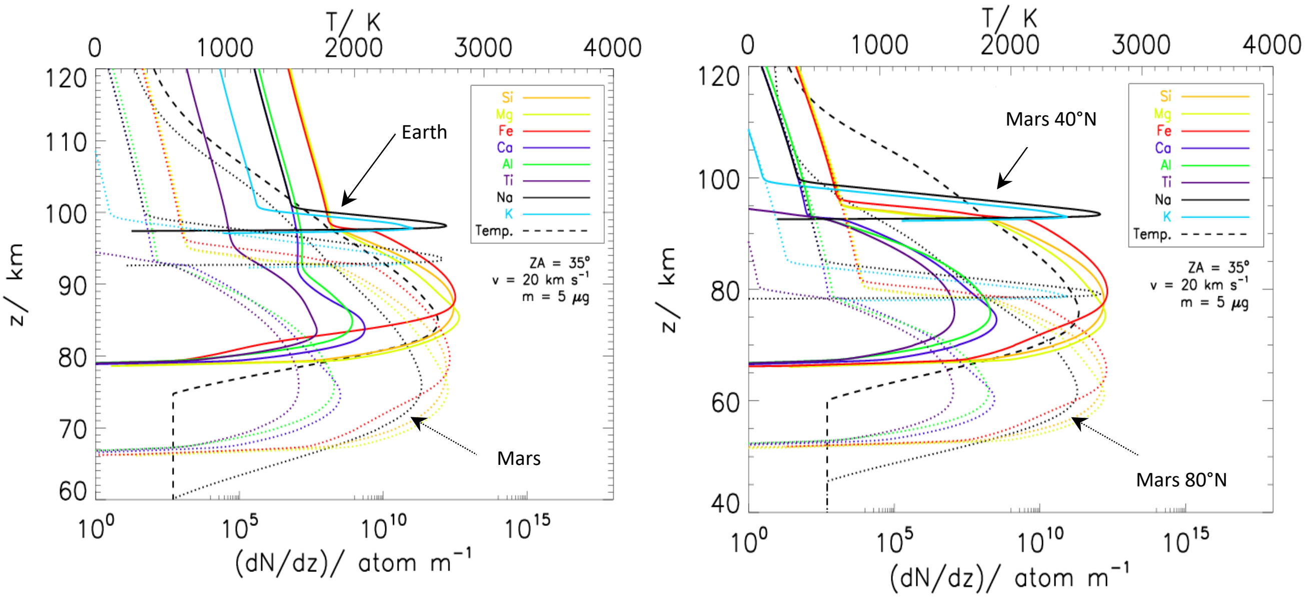

***Figure 5.2**. Ablation profiles for a 5 μg meteoroid entering with an entry velocity v =20 km s^{-1} and a zenith angle ZA = 35º. Left panel: comparison between Earth (solid lines) and Mars (dotted lines) for the same latitude (40ºN). Right panel: ablation rates profiles in the Martian atmosphere at two different latitudes, 40ºN (solid lines) and 80ºN (dotted lines).*

5.2.2. Meteoric Ablation in Venus' Atmosphere.

Several authors have reported numerical models of the chemical and physical structure of Venus' atmosphere at different latitudes and altitudes based on measurements of different spacecraft such as Venera 11 and 12 [*Keating et al.*, 1985], Pioneer Venus Orbiter [*Hedin et al.*, 1983], and Venus Express [*Peter et al.*, 2014]. *Hedin et al.* [1983] used the Pioneer Venus Orbiter Neutral Mass Spectrometer (ONMS) measurements and provided a global model of the temperature and composition in the thermosphere above 100 km by using spherical harmonics expansion to emphasize solar angle variations. Figure 5.3 (left panel) shows the vertical density profiles for the midnight side and the noon side at the equator reported by *Hedin et al.* [1983] and *Keating et al.* [1985]. Venus' atmosphere is significantly denser than the Earth's atmosphere below 150 km. The temperature and eddy diffusion profiles are shown in right panel of Figure 5.3. The vertical eddy diffusion coefficient, k_{zz}, as a function of the altitude is estimated according to the following expression [*von Zahn et al.*, 1979; *Yung and DeMore*, 1982]:

$$k_{zz}(z) = \frac{2\times10^{13}}{\sqrt{M}} \qquad [cm^2\, s^{-1}] \tag*{[5.1]}$$

where *M* is number density of the atmosphere. Equation [5.1] is derived empirically using the Pioneer Venus mass spectrometer data. Figure 5.4 shows the vertical profiles for the different chemical species [*Hedin et al.*, 1983] where CO_2 is the most abundant compound below 140 km (noon side) and 150 km (night side).

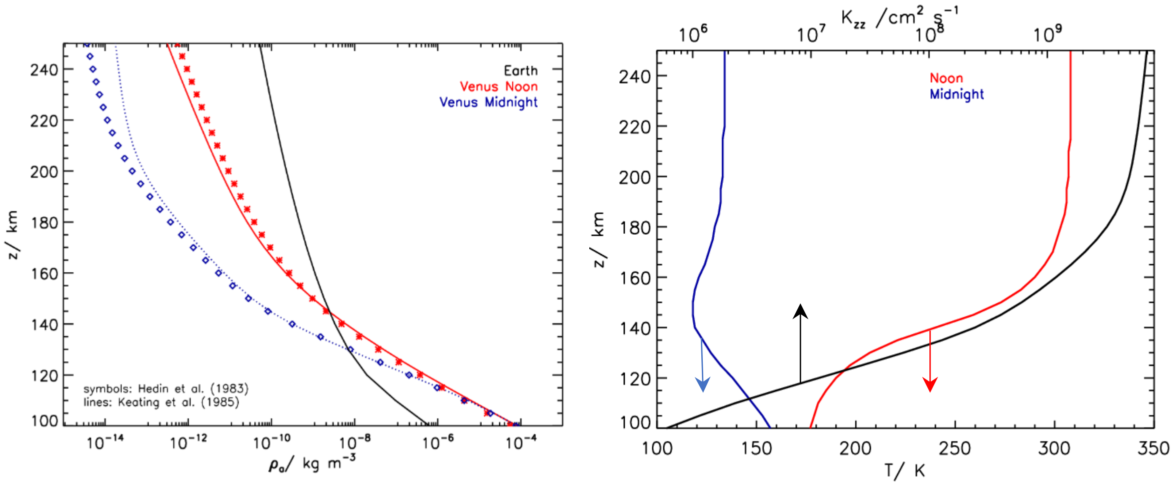

Figure 5.3*. Left panel: comparison between atmospheric density profiles for midnight (blue) and noon (red) sides reported by Hedin et al. [1983] (dots) and Keating et al. [1985] (solid line). Right panel: vertical profiles of temperature for midnight (blue) and noon (red) sides, and eddy diffusion (black) adapted from Yung and DeMore [1982].*

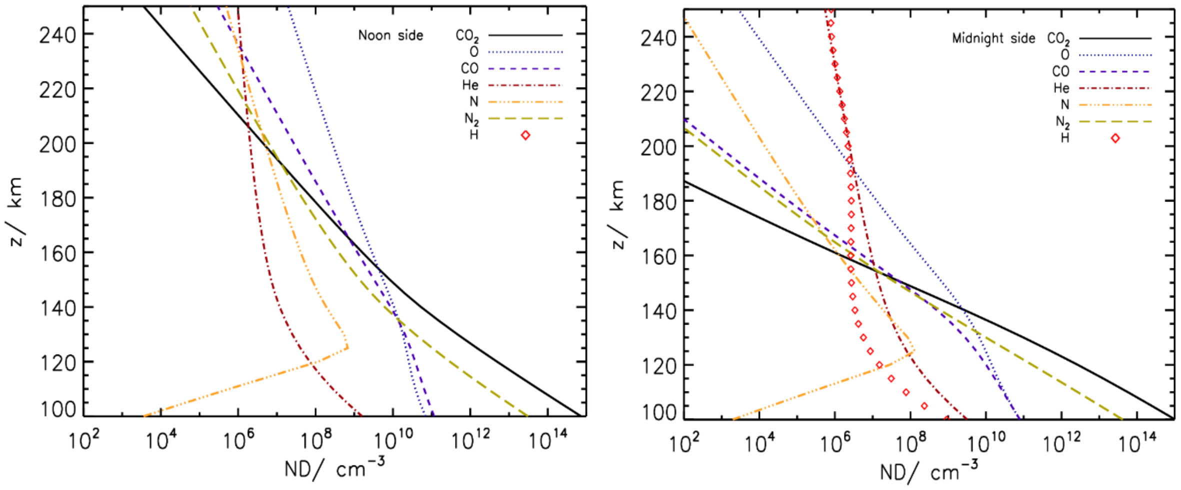

Figure 5.4*. Vertical profiles of chemical species in the atmosphere of Venus for the noon side (left panel) and the nighttime (right panel). Adapted from Hedin et al. [1983].*

The ablation profiles of two quite different particles in Venus' atmosphere are shown in Figure 5.5. There are two important details to note: 1. The ablation occurs at higher altitudes than the Earth, and 2. As a consequence of the asymmetry between the noon and midnight sides, meteoroids ablate higher in the day side. For example, for a mass of 1 µg and an entry speed of 18 km s^{-1}, the difference in altitude for alkali elements between the noon side and the midnight side is only 1 km, but this difference increases to more than 3 km for of 10^{3} µg meteoroid with an input velocity of 55 km s^{-1}.

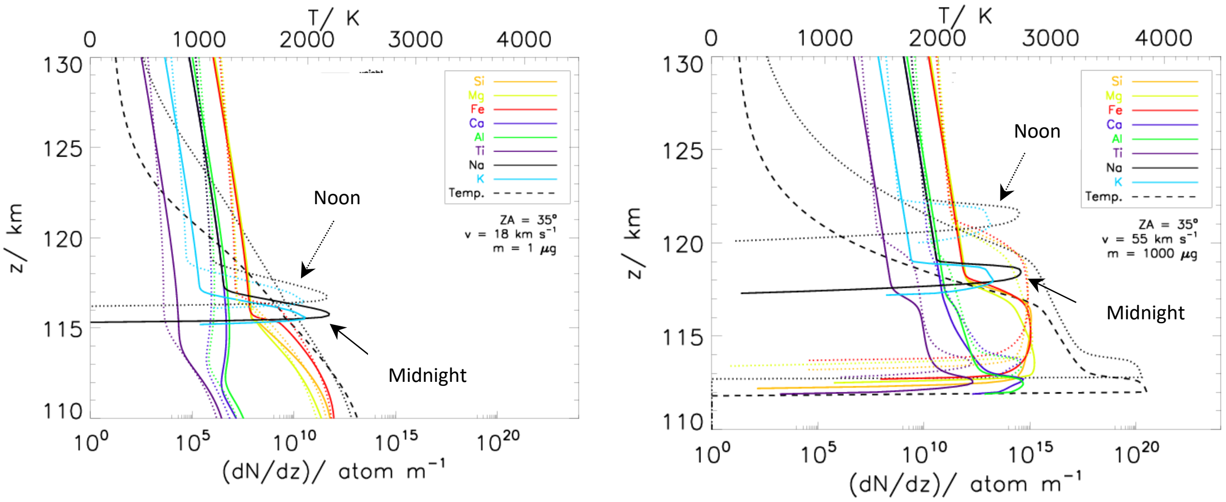

***Figure 5.5**. Differential ablation profiles in the Venusian atmosphere for the noon (dotted line) and midnight (solid lines) sides for two different particles: 1 µg mass and an entry velocity of 18 km s^{-1} (left panel), and 1 mg mass and an entry velocity of 55 km s^{-1} (right panel).*

5.2.3. Meteoric Ablation in Titan's Atmosphere.

Yelle et al. [1997] reported a model for Titan's atmospheric structure that was used in the design and analysis of the Huygens Probe. This model is based on observations made by three different instruments aboard the Voyager 1 spacecraft: Radio-Science Subsystem (RSS), Infrared Interferometer Spectrometer and Radiometer (IRIS), and Ultraviolet Spectrometer (UVS). Figure 5.6 (left panel) shows the vertical profile for atmospheric density according to this model. For this study, the recommended concentrations of CH_4 3%, Ar 2%, and N_2 95% between 1500 km and the surface of Titan are used (Figure 5.6, right panel). More recently, the Cassini-Huygens Atmospheric Structure Investigation (HASI) has collected a large quantity of atmospheric data that may be used to provide a new empirical model of Titan's atmosphere extending from the surface to the exobase [Waite et al., 2013], which is in remarkably good agreement with the earlier model of *Yelle et al.* [1997].

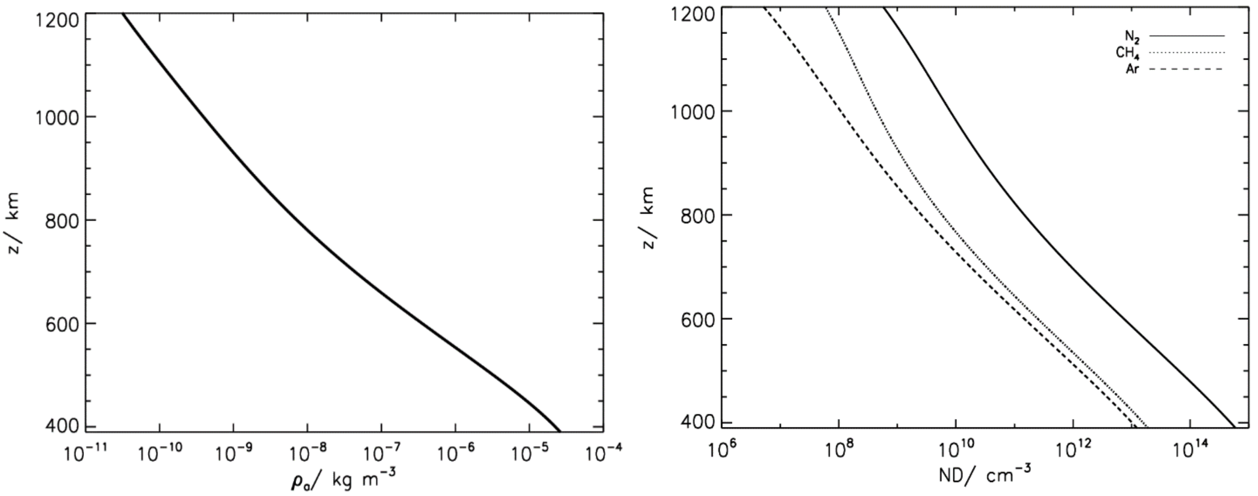

Figure 5.6. *Vertical profiles for atmospheric density (left) and chemical compounds (right) in the Titan atmosphere. Adapted from Yelle et al. [1997].*

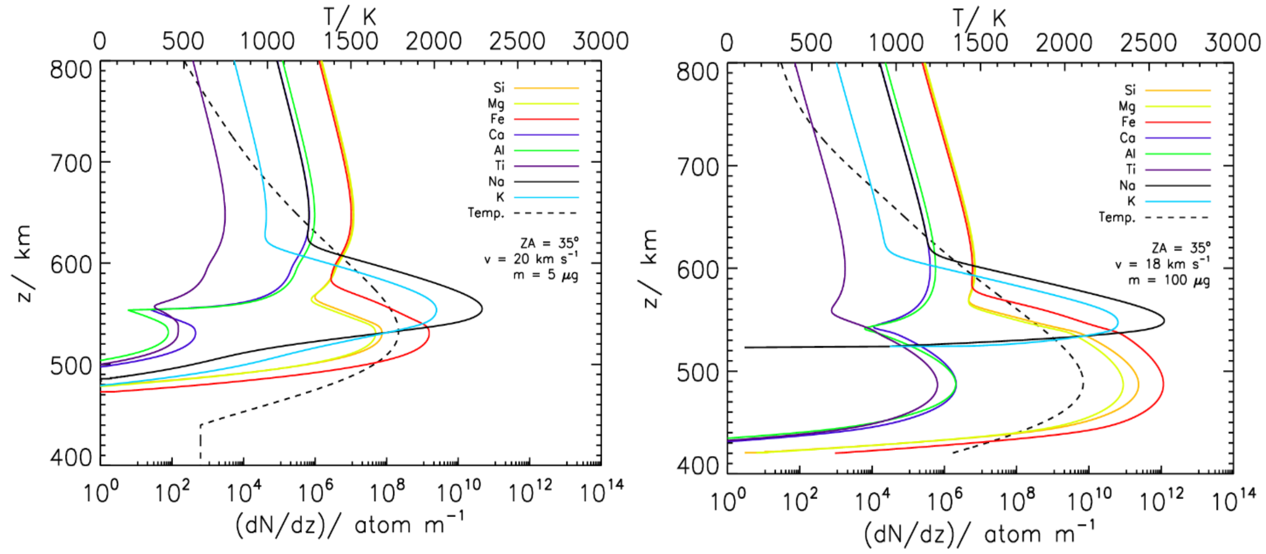

Figure 5.7. *Differential ablation profiles in the Titan's atmosphere for two different meteoroids: 5 µg mass and 20 km s^{-1} (left), and 100 µg mass with an entry velocity of 18 km s^{-1} (right).*

Figure 5.7 illustrates the differential ablation profiles in the atmosphere of Titan for two different particles: 5 µg mass and an entry velocity of 20 km s^{-1}, and 100 µg and an entry velocity of 18 km s^{-1}. Ablation is predicted to occur over a broad range of altitudes between 400 and 600 km. *Ip* [1990] studied the ablation process of two different types of particles in Titan's upper atmosphere. First, rocky meteoroids that are the main source of metals such as Na, Fe and Mg, and which could re-condense into small particles that could act as aerosol nucleation centers, as at the Earth. Second, meteoroids from stray bodies with perihelion larger than 3 AU which are rich in volatile ices (H_2O, CO_2, and

CO) and might act as oxygen-bearing sources. For stony meteoroids, *Ip* [1990] concluded that the ablation zones for IDPs of 100 µm radius (~10 µg) and a velocity of 20 km s^{-1} are between 450 and 600 km of altitude, which is in good accord with the profiles shown in Figure 5.7.

5.3. Sources of Cosmic Dust in Mars' Atmosphere

5.3.1. The Zodiacal Cloud Model applied to Mars' Atmosphere.

The ZCM can be extended to other bodies in the inner solar system (<5 AU) [*Nesvorný et al.*, 2010; *Nesvorný et al.*, 2011]. The particle velocity, entry angle and mass distributions are sampled using the procedure discussed in Section 2.3. Figures 5.8a and 5.8b show the entry velocity distributions in Mars' atmosphere of the different populations modelled by the ZCM. The average entry velocities are 10.8 km s^{-1} and 6.5 km s^{-1} for the JFCs and ASTs, respectively, because most of these particles are in prograde orbits.

Figure 5.8b illustrates that the entry velocity of HTC meteoroids depends on the mass range. Similarly to the velocity distribution shown in Figure 4.3b for HTCs particles entering Earth's atmosphere, for masses ≤ 1 µg the distribution follows a bimodal trend with a dominant peak at 22 km s^{-1} and a secondary maximum at 46 km s^{-1}. For masses > 1 µg there is a single peak at 23 km s^{-1}.

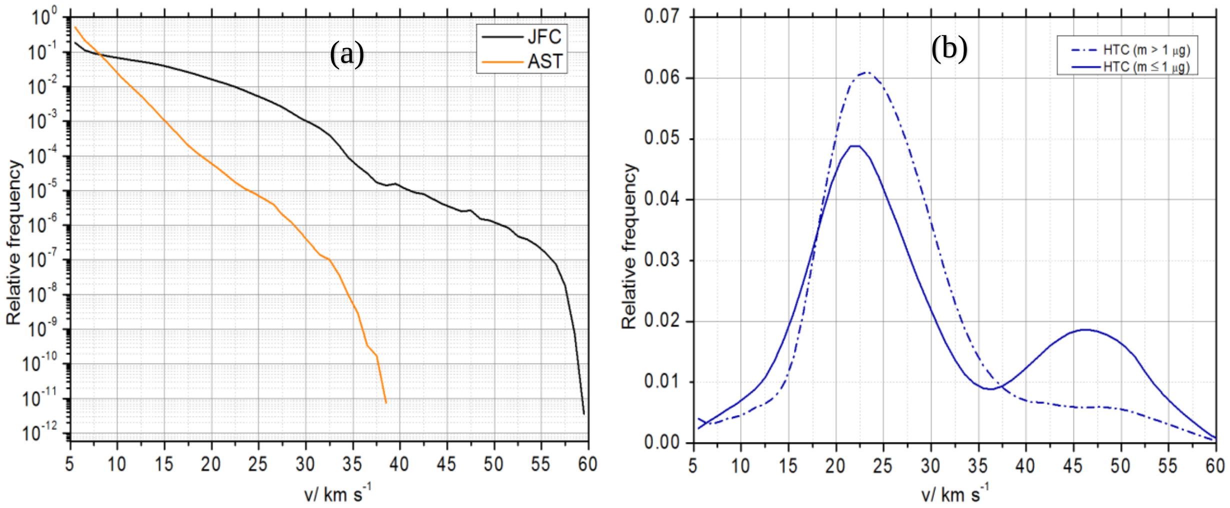

***Figure 5.8**. (a and b) Entry velocity distributions for the JFC (black), AST (orange) and HTC (blue) particles at Mars' atmosphere.*

Figure 5.9a shows the particle mass distribution for the four cosmic dust sources accreted by Mars derived from the IRAS observations. The mass influx of each source has been weighted using the optimal fits determined in Section 4.2.3 for the IRAS distribution, that is, $\alpha = 0.41 \pm 0.17$, $\beta = (2.73 \pm 2.00) \times 10^{-2}$, and $\gamma = (6.78 \pm 1.72) \times 10^{-2}$ [*Carrillo-Sánchez et al.*, 2016]. The largest mass contribution of accreted JFC and HTC particles is is ~1 µg, whereas the AST peak is ~10 µg. According to the IRAS observations, the ZCM estimates a global influx of 2.6 ± 1.3 t d^{-1} assuming the JFCs is the only contributor to the ZC emission. Meanwhile, the total influx of the AST and HTC populations are arbitrarily set to 10 t d^{-1} in the ZCM.

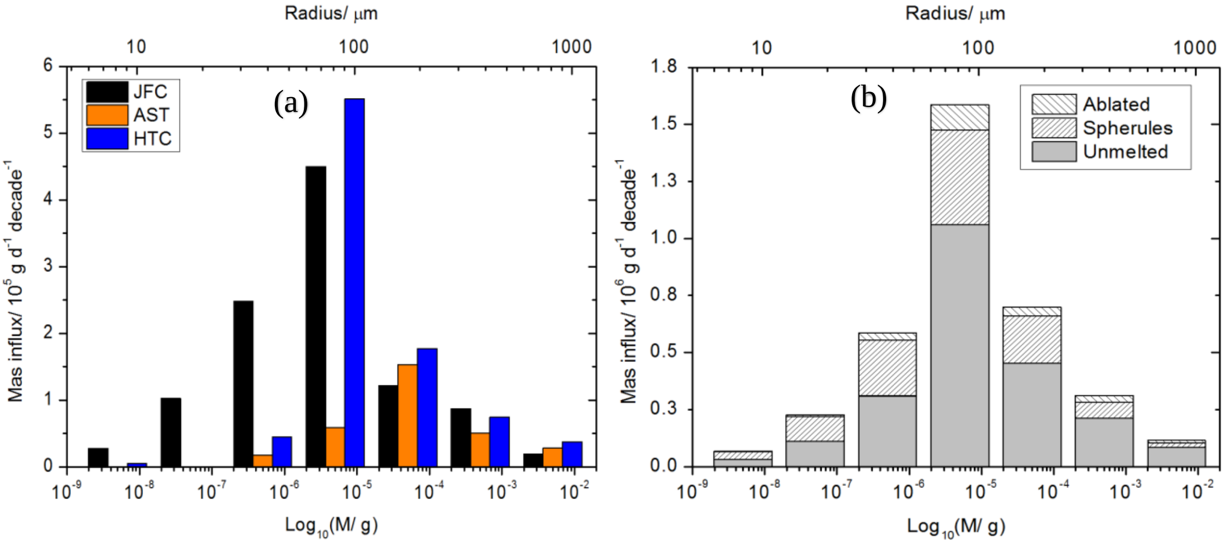

***Figure 5.9**. (a and b) Histogram illustrating the mass input rate into the Martian atmosphere as a function of the particle size. Panel a: mass contribution for JFCs (black), ASTs (orange), and HTCs (blue). Panel b: Histogram of the global mass input showing the fraction ablated, melted and unmelted.*

Figure 5.10 illustrates the injection rate profiles for individual elements from the different sources at Mars equator. These profiles have been weighted using the coefficients estimated for each source [*Carrillo-Sánchez et al.*, 2016]. In all cases the most volatile elements (Na and K) ablate 10-15 km higher than the main constituent elements (Fe, Mg, and Si). The ablation profiles for AST are about 10-20 km below that the corresponding profiles for the JFCs and HTCs. The HTCs represent the opposite extreme. In essence, all elements ablate 20 km lower in the Martian atmosphere than on Earth (see Figure 4.4, bottom panel).

Table 5.1 shows the partitioning of the accreted mass in the Martian atmosphere between micrometeorites, cosmic spherules, and ablated atoms for the JFC, AST, and LPC (=HTC) populations. Table 5.1 also illustrates the ablated mass of each element for the different cosmic dust sources. In terms of the global mass input rate, the contributions of the JFC, AST, and LPC particles are 1.06 ± 0.44 t d^{-1} (47%), 0.32 ± 0.23 t d^{-1} (14%), and 0.89 ± 0.23 t d^{-1} (39%), respectively.

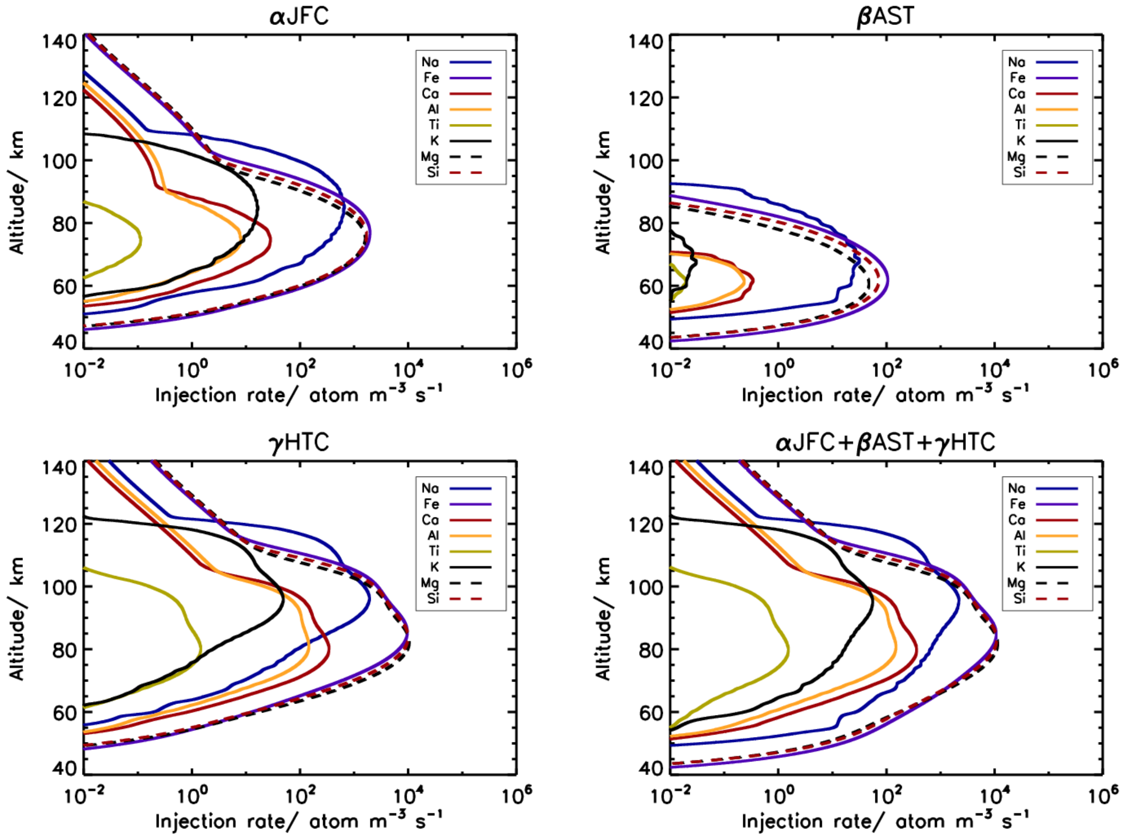

Figure 5.10. *Ablation rate profiles for individual elements in the Martian atmosphere integrated for the JFC, AST, and HTC particle populations.*

Flynn and McKay [1990] considered the gravitational focusing by Mars of cosmic dust from the asteroid belt and found the global mass influx to be 14.2 t d^{-1}, that is, 0.17 times the flux of at Earth. However, in the present study the total influx is estimated to be 2.27 ± 1.24 t d^{-1}. The main reason of this disagreement is that the ZCM is based on the observational evidences that concludes JFCs are the main contributor of cosmic dust to the inner solar system [*Nesvorný et al.*, 2010]. Moreover, *Flynn and McKay* [1990] concluded that the accretion of unmelted meteoritic material into Mars is significantly higher than Earth because the lower mean velocity of the incoming asteroidal particles to the Martian atmosphere. Table 5.1 shows that 48% of the global incoming mass survives as unmelted micrometeorites (41% on Earth for ZCM-IRAS), whilst 35% of the total input ablates. Nonetheless, the result is quite different for the AST population, where 94% of these particles do not reach the melting point compared with 34% in the Earth (see Table 4.2) owing to larger particles decelerating without experiencing significant heating.

Figure 5.9b is a histogram of the global input mass in the Martian atmosphere as a function of the particle size, partitioned into ablated, melted and unmelted mass. The ablation is significant for sizes larger than ~1 µg.

Table 5.1. *Global Mass Input from the four cosmic dust sources at Mars.*

Mass flux	**JFC (t d^{-1})**	**AST (t d^{-1})**	**LPC=HTC (t d^{-1})**	**Total (t d^{-1})**
Unmelted micrometeorites	0.7	0.3	0.06	1.1
Cosmic spherules	0.2	0.02	0.1	0.3
Ablated atoms	0.1	4.9×10^{-3}	0.7	0.8
Na	*6.8×10^{-3} (35%)*	*2.6×10^{-4} (11%)*	*0.02 (97%)*	*0.03 (60%)*
K	*2.9×10^{-4} (34%)*	*4.1×10^{-7} (0.1%)*	*7.0×10^{-4} (96%)*	*9.9×10^{-4} (53%)*
Fe	*0.04 (15%)*	*2.0×10^{-3} (2%)*	*0.2 (87%)*	*0.2 (42%)*
Si	*0.02 (11%)*	*6.6×10^{-4} (1%)*	*0.1 (81%)*	*0.1 (36%)*
Mg	*0.01 (9%)*	*3.6×10^{-4} (0.8%)*	*0.1 (78%)*	*0.1 (33%)*
Ca	*3.3×10^{-4} (2%)*	*3.2×10^{-6} (0.07%)*	*5.5×10^{-3} (46%)*	*5.8×10^{-3} (19%)*
Al	*6.7×10^{-5} (0.5%)*	*1.5×10^{-6} (0.03%)*	*1.79×10^{-3} (15%)*	*1.86×10^{-3} (6%)*
Ti	*1.6×10^{-6} (3%)*	*2.4×10^{-7} (1%)*	*2.9×10^{-5} (54%)*	*3.1×10^{-5} (23%)*
O	*0.04 (11%)*	*1.7×10^{-3} (1%)*	*0.3 (83%)*	*0.3 (38%)*
Total	**1.06**	**0.32**	**0.89**	**2.27**

5.3.2. Observations of the aftermath of the comet Siding Spring meteor shower.

The MAVEN spacecraft entered Mars orbit on 21 September 2014, on a mission to study the behavior of Mars' upper atmosphere and the escape of its constituent gases to space. MAVEN orbits Mars on a 4.5h elliptical orbit, with closest approach to Mars' surface at periapse of 150-200 km [*Jakosky et al.*, 2015; *Schneider et al.*, 2015]. Comet Siding Spring (S/2013 A1) had a close passage by Mars on 19 October 2014, one month after MAVEN was operative. The periodicity of such an encounter has been estimated at once every 10^5 years [*Ye and Hui*, 2014]. The effect of dust on Mars was of particular interest in order to identify transient layers attributed to the meteoric influx [*Withers et al.*, 2008]. Dust ejected from the comet was expected to intercept the planet about 2h after the comet's closest approach [*Schneider et al.*, 2015]. The IUVS spectrograph aboard MAVEN captures spectra of the planet and its atmosphere in the far UV (110-190 nm) and mid-UV (190-340 nm), allows atmospheric emissions from CO_2 and its dissociation and ionization products to be observed [*Schneider et al.*, 2015].

Figure 5.11 compares spectra of Mars' atmosphere 3 h prior and 6 h after the Comet Siding Spring approach, taken during Orbit 114 on 19 October 2014 and Orbit 116 on 20

October 2014, respectively [*Schneider et al.*, 2015]. The spectra exhibit new emissions from Mg^+, Mg, Fe^+, and Fe that were not present before the comet encounter. In the day preceding the encounter, the Mg^+ line was undetectable at < 4% of its post-comet peak value. The presence of Mg^+ and Fe^+ was confirmed by MAVEN's Neutral Gas and Ion Mass Spectrometer (NGMIS) instrument, which detected 10 additional ions [*Benna et al.*, 2015].

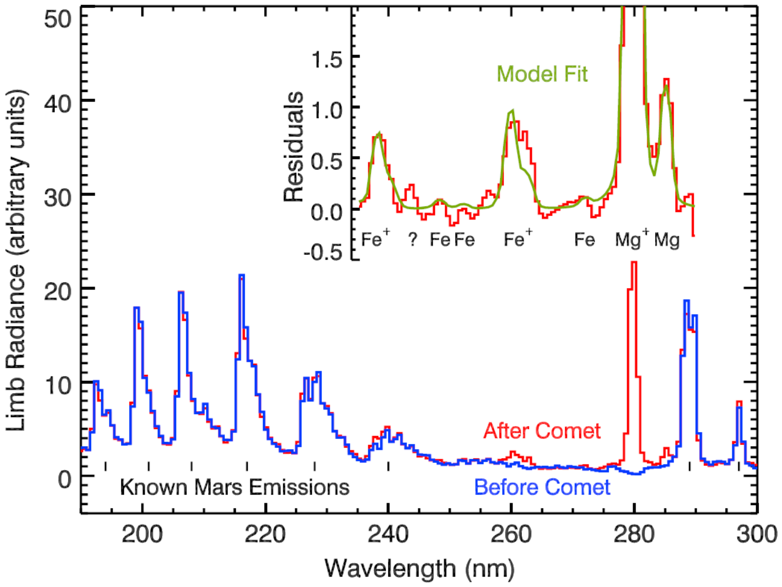

Figure 5.11. *Spectra of Mars' atmosphere immediately before and after the closest approach of the Comet Siding Spring, taken during Orbit 114 on 19 October 2014 at 15:20:00 UTC and Orbit 116 on 20 October 2014 at 00:35:39 UTC. Both 4.6 s spectra were obtained near a tangent altitude of 119 km at approximately 14 h local time and a solar zenith angle near 60º. Numerous emissions from Mg^+, Mg, Fe^+, and Fe are present. Reproduced from Schneider et al. [2015].*

Schneider et al. [2015] used the Atmospheric Ultraviolet Radiance Integrated Code (AURIC) model [*Strickland et al.*, 1999], developed initially for terrestrial use but adapted for use at Mars for IUVS retrievals. The Mg^+ is a doublet, with the stronger line at 279.6 nm twice as optically thick as the weaker line at 280.4 nm. *Schneider et al.* [2015] used the CABMOD model the ablation rates for particles with the Siding Spring entry velocity of 56 km s^{-1}. The deposition profiles of the injected metals are input into a 1-D Mars atmospheric model developed at the University of Leeds, which contains detailed chemistry of magnesium and iron based on laboratory studies of pertinent reaction rate constants including photoionization and charge exchange (see Table 5.2) [*Whalley and Plane*, 2010]. The model contains turbulent eddy diffusion up to the Mars turbopause (~135 km) and the diffusion of the metal ions above.

***Table 5.2.** Rate coefficients for important reactions of Mg and Mg^+ in the Mars' atmosphere (units: bimolecular reactions in cm^3 $molecule^{-1}$ s^{-1}, termolecular reactions in cm^6 $molecule^{-2}$ s^{-1}). Adapted from Whalley and Plane [2010].*

Neutral reactions	
$Mg + O_3 \rightarrow MgO + O_2$	$2.3 \times 10^{-10} \exp(-139\ K/T)$ [a]
$MgO + O \rightarrow Mg + O_2$	$5.8 \times 10^{-10} (T/200\ K)^{1/6}$ [b]
$MgO + CO \rightarrow Mg + CO_2$	1.5e-11$(T/200\ K)^{-0.87}$ [b]
$MgO + O_3 \rightarrow MgO_2 + O_2$	$2.2 \times 10^{-10} \exp(-548\ K/T)$ [a]
$MgO_2 + O \rightarrow MgO + O_2$	$7.9 \times 10^{-11} (T/200\ K)^{1/6}$ [a]
$MgO + O_2 (+ CO_2) \rightarrow OMgO_2 \rightarrow Mg(OH)_2$	$3.8 \times 10^{-29} (T/200\ K)^{-1.59}$ [c] ♣
$MgO + CO_2 (+ CO_2) \rightarrow MgCO_3 \rightarrow Mg(OH)_2$	$5.9 \times 10^{-29} (T/200\ K)^{-0.86}$ [c] ♣
$MgO + H_2O (+ CO_2) \rightarrow Mg(OH)_2$	$1.1 \times 10^{-26} (T/200\ K)^{-1.59}$ [c] ♣
$Mg(OH)_2 + H \rightarrow\rightarrow Mg$	$1 \times 10^{-11} \exp(-600\ K/T)$ [b]
Ion-molecule reactions	
$Mg + O_2^+ \rightarrow Mg^+ + O_2$	1.2×10^{-9} [d]
$Mg^+ + O_3 \rightarrow MgO^+ + O_2$	1.2×10^{-9} [e]
$MgO^+ + O_3 \rightarrow Mg^+ + 2O_2$ $\rightarrow MgO_2^+ + O_2$	3.0×10^{-10} [e] 5.5×10^{-10} [e]
$MgO^+ + O \rightarrow Mg^+ + O$	5.9×10^{-10} [f]
$MgO^+ + CO \rightarrow Mg^+ + CO$	3.2×10^{-10} [g]
$MgO^+ + CO_2 (+ CO_2) \rightarrow MgCO_3^+$	$1.8 \times 10^{-28} (300 / T)^{5.08}$ [h] ♠
$MgO_2^+ + O \rightarrow MgO^+ + O_2$	6.5×10^{-10} [f]
$Mg^+ + CO_2 (+ CO_2) \rightarrow Mg^+.CO_2$	$5.6 \times 10^{-29} (300\ K / T)^{1.59}$ [f] ♠
$Mg^+.CO_2 + O \rightarrow MgO^+ + CO_2$	6.5×10^{-10} [f]
$Mg^+.CO_2 + O_2 \rightarrow MgO_2^+ + CO_2$	2.4×10^{-11} [f]
$Mg.X^+ + e^- \rightarrow Mg + X$ ($X = O, O_2, CO_2$)	$3 \times 10^{-7} (200\ K / T)^{0.5}$ [i]
$MgCO_3^+ + e^- \rightarrow Mg + O + CO_2$ or $MgO + CO_2$	$3 \times 10^{-7} (200\ K / T)^{0.5}$ [i]
$Mg^+ + e^- \rightarrow Mg + h\nu$	$5.0 \times 10^{-12} (200\ K / T)^{0.64}$ [j]

♣ recombination reaction where the rate coefficient measured in N_2 has been multiplied by a factor of 2 to correct for CO_2 as third body. ♠ recombination reaction where the rate coefficient measured in He has been multiplied by a factor of 7.7 to correct for CO_2 as third body. [a] *Plane and Helmer* [1995]; [b] *Plane and Whalley* [2012]; [c] [*Rollason and Plane*, 2001]; [d] *Rutherford et al.* [1971]; [e] *Whalley et al.* [2011]; [f] *Whalley and Plane* [2010]; [g] *Rowe et al.* [1981]; [h] Calculated using RRKM theory; [i] Estimate based on review of dissociative electron recombination [*Florescu-Mitchell and Mitchell*, 2006]; [j] *Badnell* [2006].

Figure 5.12 shows that the 1-D model is able to match the observations of Mg^+ satisfactorily. According to this model, Mg^+ is converted to Mg by forming clusters with CO_2 that then undergoes dissociative recombination with electrons. As a consequence, the modelled column abundance of Mg between 100 and 120 km should reach ~50% that of Mg^+ after about 12 h. However, the observations provide strong evidence that chemical pathways at Mars are significantly different than those in the model, since relatively little Mg was observed [*Schneider et al.*, 2015]. In essence, metals deposited in Mars' atmosphere by Comet Siding Spring will be in the form of neutral compounds (oxides, hydroxides, and carbonates) that then polymerize into meteoric smoke particles [*Saunders and Plane*, 2006], which may survive in the atmosphere for several years.

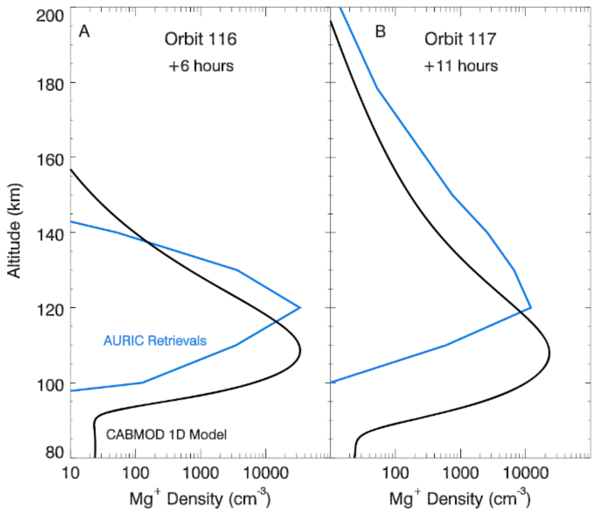

***Figure 5.12**. Retrieved Mg$^+$ density profiles from AURIC compared to CABMOD/1-D University of Leeds model output profiles. Left panel: profile showing the initial injection of Mg$^+$. Right panel: profiles showing the subsequent evolution of Mg$^+$ in the atmosphere. Reproduced from Schneider et al. [2015].*

5.4. SOURCES OF COSMIC DUST IN VENUS' ATMOSPHERE

Figure 5.13 shows the velocity distribution for different cosmic dust populations at Venus' atmosphere. The JFCs and ASTs peak at 10.5 km s^{-1} and the average entry velocities are 14.9 km s^{-1} and 11.4 km s^{-1}, respectively. The lower limit of these velocity distributions, constrained by the escape velocity of the planet, illustrates that most of these particles are in prograde orbits. Figure 5.13b shows that the velocity distribution of HTC particles with masses ≤ 1 µg follows the typical bimodal trend, as at Earth and Mars, with a dominant peak at 29 km s^{-1} and a secondary maximum at 67 km s^{-1}. For masses > 1 µg there is a single peak at 31 km s^{-1}.

Figure 5.14a illustrates the mass distribution for each cosmic dust source weighted with the corresponding coefficients for each population derived from IRAS observations. According to the IRAS observations, the ZCM estimates a global influx of 40 ± 20 tonnes per Earth day assuming the JFCs as the sole contributor to the ZC emission. As on Mars, the largest mass contribution of accreted JFC and HTC particles is from ~1 µg, whereas the AST peak is around 10 µg.

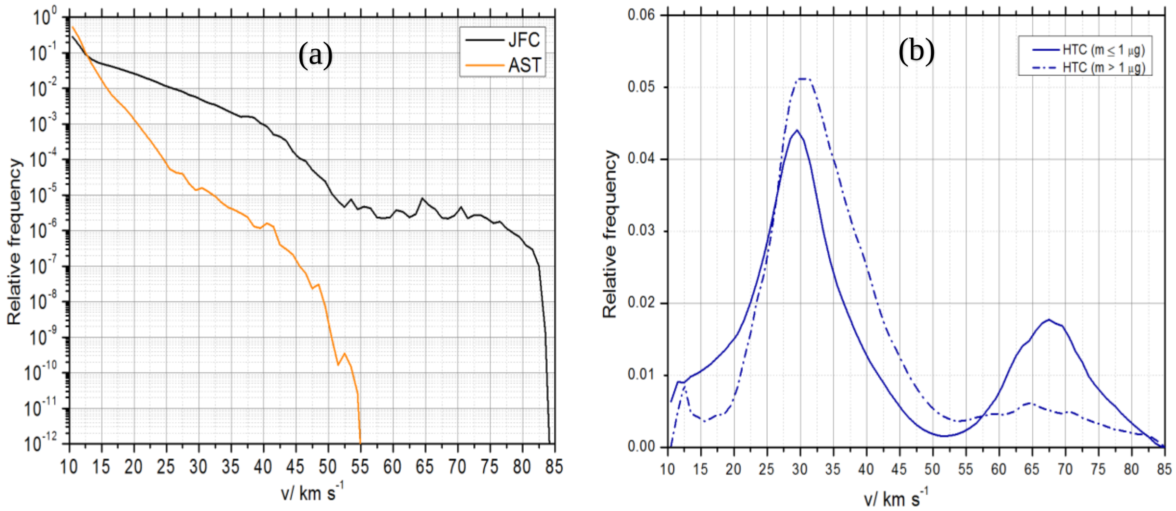

***Figure 5.13**. (a and b) Entry velocity distributions for the JFC (black), AST (orange) and HTC (blue) particles at Venus' atmosphere.*

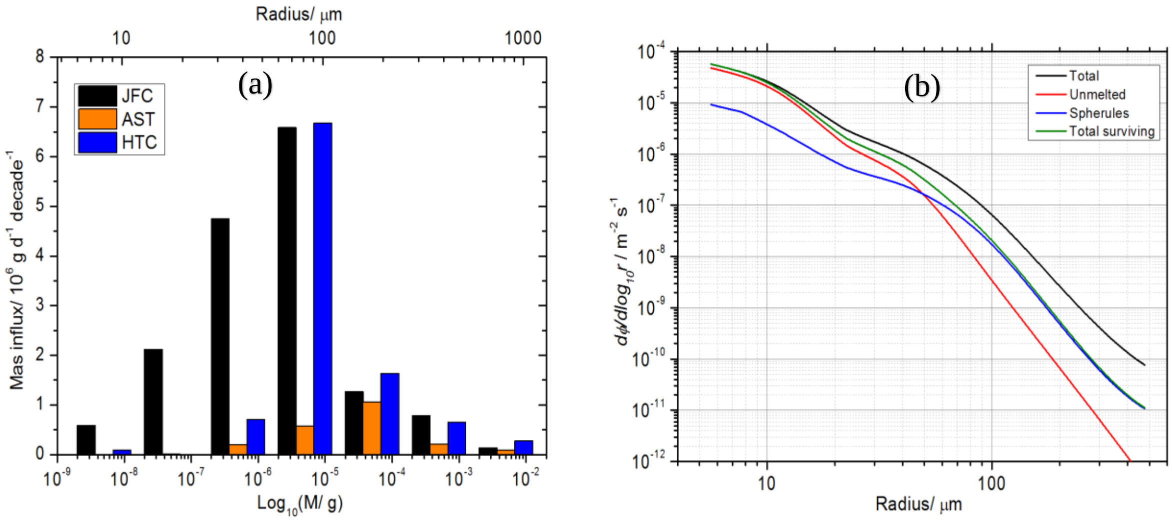

***Figure 5.14**. (a and b) Histogram illustrating the mass input rate into Venus' atmosphere as a function of the particle size. Panel a: mass contribution for JFCs (black), ASTs (orange), and HTCs (blue). Panel b: Differential flux of cosmic dust particles against the radius: the total flux made up of particles from Jupiter family comets, the asteroid belt, and Halley type comets (black line), particles which form cosmic spherules (orange), and unmelted micrometeorites (blue).*

Figure 5.15 shows the vertical deposition profiles for individual elements from different the sources, at Venus' equator. The profiles have been weighted using the coefficients for each source according to the IRAS distribution. All the ablation profiles for Venus are about 30 km above the corresponding profiles for the Earth, because Venus' atmospheric density between 100 and 130 km is about two orders of magnitude higher (Figure 5.3a).

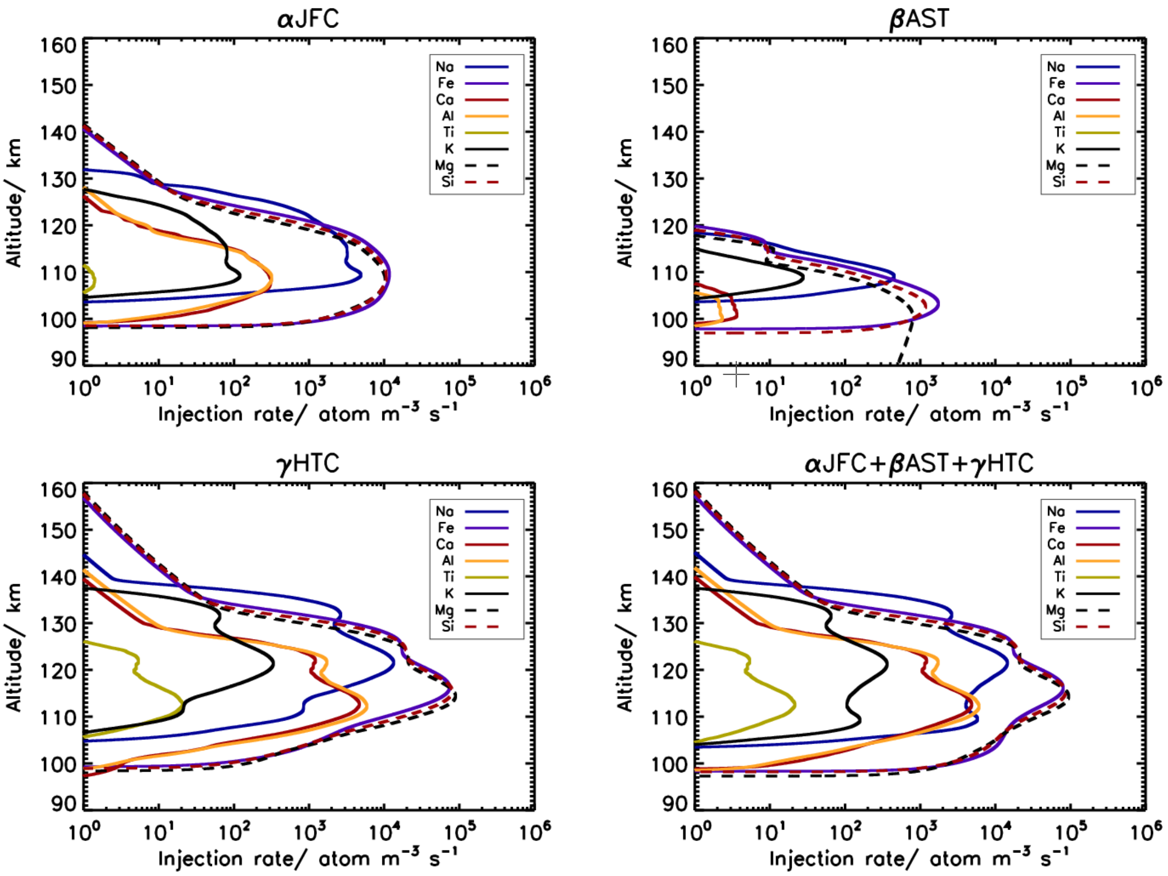

***Figure 5.15**. Ablation rate profiles for individual elements in Venus' atmosphere integrated for the JFC, AST, and HTC particle populations (noon side).*

Tables 5.3 and 5.4 list the mass balance for Venus' atmosphere on the noon and midnight sides. The contributions of the JFC, AST and LPC particles are 16.2 ± 6.8 t d^{-1} (57%), 2.2 ± 1.6 t d^{-1} (8%), and 10.0 ± 2.6 t d^{-1} (35%), respectively. The global influx is estimated to be 28.4 ± 4.4 t d^{-1}. The ablation process is favored slightly on the nightside because the concentration of CO_2 is about two factors higher than on the noon side below 110 km. Consequently, the fraction of ablated mass on the noon and midnight sides are 48% and 51%, respectively.

Figure 5.14b shows that significant ablation only occurs for particles larger than R = 15 μm, and that spherules become the major form of residual meteoroids for R > 50 μm, although most of these larger particles enter at high enough speeds to ablate completely.

Table 5.3. *Global Mass Input from the four cosmic dust sources at Venus noon side at equator.*

Mass flux	JFC (t d^{-1})	AST (t d^{-1})	LPC=HTC (t d^{-1})	Total (t d^{-1})
Unmelted micrometeorites	7.4	0.6	0.2	8.2
Cosmic spherules	4.7	1.2	0.5	6.4
Ablated atoms	4.1	0.4	9.3	13.8
Na	*0.2 (64%)*	*0.01 (79%)*	*0.2 (100%)*	*0.4 (79%)*
K	7.8×10^{-3} *(59%)*	1.4×10^{-3} *(78%)*	8.2×10^{-3} *(99%)*	*0.02 (86%)*
Fe	*1.4 (31%)*	*0.2 (28%)*	*2.7 (95%)*	*4.3 (54%)*
Si	*0.6 (24%)*	*0.06 (16%)*	*1.5 (93%)*	*2.2 (49%)*
Mg	*0.5 (20%)*	*0.03 (9%)*	*1.3 (92%)*	*1.8 (43%)*
Ca	*0.02 (9%)*	2.3×10^{-4} *(0.8%)*	*0.1 (83%)*	*0.1 (26%)*
Al	*0.01 (6%)*	1.0×10^{-4} *(0.4%)*	*0.1 (74%)*	*0.1 (27%)*
Ti	1.0×10^{-4}*(3%)*	1.6×10^{-6} *(1%)*	5.9×10^{-4} *(99%)*	6.9×10^{-4} *(40%)*
O	*1.5 (25%)*	*0.1 (17%)*	*3.5 (97%)*	*5.1 (50%)*
Total	**16.24**	**2.18**	**10.02**	**28.44**

Table 5.4. *Global Mass Input from the four cosmic dust sources at Venus midnight side at equator.*

Mass flux	JFC (t d^{-1})	AST (t d^{-1})	LPC=HTC (t d^{-1})	Total (t d^{-1})
Unmelted micrometeorites	6.7	0.5	0.2	7.4
Cosmic spherules	4.9	1.2	0.4	6.5
Ablated atoms	4.6	0.5	9.4	14.5
Na	*0.2 (64%)*	*0.01 (84%)*	*0.2 (100%)*	*0.4 (79%)*
K	8.4×10^{-3} *(63%)*	1.5×10^{-3} *(82%)*	8.2×10^{-3} *(100%)*	*0.02 (86%)*
Fe	*1.6 (35%)*	*0.2 (34%)*	*2.7 (95%)*	*4.5 (54%)*
Si	*0.7 (27%)*	*0.07 (21%)*	*1.5 (93%)*	*2.2 (49%)*
Mg	*0.5 (23%)*	*0.04 (13%)*	*1.4 (93%)*	*1.9 (46%)*
Ca	*0.02 (10%)*	3.5×10^{-4} *(1%)*	*0.1 (85%)*	*0.1 (26%)*
Al	*0.01 (7%)*	1.6×10^{-4} *(0.5%)*	*0.1 (77%)*	*0.1 (27%)*
Ti	1.2×10^{-4}*(12%)*	2.3×10^{-6} *(2%)*	6.1×10^{-4} *(100%)*	7.3×10^{-4} *(43%)*
O	*1.7 (28%)*	*0.2 (22%)*	*3.5 (97%)*	*5.4 (53%)*
Total	**16.24**	**2.20**	**10.02**	**28.44**

5.5. COSMIC DUST ENTERING TITAN'S ATMOSPHERE

Grün et al. [1985] developed a model to estimate the flux of IDPs, assuming an isotropic flux of meteoroids at the Earth with a mean velocity of v_{1AU} = 20 km s^{-1} and a meteoroid density of 2.5 g cm^{-3}. This model considers a wide mass range from 10^{-18} to 100 g. *Cuzzi and Estrada* [1998] suggested the following relationship between the orbital velocity of the meteoroids and the distance to the Sun:

$$v(\delta_S) = \frac{v_{1AU}}{\sqrt{\delta_S}} \qquad [5.2]$$

where v_{1AU} is the velocity at 1 AU and δ_S is the distance to the Sun, which is 10 AU in the case of Titan.

The gravitational focus, η_e, for Saturn and Titan can be calculated as follows:

$$\eta_e = 1 + \left(\frac{v_\infty}{v_{10AU}}\right)^2 \qquad [5.3]$$

where v_∞ is the escape velocity, 7.8 km s^{-1} for Saturn at the orbital distance of Titan and 2.35 km s^{-1} for Titan in the altitude range where most meteoric ablation occurs. Consequently, the mean velocity of meteoroids entering Titan's upper atmosphere is [*Molina-Cuberos et al.*, 2001]:

$$\bar{v}_{Titan} = v_{10AU} \cdot \eta_{eS} \cdot \eta_{eT} \approx 18\ km\ s^{-1} \qquad [5.4]$$

Frankland et al. [2016] analyzed the fraction of cosmic dust particles that ablate in Titan's atmosphere. For this purpose, EKB particles were taken to have an olivinic composition, as determined by the analysis of comet 81P/Wild 2 dust samples [*Gainsforth et al.*, 2015; *Zolensky*, 2007], with a Fe:Mg ratio of ~0.6: which implies a melting point of 1750 K according to the olivine phase diagram [*Vondrak et al.*, 2008]. Figure 5.7 (right panel) shows the elemental injection rates for a 100 µg mass meteoroid with an entry velocity of 18 km s^{-1}. The most volatile elements, Na and K, are released at ~550 km, whereas the main compounds Fe, Mg, and Si are released about 70 km below. Owing to Titan's large scale height, which is ~40 km at these meteoric ablation altitudes, ablation occurs over a wider range of altitudes compared to the terrestrial planets [*Molina-Cuberos et al.*, 2001; *Vondrak et al.*, 2008; *Whalley and Plane*, 2010].

Figure 5.16 (left panel) illustrates the mass fraction of a meteoroid that ablates estimated from CABMOD, plotted as a function of the particle size and entry velocity with a density of 2500 kg m^{-3} [*Han et al.*, 2011]. The cosmic dust entry velocity into Titan's atmosphere ranges from 2.6 to 29.1 km s^{-1}, with a mean speed of 18 km s^{-1} as discussed above. The plot shows that particles smaller than 10 µm do not reach the melting point of 1750 K, so only a very small fraction (< 1%) of mass is lost by sputtering. Larger particles exhibit more loss through melting and evaporation, e.g. a particle of 200 µm of radius (~100 µg) loses up to 90% of its mass at the highest entry velocities.

Frankland et al. [2016] concluded that only particles smaller than 10 µm contribute significantly to the available surface area for heterogeneous chemistry, whereas larger particles sediment very rapidly through Titan's atmosphere.

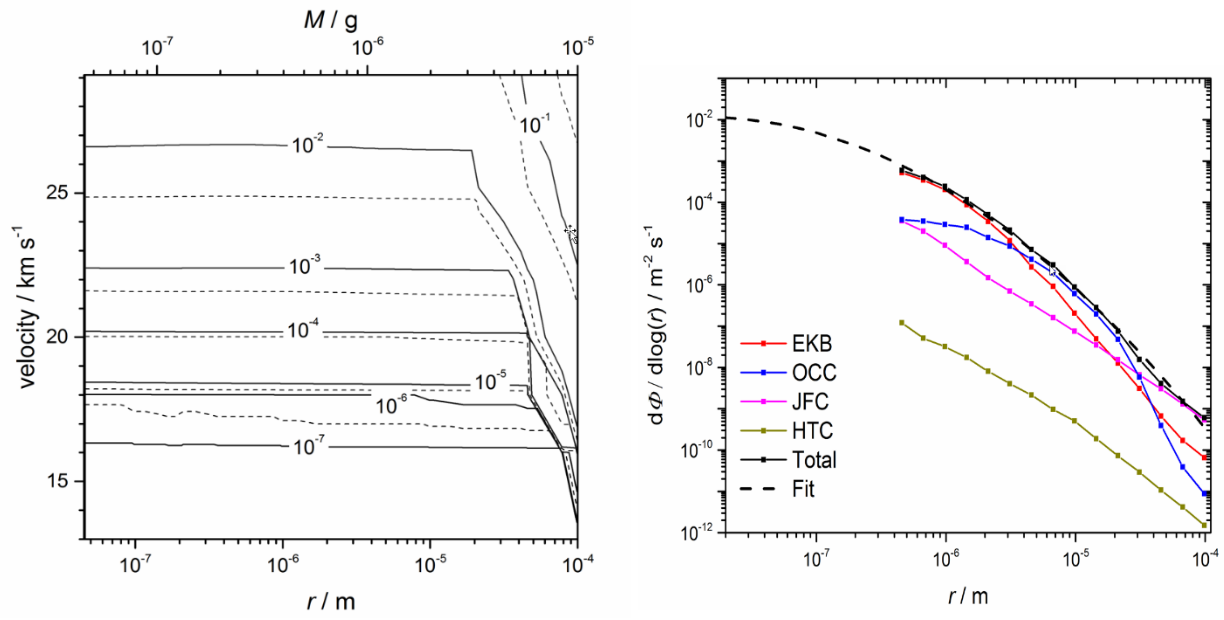

Figure 5.16*. Left panel: Ablated fraction of a meteoroid with a particle density of 2500 kg m^{-3} as a function of mass and velocity. Right panel: Differential flux of cosmic dust particles into Titan's atmosphere, showing the total flux made up of particles from EKB (Edgeworth-Kuiper Belt), JFC (Jupiter-Family Comets), OCC (Oort-Cloud Comets), and HTC (Halley-Type Comets); the line labelled Fit is the parameterization in equation [5.5]. Reproduced from Frankland et al. [2016].*

There are several sources which contribute to the flux of cosmic dust entering Titan's atmosphere including EKB objects and various cometary families (e.g. JFCs and HTCs) [*Landgraf et al.*, 2002; *Poppe*, 2016; *Poppe and Horanyi*, 2012]. Dust from EKB objects forms through either mutual collisions or interstellar dust bombardment [*Stern*, 1996; *Yamamoto and Mukai*, 1998], while cometary cosmic dust originates from sublimation and/or sporadic outbursts [*Kelley et al.*, 2013; *Sekanina*, 1996]. Data collected from the Pioneer 10 meteoroid detector and from the Student Dust Counter (SDC) on the New Horizons mission has been used to constrain the overall mass production rate from the EKB and the differential mass production distribution into the Saturnian system [*Han et al.*, 2011; *Poppe*, 2016; *Poppe and Horanyi*, 2012].

Figure 5.16 (right panel) shows the contribution of each cosmic dust source to the differential flux into Titan's atmosphere. The flux from OCCs is an upper limit, since the Pioneer 10 data can be fit with only contributions from JFC and EKB grains. The contribution of the HTCs to the overall flux is relatively low. The modelled differential flux can be fit to the following parameterization of particle radius R (in m):

$$\frac{d\emptyset}{dLog_{10}(R)} = 6.22 \times 10^{-34} R^{-(7.96+0.506log_{10}(R))} \quad \text{[particle m}^{-2}\text{ s}^{-1}\text{]} \qquad [5.5]$$

Figure 5.16 (right panel) shows this parameterization extrapolated from the measured particle size range (0.45-100 µm) down to 20 nm. The gradual fall-off in the differential is expected because solar radiation pressure ejects very small particles from the solar system [*Nesvorný et al.*, 2010], and the Saturnian magnetosphere may also prevent small particles reaching the Moons, as has been modelled in the case of Jupiter [*Colwell and Horanyi*, 1996]. According to Figure 5.16 (right panel), the total mass of un-ablated cosmic dust into Titan's atmosphere is 0.14 tonnes per Earth day, which is one order of magnitude less a previous estimate 1.4 t d^{-1} [*Molina-Cuberos et al.*, 2001]. However, *Molina-Cuberos et al.* [2001] estimated this flux based on extrapolations of dust grains models from 1 AU, which *Poppe* [2016] has pointed out will over-predict the mass input by about 1 order. However, the differential flux illustrated in Figure 5.16 (right) is essentially based on two data points (Pioneer 10 and SDC) so is probably uncertain within an order of magnitude.

5.6. SUMMARY OF THE CHAPTER

In this chapter the contribution of each cosmic dust population on the atmospheres of Venus and Mars is estimated by combining CABMOD [*Vondrak et al.*, 2008] and the ZCM constrained by the IRAS observations [*Nesvorný et al.*, 2010]. Venus' atmosphere is much denser than the atmospheres of Earth or (especially) Mars in the typical range of altitudes at which ablation occurs on each planet. This fact favors significantly the ablation process on Venus, especially on the midnight side due to the atmospheric asymmetry. [*Hedin et al.*, 1983; *Keating et al.*, 1985]. As consequence, 48% of the incoming mass flux ablates on the noon side compared with 51% in midnight side. Mars represents the opposite extreme with a 48% of unmelted mass and an ablated fraction of 35%. The total input mass has estimated to be 2.3 ± 1.2 t d^{-1} in Mars' atmosphere and 28.4 ± 7.4 t d^{-1} on Venus.

The IUVS spectrograph aboard the MAVEN spacecraft showed significantly increased emissions from Mg^+, Mg, Fe^+, and Fe that were not present before the Comet Siding Spring approach [*Schneider et al.*, 2015]. The spectra exhibit new emissions from

Mg^+, Mg, Fe^+, and Fe that were not present before the comet encounter. CABMOD was combined with the 1-D atmospheric model [*Whalley and Plane*, 2010] and satisfactorily modelled the evolution of the Mg^+ profile, though predicted that a substantial Mg layer should have been present which was not observed.

Finally, the ablated fraction of meteoroids on Titan's atmosphere was explored. Particles smaller than 10 µm (~2 µg) do not reach the melting point of 1750 K, although larger particles exhibit more loss through melting and evaporation [*Frankland et al.*, 2016]. The total mass of un-ablated cosmic dust into Titan's atmosphere is estimated to be 0.14 tonnes per Earth day, one order of magnitude less a previous estimate [*Molina-Cuberos et al.*, 2001].

CHAPTER 6: CONCLUSIONS AND FUTURE WORK

6.1. MAJOR FINDINGS

The rate of input of cosmic dust into the Earth's atmosphere has long been a subject of investigation. According to the most recent estimates, the mass input rate of IDPs ranges from 5 t d^{-1} to 270 t d^{-1} [*Plane*, 2012]. If the upper range of the estimates is correct, then vertical transport in the middle atmosphere must be faster than is generally thought to be the case, and meteoritic material is removed more rapidly; if the lower range is correct, then our understanding of the dust evolution in the solar system, and transport mechanisms from the middle atmosphere to the Earth's surface, will need to be revised. The overall aim of this thesis has been to produce a Meteoric Input Function (MIF) for the Earth's atmosphere, and then to extend this study to Venus, Mars, and Titan.

The major findings of this thesis are as follows:

1. The Chemical Ablation MODel (CABMOD) [*Vondrak et al.*, 2008] has been combined with three quite different mass/velocity distributions of cosmic dust: a model constrained by observations of mid-IR emissions from the Zodiacal Dust Cloud – the ZCM model – [*Nesvorný et al.*, 2010; *Nesvorný et al.*, 2011], a model based on direct measurements of the impact craters of meteoroids on a space-borne detector – the LDEF model – [*Love and Brownlee*, 1993; *McBride et al.*, 1999], and an astronomical model describing the portion of the incoming flux measured by meteor head echo detections with High-Power and Large-Aperture (HPLA) radars [*Fentzke and Janches*, 2008; *Pifko et al.*, 2013]. The accretion of cosmic spherules for each of these three cosmic dust models, as well as the absolute ablation fluxes of Na and Fe are estimated and compared to observations and models. The present work shows that a significant fraction of the incoming dust particles needs to consist of small (< 5 µg) and slow (< 15 km s^{-1}) particles in order to explain the measured accretion rate of cosmic spherules at the surface [*Taylor et al.*, 1998], as well as the significant differential ablation of the more refractory meteoric metals with respect to Na in the Mesosphere Lower-Thermosphere (MLT).

2. The MASI (Meteor Ablation Simulator) instrument was developed to assess and refine the assumptions of in CABMOD, in particular the melting and evaporation

rates of the elemental constituents. IDPs (for example ground-up meteorite particles) of radii between 9 and 150 µm are heated to high temperatures (2900 K) in a few seconds, thus emulating their heating profiles during atmospheric entry. Consequently, it is possible to test both the thermodynamic model within CABMOD, MAGMA [*Fegley and Cameron*, 1987; *Schaefer and Fegley*, 2004; 2005], and the Hertz-Knudsen relation to describe the evaporation kinetics.

3. Three different meteorite samples have been used in MASI to evaluate the ablation profiles of Na, Fe, and Ca: Allende (CV3), Chergach (H5), and Murchinson (CM2). CABMOD reproduces the general features of the MASI experiments, such as the relative position of the ablation curves and the position of the peaks of Na and Ca. In general, the previous version of CABMOD (CABMOD 1) does not reproduce efficiently the width of the Na and Fe peaks, and the magnitude of the Ca ablation relative to Na, i.e. instantaneous properties of single meteors that may be important for radar detection [*Gomez-Martín et al.*, 2016]. In a first attempt to improve the agreement between CABMOD and MASI, the model was upgraded with the latest version of the MAGMA code, which includes revised data for Na and K alumino-silicates [*Holland and Powell*, 2011]. Revision of the thermodynamics of Na resulted in lower equilibrium vapour pressures and thus in a lower evaporation rate, which better fits the high temperature tail of the Na pulses. A temporary solution for the Na profile was found by increasing the width of the temperature dependence of the sticking coefficient in the transition between the liquid and solid phases. This should help in the current efforts to better model radar head echoes and reduce uncertainties in the simulation of observed radar meteor rates. Due to its low ionization potential and high volatility, ablated Na is the major contributor to the threshold detectability of meteors by radar. The current version of CABMOD (CABMOD 2) produces reliable results for the integrated differential ablation of Fe, and presumably for other metals such as Si or Mg which will be studied in a future work.

4. *Nesvorný et al.* [2010] concluded that the dominant source of cosmic dust is JFCs, with a contribution of 85-95%. In the present study, the absolute contribution of each dust source – JFCs, ASTs, and HTCs – to the global input of cosmic dust is constrained by the cosmic spherule accretion rate at the bottom of an ice chamber at the Amundsen-Scott base at South Pole [*Taylor et al.*, 1998], as well as current

estimates of the vertical fluxes of Na and Fe atoms above 87.5 km in the atmosphere [*Gardner et al.*, 2016; *Gardner et al.*, 2014; *Huang et al.*, 2015]. Because HTCs and OCCs are characterized by high entry velocities, it is not possible to distinguish between them in terms of these constraints. Two different mass distributions for the JFCs are compared: the first derived from IRAS observations, and the second inferred from the most recent analysis provided by the Planck satellite. One additional constraint on the solution is the elemental abundance ratio of Na to Fe in IDPs. Several authors have reported a Na overabundance in cometary particles [*Gainsforth et al.*, 2015; *Hilchenbach et al.*, 2016; *Jessberger et al.*, 1987; *Trigo-Rodriguez and Llorca*, 2007]. Thus, the average enrichment factor is 2.9 ± 1.3. In the present study, the optimal fit for Plank and IRAS distribution is found to be when an Na enrichment factor of 2.5 is assumed. The results for the Planck and IRAS distributions are quite different. In terms of the global mass input rate, the absolute contributions of the JFC, AST and LPC particles to the Planck distribution are: 34.6 ± 13.8 t d^{-1} (80%), 3.7 ± 2.1 t d^{-1} (8%), and 5.0 ± 2.7 t d^{-1} (12%), respectively. In the case of the IRAS distribution: 13.7 ± 5.7 t d^{-1} (57%), 2.9 ± 2.1 t d^{-1} (13%) and 7.4 ± 1.9 t d^{-1} (30%), respectively. A significant result of the present study is that the JFC-Planck particles contribute (80 ± 17)% of the mass input to the terrestrial atmosphere. This is consistent with the conclusions of *Nesvorný et al.* [2010], *Yang and Ishiguro* [2015], and *Rowan-Robinson and May* [2013]. In contrast, although the JFC-IRAS is still the dominant source, its contribution is estimated to be only (57 ± 19)%.

5. CABMOD was combined with the ZCM extended to Venus and Mars and constrained by the IRAS observations. In the case of Mars, the contributions of the JFC, AST, and LPC particles are 1.1 ± 0.4 t d^{-1} (47%), 0.3 ± 0.2 t d^{-1} (14%), and 0.9 ± 0.2 t d^{-1} (39%), respectively. An important result is that 94% of the asteroidal particles on Mars do not reach the melting point compared with 34% in the Earth. For the Venusian atmosphere the contributions of the JFC, AST, and LPC particles are 16.2 ± 6.8 t d^{-1} (57%), 2.2 ± 1.6 t d^{-1} (8%), and 10.0 ± 2.6 t d^{-1} (35%), respectively.

6. The IUVS spectrograph aboard the MAVEN spacecraft captured spectra of the Martian atmosphere 3 h before and 6 h after the Comet Siding Spring approach [*Schneider et al.*, 2015]. The spectra exhibit new emissions from Mg^+, Mg, Fe^+, and Fe that were not present before the comet encounter. CABMOD was combined with

a 1-D Mars atmospheric model [*Whalley and Plane,* 2010] to follow the chemical evolution of Fe and Mg. The model outputs and the measurements of Mg^+ are in good accord, although the predicted Mg layer was not observed by MAVEN.

7. The ablated fraction of meteoroids in Titan's atmosphere is explored. Particles smaller than 10 µm (~2 µg) do not reach the melting point of 1750 K. However, larger particles exhibit more loss through melting and evaporation [*Frankland et al.*, 2016]. The total mass of un-ablated cosmic dust into Titan's atmosphere is estimated to be 0.14 tonnes per Earth day, one order of magnitude less a previous estimate [*Molina-Cuberos et al.*, 2001].

These points have achieved the specific aims set out in Chapter 1, namely: 1. To analyze the impact of the ZCM in the atmospheres of Earth, Venus, and Mars; 2. To test and refine CABMOD with the novel MASI instrument, and 3. To estimate the contribution of the different populations of cosmic dust to the global mass influx.

6.2. FUTURE WORK

The main points that will be treated in a future work are as follows:

1. **Multiphase treatment**. An important assumption in CABMOD is the mineralogy of IDPs, where a single mineral (olivine) is considered. This selection is justified by the high recurrence of this mineral phase in IDPs and by the evolution of hydrated silicates into anhydrous silicates at temperatures well below melting [*Greshake et al.*, 1998; *Sandford and Bradley,* 1989]. However, experiments with MASI have revealed that this assumption may be too simplistic in some cases [*Gomez-Martín et al.*, 2016]. For example, Chergach exhibits the presence of lower and higher temperature phases for Fe: the high temperature phase is related to forsteritic olivine, whereas the low temperature Fe-bearing phase is not considered in CABMOD and may be related to the presence of other minerals such as troilite (FeS). In essence, chondrites are assemblages of different metal alloys and minerals so that a particle may exhibit ablation profiles more complex than those simulated by CABMOD. In order to improve the agreement between CABMOD and MASI for different metals, a multi-phase aggregate treatment of IDPs should be implemented in CABMOD to cover minor mineral phases, such as troilite or Ni-Fe.

2. **Study of new metals in MASI**. The ablation of other significant meteoric metals such as Si, Mg, Al, K or Ni will be studied in MASI. The results will allow the assessment and refinement of the ablation profiles of these metals in CABMOD. In turn, these results will indicate whether more mineral phases should be considered in CABMOD.

3. **New elements in CABMOD**. The current version of MAGMA within CABMOD considers eight different metals: Na, K, Fe, Si, Mg, Ca, Al, and Ti, to model the silicate bulk. However, other elements such as S and Ni are present in chondrites in a lesser or greater proportion [*Mason*, 1979], and metals as Pt and Ir are incorporated in the particle in different phases. Nonetheless, data for Pt and Ir are scarce because they are difficult to determine, though this is now possible using recent techniques such as radiochemical neutron activation analysis [*Horan et al.*, 1999]. The ablation of Pt and Ir is important for understanding the phases in which these elements may be deposited in ice cores and deep-sea sediments [*Gabrielli et al.*, 2004b]. In future work, CABMOD should be extended to cover the analysis of these elements.

4. **Fragmentation.** Particles which pass through the atmosphere may fragment into smaller grains. There are several ways to model fragmentation. *Campbell-Brown and Koschny* [2004] and *Kikwaya et al.* [2011] assumed the mechanism of thermal disruption to fit the light curves of meteors. In this case, the meteor fragments into smaller grains when a designated temperature is reached. Normally, the selected temperature is related with the onset of the luminosity. Thermal erosion represents another way to model the fragmentation of grains [*Borovicka et al.*, 2007]. The fragmentation process of faint meteoroids is not implemented in the current version of CABMOD which treats the particle as monolith during the ablation process. In future work different ways of treating meteoroid fragmentation will be explored.

5. **Modelling meteoric ion layers in Mars' and Venus' atmospheres**. In this thesis the contribution of each cosmic dust population to these planetary atmospheres was assessed using the ZCM constrained by IRAS observations. However, *Carrillo-Sánchez et al.* [2016] concluded that the most recent version of the ZCM model constrained by the Planck satellite are quite consistent with the conclusions of *Nesvorný et al.* [2010], *Yang and Ishiguro* [2015], and *Rowan-Robinson and May*

[2013]. In future work the contribution of each cosmic source to the atmospheres of Mars and Venus should be evaluated using the ZCM constrained by Planck observations. Moreover, this analysis should be completed by a study of the diurnal variation of Na, Na^+, Mg, Mg^+, Fe and Fe^+ using the most recent version of the 1-D atmospheric model for Mars and Venus [*Whalley and Plane*, 2010].

7. REFERENCES

Ade, P. A. R., et al. (2014), Planck 2013 results. XIV. Zodiacal emission, *Astron. Astrophys.*, *571*, 25.

Adolfsson, L. G., B. A. S. Gustafson, and C. D. Murray (1996), The Martian atmosphere as a meteoroid detector, *Icarus*, *119*(1), 144-152.

Alexander, C. M. O., S. Taylor, J. S. Delaney, M. Pixue, and G. F. Herzog (2002), Mass-dependent fractionation of Mg, Si, and Fe isotopes in five stony cosmic spherules, *Geochimica et Cosmochimica Acta*, *66*(1), 173-183.

Asplund, M., N. Grevesse, A. J. Sauval, and P. Scott (2009), The Chemical Composition of the Sun, in *Annual Review of Astronomy and Astrophysics, Vol 47*, edited by R. Blandford, J. Kormendy and E. VanDishoeck, pp. 481-522.

Badnell, D. R. (2006), Radiative Recombination Data for Modeling Dynamic Finite-Density Plasmas, *Astrophys. J. Suppl. Ser.*, *167*, 334-342.

Baggaley, W. J. (2002), *Radar observations in: meteors in the Earth's atmosphere*, 123-148 pp., Cambridge University Press, Cambridge, U.K.

Baggaley, W. J., R. G. T. Bennett, D. I. Steel, and A. D. Taylor (1994), The Advanced Meteor Orbit Radar Facility - AMOR, *Quarterly Journal of the Royal Astronomical Society*, *35*(3), 293-320.

Bailey, M. E., and C. R. Stagg (1990), The origin of Short-Period Comets, *Icarus*, *86*(1), 2-8.

Bailey, M. E., and V. V. Emelyanenko (1996), Dynamical evolution of Halley-type comets, *Mon. Not. Roy. Astron. Soc.*, *278*(4), 1087-1110.

Baldwin, B., and Y. Sheaffer (1971), Ablation and Breakup of large Meteoroids during atmosphere entry, *Journal of Geophysical Research*, *76*(19), 4653-4668.

Barlow, M. J. (1978), The destruction and growth of dust grains in interstellar space - 1. Destruction by Sputtering, *Mon. Not. Roy. Astron. Soc.*, *183*, 367-395.

Benna, M., P. R. Mahaffy, J. M. Grebowsky, J. L. Fox, R. V. Yelle, and B. M. Jakosky (2015), First measurements of composition and dynamics of the Martian ionosphere by MAVEN's Neutral Gas and Ion Mass Spectrometer, *Geophys. Res. Lett.*, *42*(21), 8958-8965.

Bird (1976), *Molecular Gas Dynamics*, Clarendon Press, Oxford.

Bird, R. Dutta-Roy, S. W. Asmar, and T. A. Rebold (1997), Detection of Titan's ionosphere from Voyager 1 radio occultation observations, *Icarus*, *130*(2), 426-436.

Bones, D. L., J. C. G. Martin, C. J. Empson, J. D. C. Sanchez, A. D. James, T. P. Conroy, and J. M. C. Plane (2016), A novel instrument to measure differential ablation of meteorite samples and proxies: The Meteoric Ablation Simulator (MASI), *Review of Scientific Instruments*, *87*(9), 12.

Borovicka, J., P. Spurny, and P. Koten (2007), Atmospheric deceleration and light curves of Draconid meteors and implications for the structure of cometary dust, *Astron. Astrophys.*, *473*(2), 661-672.

Bottke, W. F., A. Morbidelli, R. Jedicke, J. M. Petit, H. F. Levison, P. Michel, and T. S. Metcalfe (2002), Debiased orbital and absolute magnitude distribution of the near-earth objects, *Icarus*, *156*(2), 399-433.

Bottke, W. F., D. D. Durda, D. Nesvorny, R. Jedicke, A. Morbidelli, D. Vokrouhlicky, and H. Levison (2005), The fossilized size distribution of the main asteroid belt, *Icarus*, *175*(1), 111-140.

Bowen, N. L. (1913), The melting phenomena of plaglioclase feldpars, *American Journal of Science*, *34*, 577-599.

Bronshten, V. (1983), *Physics of Meteoric Phenomena*, D. Reidel Publishing Co.

Brown, P., J. Jones, R. Weryk, and M. D. Campbell-Brown (2005), The velocity distribution of meteoroids at the Earth as measured by the Canadian meteor orbit radar (CMOR), *Earth Moon and Planets*, *95*(1-4), 617-626.

Brown, P., R. E. Spalding, D. O. ReVelle, E. Tagliaferri, and S. P. Worden (2002), The flux of small near-Earth objects colliding with the Earth, *Nature*, *420*(6913), 294-296.

Brownlee, D. E., D. A. Tomandl, and E. Olszewski (1977), Interplanetary dust - A new source of extraterrestrial material for laboratory studies, *Lunar Science Conference, 8th, Houston, Tex., March 14-18, 1977, Proceedings.*, *1*(A78-41551 18-91), 149-160.

Brownlee, D. E., D. J. Joswiak, S. G. Love, A. O. Nier, D. J. Schlutter, and J. P. Bradley (1993), Identification of cometary and asteroidal particles in stratospheric IDP collections, *Lunar and Planetary Inst., Twenty-fourth Lunar and Planetary Science Conference*, *1*(A-F), 205-206.

Brownlee, D. E., et al. (2006), Comet 81P/Wild 2 under a microscope, *Science*, *314*(5806), 1711-1716.

Bryan, W. B., and G. Kullerud (1975), Mineralogy and Chemistry of the Ashmore Chondrite, *Meteoritics and Planetary Science*, *10*(1), 41-50.

Burbine, T. H. (2017), Orbit and Discovering Minor Planets, in *Ateroids: Astronomical and Geological Bodies*, edited, pp. 29-58, Cambridge University Press, United Kingdom.

Burbine, T. H., T. J. McCoy, A. Meibom, B. Gladman, and K. Keil (2002), Meteoritic parent bodies: Their number and identification., in *Asteroids III*, edited by W. F. B. e. al., pp. 653-667, University of Arizona (Tucson).

Campbell-Brown, M. D., and D. Koschny (2004), Model of the ablation of faint meteors, *Astron. Astrophys.*, *418*(2), 751-758.

Capek, D., and J. Borovicka (2009), Quantitative model of the release of sodium from meteoroids in the vicinity of the Sun: Application to Geminids, *Icarus*, *202*(2), 361-370.

Carrillo-Sánchez, J. D., J. M. C. Plane, W. Feng, D. Nesvorny, and D. Janches (2015), On the size and velocity distribution of cosmic dust particles entering the atmosphere, *Geophys. Res. Lett.*, *42*(15), 6518-6525.

Carrillo-Sánchez, J. D., D. Nesvorný, P. Porkorný, D. Janches, and J. M. C. Plane (2016), Sources of Cosmic Dust in the Earth's Atmosphere, *Geophys. Res. Lett.*, *In progress*.

Ceplecha, Z., J. Borovicka, W. G. Elford, D. O. Revelle, R. L. Hawkes, V. Porubcan, and M. Simek (1998), Meteor phenomena and bodies, *Space Sci. Rev.*, *84*(3-4), 327-471.

Clarke, R., E. Jarosewich, and B. Mason (1971), *Smithsonian Contribution to the Earth Sciences (Washington: Smithsonian Institution Press)*.

Clarke, S. A. Matthews, C. G. Mundell, and A. S. Weir (1996), On the line profiles in the spectra of the zodiacal light, *Astron. Astrophys.*, *308*(1), 273-278.

Close, S., S. M. Hunt, M. J. Minardi, and F. M. McKeen (2000), Analysis of Perseid meteor head echo data collected using the Advanced Research Projects Agency Long-Range Tracking and Instrumentation Radar (ALTAIR), *Radio Science*, *35*(5), 1233-1240.

Close, S., M. Oppenheim, S. Hunt, and L. Dyrud (2002), Scattering characteristics of high-resolution meteor head echoes detected at multiple frequencies, *J. Geophys. Res-Space Phys.*, *107*(A10), 12.

Close, S., P. Brown, M. Campbell-Brown, M. Oppenheim, and P. Colestock (2007), Meteor head echo radar data: Mass-velocity selection effects, *Icarus*, *186*(2), 547-556.

Colwell, J. E., and M. Horanyi (1996), Magnetospheric effects on micrometeoroid fluxes, *J. Geophys. Res.-Planets*, *101*(E1), 2169-2175.

Consolmagno, G. J., D. T. Britt, and R. J. Macke (2008), The significance of meteorite density and porosity, *Chem. Erde-Geochem.*, *68*(1), 1-29.

Coulson, S. G. (2002), Resistance of motion to a small, hypervelocity sphere, sputtering through a gas, *Mon. Not. Roy. Astron. Soc.*, *332*(3), 741-744.

Coulson, S. G., and N. C. Wickramasinghe (2003), Frictional and radiation heating of micron-sized meteoroids in the Earth's upper atmosphere, *Mon. Not. Roy. Astron. Soc.*, *343*(4), 1123-1130.

Cour-Palais, B. G. (1992), ESA Space Debris Tutorial.

Court, R. W., and M. A. Sephton (2009), Meteorite ablation products and their contribution to the atmospheres of terrestrial planets: An experimental study using pyrolysis-FTIR, *Geochimica Et Cosmochimica Acta*, *73*(11), 3512-3521.

Court, R. W., and M. A. Sephton (2011), The contribution of sulphur dioxide from ablating micrometeorites to the atmospheres of Earth and Mars, *Geochimica Et Cosmochimica Acta*, *75*(7), 1704-1717.

Covault, C. (1983), IRAS finds new features in deep Space, *Aviation Week & Space Technology*, *119*(20), 27-28.

Cuzzi, J. N., and P. R. Estrada (1998), Compositional evolution of Saturn's rings due to meteoroid bombardment, *Icarus*, *132*(1), 1-35.

Czajkowski, J., P. Englert, A. Bosellini, and J. G. Ogg (1983), Cobalt Enriched Hardgrounds - New Sources of Ancient Extraterrestrial Materials, *Meteoritics*, *18*(4), 286-287.

Cziczo, D., and K. Froyd (2011), Effects of aerosol properties on the formation of cirrus ice clouds, *Abstracts of Papers of the American Chemical Society*, *242*, 1.

Chambers, J. E. (1997), Why Halley-types resonate but long-period comets don't: A dynamical distinction between short- and long-period comets, *Icarus*, *125*(1), 32-38.

Chapman, C. R., D. Morrison, and B. Zellner (1975), Surface properties of asteroids: A synthesis of polarimetry, radiometry, and spectrophotometry, *Icarus*, *25*(1), 104-130.

Chau, J. L., and R. F. Woodman (2004), Observations of meteor-head echoes using the Jicamarca 50 MHz radar in interferometer mode, *Atmospheric Chemistry and Physics*, *4*, 511-521.

Christiansen, E. L. (1992), Performance equations for advanced orbital debris shields, *AIAA, Space Programs and Technologies Conference, Huntsville, AL, Mar. 24-27, 1992.* .

D'Abramo, G., A. W. Harris, A. Boattini, S. C. Werner, A. W. Harris, and G. B. Valsecchi (2001), A simple probabilistic model to estimate the population of near-Earth asteroids, *Icarus*, *153*(1), 214-217.

Delsemme, A. H. (1987), Galactic Tides affect the Oort Cloud - An Observational Confirmation, *Astron. Astrophys.*, *187*(1-2), 913-918.

Della Corte, V., F. J. M. Rietmeijer, A. Rotundi, M. Ferrari, and P. Palumbo (2013), Meteoric CaO and carbon smoke particles collected in the upper stratosphere from an unanticipated source, *Tellus Ser. B-Chem. Phys. Meteorol.*, *65*, 12.

Dermott, S. F., K. Grogan, and B. A. S. Gustafson (1996), Physics, Chemistry, and Dynamics of Interplanetary Dust, in *ASP Conf. Ser. 104, IAU Coll. 150*, edited by B. A. S. Gustafson and M. S. Hanner, San Francisco, CA.

Dermott, S. F., P. D. Nicholson, J. A. Burns, and J. R. Houck (1984), Origin of the Solar System Dust Bands discovered by IRAS, *Nature*, *312*(5994), 505-509.

Dermott, S. F., D. D. Durda, K. Grogan, and T. J. J. Kehoe (2002), Asteroid dust, *Asteroids III, W. F. Bottke Jr., A. Cellino, P. Paolicchi, and R. P. Binzel (eds), University of Arizona Press, Tucson*, 423-442.

Dermott, S. F., T. J. J. Kehoe, K. Grogan, D. D. Durda, S. Jayaraman, S. J. Kortenkamp, and M. C. Wyatt (2001), Orbital Evolution of Interplanetary Dust, in *Interplanetary Dust*, edited by E. Grün, B. Å. S. Gustafson, S. Dermott and H. Fechtig, pp. 569-639, Springer Berlin Heidelberg, Berlin, Heidelberg.

Dhomse, S. S., R. W. Saunders, W. Tian, M. P. Chipperfield, and J. M. C. Plane (2013), Plutonium-238 observations as a test of modeled transport and surface deposition of meteoric smoke particles, *Geophys. Res. Lett.*, *40*(16), 4454-4458.

Dikarev, V., E. Grün, J. Baggaley, D. Galligan, M. Landgraf, and R. Jehn (2005), The new ESA meteoroid model, in *Space Debris*, edited by L. Anselmo, pp. 1282-1289, Pergamon-Elsevier Science Ltd, Kidlington.

Divine, N. (1993), 5 Populations of Interplanetary Meteoroids, *J. Geophys. Res.-Planets*, *98*(E9), 17029-17048.

Divine, N. (1993b), *Modelling the meteoroid distributions in interplanetary space and near Earth*, ESA SD-01.

Dobrica, E., C. Engrand, J. Duprat, M. Gounelle, H. Leroux, E. Quirico, and J. N. Rouzaud (2009), Connection between micrometeorites and Wild 2 particles: From Antarctic snow to cometary ices, *Meteoritics & Planetary Science*, *44*(10), 1643-1661.

Dohnanyi, J. S. (1976), Sources of interplanetary dust: Asteroids, in *Interplanetary Dust and Zodiacal Light: Proceedings of the IAU-Colloquium No. 31, Heidelberg, June 10–13, 1975*, edited by H. Elsässer and H. Fechting, pp. 187-205, Springer Berlin Heidelberg, Berlin, Heidelberg.

Draine, B. T. (1989), Destruction processes for interstellar dust, in *Evolution of Interstellar Dust and Related Topics Enrico Fermi*, edited by J. M. G. A. Bonetti, S. Aiello, Proceedings of the International School of Physics North-Holland, Amsterdam.

Duncan, M., and H. F. Levison (1997), A scattered comet disk and the origin of Jupiter-family comets, *Science*, *276*, 1670-1672.

Duncan, M., T. Quinn, and S. Tremaine (1987), The formation and Extend of the Solar-System comet cloud, *Astron. J.*, *94*(5), 1330-1338.

Durda, D. D., and S. F. Dermott (1997), The collisional evolution of the asteroid belt and its contribution to the zodiacal cloud, *Icarus*, *130*(1), 140-164.

English, M. A., L. M. Lara, R. D. Lorenz, P. R. Ratcliff, and R. Rodrigo (1996), Ablation and chemistry of meteoric materials in the atmosphere of Titan, *Advances in space research : the official journal of the Committee on Space Research (COSPAR)*, *17*(12), 157-160.

Erickson, J. E. (1969), Analysis of the meteoroid flux measured by Explorer 16 and Lunar Orbiter, *Antronomical Journal*, *74*, 279-283.

Evans, J. V. (1965), A comparison of rocket, satellite, and radar determinations of electron temperature at midlatitudes, *Journal of Geophysical Research*, *70*(17), 4365-4374.

Fechtig, H., C. Leinert, and O. E. Berg (2001), Historical perspectives, in *Interplanetary Dust*, edited by B. A. S. G. E. Grün, S. F. Dermott, and H. Fechtig, pp. 1-55, Springer-Verlag, Berlin, Germany.

Fegley, B., and A. G. W. Cameron (1987), A vaporization model for Iron Silicate fractionation in the Mercury protoplanet, *Earth and Planetary Science Letters*, *82*(3-4), 207-222.

Feng, W., D. R. Marsh, M. P. Chipperfield, D. Janches, J. Höffner, F. Yi, and J. M. C. Plane (2013), A global atmospheric model of meteoric iron, *J. Geophys. Res.*, *118*(16), 9456-9474.

Fentzke, J. T., and D. Janches (2008), A semi-empirical model of the contribution from sporadic meteoroid sources on the meteor input function in the MLT observed at Arecibo, *J. Geophys. Res.* , *113*(A3), A03304.

Fernández, J. A. (1980), On the existence of a Comet Belt beyond Neptune, *Mon. Not. Roy. Astron. Soc.*, *192*(2), 481-491.

Fernández, J. A. (2005), *Nature, Dynamics, Origin, and their Cosmogonical Relevance*, 28-29 pp., Springer, Dordrecht, The Netherlands.

Fernández, J. A., and T. Gallardo (1994), The transfer of Comets from parabolic Orbits to Short-Period Orbits - Numerical Studies, *Astron. Astrophys.*, *281*(3), 911-922.

Fernández, J. A., and A. Morbidelli (2006), The population of faint Jupiter family comets near the Earth, *Icarus*, *185*(1), 211-222.

Festou, M. C., H. U. Keller, and H. A. Weaver (2004), *Comets II*, 223-264 pp., The University of Arizona Press (Tucson). In collaboration with Lunar and Planetary Institute (Houston), United States of America.

Fish, R. H., and J. L. Summers (1965), The effect of material Properties on Threshold Perforation, *Proc. of the 7th Hypervelocity Impact Symposium*, *6*.

Fisher, A. A., R. L. Hawkes, I. S. Murray, M. D. Campbell, and A. G. LeBlanc (2000), Are meteoroids really dustballs?, *Planet Space Sci.*, *48*, 911-920.

Fixsen, D. J., and E. Dwek (2002), The Zodiacal Emission Spectrum as Determined by COBE and Its Implications, *The Astrophysical Journal*, *578*(2), 1009.

Fjeldbo, G., W. C. Fjeldbo, and V. R. Eshleman (1966), Atmosphere of Mars - Mariner IV models compared, *Science*, *153*(3743), 1518-1524.

Florescu-Mitchell, A. I., and J. B. A. Mitchell (2006), Dissociative recombination, *Phys. Lett.*, *430*(5-6), 277-374.

Flynn, G. J. (1989), Atmospheric entry heating: A criterion to distinguish between asteroidal and cometary sources of Interplanetary Dust, *Icarus*, *77*(2), 287-310.

Flynn, G. J. (2002), Meteor's in the Earth's atmosphere, edited by I. P. W. E. Murad, Cambridge University Press, Cambridge, UK.

Flynn, G. J., and D. S. McKay (1990), An assessment of the Meteoritic contribution to the Martian soil, *Journal of Geophysical Research-Solid Earth and Planets*, *95*(B9), 14497-14509.

Fomenkova, M. N., S. Chang, and L. M. Mukhin (1994), Carbonaceous Components in the Comet Halley Dust, *Geochimica Et Cosmochimica Acta*, *58*(20), 4503-4512.

Fox, J. L., and W. T. Kasprzak (2007), Near-terminator venus ionosphere: Evidence for a dawn/dusk asymmetry in the thermosphere, *J. Geophys. Res.-Planets*, *112*(E9), 9.

Frankland, V. L., A. D. James, J. D. C. Sanchez, T. P. Mangan, K. Willacy, A. R. Poppe, and J. M. C. Plane (2016), Uptake of acetylene on cosmic dust and production of benzene in Titan's atmosphere, *Icarus*, *278*, 88-99.

Fredriksson, K., and R. Gowdy (1963), Meteoric Debris from the Southern California Desert, *Geochimica Et Cosmochimica Acta*, *27*(MAR), 241-242.

Fuschs, L. H., E. Olsen, and K. J. Jensen (1973), Mineralogy, Mineral chemistry and composition of the Murchinson (CM2) Meteorite, *Smithsonian Contribution to the Earth Sciences*, *10*(1).

Gabrielli, P., et al. (2004a), Determination of Ir and Pt down to the sub-femtogram per gram level in polar ice by ICP-SFMS using preconcentration and a desolvation system, *Journal of Analytical Atomic Spectrometry*, *19*(7), 831-837.

Gabrielli, P., et al. (2004b), Meteoric smoke fallout over the Holocene epoch revealed by iridium and platinum in Greenland ice, *Nature*, *432*(7020), 1011-1014.

Gainsforth, Z., et al. (2015), Constraints on the formation environment of two chondrule-like igneous particles from comet 81P/Wild 2, *Meteoritics & Planetary Science*, *50*(5), 976-1004.

Galligan, D. P., and W. J. Baggaley (2004), The orbital distribution of radar-detected meteoroids of the Solar system dust cloud, *Mon. Not. Roy. Astron. Soc.*, *353*(2), 422-446.

Gardner, C. S., A. Z. Liu, and Y. Guo (2016), Vertical and horizontal transport of mesospheric Na: Implications for the mass influx of cosmic dust, *J. Atmos. Sol.-Terr. Phys.*

Gardner, C. S., A. Z. Liu, D. R. Marsh, W. H. Feng, and J. M. C. Plane (2014), Inferring the global cosmic dust influx to the Earth's atmosphere from lidar observations of the vertical flux of mesospheric Na, *J. Geophys. Res-Space Phys.*, *119*(9), 10.

Gardner, C. S., X. Z. Chu, P. J. Espy, J. M. C. Plane, D. R. Marsh, and D. Janches (2011), Seasonal variations of the mesospheric Fe layer at Rothera, Antarctica (67.5 degrees S, 68.0 degrees W), *Journal of Geophysical Research-Atmospheres*, *116*, 12.

Giese, R. H., and G. Kinateder (1986), The 3-Dimensional Structure of the Interplanetary Dust Cloud, in *The Sun and the Heliosphere in Three Dimensions: Proceedings of the XIXth ESLAB Symposium, held in Les Diablerets, Switzerland, 4–6 June 1985*, edited by R. G. Marsden, pp. 441-454, Springer Netherlands, Dordrecht.

Gomez-Martín, J. C., D. Bones, J. D. Carrillo-Sánchez, and J. M. C. Plane (2016), Novel experimental simulations of the atmospheric injection of meteoric metals, *Astrophys. J.*, *Submitted*.

Gómez-Martín, J. C., D. L. Bones, C. J. Empson, J. D. Carrillo-Sanchez, A. D. James, J. M. Trigo-Rodriguez, B. Fegley, and J. M. C. Plane (2016), Novel Experimental Simulations of the Atmospheric Injection of Meteoric Metals, *In progress*.

Gorkavyi, N., L. Ozernoy, J. Mather, and T. Taidakova (2000), *NGST and the zodiacal light in the solar system*, 462-467 pp., Astronomical Soc Pacific, San Francisco.

Gradie, J., and E. Tedesco (1982), Compositional Structure of the Asteroid Belt, *Science*, *216*(4553), 1405-1407.

Grebowsky, J. M., R. A. Goldberg, and W. D. Pesnell (1998), Do meteor showers significantly perturb the ionosphere?, *J. Atmos. Sol.-Terr. Phys.*, *60*(6), 607-615.

Greenberg, R. (1982), What are comets made of - A model based on interstellar dust, *University of Arizona Press, Research supported by the Nederlandse Organisatie voor Zuiver-Wetenschappelijk Onderzoek and Stichting voor Fundamenteel Onderzoek der Materie.*, 131-163.

Greenberg, R., and M. C. Nolan (1989), Delivery of asteroids and meteorites to the inner solar system, in *Asteroid II*, edited by R. P. Binzel, T. Gehrels and M. S. Matthews, pp. 778-804, University of Arizona (Tucson).

Greshake, A., W. Klock, P. Arndt, M. Maetz, G. J. Flynn, S. Bajt, and A. Bischoff (1998), Heating experiments simulating atmospheric entry heating of micrometeorites: Clues to their parent body sources, *Meteoritics & Planetary Science*, *33*(2), 267-290.

Grogan, K., S. F. Dermott, and D. D. Durda (2001), The size-frequency distribution of the zodiacal cloud: Evidence from the solar system dust bands, *Icarus*, *152*(2), 251-267.

Grogan, K., S. F. Dermott, S. Jayaraman, and Y. L. Xu (1997), Origin of the ten degree Solar System dust bands, *Planet Space Sci.*, *45*(12), 1657-1665.

Grün, E., H. A. Zook, H. Fechtig, and R. H. Giese (1985), Collisional balance of the Meteoritic complex, *Icarus*, *62*(2), 244-272.

Grün, E., M. Baguhl, S. Kaekan, and H. A. Zook (2001), In situ measurents of Cosmic Dust, in *Interplanetary Dust*, edited by B. A. S. G. E. Grün, S. F. Dermott, and H. Fechtig, pp. 295-346, Springer-Verlag, Berlin, Germany.

Hagen, E. H. (1988), Geochemical studies of Neogene Till in the Transantarctic Mountains: evidence for an extraterrestrial component, The Ohio State University.

Hahn, J. M., H. A. Zook, B. Cooper, and B. Sunkara (2002), Clementine observations of the zodiacal light and the dust content of the inner solar system, *Icarus*, *158*(2), 360-378.

Hammer, C., and M. Maurette (1996), Micrometeorite flux on the melt zone of the west Greenland ice sheet (abstract), *Meteorit. Planet. Sci.*, *31* (A56).

Han, D., A. R. Poppe, M. Piquette, E. Grun, and M. Horanyi (2011), Constraints on dust production in the Edgeworth-Kuiper Belt from Pioneer 10 and New Horizons measurements, *Geophys. Res. Lett.*, *38*, 5.

Hanel, R., et al. (1981), Infrared Observations of the Saturnian System from Voyager-1, *Science*, *212*(4491), 192-200.

Hawkes, R. L., and J. Jones (1975), A quantitative model for the ablation of dustball meteors, *Monthly Notices of the Royal Astronomical Society, Research supported by the National Research Council of Canada*, *173*, 339-356.

Hedin, A. E., H. B. Niemann, W. T. Kasprzak, and A. Seiff (1983), Global empirical model of the Venus thermosphere, *J. Geophys. Res-Space Phys.*, *88*(NA1), 73-83.

Hervig, M. E., L. L. Gordley, L. E. Deaver, D. E. Siskind, M. H. Stevens, J. M. Russell, S. M. Bailey, L. Megner, and C. G. Bardeen (2009), First Satellite Observations of Meteoric Smoke in the Middle Atmosphere, *Geophys. Res. Lett.*, *36*, 5.

Hilchenbach, M., et al. (2016), Comet 67P/Churyumov-Gerasimenko: Close up on dust particles fragments, *Astrophys. J. Lett.*, *816*(2), 6.

Hirschi, D. C., and D. B. Beard (1987), Doppler shifts in the Zodiacal Light, *Planet Space Sci.*, *35*(8), 1021-1027.

Holland, T. J. B., and R. Powell (2011), An improved and extended internally consistent thermodynamic dataset for phases of petrological interest, involving a new equation of state for solids, *Journal of Metamorphic Geology*, *29*(3), 333-383.

Hong, S. S. (1985), Henvey-Greenstein Representation of the mean volumen scattering phase function for Zodiacal Dust, *Astron. Astrophys.*, *146*(1), 67-75.

Horan, M. F., R. J. Walker, and J. W. Morgan (1999), High Precision Measurements of Pt and OS in Chondrites, *30th Annual Lunar and Planetary Science Conference, March 15-29, 1999, Houston, TX, abstract no. 1412*.

Horner, J., N. W. Evans, and M. E. Bailey (2004), Simulations of the population of Centaurs - I. The bulk statistics, *Mon. Not. Roy. Astron. Soc.*, *354*(3), 798-810.

Hsieh, H. H., and N. Haghighipour (2016), Potential Jupiter-Family comet contamination of the main asteroid belt, *Icarus*, *277*, 19-38.

Huang, W., X. Chu, C. S. Gardner, J. D. Carrillo-Sánchez, W. Feng, J. M. C. Plane, and D. Nesvorný (2015), Measurements of the vertical fluxes of atomic Fe and Na at the mesopause: Implications for the velocity of cosmic dust entering the atmosphere, *Geophys. Res. Lett.*, 2014GL062390.

Hughes (1978), Meteors, in *Cosmic Dust*, edited by J. A. M. McDonnell, pp. 123-185, Wiley, London, UK.

Hughes (2003), The variation of short-period comet size and decay rate with perihelion distance, *Mon. Not. Roy. Astron. Soc.*, *346*(2), 584-592.

Hughes, D. W. (1988), Cometary magnitude distribution and the ratio between the numbers of long- and short-period comets, *Icarus*, *73*(1), 149-162.

Hughes, D. W. (1989), Cometary absolute magnitudes, their significance and distribution, *Asteroids, comets, meteors III, Proceedings of a meeting (AMC 89) held at the Astronomical Observatory of the Uppsala University*, 327.

Hughes, D. W., and P. A. Daniels (1983), The secular variation of Cometary Magnitude, *Icarus*, *53*(3), 444-452.

Humes, D. H. (1992), Large craters on the meteoroid and space debris impact experiment, *LDEF: 69 Months in Space. First Post-Retrieval Symposium, Part 1; p 399-418*.

Hunten, D. M., R. P. Turco, and O. B. Toon (1980), Smoke and Dust Particles of Meteoric Origin in the Mesosphere and Stratosphere, *J. Atmos. Sci.*, *37*(6), 1342-1357.

Hut, P., and S. Tremaine (1985), Have Interstellar Clouds disrupted the Oort Cloud Comet?, *Astron. J.*, *90*(8), 1548-1557.

Ip, W. H. (1990), Meteoroid ablation processes in Titan's atmosphere, *Nature*, *345*(6275), 511-512.

Ipatov, S. I., A. S. Kutyrev, G. J. Madsen, J. C. Mather, S. H. Moseley, and R. J. Reynolds (2008), Dynamical zodiacal cloud models constrained by high resolution spectroscopy of the zodiacal light, *Icarus*, *194*(2), 769-788.

Ishiguro, M., R. Nakamura, Y. Fujii, and T. Mukai (1999), Comparative studies of visible and IRAS interplanetary dust bands, *Publications of the Astronomical Society of Japan*, *51*(3), 363-366.

Jacchia, L. G. (1963), *The Moon, Meteorites and Comets*, University of Chicago Press.

Jakosky, B. M., et al. (2015), The Mars Atmosphere and Volatile Evolution (MAVEN) Mission, *Space Sci. Rev.*, *195*(1-4), 3-48.

Janches, D., and D. O. ReVelle (2005), Initial altitude of the micrometeor phenomenon: Comparison between Arecibo radar observations and theory, *J. Geophys. Res.*, *110*(A8), A08307.

Janches, D., and J. L. Chau (2005), Observed diurnal and seasonal behavior of the micrometeor flux using the Arecibo and Jicamarca radars, *J. Atmos. Sol.-Terr. Phys.*, *67*(13), 1196-1210.

Janches, D., S. Close, and J. T. Fentzke (2008), A comparison of detection sensitivity between ALTAIR and Arecibo meteor observations: Can high power and large aperture radars detect low velocity meteor head-echoes, *Icarus*, *193*(1), 105-111.

Janches, D., L. P. Dyrud, S. L. Broadley, and J. M. C. Plane (2009), First observation of micrometeoroid differential ablation in the atmosphere, *Geophys. Res. Lett.*, *36*, 5.

Janches, D., C. J. Heinselman, J. L. Chau, A. Chandran, and R. Woodman (2006), Modeling the global micrometeor input function in the upper atmosphere observed by high power and large aperture radars, *J. Geophys. Res.*, *111*(A7), A07317.

Janches, D., M. C. Nolan, D. D. Meisel, J. D. Mathews, Q. H. Zhou, and D. E. Moser (2003), On the geocentric micrometeor velocity distribution, *J. Geophys. Res-Space Phys.*, *108*(A6), 14.

Janches, D., J. M. C. Plane, D. Nesvorný, W. Feng, D. Vokrouhlický, and M. J. Nicolls (2014), Radar Detectability Studies of Slow and Small Zodiacal Dust Cloud Particles. I. The Case of Arecibo 430 MHz Meteor Head Echo Observations, *Astrophys. J.*, *796:41*.

Janches, D., N. Swarnalingam, J. M. C. Plane, D. Nesvorny, W. Feng, D. Vokrouhlicky, and M. J. Nicolls (2015), Radar detectability studies of slow and small Zodiacal Dust Cloud Particles II. A study of three radars with different sensitivity, *Astrophys. J.*, *807*(1), 16.

Jehanno, C., D. Boclet, P. Bonte, A. Castellarin, and R. Rocchia (1987), Identification of two populations of extraterrestrial particles in a Jurassic hardground of the southern Alps, *Lunar and Planetary Science Conference, 18th, Houston, TX, Mar. 16-20, Proceedings. Cambridge and New York/Houston, TX, Cambridge University Press/Lunar and Planetary Institute*(A89-10851 01-91), 623-630.

Jenniskens, P. (2006), *Meteor Showers and their Parent Comets*, 790 pp., Cambridge University Press, Cambridge, United Kingdom.

Jenniskens, P. (2008), Mostly dormant comets and their disintegration into meteoroid streams: A review, *Earth Moon and Planets*, *102*(1-4), 505-520.

Jessberger, E. K., and J. Kissel (1991), *Chemical properties of Cometary Dust and a note on Carbon Isotopes*, 1075-1092 pp., Kluwer Academic Publ, Dordrecht.

Jessberger, E. K., A. Christoforidis, and J. Kissel (1988), Aspects of the major element compostion of Halley dust, *Nature*, *332*(6166), 691-695.

Jessberger, E. K., A. Christoforidis, M. Solc, and J. Kissel (1987), News on Halley's Dust, *Meteoritics*, *22*(4), 419-420.

Jessberger, E. K., R. Albrecht, H. Miller, and M. Schieber (2001), Asteroids, meteorites, impacts and their consequences (Amico 2000) - Introduction, *Planet Space Sci.*, *49*(8), 761-761.

Jones (1997), Theoretical and observational determinations of the ionization coefficient of meteors, *Mon. Not. Roy. Astron. Soc.*, *288*(4), 995-1003.

Jones, J., and P. Brown (1993), Sporadic Meteor Radiant Distributions: Orbital Survey results, *Mon. Not. Roy. Astron. Soc.*, *265*(3), 524-532.

Jones, W., and I. Halliday (2001), Effects of excitation and ionization in meteor trains, *Monthly Notices aof the Royal Astronomical Society*, *320*(4), 417-423.

Kalashnikova, O., M. Horányi, G. E. Thomas, and O. B. Toon (2000), Meteoric smoke production in the atmosphere, *Geophys. Res. Lett.*, *27*(20), 3293-3296.

Kazimirchak-Polonskaya, E. I. (1967), Evolution of Short-Period Comet Orbits from 1660 to 2060, and the Role of the Outer Planets., *Astronomicheskii Zhurnal*, *44*, 439.

Keating, G. M., et al. (1985), Models of Venus neutral upper atmosphere: Structure and composition, *Advances in Space Research*, *5*(11), 117-171.

Keating, G. M., et al. (1998), The structure of the upper atmosphere of Mars: In situ accelerometer measurements from Mars global surveyor, in *Science*, edited, pp. 1672-1676.

Kelsall, T., et al. (1998), The COBE Diffuse Infrared Background Experiment search for the cosmic infrared background. II. Model of the interplanetary dust cloud, *Astrophys. J.*, *508*(1), 44-73.

Kelley, M. S., et al. (2013), The persistent activity of Jupiter-family comets at 3-7 AU, *Icarus*, *225*(1), 475-494.

Kessler-Silacci, J. E., C. P. Dullemond, J. C. Augereau, B. Merin, V. C. Geers, E. F. van Dishoeck, N. J. Evans, G. A. Blake, and J. Brown (2007), Probing protoplanetary disks with silicate emission: Where is the silicate emission zone?, *Astrophys. J.*, *659*(1), 680-684.

Kessler, D. J. (1969), Average relative velocity of sporadic meteoroids in Inerplanetary Space, *AIAA J.*, *7*, 2337-2338.

Khanukaeva, D. Y. (2003), On the coefficients in meteor physics equations, in *Rarefied Gas Dynamics*, edited by A. D. Ketsdever and E. P. Muntz, pp. 726-732, Amer Inst Physics, Melville.

Kikwaya, J. B., M. Campbell-Brown, and P. G. Brown (2011), Bulk density of small meteoroids, *Astron. Astrophys.*, *530*, 17.

Kissel, J., et al. (1986), Composition of Comet Halley Dust Particles from Giotto Observations, *Nature*, *321*(6067), 336-337.

Klinrad, H., J. Bendisch, H. Sdunnus, P. Wegener, and R. Westerkamp (1997b), *An introduction to the 1997 ESA MASTER model*, In Proc. Second European Conference introduction on Space Debris.

Kliore, A. J., I. R. Patel, A. F. Nagy, T. E. Cravens, and T. I. Gombosi (1979), Initial obervations of the nightside ionosphere of Venus from Pioneer Venus Orbiter Radio Occultations, *Science*, *205*(4401), 99-102.

Kneissel, B., and I. Mann (1991), *Spatial Distribution and orbital properties of Zodiacal Dust*, 139-146 pp., Kluwer Academic Publ, Dordrecht.

Koeberl, C., and E. H. Hagen (1989), Extraterrestrial Spherules in Glacial sediment from the Transartartic Mountains, Antarctica - Structure, mineralogy, and chemical-composition, *Geochimica Et Cosmochimica Acta*, *53*(4), 937-944.

Kohout, T., A. Kallonen, J. P. Suuronen, P. Rochette, A. Hutzler, J. Gattacceca, D. D. Badjukov, R. Skála, V. Böhmová, and J. Čuda (2014), Density, porosity, mineralogy, and internal structure of cosmic dust and alteration of its properties during high-velocity atmospheric entry, *Met. Planet. Sci.*, *49*(7), 1157-1170.

Kopp, E. (1997), On the abundance of metal ions in the lower ionosphere, *J. Geophys. Res-Space Phys.*, *102*(A5), 9667-9674.

Kortenkamp, S. J., and S. F. Dermott (1998), Accretion of interplanetary dust particles by the Earth, *Icarus*, *135*(2), 469-495.

Krasnopolsky, V. A., V. I. Moroz, A. A. Krysko, A. Y. Tkachuk, G. Moreels, J. Clairemidi, J. P. Parisot, M. Gogoshev, and T. Gogosheva (1987), Properties of Dust in Comet P/Halley measured by the VEGA-2 3-Channel Spectrometer, *Astron. Astrophys.*, *187*(1-2), 707-711.

Krinov, E. L. (1959), Über die Natur der Mikrometeoriten, *Chem. Erde*, *20*, 28-35.

Krinov, E. L. (1970), Meteoritical Bulletin Archive, *The Meteoritical Society*, *48*(5), 85-109.

Krueger, F. R., and J. Kissel (1987), The Chemical composition of the dust of comet P/Halley as measured by PUMA on board VEGA-1, *Naturwissenschaften*, *74*(7), 312-316.

Kuchynka, P., and W. M. Folkner (2013), A new approach to determining asteroid masses from planetary range measurements, *Icarus*, *222*(1), 243-253.

Kumar, P., J. Howarth, and I. Dutta (2014), Electric current induced flow of liquid metals: Mechanism and substrate-surface effects, *Journal of Applied Physics*, *115*(4), 11.

Kyte, F. T. (1983), *Analysis of extraterrestrial materials in terrestrial sediments*, 152 pp., PhD thesis, University of califormia, Los Angeles, California, USA.

Lanci, L., and D. V. Kent (2006), Meteoric smoke fallout revealed by superparamagnetism in Greenland ice, *Geophys. Res. Lett.*, *33*(13), 4.

Lanci, L., B. Delmonte, D. V. Kent, V. Maggi, P. E. Biscaye, and J. R. Petit (2012), Magnetization of polar ice: a measurement of terrestrial dust and extraterrestrial fallout, *Quaternary Science Reviews*, *33*, 20-31.

Landgraf, M., J. C. Liou, H. A. Zook, and E. Grun (2002), Origins of solar system dust beyond Jupiter, *Astron. J.*, *123*(5), 2857-2861.

Langowski, M., C. von Savigny, J. P. Burrows, W. Feng, J. M. C. Plane, D. R. Marsh, D. Janches, M. Sinnhuber, and A. C. Aikin (2014), Global investigation of the Mg atom and ion layers using SCIAMACHY/Envisat observations between 70 km and 150 km altitude and WACCM-Mg model results, *Atmos. Chem. Phys. Discuss.*, *14*(2), 1971-2019.

LevasseurRegourd, A. C., E. Hadamcik, and J. B. Renard (1996), Evidence for two classes of comets from their polarimetric properties at large phase angles, *Astron. Astrophys.*, *313*(1), 327-333.

Levison, H. F., and M. J. Duncan (1997), From the Kuiper Belt to Jupiter-family comets: The spatial distribution of ecliptic comets, *Icarus*, *127*(1), 13-32.

Levison, H. F., L. Dones, and M. J. Duncan (2001), The origin of halley-type comets: Probing the inner Oort cloud, *Astron. J.*, *121*(4), 2253-2267.

Levison, H. F., M. J. Duncan, L. Dones, and B. J. Gladman (2006), The scattered disk as a source of Halley-type comets, *Icarus*, *184*(2), 619-633.

Levison, H. F., A. Morbidelli, L. Dones, R. Jedicke, P. A. Wiegert, and W. F. Bottke (2002), The mass disruption of Oort cloud comets, *Science*, *296*(5576), 2212-2215.

Lewis, S. R., M. Collins, P. L. Read, F. Forget, F. Hourdin, R. Fournier, C. Hourdin, O. Talagrand, and J.-P. Huot (1999), A climate database for Mars, *Journal of Geophysical Research: Planets*, *104*(E10), 24177-24194.

Liou, J. C., S. F. Dermott, and Y. L. Xu (1995), The contribution of Cometary Dust to the Zodiacal Cloud, *Planet Space Sci.*, *43*(6), 717-722.

Lodders, S. G., and F. B. Fegley (1988), *The Planetary Scientist's Companion*, Oxford University Press, New York, USA.

Love, S. G., and D. E. Brownlee (1991), Heating and thermal transformation of micrometeoroids entering the Earth's atmosphere, *Icarus*, *89*(1), 26-43.

Love, S. G., and D. E. Brownlee (1993), A Direct Measurement of the Terrestrial Mass Accretion Rate of Cosmic Dust, *Science*, *262*(5133), 550-553.

Love, S. G., D. E. Brownlee, N. L. King, and F. Hörz (1995), Morphology of meteoroid and debris impact craters formed in soft metal targets on the LDEF satellite, *Inter. J. Impact Eng.*, *16*(3), 405-418.

Low, F. J., et al. (1984), Infrared Cirrus: New components of the extended Infrared-Emission, *Astrophys. J.*, *278*(1), L19-L22.

Lowry, S., A. Fitzsimmons, P. Lamy, and P. Weissman (2008), *Kuiper Belt Objects in the Planetary Region: The Jupiter-Family Comets*, 592 pp., University of Arizona Press, Tucson,.

Macke, R. J., G. J. Consolmagno, and D. T. Britt (2011), Density, porosity, and magnetic susceptibility of carbonaceous chondrites, *Meteoritics & Planetary Science*, *46*(12), 1842-1862.

Mackinnon, I. D. R., and F. J. M. Rietmeijer (1987), Mineralogy of chondritic Interplanetary Dust Particles, *Reviews of Geophysics*, *25*(7), 1527-1553.

Maguire, W. C., R. A. Hanel, D. E. Jennings, V. G. Kunde, and R. E. Samuelson (1981), C3H8 and C3H4 in Titan's atmosphere, *Nature*, *292*(5825), 683-686.

Maris, M., C. Burigana, and S. Fogliani (2006), Zodiacal light emission in the PLANCK mission, *Astron. Astrophys.*, *452*(2), 685-700.

Markova, O. M., O. L. Yakovlev, G. L. Semenov, and A. N. Belov (1986), Some general Results on Natural Melt Evaporation in the Knudsen Cell, *Geokhimiya*, *11*, 1559-1569.

Marsh, D. R., D. Janches, W. Feng, and J. M. C. Plane (2013), A global model of meteoric sodium, *J. Geophys. Res.*, *118*(19), 11442-11452.

Marvin, U. B., and M. T. Einaudi (1967), Black magnetic spherules from pleistocene and recent beach sands, *Geochimica Et Cosmochimica Acta*, *31*(10), 1871-&.

Mason, B. (1979), *Data of Geochemistry: Chapter B., Cosmochemistry*, Sixth Edition ed., Geological Survey, Washington, USA.

Mathews, J. D., D. Janches, D. D. Meisel, and Q. H. Zhou (2001), The micrometeoroid mass flux into the upper atmosphere: Arecibo results and a comparison with prior estimates, *Geophys. Res. Lett.*, *28*(10), 1929-1932.

Mathews, J. D., D. D. Meisel, K. P. Hunter, V. S. Getman, and Q. Zhou (1997), Very High Resolution Studies of Micrometeors Using the Arecibo 430 MHz Radar, *Icarus*, *126*(1), 157-169.

Maurette, M., C. Jehanno, E. Robin, and C. Hammer (1987), Characteristics and mass distribution of extraterrestrial dust from the Greenland ice CAP, *Nature*, *328*(6132), 699-702.

Maurette, M., C. Hammer, D. E. Brownlee, N. Reeh, and H. H. Thomsen (1986), Placers of Cosmic Dust in the Blue Ice Lakes of Greenland, *Science*, *233*(4766), 869-872.

McAuliffe, J. P., and A. A. Christou (2006), Modelling meteor ablation in the venusian atmosphere, *Icarus*, *180*(1), 8-22.

McBride, N., S. F. Green, and J. A. M. McDonnell (1999), Meteoroids and small sized debris in low earth orbit and at 1 AU: Results of recent modelling, *Adv. Space Res.*, *23*(1), 73-82.

McCord, T. B., T. V. Johnson, and J. B. Adams (1970), Asteroid Vesta: Spectra reflectivity and compositional implications, *Science*, *168*(3938), 1445-&.

McDonnell, J. A. M. (1978), *Cosmic dust*, 714 pp., John Wiley & Sons Ltd.

McDonnell, J. A. M., and K. Sullivan (1992), *Hypervelocity Impacts on Space Detectors: Decoding the Projectile Parameters, Hypervelocity Impacts in Space* Unit for Space Sciences, University of Kent (Canterbury).

McDonnell, J. A. M., S. P. Deshpande, D. H. Niblett, M. J. Neish, and P. J. Newman (1993), The Near-Earth Space Impact Environment - An LDEF Overview, *Advances in Space Research*, *13*(8), 87-101.

McKinley, D. W. R. (1961), *Meteor science and engineering*.

McNeil, W. J., S. T. Lai, and E. Murad (1998), Differential ablation of cosmic dust and implications for the relative abundances of atmospheric metals, *J. Geophys. Res.*, *103*(D9), 10899-10911.

McSween, H. Y. (1999), *Meteorites and Their Parent Planets*, Cambridge University Press.

Molina-Cuberos, G. J., J. J. Lopez-Moreno, and F. Arnold (2008), Meteoric layers in planetary atmospheres, *Space Sci. Rev.*, *137*(1-4), 175-191.

Molina-Cuberos, G. J., J. J. Lopez-Moreno, R. Rodrigo, and L. M. Lara (1999a), Chemistry of the galactic cosmic ray induced ionosphere of Titan, *J. Geophys. Res.-Planets*, *104*(E9), 21997-22024.

Molina-Cuberos, G. J., J. J. Lopez-Moreno, R. Rodrigo, L. M. Lara, and K. O'Brien (1999b), Ionization by cosmic rays of the atmosphere of Titan, *Planet Space Sci.*, *47*(10-11), 1347-1354.

Molina-Cuberos, G. J., O. Witasse, J. P. Lebreton, R. Rodrigo, and J. J. Lopez-Moreno (2003), Meteoric ions in the atmosphere of Mars, *Planet Space Sci.*, *51*(3), 239-249.

Molina-Cuberos, G. J., H. Lammer, W. Stumptner, K. Schwingenschuh, H. O. Rucker, J. J. Lopez-Moreno, R. Rodrigo, and T. Tokano (2001), Ionospheric layer induced by meteoric ionization in Titan's atmosphere, *Planet Space Sci.*, *49*(2), 143-153.

Morbidelli, A., K. J. Walsh, D. P. O'Brien, D. A. Minton, and W. F. Bottke (2015), The Dynamical Evolution of the Asteroid Belt, in *Asteroids IV*, edited by P. Michel, University of Arizona (Tucson).

Moro-Martin, A., and R. Malhotra (2002), A study of the dynamics of dust from the Kuiper belt: Spatial distribution and spectral energy distribution, *Astron. J.*, *124*(4), 2305-2321.

Mukai, T., and I. Mann (1993), Analysis of Doppler shifts in the Zodiacal Light, *Astron. Astrophys.*, *271*(2), 530-534.

Murrell, M. T., P. A. Davis, K. Nishizumi, and H. T. Millard (1980), Deep-Sea Spherules from Pacific Clay - Mass-distribution and Influx Rate, *Geochimica Et Cosmochimica Acta*, *44*(12), 2067-&.

Nesvorný, D., D. Vokrouhlicky, W. F. Bottke, and M. Sykes (2006), Physical properties of asteroid dust bands and their sources, *Icarus*, *181*(1), 107-144.

Nesvorný, D., P. Jenniskens, H. F. Levison, W. F. Bottke, D. Vokrouhlický, and M. Gounelle (2010), Cometary Origin of the Zodiacal Cloud and Carbonaceous Micrometeorites. Implications for Hot Debris Disks, *Astrophys. Journal*, *713*(2), 816-836.

Nesvorný, D., D. Janches, D. Vokrouhlický, P. Pokorný, W. F. Bottke, and P. Jenniskens (2011), Dynamical Model for the Zodiacal Cloud and Sporadic Meteors, *Astrophys. J.*, *743 (2)*, 129-144.

Noguchi, T., N. Ohashi, S. Tsujimoto, T. Mitsunari, J. P. Bradley, T. Nakamura, S. Toh, T. Stephan, N. Iwata, and N. Imae (2015), Cometary dust in Antarctic ice and snow: Past and present chondritic porous micrometeorites preserved on the Earth's surface, *Earth and Planetary Science Letters*, *410*, 1-11.

Nurmi, P., M. J. Valtonen, J. Q. Zheng, and H. Rickman (2002), Long-term evolution of Oort Cloud comets: capture of comets, *Mon. Not. Roy. Astron. Soc.*, *333*(4), 835-846.

Olsson-Steel, D., and W. G. Elford (1987), The height distribution of Radio-Meteors: Observations at 2 MHz, *Journal of Atmospheric and Terrestrial Physics*, *49*(3), 243-258.

Öpik, E. J. (1951), Collision Probabilities with the Planets and the Distribution of Interplanetary Matter, *Proceedings of the Royal Irish Academy. Section A: Mathematical and Physical Sciences*, *54*, 165-199.

Öpik, E. J. (1958), *Physics of Meteor Flight in the Atmosphere*, InterScience, New York.

Ozernoy, L. M. (2001), Physical modeling of the zodiacal dust cloud, in *Extragalactic Infrared Background and Its Cosmological Implications*, edited by M. Harwit and M. G. Hauser, pp. 17-34, Astronomical Soc Pacific, San Francisco.

Pandya, B. M., and S. A. Haider (2012), Meteor impact perturbation in the lower ionosphere of Mars: MGS observations, *Planet Space Sci.*, *63-64*, 105-109.

Patzold, M., S. Tellman, B. Hausler, D. Hinson, R. Schaa, and G. L. Tyler (2005), A sporadic third layer in the ionosphere of Mars, *Science*, *310*(5749), 837-839.

Pellinen-Wannberg, A., and G. Wannberg (1994), Meteor observations with the European Incoherent Scatter UHF Radar, *Journal of Geophysical Research: Space Physics*, *99*(A6), 11379-11390.

Peng, H., and Z. Lui (1989), Measurement of the annual flux of cosmic dust in deep-sea sediments, *Abstracts and Program for the 52nd Annual Meeting of the Meteoritical Society*, 194.

Peter, K., et al. (2014), The dayside ionospheres of Mars and Venus: Comparing a one-dimensional photochemical model with MaRS (Mart Express) and VeRa (Venus Express) observations, *Icarus*, *233*, 66-82.

Petit, J., J. Chambers, F. Franklin, and M. Nagasawa (2002), Primordial excitation and depletion of the main belt, in *Asteroids III*, edited by W. F. B. e. al., pp. 711-738, University of Arizona (Tucson).

Peucker-Ehrenbrink, B. (1996), Accretion of extraterrestrial matter during the last 80 million years and its effect on the marine osmium isotope record, *Geochimica Et Cosmochimica Acta*, *60*(17), 3187-3196.

Peucker-Ehrenbrink, B., and G. Ravizza (2000), The effects of sampling artifacts on cosmic dust flux estimates: A reevaluation of nonvolatile tracers (Os, Ir), *Geochimica Et Cosmochimica Acta*, *64*(11), 1965-1970.

Pifko, S., D. Janches, S. Close, J. Sparks, T. Nakamura, and D. Nesvorny (2013), The Meteoroid Input Function and predictions of mid-latitude meteor observations by the MU radar, *Icarus*, *223*(1), 444-459.

Plane, J. M. C. (2004), A time-resolved model of the mesospheric Na layer: constraints on the meteor input function, *Atmospheric Chemistry and Physics*, *4*, 627-638.

Plane, J. M. C. (2012), Cosmic dust in the earth's atmosphere, *Chemical Society Reviews*, *41*(19), 6507-6518.

Plane, J. M. C., and M. Helmer (1995), Laboratory study of the reactions Mg + O3 and MgO + O3. Implications for the chemistry of magnesium in the upper atmosphere, *Faraday Discussions*, *100*, 411-430.

Plane, J. M. C., and C. L. Whalley (2012), A New Model for Magnesium Chemistry in the Upper Atmosphere, *J. Phys. Chem. A*, *116*(24), 6240-6252.

Plane, J. M. C., W. Feng, and E. C. M. Dawkins (2015), The Mesosphere and Metals: Chemistry and Changes, *Chemical Reviews*, *115*(10), 4497-4541.

Plane, J. M. C., W. Feng, E. Dawkins, M. P. Chipperfield, J. Höffner, D. Janches, and D. R. Marsh (2014), Resolving the strange behavior of extraterrestrial potassium in the upper atmosphere, *Geophys. Res. Lett.*, *41*(13), 2014GL060334.

Poppe, A. R. (2016), An improved model for interplanetary dust fluxes in the outer Solar System, *Icarus*, *264*, 369-386.

Poppe, A. R., and M. Horanyi (2012), On the Edgeworth-Kuiper Belt dust flux to Saturn, *Geophys. Res. Lett.*, *39*, 6.

Prasad, M. S., N. G. Rudraswami, and D. K. Panda (2013), Micrometeorite flux on Earth during the last similar to 50,000 years, *J. Geophys. Res.-Planets*, *118*(11), 2381-2399.

Quinn, T., S. Tremaine, and M. Duncan (1990), Planetary perturbations and the origin of short-period comets, *Astrophys. J.*, *355*(2), 667-679.

Rabinowitz, D., E. Helin, K. Lawrence, and S. Pravdo (2000), A reduced estimate of the number of kilometre-sized near-Earth asteroids, *Nature*, *403*(6766), 165-166.

Reach, W. T., B. A. Franz, and J. L. Weiland (1997), The three-dimensional structure of the zodiacal dust bands, *Icarus*, *127*(2), 461-484.

Reynolds, R. J., G. J. Madsen, and S. H. Moseley (2004), New measurements of the motion of the zodiacal dust, *Astrophys. J.*, *612*(2), 1206-1213.

Robertson, H. P. (1937), Dynamical effects of Radiation in the Solar System, *Mon. Not. R. astr. Soc.*, *67*, 423-438.

Rogers, L. A., K. A. Hill, and R. L. Hawkes (2005), Mass loss due to sputtering and thermal processes in meteoroid ablation, *Planet Space Sci.*, *53*(13), 1341-1354.

Rollason, R. J., and J. M. C. Plane (2001), A kinetic study of the reactions of MgO with H_2O, CO_2 and O_2: implications for magnesium chemistry in the mesosphere, *Phys. Chem. Chem. Phys.*, *3*(21), 4733-4740.

Rowan-Robinson, M., and B. May (2013), An improved model for the infrared emission from the zodiacal dust cloud: cometary, asteroidal and interstellar dust, *Mon. Not. Roy. Astron. Soc.*, *429*(4), 2894-2902.

Rowe, B. R., D. W. Fahey, E. E. Ferguson, and F. C. Fehsenfeld (1981), Flowing afterflow studies of gas phase magnesium ion chemistry, *J. Chem. Phys.*, *75*, 3325-3328.

Rubio, L. R. B., M. J. M. Gonzalez, L. R. Herrera, J. Licandro, D. M. Delgado, P. R. Gil, and M. Serra-Ricart (2001), Modeling the dynamical and photometric behavior of faint meteors in the earth's atmosphere, in *Proceedings of the Meteoroids 2001 Conference*, edited by B. Warmbein, pp. 525-529, Esa Publications Division C/O Estec, 2200 Ag Noordwijk.

Rutherford, J. A., R. F. Mathis, B. R. Turner, and D. A. Vroom (1971), Formation of Magnesium Ions by Charge Transfer, *J. Chem. Phys.*, *55*(8), 3785.

Safarian, J., and T. A. Engh (2013), Vacuum Evaporation of Pure Metals, *Metallurgical and Materials Transactions a-Physical Metallurgy and Materials Science*, *44A*(2), 747-753.

Samuelson, R. E., W. C. Maguire, R. A. Hanel, V. G. Kunde, D. E. Jennings, Y. L. Yung, and A. C. Aikin (1983), CO2 on Titan, *J. Geophys. Res-Space Phys.*, *88*(NA11), 8709-8715.

Sandford, S. A., and J. P. Bradley (1989), Interplanetary Dust Particles collected in the Stratosphere - Observations of Atmospheric heating and constraints on their interrelationships and sources, *Icarus*, *82*(1), 146-166.

Saunders, R. W., and J. M. C. Plane (2006), A laboratory study of meteor smoke analogues: Composition, optical properties and growth kinetics, *J. Atmos. Sol.-Terr. Phys.*, *68*(18), 2182-2202.

Savich, N. A., V. A. Samovol, M. B. Vasilyev, A. S. Vyshlov, L. N. Samoznaev, A. I. Sidorenko, and D. Y. Shtern (1976), The nighttime ionosphere of Mars from Mars-4 and Mars-5 radio occultation dual-frequency measurements, *NASA. Goddard Space Flight Center Solar-Wind Interaction with the Planets Mercury, Venus, and Mars*, 41-46.

Schaefer, L., and B. Fegley (2004), A thermodynamic model of high temperature lava vaporization on Io, *Icarus*, *169*(1), 216-241.

Schaefer, L., and B. Fegley (2005), Application of an equilibrium vaporization model to the ablation of chondritic and achondritic meteoroids, *Earth Moon and Planets*, *95*(1-4), 413-423.

Schneider, N. M., et al. (2015), MAVEN IUVS observations of the aftermath of the Comet Siding Spring meteor shower on Mars, *Geophys. Res. Lett.*, *42*(12), 4755-4761.

Schulz, R., et al. (2015), Comet 67P/Churyumov-Gerasimenko sheds dust coat accumulated over the past four years, *Nature*, *518*(7538), 216-218.

Sdunnus, H. (1995), Meteoroid and space debris terrestrial environment reference model - final report, *Institute of Space flight Technology and Nuclear Reactor Technology, Technical University of Braunschweig, Germany, ESA contract No.10453/93/D/CS*.

Sdunnus, H., G. Drolshagen, and C. Lemcke (1997), Enhanced Meteoroid/debris 3-D Analysis Tool, *Second European Conference on Space Debris, Organised by ESA, held 17-19 March, 1997, ESOC, ESA-SP 393*, 655.

Sears, D. W., and R. T. Dodd (1988), Overview and Classification of Meteorites, in *Meteorites and the Early Solar System*, edited by J. F. Kerridge and M. S. Matthews, pp. 3-31, University of Arizona Press, Tucson.

Sekanina, Z. (1996), Activity of comet Hale-Bopp (1995 O1) beyond 6 AU from the Sun, *Astron. Astrophys.*, *314*(3), 957-965.

Sekanina, Z., and R. B. Southworth (1975), Physical and dynamical studies of meteors. Meteor-fragmentation and stream-distribution studies *NASA Contractor Report CR-2615, Smithsonian Institution, Cambridge, Ma, USA*, 94pp.

Simpson, J. A., D. Rabinowitz, A. J. Tuzzolino, L. V. Ksanfomality, and R. Z. Sagdeev (1987), The Dust Coma of Comet P/Halley - Measurements on the VEGA-1 and VEGA-2 Spacecraft, *Astron. Astrophys.*, *187*(1-2), 742-752.

Southworth, R. B. (1964), The size distribution of the Zodiacal Particles, *Annals of the New York, Academy of Sciences*, *119*, 54-67.

Southworth, R. B., and Z. Sekanina (1973), Physical and dynamical studies of meteors, *NASA Contractor Report CR-132535*(Special Progress Report), 106pp.

Stagg, C. R., and M. E. Bailey (1989), Stochastic capture of Short-Period Comets, *Mon. Not. Roy. Astron. Soc.*, *241*(3), 507-541.

Steel, D. I., and W. G. Elford (1991), The height distribution of Radio-Meteors: comparison of observations at different frequencies on the basis od standard Echo theory, *Journal of Atmospheric and Terrestrial Physics*, *53*(5), 409-417.

Stern, S. A. (1996), Signatures of collisions in the Kuiper Disk, *Astron. Astrophys.*, *310*(3), 999-1010.

Stokes, G. H., D. K. Yeomans, and W. F. Bottke (2003), Study to Determine the Feasibility of Extending the Search for Near-Earth Objects to Smaller Limiting Diameters *Report of the Near-Earth Object Science Definition Team. NASA Office of Space Science Report*, 154 (157-158).

Strickland, D. J., J. Bishop, J. S. Evans, T. Majeed, P. M. Shen, R. J. Cox, R. Link, and R. E. Huffman (1999), Atmospheric Ultraviolet Radiance Integrated Code (AURIC): theory, software architecture, inputs, and selected results, *Journal of Quantitative Spectroscopy & Radiative Transfer*, *62*(6), 689-742.

Stuart, J. S., and R. P. Binzel (2004), Bias-corrected population, size distribution, and impact hazard for the near-Earth objects, *Icarus*, *170*(2), 295-311.

Subasinghe, D., M. D. Campbell-Brown, and E. Stokan (2016), Physical characteristics of faint meteors by light curve and high-resolution observations, and the implications for parent bodies, *Mon. Not. Roy. Astron. Soc.*, *457*(2), 1289-1298.

Sykes, M. V., and R. Greenberg (1986), The formation and origin of the IRAS Zodiacal Dust Bands as a consequence of single collisions between asteroids., *Icarus*, *65*(1), 51-69.

Taylor (1995a), The Harvard Radio Meteor Project Meteor Velocity Distribution Reappraised, *Icarus*, *116*(1), 154-158.

Taylor (1995b), Earth encounter velocities for interplanetary meteoroids, *Advances in Space Research*, *17*(12), 205-209.

Taylor, S., and D. E. Brownlee (1991), Cosmic Spherules in the Geologic Record, *Meteoritics*, *26*(3), 203-211.

Taylor, S., J. H. Lever, and R. P. Harvey (1998), Accretion rate of cosmic spherules measured at the South Pole, *Nature*, *392*(6679), 899-903.

Taylor, S., J. H. Lever, and R. P. Harvey (2000), Numbers, types, and compositions of an unbiased collection of cosmic spherules, *Meteoritics & Planetary Science*, *35*(4), 651-666.

Taylor, S., G. Matrajt, and Y. B. Guan (2012), Fine-grained precursors dominate the micrometeorite flux, *Meteoritics & Planetary Science*, *47*(4), 550-564.

Taylor, S., G. Matrajt, J. H. Lever, D. J. Joswiak, D. E. Brownlee, and Esa (2007), Size distribution of antarctic micrometeorites, in *Workshop on Dust in Planetary Systems*, edited, pp. 145-148, Esa Publications Division C/O Estec, 2200 Ag Noordwijk.

Thomas, E., M. Horanyi, D. Janches, T. Munsat, J. Simolka, and Z. Sternovsky (2016), Measurements of the ionization coefficient of simulated iron micrometeoroids, *Geophys. Res. Lett.*, *43*(8), 3645-3652.

Tisserand, F. (1896), *Traité de Mèchanique Celeste (Paris)*.

Toppani, A., G. Libourel, C. Engrand, and M. Maurette (2001), Experimental simulation of atmospheric entry of micrometeorites, *Meteoritics & Planetary Science*, *36*(10), 1377-1396.

Trigo-Rodriguez, J. M., and J. Llorca (2007), On the sodium overabundance in cometary meteoroids, *Advances in Space Research*, *39*(4), 517-525.

Vaghi, S. (1973), The origin of Jupiter's Family of Comets, *Astron. Astrophys.*, *24*, 107-110.

Vedder, J. F., and J. C. Mandeville (1974), Microcraters formed in Glass by Projectiles of various densities, *Journal of Geophysical Research*, *79*(23), 3247-3256.

von Zahn, U. V., J. Höffner, and W. J. McNeil (2002), Meteor trails as observed by lidars, in *Meteors in the Earth's Atmosphere*, edited by E. M. a. I. P. Williams, Cambridge Univ. Press, New York.

von Zahn, U. V., K. H. Fricke, H. J. Hoffmann, and K. Pelka (1979), Venus - Eddy coefficients in the thermosphere and the inferred Helium content of the lower atmosphere, *Geophys. Res. Lett.*, *6*(5), 337-340.

Vondrak, T., J. M. C. Plane, S. Broadley, and D. Janches (2008), A chemical model of meteoric ablation, *Atmos. Chem. Phys.* , *8*, 7015-7031.

Waite, J. H., J. Bell, R. Lorenz, R. Achterberge, and F. M. Flasar (2013), A model of variability in Titan's atmospheric structure, *Planet Space Sci.*, *86*, 45-56.

Wang, J. H., and R. Brasser (2014), An Oort Cloud origin of the Halley-type comets, *Astron. Astrophys.*, *563*, 9.

Wasson, J. T., and F. T. Kyte (1987), On the Influx of Small Comets into the Earth's Atmosphere: Interpretation and comment., *Geophys. Res. Lett.*, *14*(7), 779-780.

Weidenschilling, S. J. (1977), The distribution of mass in the planetary system and solar nebula, *Astrophysics Space Science*, *51*, 153-158.

Weissman, P. R. (1979), Dynamics of the Solar System, edited by D. R. R. L. Duncombe, p. 277, Springer, Dordrecht.

Weissman, P. R. (1996), The Oort Cloud, *Completing the Invetory of the Solar System, ASP Conference Series*, *107*, 265-288.

Werner, S. C., A. W. Harris, G. Neukum, and B. A. Ivanov (2002), The near-earth asteroid size-frequency distribution: A snapshot of the lunar impactor size-frequency distribution, *Icarus*, *156*(1), 287-290.

Whalley, C. L., and J. M. C. Plane (2010), Meteoric ion layers in the Martian atmosphere, *Faraday Discussions*, *147*, 349-368.

Whalley, C. L., J. C. Gomez Martin, T. G. Wright, and J. M. C. Plane (2011), A kinetic study of Mg^+ and Mg-containing ions reacting with O_3, O_2, N_2, CO_2, N_2O and H_2O: implications for magnesium ion chemistry in the upper atmosphere, *Phys. Chem. Chem. Phys*, *13*(13), 6352-6364.

Whipple, F. L. (1967), On maintaining the meteoritic complex. Smithsonian Astrophysical *NASA Technical Reports Server (NTRS), Smithsonian Astrophysical Observatory; Cambridge, MA, United States*, 45pp.

Wieisberg, M. K., C. Smith, G. Benedix, L. Folco, K. Righter, J. Zipfel, A. Yamaguchi, and H. Chennaqui Aoudjehane (2008), The Meteoritical Bulletin, *Meteoritics and Planetary Science, 94*.

Wilkinson, S. L., and M. S. Robinson (2000), *Meteoritics and Planetary Science*, *35*, 1203.

Williams, L. P. (2002), *Meteors in the Earth's atmosphere*, 2-32 pp., Cambridge University Press, Cambridge.

Withers, P., M. Mendillo, D. P. Hinson, and K. Cahoy (2008), Physical characteristics and occurrence rates of meteoric plasma layers detected in the Martian ionosphere by the Mars Global Surveyor Radio Science Experiment, *J. Geophys. Res-Space Phys.*, *113*(A12), 15.

Wyatt, M. C. (2005), *The origin and evolution of dust belts*, 383-392 pp., Cambridge Univ Press, New York.

Yada, T., T. Nakamura, N. Takaoka, T. Noguchi, K. Terada, H. Yano, T. Nakazawa, and H. Kojima (2004), The global accretion rate of extraterrestrial materials in the last glacial period estimated from the abundance of micrometeorites in Antarctic glacier ice, *Earth Planets Space*, *56*(1), 67-79.

Yamamoto, S., and T. Mukai (1998), Dust production by impacts of interstellar dust on Edgeworth-Kuiper Belt objects, *Astron. Astrophys.*, *329*(2), 785-791.

Yang, H. G., and M. Ishiguro (2015), Origin of Interplanetary Dust through Optical Properties of the Zodiacal Light, *Astrophys. J.*, *813*(2), 9.

Ye, Q. Z., and M. T. Hui (2014), An early look of Comet C/2013 A1 (Siding Spring): Breathtaker or Nightmare?, *Astrophys. J.*, *787*(2), 10.

Yelle, R. V., D. F. Strobell, E. Lellouch, and D. Gautier (1997), Engineering Models for Titan's Atmosphere, *ESA SP*, *1177*, 243-256.

Yiou, F., and G. M. Raisbeck (1990), Cosmic spherules from Antarctic ice cores as proxy indicators of extraterrestrial matter influx during the last 150,000 years. In Workshop on Differences between Antarctic and non-Antarctic Meteorites, *LPI Technical Report 90-01. Houston: Lunar and Planetary Institute*, 99-100.

Yiou, F., G. M. Raisbeck, and C. Jehanno (1989), Influx of Cosmic Spherules to the Earth during the last approximately 10(5) years as deduced from concentrations in Antarctic Ice Cores, *Meteoritics*, *24*(4), 344-344.

Yung, Y. L., and W. B. DeMore (1982), Photochemistry of the Stratosphere of Venus - Implications for atmospheric evolution, *Icarus*, *51*(2), 199-247.

Yung, Y. L., and W. B. DeMore (1999), Introdution, in *Photochemistry of Planetary Atmospheres*, edited, Oxford University Press, New York, United States of America.

Zhang, J., D. J. Kessler, M. J. Matney, P. Eichler, R. C. Reynolds, P. D. AnzMeador, and E. G. Stansbery (1997), The NASA engineering model: A new approach, in *Space Debris*, edited by W. Flury, pp. 281-290, Pergamon Press Ltd, Oxford.

Zolensky, M. E. (2007), Report - Mineralogy and petrology of comet 81P/Wild 2 nucleus samples (vol 314, pg 1735, 2006), *Science*, *316*(5824), 543-543.

Zolensky, M. E., and D. J. Lindstrom (1992), Mineralogy of 12 large chondritic Interplanetary Dust Particles, *Proceedings of Lunar and Planetary Science*, *22*, 161-169.

Zook, H. A. (2001), Spacecraft Measurements of the Cosmic Dust Flux, in *Accretion of Extraterrestrial Matter Throughout Earth's History*, edited by B. Peucker-Ehrenbrink and B. Schmitz, pp. 75-92, Springer US, Boston, MA.